



University of Kentucky  
UKnowledge

---

Theses and Dissertations--Chemical and  
Materials Engineering

Chemical and Materials Engineering

---

2023

## **Application of multi-scale computational techniques to complex materials systems**

Mujan N. Seif

University of Kentucky, [muji.seif@comcast.net](mailto:muji.seif@comcast.net)

Author ORCID Identifier:

<https://orcid.org/0000-0002-5839-479X>

Digital Object Identifier: <https://doi.org/10.13023/etd.2023.011>

[Right click to open a feedback form in a new tab to let us know how this document benefits you.](#)

### **Recommended Citation**

Seif, Mujan N., "Application of multi-scale computational techniques to complex materials systems" (2023). *Theses and Dissertations--Chemical and Materials Engineering*. 147.  
[https://uknowledge.uky.edu/cme\\_etds/147](https://uknowledge.uky.edu/cme_etds/147)

This Doctoral Dissertation is brought to you for free and open access by the Chemical and Materials Engineering at UKnowledge. It has been accepted for inclusion in Theses and Dissertations--Chemical and Materials Engineering by an authorized administrator of UKnowledge. For more information, please contact [UKnowledge@lsv.uky.edu](mailto:UKnowledge@lsv.uky.edu).

## **STUDENT AGREEMENT:**

I represent that my thesis or dissertation and abstract are my original work. Proper attribution has been given to all outside sources. I understand that I am solely responsible for obtaining any needed copyright permissions. I have obtained needed written permission statement(s) from the owner(s) of each third-party copyrighted matter to be included in my work, allowing electronic distribution (if such use is not permitted by the fair use doctrine) which will be submitted to UKnowledge as Additional File.

I hereby grant to The University of Kentucky and its agents the irrevocable, non-exclusive, and royalty-free license to archive and make accessible my work in whole or in part in all forms of media, now or hereafter known. I agree that the document mentioned above may be made available immediately for worldwide access unless an embargo applies.

I retain all other ownership rights to the copyright of my work. I also retain the right to use in future works (such as articles or books) all or part of my work. I understand that I am free to register the copyright to my work.

## **REVIEW, APPROVAL AND ACCEPTANCE**

The document mentioned above has been reviewed and accepted by the student's advisor, on behalf of the advisory committee, and by the Director of Graduate Studies (DGS), on behalf of the program; we verify that this is the final, approved version of the student's thesis including all changes required by the advisory committee. The undersigned agree to abide by the statements above.

Mujan N. Seif, Student

Dr. Matthew J. Beck, Major Professor

Dr. Matthew J. Beck, Director of Graduate Studies



Application of multi-scale computational techniques to complex materials systems

---

DISSERTATION

---

A dissertation submitted in partial fulfillment of the  
requirements for the degree of Doctor of Philosophy in the  
College of Engineering at the University of Kentucky

By  
Mujan N. Seif  
Lexington, Kentucky

Director: Dr. Matthew J. Beck, Associate Professor of Materials Engineering  
Lexington, Kentucky  
2022

Copyright© Mujan N. Seif 2022

## ABSTRACT OF DISSERTATION

Application of multi-scale computational techniques to complex materials systems

The applications of computational materials science are ever-increasing, connecting fields far beyond traditional subfields in materials science. This dissertation demonstrates the broad scope of multi-scale computational techniques by investigating multiple unrelated complex material systems, namely scandate thermionic cathodes and the metallic foam component of micrometeoroid and orbital debris (MMOD) shielding. Sc-containing “scandate” cathodes have been widely reported to exhibit superior properties compared to previous thermionic cathodes; however, knowledge of their precise operating mechanism remains elusive. Here, quantum mechanical calculations were utilized to map the phase space of stable, highly-faceted and chemically-complex W nanoparticles, accounting for both finite temperature and chemical environment. The precise processing conditions required to form the characteristic W nanoparticle observed experimentally were then distilled. Metallic foams, a central component of MMOD shielding, also represent a highly-complex materials system, albeit at a far higher length scale than W nanoparticles. The non-periodic, randomly-oriented constituent ligaments of metallic foams and similar materials create a significant variability in properties that is generally difficult to model. Rather than homogenizing the material such that its unique characteristic structural features are neglected, here, a stochastic modeling approach is applied that integrates complex geometric structure and utilizes continuum calculations to predict the resulting probabilistic distributions of elastic properties. Though different in many aspects, scandate cathodes and metallic foams are united by complexity that is impractical, even dangerous, to ignore and well-suited to exploration with multi-scale computational methods.

KEYWORDS: multi-scale, stochastic, complexity, electronic structure, mechanics

---

Mujan N. Seif

---

December 16, 2022

Application of multi-scale computational techniques to complex materials systems

By  
Mujan N. Seif

Dr. Matthew J. Beck  
Director of Dissertation

Dr. Matthew J. Beck  
Director of Graduate Studies

December 16, 2022  
Date

“That the powerful play goes on, and you may contribute a verse.”

–Walt Whitman, *Leaves of Grass*, 1892.

“One does not substitute oneself for the past, one merely adds to it a new link.”

–Paul Cézanne, 1839-1906.

“If I have seen further it is by standing on the shoulders of Giants.”

–Isaac Newton to Robert Hooke, 1675.

## ACKNOWLEDGMENTS

I passed my final doctoral examination ten years after I started at the University of Kentucky as an undergraduate. During that time, I have been incredibly fortunate to have several sources of support. The first of these is of course my wonderful family, whom I owe a great deal for all the opportunities they have provided me over the last twenty-eight years. Even though I generally do a poor job of communicating with them and frequently travel to conferences and meetings hundreds of miles away with barely a mention, their attitude has always been one of unrelenting excitement and encouragement. Thank you, Mom, Dad, and Maysam. At times when life at school became incredibly stressful, I was lucky to have John and Ilka, who always helped me see it through. Their kindness has been truly endless. They also gave me my friendship with Jake, who was the best, and Yeti, who is taking after his brother.

Even while excelling in their own fields, my friends have always made time to buoy my spirits and make me laugh. Ellie, thank you for listening when I was ecstatic, frustrated, or frenzied. I know being a good friend to a Ph.D. student while being a medical student and neurosurgeon could not have been easy, but you always made it seem that way. Also, thank you for buying a house just so I could have a nice place to visit whenever I needed a vacation and rescuing Obie just to give me another sweet friend. Ashley, Dalia, and Max, thank you for years and years of wonderful memories, particularly our annual cookie decorating nights and summer boating adventures.

As an undergraduate, I had a cohort full of close friends. Entering graduate school, I wondered if I would be lucky again. Thankfully, I was. Kristen, I am so grateful for your friendship as we have navigated our unending research issues and [unrelated] theological discussions, and our Harry Potter nights with themed snacks were highlights of my time in graduate school. Joree, our endless discussions about

the triumphs and trials of graduate school amplified the good days and tempered the bad ones. Kerry, Alyssa, and Alex, thank you for making graduate school fun—from Keeneland to pumpkin carving to Bark in the Parks—always having something to look forward to outside of work made all the difference.

Whether or not my current career goals are ever realized, I will be forever grateful to a few faculty members who worked tirelessly to help me reach them. I owe a tremendous debt of gratitude to Dr. Alexandre Martin, who, despite making the profound mistake of not hiring me as a freshman undergraduate, became someone I turn to frequently for advice as a graduate student and soon-to-be postdoc. Thank you for welcoming me as a long-term “visiting scholar” in GSIL+ and giving me so many opportunities to explore new work, attend new conferences, and meet new colleagues. You were, and remain, a fantastic guide to the aerospace research community. Oh, and a fantastic guide to the lands and language of the Quebecois!

I would simply have not reached this stage of my academic career without the support of Dr. John Balk. Thank you for introducing me to research as an undergraduate and to many “behind-the-scenes” aspects of academia, solidifying my interest in graduate school and allowing me to pursue an academic career with realistic expectations of its advantages and disadvantages. Letting me follow you around my first few conferences was invaluable in building my confidence and making me feel like I was a real member of the materials engineering community. My first TMS (San Diego in 2017) remains my favorite, in large part because of how much you guided the undergraduates through the talks and events. Also, thank you for hiring a few students to your group who became a few of my closest friends in graduate school.

In many ways, I believe my advisor, Dr. Matthew J. Beck, has been a true embodiment of what a Ph.D. advisor should be. As an undergraduate, our many career discussions helped me discover that I wanted to be a professor. But once I got that sorted, I still had an endless supply of questions. How do interests become

experiments or calculations? How does the tenure process work? How is funding won? Years later, I can answer each of these questions. However, I have absolutely no recollection of consciously learning any of it. That said, I'm sure it was thanks to the lightly constrained freedom I was given during graduate school. I was able to inflict my presence on my experimentalist friends, my microscopy friends, my friends in other departments, my friends at other institutions, and even the friends of my friends I met at meetings and conferences. Thank you for encouraging, not just "allowing" me to pursue entirely extracurricular experiences like forming a GradSWE group and teaching an undergraduate course. These freedoms gave me a sense of belonging in our program and field, which made the tremendous amount of time I did spend working feel like it was all going to something much larger than a three-letter postnominal.

Lastly, I want to remember my friend, Dr. Eric Grulke, who passed away in late 2019. Dr. Grulke was more than a mentor during both my undergraduate and graduate studies, he was truly a kind and generous person. I will always treasure our discussions on classic fashion over morning espressos, and the time he and Ginny taught me and my family to ride horses at their farm. I wish he had seen me graduate and know he would have been proud.

Finally, a great deal of the work presented here was financially supported by the Defense Advanced Research Projects Agency (DARPA) Innovative Vacuum Electronics Science and Technology (INVEST) program, under grant number N66001-16-1-4041. As a graduate student, I was incredibly fortunate to be awarded a NASA Space Technology Graduate Research Opportunity (grant number 80NSSC20K1196), a graduate fellowship that supported my work for the final two years of my degree. All calculations presented in this dissertation made heavy use of resources maintained by the University of Kentucky Center for Computational Sciences, and I want to thank Vikram Gazula in particular for helping me navigate them.

# TABLE OF CONTENTS

|   |     |
|---|-----|
| Acknowledgments . . . . .   | iii |
| List of Tables . . . . .  | ix  |
| List of Figures . . . . .   | x   |
| Chapter 1 Introduction . . . . .  | 1   |
| 1.1 Objectives . . . . .  | 1   |
| 1.2 Outline . . . . .   | 1   |
| Chapter 2 A brief history . . . . .   | 3   |
| 2.1 Atomic bombs, solitaire, and the first materials science calculation:<br>The Monte Carlo method . . . . . | 3   |
| 2.2 The density functional framework . . . . .  | 4   |
| 2.3 The finite element method . . . . .   | 6   |
| I Atomistic scale . . . . .   | 7   |
| Chapter 3 Quantum mechanical methods . . . . .  | 8   |
| 3.1 Density functional theory . . . . .   | 8   |
| 3.1.1 Schrödinger, Hartree, and Fock . . . . .  | 8   |
| 3.1.2 Hohenberg-Kohn, Kohn-Sham, and DFT . . . . .  | 10  |
| 3.1.3 Solving the Kohn-Sham equations . . . . .   | 12  |
| 3.1.4 The pseudopotential approximation . . . . .   | 14  |
| 3.1.5 Minimization of the total energy . . . . .  | 14  |
| 3.2 Density functional perturbation theory . . . . .  | 15  |
| 3.2.1 Response functions . . . . .  | 15  |
| 3.2.2 Perturbation theory . . . . .   | 16  |
| 3.2.3 Basic equations in DFPT . . . . .   | 18  |
| Chapter 4 Wulff shape prediction from surface excess free energies . . . . .                                  | 20  |
| 4.1 Motivation . . . . .  | 20  |
| 4.2 Methods . . . . .   | 22  |
| 4.2.1 Thermodynamic approach to surface energy calculation . . . . .  | 22  |



|           |  |    |
|-----------|--|----|
| 4.2.2     | Calculation details . . . . .  | 24 |
| 4.3       | Results and Discussion . . . . .                                     | 25 |
| 4.3.1     | Temperature-dependent bulk reference free energies . . . . .         | 25 |
| 4.3.2     | Temperature-dependent W surface energies . . . . .                   | 27 |
| 4.3.3     | M/MO <sub>x</sub> stability . . . . .                                | 28 |
| 4.3.4     | W particles in a Ba/O-containing environment . . . . .               | 31 |
| 4.3.5     | W particles in an O-containing environment . . . . .                 | 35 |
| 4.4       | Summary . . . . .  | 36 |
| Chapter 5 | Scandate cathode operating conditions from observed Wulff shapes     | 38 |
| 5.1       | Motivation . . . . .   | 38 |
| 5.2       | Methods . . . . .  | 40 |
| 5.2.1     | Overview . . . . .   | 40 |
| 5.2.2     | Target surface energy ranges . . . . .                               | 42 |
| 5.2.3     | Computing surface energies . . . . .                                 | 43 |
| 5.2.4     | Oxygen thermochemical data . . . . .                                 | 45 |
| 5.2.5     | Work function . . . . .  | 45 |
| 5.2.6     | Calculation details . . . . .  | 46 |
| 5.3       | Ba <sub>x</sub> Sc <sub>y</sub> O/W surface configurations . . . . . | 46 |
| 5.3.1     | M/MO <sub>x</sub> stability . . . . .                                | 46 |
| 5.3.2     | Surface energies . . . . .   | 47 |
| 5.3.3     | Chemical conditions required to yield observed shapes . . . . .      | 49 |
| 5.3.4     | Effective work functions . . . . .                                   | 52 |
| 5.4       | Additional Sc <sub>y</sub> -containing W surfaces . . . . .          | 55 |
| 5.4.1     | Surface energies, chemical conditions, and work functions . . . . .  | 55 |
| 5.4.2     | Sc and imaginary phonon modes . . . . .                              | 60 |
| 5.5       | Summary . . . . .  | 62 |
| II        | Continuum scale . . . . .  | 64 |
| Chapter 6 | Finite Element Method . . . . .                                      | 65 |
| 6.1       | Overview . . . . .   | 65 |
| 6.2       | Implementation . . . . .   | 66 |
| 6.2.1     | Algebraic approach . . . . .   | 66 |
| 6.2.2     | Solution . . . . .   | 68 |

|           |   |     |
|-----------|---|-----|
| Chapter 7 | The Kentucky Random Structures Toolkit and a prototypical nanoporous system . . . . . | 69  |
| 7.1       | Motivation . . . . .  | 69  |
| 7.2       | Method overview . . . . .   | 72  |
| 7.3       | Sampling bulk effective properties with mRVEs . . . . .                               | 74  |
| 7.3.1     | Isotropic mRVEs . . . . .   | 74  |
| 7.3.2     | Orthotropic mRVEs . . . . .   | 77  |
| 7.4       | Computing mRVE strain energies from FEM . . . . .                                     | 79  |
| 7.5       | Approach validation . . . . .   | 79  |
| 7.6       | Properties of prototype NP geometry . . . . .   | 85  |
| 7.6.1     | Network connectivity dependence: Extending Gibson-Ashby . . . . .                     | 85  |
| 7.6.2     | Effect of short- and long-range disorder . . . . .                                    | 88  |
| 7.6.3     | Transferability of EGA model . . . . .  | 90  |
| 7.7       | Summary . . . . .   | 90  |
| Chapter 8 | Stochastic mesoscale mechanical modeling of Duocel . . . . .                          | 93  |
| 8.1       | Motivation . . . . .  | 93  |
| 8.2       | Defect-free structures . . . . .  | 96  |
| 8.2.1     | mRVE generation . . . . .   | 96  |
| 8.2.2     | Computational details . . . . .   | 97  |
| 8.2.3     | Feature-scale to mesoscale transition . . . . .                                       | 99  |
| 8.2.4     | Stochastic model predictions of Duocel properties . . . . .                           | 103 |
| 8.2.5     | MMOD interaction scale . . . . .  | 105 |
| 8.3       | Defected structures . . . . .   | 105 |
| 8.3.1     | mRVE generation . . . . .   | 106 |
| 8.3.2     | Computational details . . . . .   | 106 |
| 8.3.3     | Directional disparities due to cavities . . . . .                                     | 106 |
| 8.3.4     | Stochastic model predictions of cavity effects in Duocel . . . . .                    | 109 |
| 8.4       | Summary . . . . .   | 113 |
| Chapter 9 | Conclusions . . . . .   | 115 |
| 9.1       | Concluding remarks . . . . .  | 115 |
| 9.2       | Key findings . . . . .  | 115 |
|           | Bibliography . . . . .  | 118 |
|           | Vita . . . . .  | 142 |

## LIST OF TABLES

|     |   |     |
|-----|---|-----|
| 5.1 | Summary M/MO <sub>X</sub> stability transitions (eV) at 0 and 2000 K. . . . .   | 47  |
| 5.2 | Surface configurations evaluated in this work. . . . .  | 49  |
| 5.3 | Comparing imaginary modes of Sc <sub>y</sub> -containing surface configurations. . .  | 61  |
| 7.1 | Parameters used to generate all sets of random mRVEs. . . . .   | 80  |
| 7.2 | Effective bulk mechanical properties ( $E^*$ , $\nu^*$ , and $K^*$ in GPa) and their respective statistical distribution parameters for prototype random network mRVE sets. The quantities $a$ , $b$ , $\sigma$ , and $R$ correspond to the gamma shape parameter, gamma scale parameter, standard deviation, and correlation, respectively, for the prototype random network mRVE $E^*$ results. . . . . | 82  |
| 8.1 | Structural parameters for each class of mRVEs examined in this section.   | 97  |
| 8.2 | The $\Gamma$ -distribution parameters, $a$ and $b$ , and corresponding statistical quantities, $\mu_E$ and $\sigma_E$ , for each <b>L</b> , <b>M</b> , and <b>H</b> mRVE set. . . . .   | 100 |
| 8.3 | Reduced average IP and TTT stiffnesses, comparing 0% and 20% volume cavity mRVE sets. . . . .   | 108 |
| 8.4 | The $\Gamma$ -distribution parameters, $a$ and $b$ , and corresponding statistical quantities, $\mu_E$ and $\sigma_E$ of the defected mRVE sets in both the IP and <b>TTT</b> directions. . . . .   | 110 |
| 8.5 | Similarity measures of the 0% and 20% cavity volume $\Gamma$ -distributions of each reduced density class and both orientations. . . . .  | 113 |

## LIST OF FIGURES

|     |   |    |
|-----|---|----|
| 4.1 | $\hat{\mu}_W$ as a function of temperature for five W structures: two cubic cells and three slabs. Reproduced with permission from Ref. [128]. . . . .  | 26 |
| 4.2 | Bulk $\hat{\mu}$ values for <b>(a)</b> W, <b>(b)</b> Ba, <b>(c)</b> $\text{WO}_3$ , and <b>(d)</b> BaO, each from 0-2000 K. Reproduced with permission from Ref. [128]. . . . .   | 26 |
| 4.3 | Surface energies and correlated equilibrium Wulff shapes of W surfaces at three temperatures: 300 K, 1000 K, 2000 K. Reproduced with permission from Ref. [128]. . . . .  | 27 |
| 4.4 | The W (001) surface with <b>(a)</b> an ideal termination and <b>(b)</b> the lower energy reconstruction. Reproduced with permission from Ref. [128]. . .  | 28 |
| 4.5 | The regions of stability for a metal and its respective oxide as a function of temperature for W and Ba. Reproduced with permission from Ref. [128].  | 29 |
| 4.6 | Four combinations of $P_{O_2}$ and $T$ are highlighted in <b>(c)</b> . These pairs are extended to <b>(a)</b> and <b>(b)</b> , which show $\hat{\gamma}$ as a function of $\mu_O$ at two temperatures: 1500 K and 1950 K. The minimum $\hat{\gamma}$ surfaces were used to construct four Wulff shapes, each exhibiting varying degrees of (001), (110), and (112) facets, highlighting the critical dependence of $\hat{\gamma}$ on both $T$ and $\mu_O$ . Figs. <b>(d)</b> and <b>(f)</b> are both comprised only of W facets, and appear quite similar except for the slight appearance of (112) in Fig. <b>(d)</b> . Fig. <b>(g)</b> prominently exhibits all three facets, and is comprised of the $\text{Ba}_{0.50}\text{O-top/W}$ (001), $\text{Ba}_{0.25}\text{O-tri/W}$ (110), and is the $\text{Ba}_{0.50}\text{O-top/W}$ (112) configurations. Fig. <b>(e)</b> does not exhibit the (110) facet, only including the $\text{Ba}_{0.50}\text{O-top/W}$ (001) and $\text{Ba}_{0.50}\text{O-top/W}$ (112) configurations. At both of these temperatures, W (001) refers to the reconstruction. Reproduced with permission from Ref. [128]. . . . . | 30 |
| 4.7 | Phonon density of states for each of the surfaces examined here. Reproduced with permission from Ref. [128]. . . . .  | 31 |
| 4.8 | The $\text{Ba}_{0.50}\text{O-top/W}$ (112) $[2 \times 2]$ with Ba atoms in a <b>(a)</b> “row” pattern and a <b>(b)</b> “zig-zag” pattern. W atoms are gray, O atoms red, and Ba atoms green. Reproduced with permission from Ref. [128]. . . . .  | 32 |

|      |  |    |
|------|--|----|
| 4.9  | Prominent surface facets for W nanoparticles as a function of temperature, $\mu_O$ , and adsorbed Ba/O species. $\text{WO}_3$ exists at all temperatures given a $\mu_O > \sim -8.25$ eV. At low $\mu_O$ and high $\mu_O$ (before it fully oxides to $\text{WO}_3$ ) the nanoparticle is predominantly (110) terminated. At low $\mu_O$ , the surface is bare; at high $\mu_O$ , the surface is Ba-O-terminated. At moderate $\mu_O$ , the nanoparticle is dominated by the (112) facet. With the addition of Ba to the O-W system, there is no $\mu_O$ or temperature wherein a O-terminated configuration is featured on the nanoparticle. Reproduced with permission from Ref. [128]. . . . .   | 34 |
| 4.10 | Prominent surface facets for W nanoparticles as a function of temperature, $\mu_O$ , and adsorbed O species. $\text{WO}_3$ exists at almost all temperatures given a $\mu_O > -7.75$ eV. While the nanoparticles are terminated with the (110) facet at almost all temperatures and $\mu_O$ , the facet is O-terminated given a $\mu_O$ from -9.5 to -8.75 eV, depending on the temperature. Reproduced with permission from Ref. [128]. . . . .   | 36 |
| 5.1  | Examples of Wulff constructions where (a) $d_{hkl}/d_{pqr} \gg 1$ , (b) $d_{hkl}/d_{pqr} = 1$ , (c) $d_{hkl}/d_{pqr} \ll 1$ , (d) $d_{h'k'l'}/d_{p'q'r'} = d_{hkl}/d_{pqr} = 1$ . The labels $hkl$ and $pqr$ refer to two unique families of planes. Reproduced with permission from Ref. [159]. . . . .   | 42 |
| 5.2  | (left) Wulff construction of the equilibrium W grain shape present throughout thermionic cathodes (right) SEM images of a high-performance cathode, always exhibiting a characteristic W grain shape. Reproduced with permission from Ref. [159]. . . . .  | 44 |
| 5.3  | (a) An isotherm at 1450 K showing the surface energies of all fourteen surface configurations evaluated. (b) The same data as in (a), but with sections of surface energy curves shown in bold only if/when the surface configuration has the minimum surface for its orientation. Other sections of surface energy curves (where the particular configuration does not have the lowest surface energy for its facet) are lightened to highlight that only a subset of all considered configurations are ever the lowest energy configuration for their facet. The black stars indicate $\mu_O$ values where relative surface energies that will yield the characteristic Wulff shape occur, and they correspond to similar stars shown in subsequent figures. Reproduced with permission from Ref. [159]. . . . . | 50 |

|     |  |    |
|-----|--|----|
| 5.4 | Contour plot of $\mu_O$ as a function of oxygen partial pressure and temperature, overlaid with gray bands indicating conditions wherein the characteristic shape is expected. The stars are equivalent to those in Fig. 5.3b. Reproduced with permission from Ref. [159]. . . . .   | 52 |
| 5.5 | (a) Contour plot of $\Phi_{\text{eff}}$ as a function of oxygen partial pressure and temperature, overlaid with gray bands indicating conditions wherein the characteristic shape is expected. (b) $\Phi_{\text{eff}}$ as a function of oxygen partial pressure and temperature plotted as a scatter plot. Reproduced with permission from Ref. [159]. . . . .   | 53 |
| 5.6 | (a) An isotherm at 1450 K showing the surface energies of all seventeen surface configurations evaluated. (b) The same data as in (a), but with sections of surface energy curves shown in bold colors only if/when the surface configuration has the minimum surface for its facet. Other sections of surface energy curves (where the particular configuration does not have the lowest surface energy for its facet) are lightened to highlight that only a subset of all considered configurations are ever the lowest energy configuration for their facet. Black stars indicate $\mu_O$ yield the characteristic W shape. . . . .    | 57 |
| 5.7 | (a) An isotherm at 1450 K showing the surface energies of all twenty-seven surface configurations evaluated. (b) The same data as in (a), but with sections of surface energy curves shown in bold colors only if/when the surface configuration has the minimum surface for its facet. Other sections of surface energy curves (where the particular configuration does not have the lowest surface energy for its facet) are lightened to highlight that only a subset of all considered configurations are ever the lowest energy configuration for their facet. Black stars indicate $\mu_O$ yield the characteristic W shape. . . . . | 58 |
| 5.8 | Contour plots of $\mu_O$ as a function of oxygen partial pressure and temperature, overlaid with gray bands indicating conditions wherein the characteristic shape is expected. (a) The resulting plot of the W, O/W, $\text{Ba}_x\text{O}/\text{W}$ , and $\text{Ba}_x\text{O}_z\text{Sc}/\text{W}$ (hkl) configurations (those plotted in Fig. 5.6). (b) The resulting plot of the W, O/W, $\text{Ba}_x\text{O}/\text{W}$ , $\text{Ba}_x\text{O}_z\text{Sc}/\text{W}$ , $\text{Sc}_y/\text{W}$ , $\text{O}_z\text{Sc}/\text{W}$ , and $\text{Sc}_y\text{O}/\text{W}$ (hkl) configurations (those plotted in Fig. 5.7). . . . .           | 59 |
| 5.9 | Vector representations of imaginary phonon modes exhibited by the $\text{Ba}_{0.50}\text{O-triSc-top}/\text{W}$ (001) configuration. . . . .   | 62 |

|      |  |    |
|------|--|----|
| 7.1  | The unit cell defining the Gibson-Ashby model for low-density cellular open foams. Reproduced with permission from Ref. [226]. . . . .   | 70 |
| 7.2  | Boundary conditions to compute three pairs of elastic constants for each mRVE. . . . .   | 74 |
| 7.3  | Boundary conditions to compute each non-zero elastic constant in the stiffness matrix of an orthotropic material. . . . .  | 78 |
| 7.4  | Example mRVEs of random structures used in this section. Each are unique due to the varied minimum and maximum sphere radii and network connectivity indicated in Table 7.1. Reproduced with permission from Ref. [236]. . . . .   | 80 |
| 7.5  | (top) Qualitative evidence that there is no correlation between $E_x^\alpha$ and $E_y^\alpha$ for individual prototype random network mRVEs, $\alpha$ . The points located at $(E_i^\alpha, E_y^\alpha - \overline{E_x^\alpha})$ appear randomly distributed about a central mean $(\overline{E_x^\alpha})$ . (bottom) $E_i^*$ for all mRVEs plotted as $\Gamma$ -distributions, positioned directly below their respective point clouds. The break on the y-axis indicates that the first three distributions are significantly taller than the rest. Reproduced with permission from Ref. [236]. . . . . | 81 |
| 7.6  | (a) $\Gamma$ -distributions of $E_i^\alpha$ for the 3NN <sup>-</sup> mRVE set as a function of $\lambda$ , a quantity corresponding to mRVE size with respect to structural feature size. (b) $\Gamma$ -distributions of a set of structures generated according to the 3NN <sup>-</sup> parameters as a function of $E_i^\alpha$ . Since three $E_i^\alpha$ values are calculated for each mRVE, the quantity 3N corresponds to a number N of mRVEs. Reproduced with permission from Ref. [236]. . . . .  | 83 |
| 7.7  | Comparison of E results for a set of mRVEs treated as isotropic and orthotropic. . . . .   | 85 |
| 7.8  | (a) Effective elastic modulus values and (b) effective bulk modulus values for all prototype random network mRVEs. Reproduced with permission from Ref. [236]. . . . .   | 86 |
| 7.9  | (a) The surface fit of all prototype random network mRVEs, allowing for future calculation of $E^*/E_S$ as a function of $\phi$ and $N_C^*$ . (b) The difference between the $E^*$ values generated via FEM and via the fit in Fig. 7.9a. Reproduced with permission from Ref. [236]. . . . .  | 87 |
| 7.10 | (a) The surface fit of all prototype random network mRVEs, allowing for future calculation of $K^*/K_S$ as a function of $\phi$ and $N_C^*$ . (b) The difference between the $K^*$ values generated via FEM and via the fit in Fig. 7.10a. Reproduced with permission from Ref. [236]. . . . .   | 88 |

|      |  |     |
|------|--|-----|
| 7.11 | (a) Voigt-Reuss-Hill elastic modulus approximations for all regular mRVEs.<br>(b) Bulk modulus approximations for the regular mRVEs. The 4NN-random and 6NN-random lines were obtained by fitting the relevant data points in Fig. 7.8a. Reproduced with permission from Ref. [236]. . . . .                             | 89  |
| 8.1  | Examples of MMOD impacts: (a) Surface of an ISS radiator panel [244] and (b) MMOD impact on satellite component retrieved during the STS-41C Solar Max repair mission [245]. . . . .   | 93  |
| 8.2  | A diagram of a projectile striking an open cell metallic foam sandwich panel.  | 94  |
| 8.3  | A “map” of each set of structures utilized in this section of defect-free mRVEs. Each image is a single example of the hundreds of mRVEs in each set. . . . .  | 97  |
| 8.4  | $E$ results for each mRVE set for each class. . . . .  | 99  |
| 8.5  | $E$ results for the high density sets, plotted as both scatter and $\Gamma$ -distributions. The $\Gamma$ parameters and statistical quantities are found in Table 8.4. . . .   | 101 |
| 8.6  | $E$ results for each mRVE set, plotted as $\Gamma$ -distributions. The $\Gamma$ parameters and statistical quantities are found in Table 8.4. . . . .  | 102 |
| 8.7  | The quantity $\lambda$ is plotted for each mRVE set. Within each class of mRVEs, the range of $\lambda$ where $\mu_E$ and $\sigma_E$ converge below 2% is highlighted with a colored line segment. The black shaded region indicates the range of $\lambda$ s where the converged windows of each class overlap. . . . . | 102 |
| 8.8  | Comparison of in-house ERG measurements and KRaSTk-generated results.  | 104 |
| 8.9  | Example structures of each of the twelve mRVE sets utilized in this series of calculations. . . . .  | 107 |
| 8.10 | A diagram indicating the directions referenced in this section with respect to mRVEs. . . . .  | 107 |
| 8.11 | A scatter plot showing the mean elastic modulus values of all mRVE sets, including both IP and TTT directions. . . . .   | 108 |
| 8.12 | Elastic modulus distributions, in both IP and TTT orientations, for all mRVE sets. . . . .   | 111 |
| 8.13 | Plots showing the overlap between distributions of 0% and 20% cavity volume elastic modulus values, both in the IP and TTT orientations. . .   | 112 |
| 8.14 | A representation of the physical implications of the overlapping $\Gamma$ -distributions in Figs. 8.13e and 8.13f. . . . .   | 113 |



## Chapter 1: Introduction

### 1.1 Objectives

The term “complex materials systems” can certainly be broadly defined, but moving forward will refer to structures that are impossible to describe as infinite, regular crystals, as one could describe many alloys and ceramics. The overarching objective of this dissertation is to demonstrate how computational materials science approaches can be used to embrace a material’s complexity and move away from oversimplifications that negate unique microstructural features. A related objective is to highlight the broad scope of computational methods with respect to both subject and scale. In the next several chapters, a number of materials—e.g. metallic nanoparticles, scandate cathodes, nanoporous gold, and metallic foam—are investigated at a range of length scales—e.g. the atomic scale, where electronic structure dominates behavior, and the continuum scale, where the atomic structure of the material is assumed to be uniform and inconsequential. Such a broad set of results is only possible with an arsenal of computational approaches!

### 1.2 Outline

In Part I, efforts are focused on systems directly related to scandate cathodes, a class of Sc-containing thermionic cathodes observed to exhibit a greater current density at lower temperature than state-of-the-art, generally M-type, thermionic cathodes. Systems comprising W surfaces covered by a range of adsorbates (combinations Ba, Sc, O) in a range of configurations were evaluated for their absolute surface energies, relative surface energies, and work functions. While traditional methods for computing surface energy must be done at the ground state, the work presented here utilizes a method that allows for finite temperature to be incorporated. With temperature-dependent surface energies, temperature-dependent Wulff shapes can also be computed. From these calculations, “particle configuration maps”—graphical maps of the equilibrium shape and surface chemistry of particles over a range of temperatures and environmental conditions—were constructed. In a sense, this is a Wulff construction procedure, albeit with relative stability of surface configurations incorporated. An “inverse” Wulff construction approach is also presented, where previous knowledge of microstructure and emission performance obtained with experimental methods is

used as computational *input* to search for the possible chemical conditions present during cathode activation and operation. Calculations show that small deviations from these conditions result in large changes in cathode work function (and therefore thermionic emission). The yet-unknown role of Sc in enhancing emission performance is hypothesized to not directly modify surface work functions, but rather to control chemical conditions to stabilize (Sc-free) low work function surface configurations.

In Part II, nanoporous gold is studied as a prototypical nanoporous material, and Duocel aluminum foam is studied specifically for its use in MMOD shielding. In assessing each material, the common theme is predicting mesoscale scale properties. Mesoscale in this dissertation is defined as the length scale at which local, individual features (e.g. nodes, ligaments) no longer determine properties, but, at the same time, macroscopic bulk properties have yet to emerge. Because these length scales are unique to each material, it is not possible (or prudent) to designate mesoscale as “nano”-scale or even “micro”-scale. That is, mesoscale should not necessarily be associated with nanometers or microns or any other lengths. When nanoporous gold is the model system, feature-scale and mesoscale behavior manifests at the nanometer scale while macroscopic properties are observed on the micron scale. Conversely, mesoscale behavior in Duocel originates at the micron and millimeter scale. These are massive lengths compared to nanoporous gold. In fact, the feature-scale in Duocel is already three orders of magnitude longer than the macroscopic scale of nanoporous gold. The results in these studies illustrate that average mesoscale properties do not adequately capture the surrounding scatter, variability, or uncertainty associated with complex, stochastic microstructures.

As an important note, the reader will find this dissertation easier to follow if the meaning of symbols are only considered within a chapter or part. For example, the Greek letter epsilon ( $\epsilon$ ) refers to an eigenvalue in the context of quantum mechanics; however, it refers to strain in the context of solid mechanics. Substitutes were considered, but it was decided that inserting characters too distant from the classic, well-known symbols would cause significantly more confusion. Broadly, symbols used in Part I will *not* have the same meaning in Part II.

## Chapter 2: A brief history

### 2.1 Atomic bombs, solitaire, and the first materials science calculation: The Monte Carlo method

Materials science has been studied since homonins learned to sharpen stone 3.3 million years ago; however, it was not until the 20th century that the distinct field of computational materials science emerged. In the wake of WWII, physicists at Los Alamos National Laboratory in the late 1940s were investigating neutron diffusion in the core of a nuclear weapon. Despite having critical data, e.g. the average distance a neutron would travel in a substance before it collided with an atomic nucleus, computing the energy the neutron was likely to give off following a collision proved impossible to solve using conventional, deterministic mathematical methods. Eventually, a game of solitaire gave the solution.

While an earlier variant of Monte Carlo was used to solve Buffon’s Needle Problem in the 18th century (Ref. [1]), Stanislaw Ulam formulated the modern Monte Carlo Method in 1946 while recovering from an illness and playing solitaire in bed. The following is from a 1987 tribute: “The question was ‘what are the chances that a Canfield solitaire laid out with 52 cards will come out successfully?’ After spending a lot of time trying to estimate them by pure combinatorial calculations, [Ulam] wondered whether a more practical method than ‘abstract thinking’ might not be to lay it out say one hundred times and simply observe and count the number of successful plays.” He then “described the idea to John von Neumann and [Ulam and von Neumann] began to plan actual calculations” [2]. Since this project was top secret, their work required a code name. Nicholas Metropolis, a colleague at Los Alamos, suggested “Monte Carlo,” referring to the Monte Carlo Casino in Monaco [3]. Metropolis would later explain that an uncle of Ulam had a habit of borrowing money from relatives because he “just had to go to Monte Carlo” [3]. Considering Ulam’s original bedridden motivation, the name was embraced and has endured to this day! Von Neumann, Metropolis and others then programmed ENIAC (Electronic Numerical Integrator and Computer)—the first programmable, electronic, general-purpose digital computer, developed at the University of Pennsylvania in 1945 [3]—to perform the first fully automated Monte Carlo calculations, of a fission weapon core, in the spring of 1948 [4]. Interestingly, Emilio Segré, another colleague at Los Alamos, revealed in 1980 that his doctoral advisor, Enrico Fermi, had invented

[but not named] the Monte Carlo method fifteen years earlier while studying the moderation of neutrons in Rome, though he did not publish anything on the topic [5]. Most would still argue that Fermi had a rather successful career.

From these beginnings as a method of modeling the motion of a handful of subatomic particles, the use of computation as a tool for explaining material behavior has exploded in popularity. However, the use of computational materials science approaches to investigate complex systems remains less prevalent. The reason is obvious—it is extremely difficult! It often requires applying well-known accepted approaches in new ways or combining aspects of multiple methods. The following sections describe computational methods utilized in this dissertation to investigate materials with a great deal of inherent complexity and little uniformity.

## **2.2 The density functional framework**

Density functional theory (DFT) has a rich history rooted in the formulation of quantum mechanics. In turn, quantum mechanics would surely never have been developed without—to name only a fraction of important contributors—the early wave theory of light proposed by Robert Hooke and Christiaan Huygens in the 17th century [6], Thomas Young’s double slit experiment in 1802 [7], the formation of the kinetic theory of gases by James Clerk Maxwell [8] and Ludwig Boltzmann [9] in the late 19th century, and the discovery of the electron by J.J. Thomson in 1897 [10]. Quantum mechanics as a field might be said to have begun with Max Planck’s 1900 solution to the black-body radiation problem discovered by Gustav Kirchhoff in 1859. Planck proposed that energy is radiated and absorbed in discrete quanta, or energy packets, yielding a calculation that precisely matched the observed patterns of black-body radiation [11]. Amusing in hindsight, Planck considered this quantum hypothesis to be a mathematical trick to get the right answer rather than a revolutionary discovery [12]. Incidentally, the word “quantum” is Latin for “how much” or “portion.” Following Planck’s hypothesis literally, Albert Einstein developed the idea in 1905 to show that an electromagnetic wave such as light could also be described as a particle, now called a photon, with a discrete amount of energy that depends on its frequency [13]. Neils Bohr and Ernest Rutherford, both students of J.J. Thomson, also utilized Planck’s hypothesis to develop the Bohr or Rutherford-Bohr model of the hydrogen atom, which successfully predicted the spectral lines of hydrogen in 1913 [14]. In 1923, Louis de Broglie postulated that all matter has wave properties, a statement now known as the de Broglie hypothesis [15]. Within only a few years,

Werner Heisenberg, Max Born, and Pascual Jordan [16] developed matrix mechanics and the Austrian physicist Erwin Schrödinger invented wave mechanics [17]. Soon following these developments, the field of quantum physics received wider acceptance at the eminent Fifth Solvay Conference in 1927.

Density functional theory has its roots in the Thomas-Fermi model [18, 19], which is a quantum mechanical theory for the electronic structure of many-body systems developed after the introduction of the Schrödinger equation [20] and the Hartree-Fock method [21, 22, 23] in the late 1920s. DFT was formally established by Walter Kohn and Pierre Hohenberg with the introduction of the Hohenberg-Kohn theorems in the 1960s [24]. The first Hohenberg-Kohn theorem demonstrates that the ground-state properties of a many-electron system are uniquely determined by an electron density that depends on only three spatial coordinates. The second Hohenberg-Kohn theorem defines an energy functional for the system and proves that the ground-state electron density minimizes this energy functional. The Hohenberg-Kohn theorems would soon be further developed by Walter Kohn and Lu Jeu Sham, work which would later win the Nobel Prize in Chemistry in 1998. Within Kohn-Sham DFT, the intractable many-body problem of interacting electrons in a static external potential is reduced to a tractable problem of non-interacting electrons moving in an effective potential [25].

A few decades after the formation of DFT, density functional perturbation theory (DFPT) arose as a particularly powerful and flexible theoretical technique within the density functional framework. DFPT can be utilized to calculate system responses to external perturbations, which had previously been explored by methods that involved obtaining the system response through a series of single-point energy calculations carried out at varying strengths of the external perturbation. The two main formalisms of DFPT are attributed to Stefano Baroni [26] and Xavier Gonze [27]; although the two may be shown to be equivalent, there are differences in the implementation that may result in one method being preferable to another. The Baroni formalism is centered upon obtaining a series of equations that may be solved self-consistently using Green's function methods. In contrast, the Gonze formalism is based upon a perturbative expansion of the Kohn-Sham energy functional.

Combined, density functional theory and density functional perturbation theory are outstanding tools for evaluating materials at the atomic scale. In this dissertation, the dual-method approach is used to answer questions about highly-complex surfaces directly related to their thermodynamic stability, response to environment, and electronic behavior at high, finite temperatures.

### 2.3 The finite element method

Although the term “finite element method (FEM)” was not coined by Ray Clough until 1960 [28], a number of pioneering studies were critical to its development. In the 1940s, Richard Courant [29] and Alexandre Hrennikoff [30] formulated bar element assemblages to simulate plane stress systems. The next decade saw the matrix generalization of structural theory, wherein the analysis was formulated as a form of coordinate transformation. The earliest known references to the assembly of structural elements by a matrix coordination transformation were made by Helmut Falkenheimer [31] and Börge Langefors [32] in the 1950s. In 1953, computerized FEM was developed at the Boeing Airplane Company to evaluate the stiffness of a delta airplane wing for use in flutter analysis. The first complete statement on the matrix formulation of structural theory, which clearly outlined the parallel procedures of the force and displacement methods, was published by John Argyris and Sydney Kelsey in 1960 [33]. It was this work which demonstrated that the concepts of classical structural analysis can be generalized for application to assemblages of any type of structural elements. Decades later, FEM has become the computational workhorse for engineering design analysis, as it a possible approach for solving any problem that can be described by partial differential equations e.g., structural mechanics, fluid flow, thermal conduction, electromagnetics, etc.

In this dissertation, FEM allows for the evaluation of materials with complexity at the microstructure, rather than atomic, length scale. Unlike DFT/DFPT, where changes in electronic structure are of great importance, at the continuum scale of FEM, electronic structure is presumed to be simple and unchanging. Efforts were therefore spent understanding the relationship between intrinsic structural complexity, geometric features, and major defects.

# Part I

## Atomistic scale

## Chapter 3: Quantum mechanical methods

### 3.1 Density functional theory

“I think I can safely say that nobody understands quantum mechanics.”

— Richard P. Feynman, The Messenger Lectures, 1964

#### 3.1.1 Schrödinger, Hartree, and Fock

Density functional theory (DFT) originates with the truly astonishing formulation of quantum mechanics at the beginning of the 20th century. Axiomatic to the theory of quantum mechanics is the notion that the probabilities of the possible results of measurements made on a quantum system can be derived from a complex function. This function shares many characteristics with classical waves, and is therefore known as a wave function, denoted as  $\psi$  or  $\Psi$ . A number of physical properties—position, momentum, time, spin—of the particle or system may be extracted from the wave function through the application of an operator.

The total energy operator, or Hamiltonian, for a single particle in an external potential field,  $\nu(\mathbf{r})$  is

$$h = -\frac{1}{2}\nabla^2 + \nu(\mathbf{r}) \quad (3.1)$$

Applying this operator gives the full time-independent, single-particle Schrödinger equation. The solutions of this equation define a set of allowed eigenfunctions and their eigenvalues:

$$h\psi_i(\mathbf{r}\sigma) = \epsilon_i\psi_i(\mathbf{r}\sigma) \quad (3.2)$$

The quantities  $\mathbf{r}$  and  $\sigma$  denote coordinates in space and the spin quantum number, respectively. For fermions (and therefore electrons), the spin quantum number has the value  $\pm\frac{1}{2}$ .

For a system of  $N$  electrons, the Schrödinger equation may be written as:

$$H\Psi = E\Psi \quad (3.3)$$

The total energy operator, the Hamiltonian, is denoted  $H$ . The ground state energy of the system is  $E$ . A common approximation for the solution of Eq. 3.3 is the Born-Oppenheimer Approximation [34]. Here, it is posited that, in a system of interacting electrons and nuclei, the nuclei must have much smaller velocities than the electrons



due to their far greater mass. On the time scale of nuclear motion, one can therefore consider the electrons to relax to a ground state given by the Hamiltonian.

Further defining the Hamiltonian, Eq. 3.3 becomes

$$H\Psi = (T + V_{ext} + V_{ee})\Psi = E\Psi \quad (3.4)$$

where  $T$  is the kinetic energy operator (the first term in Eq. 3.1),  $V_{ext}$  is an externally applied potential field, and  $V_{ee}$  represents an effective potential defined as the net effects of all electron-electron interactions in the system. Given the wave function  $\Psi(\mathbf{r}_1\sigma_1, \dots, \mathbf{r}_N\sigma_N)$ —having  $3N + N$  degrees of freedom—the probability of finding an electron with spin  $\sigma$  at a point  $\mathbf{r}$ —is

$$n_\sigma(\mathbf{r}) = N \int \dots \int |\Psi(\mathbf{r}_1\sigma_1, \dots, \mathbf{r}_N\sigma_N)|^2 d\mathbf{r}_2 d\mathbf{r}_3 \dots d\mathbf{r}_N \quad (3.5)$$

Computation of the Hamiltonian for a many-body system is prohibitively challenging. The electron-electron interaction term requires that the individual electron wave function cannot be found without simultaneously considering the individual electron wave functions associated with all the other electrons. Hartree-Fock theory addresses this with an approximation of the wave function that is antisymmetric with respect to an interchange of any two electron positions, as required by the Pauli exclusion principle:

$$\Psi(\mathbf{r}_1\sigma_1, \dots, \mathbf{r}_i\sigma_i, \dots, \mathbf{r}_j\sigma_j, \dots, \mathbf{r}_N\sigma_N) = -\Psi(\mathbf{r}_1\sigma_1, \dots, \mathbf{r}_i\sigma_i, \dots, \mathbf{r}_j\sigma_j, \dots, \mathbf{r}_N\sigma_N) \quad (3.6)$$

This expression of the wave function is the Hartree product. The Slater determinant of  $N$  spin-orbitals can then be constructed:

$$\Psi_{HF}(\mathbf{x}_1, \dots, \mathbf{x}_N) = \frac{1}{\sqrt{N!}} \begin{vmatrix} \psi_1(\mathbf{x}_1) & \psi_1(\mathbf{x}_2) & \dots & \psi_1(\mathbf{x}_N) \\ \psi_2(\mathbf{x}_1) & \psi_2(\mathbf{x}_2) & \dots & \psi_2(\mathbf{x}_N) \\ \vdots & \vdots & \ddots & \vdots \\ \psi_N(\mathbf{x}_1) & \psi_N(\mathbf{x}_2) & \dots & \psi_N(\mathbf{x}_N) \end{vmatrix} \quad (3.7)$$

where the single electron eigenfunctions,  $\psi_i(\mathbf{x}_i) = \psi_i(\mathbf{r}_i\sigma_i)$ , are the solutions of an effective one-particle Hamiltonian representing a single electron in an effective potential constructed from the electrostatic field of all other electrons in the system, thereby eliminating any self-interaction.

This gives the Hartree-Fock Hamiltonian:

$$H_{HF} = -\frac{1}{2}\nabla_i^2 + \nu(\mathbf{r}) + \nu_H(\mathbf{r}) + \nu_x^{i,\sigma}(\mathbf{r}) \quad (3.8)$$

where  $\nu(\mathbf{r}) + \nu_x^{i,\sigma}(\mathbf{r})$  is the Hartree-Fock approximation for  $V_{ee}$ . The quantity  $\nu_H(\mathbf{r})$  is the Hartree term:

$$\nu_H(\mathbf{r}) = \sum_j \int d\mathbf{r}' \frac{|\psi_j(\mathbf{r}')|^2}{|\mathbf{r} - \mathbf{r}'|} \psi_i(\mathbf{r}) \quad (3.9)$$

As written, the term includes an unphysical self-interaction of electrons when  $j = i$ . The final term is the exchange term, which results from the inclusion of the Pauli principle and the assumed determinantal form of the wave function:

$$\nu_x^{i,\sigma}(\mathbf{r}) = - \sum_j \delta_{\sigma_i \sigma_j} \int d\mathbf{r}' \frac{\psi_j^*(\mathbf{r}') \psi_i(\mathbf{r}')}{|\mathbf{r} - \mathbf{r}'|} \psi_j(\mathbf{r}) \quad (3.10)$$

Hartree-Fock theory, by assuming a single-determinant form for the wave function, neglects correlation between electrons. The electrons are subject to an average non-local potential arising from the other electrons, which can lead to a poor description of the electronic structure [35]. Although qualitatively correct in many materials and compounds, Hartree-Fock theory is insufficient to make accurate quantitative predictions.

### 3.1.2 Hohenberg-Kohn, Kohn-Sham, and DFT

The Hohenberg-Kohn theorems [24] postulate that the full potential acting on the system is uniquely determined by the ground state electron density,  $n_0(\mathbf{r})$  of an  $N$  electron system. The exact ground electron density may be determined variationally by minimizing the functional  $E[n(\mathbf{r})]$ :

$$\min_{n(\mathbf{r})} E[n] = \min_{n(\mathbf{r})} (T[n] + V_{eff}[n]) \quad (3.11)$$

where  $V_{eff} = V_{ext} + V_H + V_{XC}$ . As discussed previously,  $T$  and  $V_{ext}$  are the kinetic energy and Coulomb interaction with any external applied potential, respectively. The quantity  $V_H$  is the Hartree interaction of the electrons and, finally,  $V_{XC}$  is the exchange-correlation functional, consisting of any remaining pieces of  $V_{ee}$ . The complex Hamiltonian based on  $3N + N$  degrees of freedom of the full quantum mechanical wave function has thus been reduced to a functional dependent on only the three real spatial coordinates. While this restatement of the Schrödinger Hamiltonian forms the

foundation of DFT, the powerful Hohenberg-Kohn theorems do not offer a method of computing the ground state density of a system in practice.

Kohn and Sham [25] later simplified solving the Hohenberg-Kohn theorems by showing that the task of finding the right electron density can be expressed in a way that involves solving a set of equations in which each equation only involves a single electron. The Kohn-Sham Hamiltonian has the form

$$H_{KS} = -\frac{1}{2}\nabla^2 + V(\mathbf{r}) + V_H(\mathbf{r}) + V_{XC}(\mathbf{r}) \quad (3.12)$$

and the Schrödinger-like Kohn-Sham equations are

$$\left[ -\frac{1}{2}\nabla^2 + V(\mathbf{r}) + V_H(\mathbf{r}) + V_{XC}(\mathbf{r}) \right] \psi_i = E_i \psi_i \quad (3.13)$$

where the exchange-correlation term,  $V_{XC}$ , is:

$$V_{XC}(\mathbf{r}) = \frac{\delta E_{XC}(\mathbf{r})}{\delta n(\mathbf{r})} \quad (3.14)$$

Expressed without specifying the exchange-correlation term, the Kohn-Sham Hamiltonian is the exact Hamiltonian for the ground state of a many-body system. Although  $T$ ,  $V_{ext}$ , and  $V_H$  are known, the general form of  $V_{XC}$ , and therefore  $\nu_{XC}(\mathbf{r})$ , is unknown. Therefore, approximations for this quantity are required in order to utilize DFT and the Kohn-Sham Hamiltonian.

The first approximation of the true exchange-correlation potential, proposed in Hohenberg and Kohn's original DFT paper [24], is the local density approximation (LDA). The LDA consists of locally approximating the true exchange-correlation energy of a system by the exchange-correlation energy associated with a homogeneous electron gas of the same density. The homogeneous gas is the only system for which the form of the exchange-correlation energy is known exactly. Depending on only the local density, the total energy is commonly written as:

$$E_{XC}^{LDA}[n(\mathbf{r})] = \int n(\mathbf{r}) \epsilon_{XC}[n(\mathbf{r})] d\mathbf{r} \quad (3.15)$$

where  $E_{XC}^{LDA}[n(\mathbf{r})]$  is the exchange-correlation energy density corresponding to a homogeneous electron gas of density  $n(\mathbf{r})$ . Despite its simplicity, the LDA works well for solid systems and has been used in solid state calculations.

However, because the LDA assumes a uniform density, it has a tendency to underestimate the exchange energy and over-estimate the correlation energy [36]. The

errors due to the exchange and correlation parts tend to compensate each other to a certain degree; however, to actively correct for this tendency, it is common to expand in terms of the gradient of the density in order to account for the non-homogeneity of the true electron density. This allows corrections based on the changes in density away from the coordinate. These expansions are referred to as generalized gradient approximations (GGA) [36, 37, 38].

### 3.1.3 Solving the Kohn-Sham equations

While the Kohn-Sham Hamiltonian provides a mathematical framework of the ground state energy of any system of  $N$  electrons in the presence of an applied potential field in only three degrees of freedom, computation of the Kohn-Sham orbitals and eigenvalues is inherently difficult. Defining the effective potential terms in Eq. 3.12 requires knowledge of the charge density, which requires knowledge of the Kohn-Sham orbitals, which themselves must be calculated using the as yet unknown Kohn-Sham Hamiltonian. To address this complexity, the following procedure for an iterative, or self-consistent, method was implemented:

1. Define an initial, trial electron density,  $n(\mathbf{r})$
2. Calculate the effective potential,  $V_{eff}$
3. Solve the Kohn-Sham equations defined using the trial electron density to find the single-particle wave functions,  $\psi_i(\mathbf{r})$
4. Calculate the electron density defined by the Kohn-Sham single-particle wave functions from Step 3,

$$n_{KS}(\mathbf{r}) = \sum_i^N |\psi_i(\mathbf{r})|^2$$

5. Compare the calculated electron density,  $n_{KS}(\mathbf{r})$ , with the electron density used in solving the Kohn-Sham equations,  $n(\mathbf{r})$ . If the two densities are the same (i.e. within some tolerance), the ground state electron density has been found. If the two densities are different, then the trial electron density must be updated, generally by mixing this output density with densities from previous iterations [39]. The process then begins again from Step 2.

When studying the electronic structure of condensed matter systems, massive numbers of electrons, on the order of  $10^{28}$  per mole of atoms, are being investigated. Naturally, even numerically with the aid of computationally resources, it is not feasible

to solve the Kohn-Sham equations for all points in such an enormous space. However, many extended systems are periodic in structure, corresponding to one of the fourteen Bravais lattices. Therefore, a periodic system that is, in practice, infinite (e.g. a crystal), can be represented as a periodic cell and calculations are only required on electrons associated with the periodic cell.

Bloch's theorem [40] shows that the wave function,  $\psi_n$ , of an electron band  $n$  for a periodic system can be expressed as a combination of two parts: a plane wave part and a periodic cell part:

$$\psi_n(\mathbf{r}) = u_n(\mathbf{r})e^{i\mathbf{k}\cdot\mathbf{r}} \quad (3.16)$$

where the plane wave part has the wave vector,  $\mathbf{k}$ , which is confined to the first Brillouin zone. The periodic part has the same periodicity of the lattice,  $u_n(\mathbf{r} + \mathbf{R}) = u_n(\mathbf{r})$ , where  $\mathbf{R}$  is a lattice vector.

The wave function within the periodic cell can then be described by a plane wave basis set. The periodic part of the wave function can then be written as:

$$u_n(\mathbf{r}) = \sum_{\mathbf{G}} c_{n,\mathbf{G}} e^{i\mathbf{G}\cdot\mathbf{r}} \quad (3.17)$$

where  $c_{n,\mathbf{G}}$  is the set of plane wave coefficients and  $\mathbf{G}$  are the reciprocal lattice vectors that satisfy the relation  $\mathbf{G} \cdot \mathbf{R} = 2\pi m$ , where  $m$  is an integer. Combining Eq. 3.16 and Eq. 3.17, the Kohn-Sham orbitals can be written as an infinite sum of plane waves:

$$\psi_n(\mathbf{r}) = \sum_{\mathbf{G}} c_{n,(\mathbf{k}+\mathbf{G})} e^{i(\mathbf{k}+\mathbf{G})\cdot\mathbf{r}} \quad (3.18)$$

where  $c_{n,(\mathbf{k}+\mathbf{G})}$  are the coefficients of the plane waves describing the wave function.

Efficient  $\mathbf{k}$ -point sampling schemes have been developed, such as the one given by Monkhorst and Pack [41]. Here, the symmetry of the lattice can be used to reduce the number of  $\mathbf{k}$ -points required. The Brillouin zone is made irreducible by applying the point group symmetries of the lattice, leaving no  $\mathbf{k}$ -point related by symmetry [35]. The sum over  $\mathbf{G}$  vectors in Eq. 3.18 is infinite in order to fully describe the wave function; in practice, a finite end to the sum must be selected. For most wave functions, there will be a scale below which the wave function can be described as smoothly varying. This means that the coefficients  $c_{n,(\mathbf{k}+\mathbf{G})}$  will become small for large  $|\mathbf{k} + \mathbf{G}|$ . The cutoff point is referred to as the plane wave kinetic energy cutoff:

$$E_{cut} \geq \frac{1}{2}|\mathbf{k} + \mathbf{G}|^2 \quad (3.19)$$

The use of plane waves as a basis set is advantageous in a number of ways. In terms of the accuracy required for the system in question, one can always improve the accuracy by increasing the plane wave cutoff energy and therefore tending towards the complete basis set. Real space quantities, such as potentials, can be easily transformed to reciprocal space using standard numerical techniques, in order to obtain the plane wave coefficients. Derivatives in real space become multiplications in reciprocal space, so quantities such as the kinetic energy of the Kohn-Sham orbitals can be easily evaluated. Finally, as plane waves treat all regions of space equally, they can be applied generally, even for non-periodic systems, if an appropriate periodic supercell is used [35].

### 3.1.4 The pseudopotential approximation

Electrons in the vicinity of the nuclei will be under the influence of a steep Coulomb potential and have rapidly varying wave functions in the nuclear regions. This requires a correspondingly large number of plane waves to adequately describe the wave function and the nuclear potential. This expense is reduced by the pseudopotential approximation [42, 43, 44], which reduces the required number of plane waves by many orders of magnitude.

Electrons in condensed matter can be considered to belong to one of two categories: core or valence. Core electrons are localised in the vicinity of the nucleus. Valence electrons are those outside the core region and for most situations are responsible for the physical properties of a system. As the core electrons are generally unaffected by external potentials, they, along with the nuclear potential, can be replaced to create a relatively weak pseudopotential. This pseudopotential acts on a set of pseudo wave functions that, outside of a specified core radius, are identical to the wave functions where all the electrons are taken into account. As these pseudo wave functions have no nodes in the core region, the number of plane waves required to describe the system are reduced by many orders of magnitude. This reduces the number of required Kohn-Sham orbitals, and subsequently the computational expense.

### 3.1.5 Minimization of the total energy

The Kohn-Sham equations (Eq. 3.13) become a matrix diagonalization problem when expressed in terms of plane waves. Unfortunately, numerical algorithms for matrix diagonalization do not scale well for large matrices, limiting the number of plane waves and number of atoms in the periodic cell that can be studied. Alternative methods

involve direct minimization of Eq. 3.11, the Kohn-Sham total energy functional. This is done through variation of the plane wave coefficients of the Kohn-Sham orbitals while ensuring that each band is orthogonal to the others [35]. Among those methods one of the most efficient is the conjugate gradients technique [45]. This procedure begins by taking an initial search direction to be that with the steepest gradient for the function and variable in question. That line is then followed to find the minimum. Subsequent search directions are then chosen such that they are independent of any previous minimisation directions. This guarantees the minimum will be found in the same number of steps as there are dimensions in the system.

## 3.2 Density functional perturbation theory

As discussed in the previous section, density functional theory has been used successfully to calculate the ground state properties of electronic systems. As the method provides only the ground state density and total energy, there are numerous examples of failures related to electronic excited states. However, if the system is perturbed very lightly such that it remains close to its electronic ground state, one can easily apply the traditional quantum formalism for perturbation theory, giving rise to density functional perturbation theory (DFPT) [46].

### 3.2.1 Response functions

Many materials properties originate from an external perturbation to the system. Response functions are derivatives of the total energy with respect to applied perturbation(s). Common perturbations include atomic displacements, homogeneous external electric or magnetic fields, and strain. Physical properties related to the derivatives of the total energy include [47]:

- 1st order: forces, stress, dipole moment
- 2nd order: phonon dynamical matrix, elastic constants,  
dielectric susceptibility, Born effective charges,  
piezoelectricity, internal strain
- 3rd order: non-linear dielectric susceptibility,  
phonon-phonon interaction, Grüneisen parameters,  
Raman susceptibilities

### 3.2.2 Perturbation theory

General perturbation theory begins with the identification of a small parameter,  $\lambda$ , characterizing the change in the unperturbed Hamiltonian of the system  $H^{(0)}$  due to some external potential  $V_{ext}$ :

$$H = H^{(0)} + \lambda V_{ext} \quad (3.20)$$

It is assumed that the unperturbed Schrödinger equation, shown below,

$$H^{(0)}\psi_i = E_i\psi_i \quad (3.21)$$

can be solved for  $H^{(0)}$ . Perturbation theory aims to solve the perturbed Schrödinger equation, which as an eigenvalue equation reads:

$$H\psi_i = E_i\psi_i \quad (3.22)$$

The fundamental hypothesis of perturbation theory is that all physical quantities can be expanded in Taylor series with respect to  $\lambda$ , and that these series are well-defined and will converge [46]. A perturbation of the Hamiltonian will change the resulting eigenstates and eigenvalues, generically to arbitrary order in  $\lambda$ . The quantities  $H$ ,  $E$ , and  $\psi$  can be expanded about  $\lambda$ :

$$H = H^{(0)} + \lambda H^{(1)} \quad (3.23)$$

$$\psi_i = \psi_i^{(0)} + \lambda \psi_i^{(1)} + \lambda^2 \psi_i^{(2)} + \dots \quad (3.24)$$

$$E_i = E_i^{(0)} + \lambda E_i^{(1)} + \lambda^2 E_i^{(2)} + \dots \quad (3.25)$$

By substituting Eqs. 3.23, 3.24 and 3.25 into Eq. 3.22, one obtains the expanded perturbed Schrödinger equation:

$$\begin{aligned} & H^{(0)}\psi_i^{(0)} + \lambda(H^{(1)}\psi_i^{(0)} + H^{(0)}\psi_i^{(1)}) + \lambda^2(H^{(1)}\psi_i^{(1)} + H^{(0)}\psi_i^{(2)}) + \dots \\ &= E_i^{(0)}\psi_i^{(0)} + \lambda(E_i^{(1)}\psi_i^{(0)} + E_i^{(0)}\psi_i^{(1)}) + \lambda^2(E_i^{(2)}\psi_i^{(0)} + E_i^{(1)}\psi_i^{(1)} + E_i^{(0)}\psi_i^{(2)}) + \dots \end{aligned} \quad (3.26)$$

Eq. 3.26 can then be solved order by order in  $\lambda$ .



At order  $\lambda^0$  (no perturbation):

$$H^{(0)}\psi_i^{(0)} = E_i^{(0)}\psi_i^{(0)} \quad (3.27)$$

At order  $\lambda^1$  (first order of perturbation):

$$H^{(1)}\psi_i^{(0)} + H^{(0)}\psi_i^{(1)} = E_i^{(1)}\psi_i^{(0)} + E_i^{(0)}\psi_i^{(1)} \quad (3.28)$$

At order  $\lambda^2$  (second order of perturbation):

$$H^{(1)}\psi_i^{(1)} + H^{(0)}\psi_i^{(2)} = E_i^{(2)}\psi_i^{(0)} + E_i^{(1)}\psi_i^{(1)} + E_i^{(0)}\psi_i^{(2)} \quad (3.29)$$

In Dirac notation, taking the scalar product of Eq. 3.28 with  $\psi_i^{(0)}$  yields:

$$\langle\psi_i^{(0)}|H^{(1)}|\psi_i^{(0)}\rangle + \langle\psi_i^{(0)}|H^{(0)}|\psi_i^{(1)}\rangle = E_i^{(1)}\langle\psi_i^{(0)}|\psi_i^{(0)}\rangle + E_i^{(0)}\langle\psi_i^{(0)}|\psi_i^{(1)}\rangle \quad (3.30)$$

As  $\langle\psi_i^{(0)}|H^{(0)} = \langle\psi_i^{(0)}|E_i^{(0)}$  and  $\langle\psi_i^{(0)}|\psi_i^{(0)}\rangle = 1$ , one is left with:

$$E_i^{(1)} = \langle\psi_i^{(0)}|H^{(1)}|\psi_i^{(0)}\rangle \quad (3.31)$$

This is the Hellmann-Feynman theorem [48, 49], which states that the first derivative of the eigenvalues of the Hamiltonian  $H(\lambda)$  is given by the expectation value of the derivative of the Hamiltonian with respect to the parameter  $\lambda$ . This is an extremely powerful statement, as it shows that first-order corrections to the energy can be computed from the unperturbed wave functions and from the first-order change in the external potential.

To compute the second order derivative of the total energy, one begins with Eq. 3.29, and again applies the scalar product with  $\psi_i^{(0)}$ , which yields [47]:

$$E_i^{(2)} = \frac{1}{2}(\langle\psi_i^{(0)}|H^{(1)} - E_i^{(1)}|\psi_i^{(1)}\rangle + \langle\psi_i^{(1)}|H^{(1)} - E_i^{(1)}|\psi_i^{(0)}\rangle) \quad (3.32)$$

Using the first order normalization condition  $\langle\psi_i^{(0)}|\psi_i^{(1)}\rangle + \langle\psi_i^{(1)}|\psi_i^{(0)}\rangle = 0$ , one obtains:

$$E_i^{(2)} = \frac{1}{2}(\langle\psi_i^{(0)}|H^{(1)}|\psi_i^{(1)}\rangle + \langle\psi_i^{(1)}|H^{(1)}|\psi_i^{(0)}\rangle) \quad (3.33)$$

While no knowledge of  $\psi_i^{(2)}$  is required to compute  $E_i^{(2)}$ , knowledge of  $\psi_i^{(1)}$  is. This requires returning to the first order perturbation Schrödinger equation, Eq. 3.28. The

terms containing  $|\psi_i^{(1)}\rangle$  are gathered, such that:

$$(H^{(0)} - E_i^{(0)})|\psi_i^{(1)}\rangle = -(H^{(1)} - E_i^{(1)})|\psi_i^{(0)}\rangle \quad (3.34)$$

This is the Sternheimer equation [50], which is equivalent to the common matrix equation  $A\mathbf{x} = \mathbf{y}$ .

### 3.2.3 Basic equations in DFPT

As shown in the previous section, the basic ansatz behind DFPT is that quantities may be recast as perturbation series:

$$X(\lambda) = X^{(0)} + \lambda X^{(1)} + \lambda^2 X^{(2)} + \dots$$

where  $X(\lambda)$  is a generic physical quantity that could be, for example, the Kohn-Sham orbitals, Kohn-Sham energy, or electronic density. The variation in the Kohn-Sham orbitals may be determined by solution of the Sternheimer equation:

$$(H_{KS}^{(0)} - E_i^{(0)})|\psi_i^{(1)}\rangle = -(H_{KS}^{(1)} - E_i^{(1)})|\psi_i^{(0)}\rangle \quad (3.35)$$

The first order correction to the electronic energy can be computed as:

$$E^{(1)} = \sum_{i=1}^{N_e} \langle \psi_i^{(0)} | H^{(1)} | \psi_i^{(0)} \rangle = \sum_{i=1}^{N_e} \langle \psi_i^{(0)} | (T + V_{ext})^{(1)} | \psi_i^{(0)} \rangle + \left. \frac{dE_{H_{XC}}[\mathbf{n}^{(0)}]}{d\lambda} \right|_{\lambda=0} \quad (3.36)$$

which is the Hellmann-Feynman theorem for DFT. This expression includes  $H_{KS}^{(1)}$ , the first order change in the Kohn-Sham Hamiltonian, which can be written:

$$H_{KS}^{(1)} = T^{(1)} + V_{ext}^{(1)} + \int \left. \frac{\partial^2 E_{H_{XC}}}{\partial \mathbf{n}(\mathbf{r}) \partial \mathbf{n}(\mathbf{r}')} \right|_{\mathbf{n}^{(0)}} \mathbf{n}^{(1)}(\mathbf{r}') d\mathbf{r}', \quad (3.37)$$

In turn, this quantity requires the first order electron density,  $\mathbf{n}^{(1)}$ :

$$\mathbf{n}(\mathbf{r}; \lambda) = \sum_{i=1}^{N_e} \psi_i^*(\mathbf{r}; \lambda) \psi_i(\mathbf{r}; \lambda) \quad (3.38)$$

Still, the first order change to the wave function,  $\psi_i^{(0)}$ , must be found. Rather than inverting the  $(H_{KS}^{(0)} - E_i^{(0)})$  operator from Eq. 3.35, the problem can be solved by

expanding  $\psi_i^{(1)}\rangle$  in the basis of  $\psi_i^{(0)}\rangle$ , which is orthonormal and complete:

$$\psi_i^{(1)}\rangle = \sum_j c_{ij}^{(1)} |\psi_i^{(0)}\rangle \quad (3.39)$$

where the expansion coefficient  $c_{ij}^{(1)}$  is given by:

$$c_{ij}^{(1)} = \frac{\langle \psi_i^{(0)} | H_{KS}^{(1)} | \psi_i^{(0)} \rangle}{E_i^{(0)} - E_j^{(0)}} \quad (3.40)$$

These equations form a set of self-consistent equations that must be solved in order to determine the behaviour of the perturbed system. For an N-electron system, the linear dependence of the first order Kohn-Sham Hamiltonian upon the first order density and subsequently the first order Kohn-Sham orbitals, leads to a coupling of the N equations.

## Chapter 4: Wulff shape prediction from surface excess free energies

### 4.1 Motivation

Proposed applications for nanoparticles are numerous and span seemingly unrelated fields, including drug delivery [51, 52, 53, 54, 55, 56, 57, 58, 59], catalysis [60, 61, 62, 63, 64], and electron devices [65, 66, 67, 68, 69]. In nearly all applications, nanoparticle shape is known to have a significant impact on particle properties and behavior [70, 71]. Therefore, the ability to predict, or even tailor, particle shape is crucial for improving properties and performance. Both equilibrium particle shape and shape evolution during fabrication are controlled by details of a particle’s exposed surfaces—details which are, in turn, controlled by the chemical, thermodynamic, and mechanical conditions or environment in which a particle is found [72, 73, 74, 75, 76].

The connections between the conditions in which a particle is found—e.g., chemical environment and/or temperature—and particle shape are complex, as reflected in the diversity of possible surface configurations at the atomic-scale. In this chapter, the calculation of temperature- and chemical environment-dependent surface excess free energies from density functional theory (DFT) is demonstrated. From these quantities, maps of equilibrium nanoparticle shapes are distilled, relating surface chemistry, temperature, and chemical environment. While the approach described here can be applied to the prediction and optimization of equilibrium nanoparticle shapes generally, this chapter focuses on systems relevant to thermionic, or “hot”, cathodes. State-of-the-art Sc-containing (“scandate”) cathodes have been shown to exhibit significantly improved performance as compared to related “B-type” cathodes [77, 78]. Both scandate and B-type cathodes consist of pellets of loosely sintered W crystallites (500-1000 nm in diameter) with Ba-containing mixed oxide powders in the pores of the pellet. The addition of Sc (to form a scandate cathode) both enhances performance and results in W crystallites with a highly characteristic shape after annealing at high temperatures ( $\sim 1150^\circ\text{C}$  for on the order of 24 hours) [79].

Significant current research is focused on understanding the origin of this characteristic (001)-, (110)-, and (112)-terminated W crystallite shape and the roles that surface composition and annealing temperature play in its stabilization [80, 81, 82, 79, 83]. The work presented in this chapter directly supports these studies by examining temperature- and chemical environment-dependent surface free energies and reporting “particle configuration maps” for B-type conditions: particles with bare,

O-terminated, and  $\text{Ba}_x\text{O}$ -terminated W (001), (110), and (112) surfaces.

As-fabricated nanoparticle shapes are the product of kinetic and thermodynamic factors governing surface configuration and behavior, with kinetics playing a particularly important role in solution processing [72]. For nanoparticles in high-temperature or gas-phase applications, thermodynamic factors increasingly control surface configurations, and therefore the stability and evolution of particle shape. Numerous experimental studies have examined the effect of temperature on stable particle shape [84, 85, 86, 87, 88, 89, 90, 91]. Though the thermodynamic effects of chemical environment are often challenging to distinguish from kinetic effects, significant recent effort has focused on effects of gas-phase environments on particle shape [92, 93, 94, 95, 96, 97, 98], including a large subset that have focused on the role of oxygen availability [83, 99, 100, 101, 102, 103, 104, 105, 106, 107, 108, 109, 110].

Density functional theory (DFT), described in Chapter 3, allows accurate calculation of ground state, or “zero-temperature”, atomic-scale structures and energies of possible surface configurations. Alone, these temperature- and environment-independent results can be used to approximate stable particle shapes in qualitatively described chemical environments by treating the reference energies of environmental species as free parameters [97]. Temperature effects due to changes in the chemical environment can be approximated by treating the temperature dependence of these reference energies as that of an ideal gas [109, 111]. Measured thermochemical data [112] has been used for the reference energies of gas-phase environmental species allowing improved comparisons to measurable temperatures and chemical environments (via partial pressures). This combination of DFT-calculated properties of the solid and surface and thermochemical data for the gas-phase environment has been widely used to predict the stability of particular surface configurations [102, 108, 110, 113, 114]. Despite the incorporation of temperature-dependent environmental properties, all of these predictions for particle shape and/or surface stability are still limited in that “zero-temperature” DFT calculations of the solid and its surfaces neglect entropic contributions—that is, such calculations do not yield the surface *free energies* that ultimately govern particle shape.

Separately, density functional perturbation theory (DFPT) has been widely applied to compute the properties of phonons from DFT, including the phonon density of states and vibrational contributions to entropy [115, 116, 117]. This has allowed direct calculation of both bulk reference free energies [113, 114] and surface free energies [116, 118, 119, 120]. Calculations of this type are generally limited to a small number of surface configurations, and do not address equilibrium particle shape or chemical

effects due to a particle’s environment. Recently DFPT has been used to augment thermochemical data (applicable to isolated molecules) by adding a correction for changes in vibrational entropy of environmental species due to surface adsorption [119]. In addition, a recent paper has used DFPT calculated surface free energies to predict the Wulff shape of W in pure vacuum conditions (that is, absent any chemical environment) [120]. In the following, these approaches are extended to directly compute temperature- and chemical environment-dependent equilibrium shapes for W particles exposed to O and/or Ba. Configurational entropy arising from adsorbate diffusion on solid surfaces is also addressed. This approach allows formulation of maps of equilibrium particle shape under realistic experimental conditions—including those relevant to the optimization and application of W-based thermionic cathodes [79, 80, 81, 82, 83].

## 4.2 Methods

### 4.2.1 Thermodynamic approach to surface energy calculation

In the thermodynamic limit, a particle will assume the shape that minimizes the total surface excess free energy. This equilibrium shape is called the Wulff shape, and can be deduced, via the Wulff construction, from knowledge of the surface excess free energies of any surface configurations that may appear [72, 121]. A “surface configuration” is a specific composition and arrangement of atoms at, near, or on a particular surface. For crystals, surface configurations are first classified by their planar orientation relative to the underlying crystal’s principle axes. Facets are regions of appreciable surface area sharing a common, identifiable orientation. Patterns of atoms present at a surface facet may be reconstructions of the underlying bulk structure, have compositions that differ from the bulk, and/or be decorated with atomic or molecular adsorbates. Full determination of the true Wulff shape requires knowledge of the free energies of the non-finite set of all possible surface configurations. In practice, only a small subset of all possible configurations have any meaningful likelihood of being expressed by a real particle: essentially configurations that are minimal, or highly regular, reconstructions of the underlying crystal structure (most likely driven by changes that satisfy broken surface bonds), and/or configurations with environmentally-determined atoms or molecules incorporated or adsorbed at high-symmetry or broken bond sites on the surface.

A key challenge in applying the Wulff construction with DFT-computed surface energies is that, alone, DFT only yields ground-state, zero-temperature energies that

do not account for entropy or zero-point vibrational energy [ $E_{DFT} \equiv E(T=0)$ ]. In addition, DFT computed energies characterize particles in a perfect vacuum [ $E_{DFT} \equiv E(P=0)$ ]. More formally, for  $\hat{G}(T, P) = U - T\hat{S} + PV$ , where the hatted notation ( $\hat{x}$ ) highlights that  $x$  depends on temperature:

$$E_{DFT} \equiv G(T=0, P=0) = U$$

Therefore,  $E_{DFT}$  values are not free energies, as required in the Wulff construction.

Free energies require accounting for entropy and zero-point energies. At elevated temperatures the contribution of entropy to the total free energy grows dramatically. At temperatures below a crystal's melting temperature, vibrational entropy ( $\hat{S}_V$ ) and vibrational zero-point energy ( $E_{VZP}$ ) will be the major components of this contribution [122]. For surfaces where not every equivalent surface site is occupied, configurational entropy ( $S_C$ ) arising from the exchange of positions of surface adsorbates and vacancies is included. With  $E_{DFT}$ , one may write:

$$\begin{aligned} \hat{G} &= E_{DFT} + \hat{F}_V - TS_C \\ \text{where } \hat{F}_V &= E_{VZP} - T\hat{S}_V \end{aligned} \tag{4.1}$$

Here, the combination of DFPT-computed vibrational entropy and zero-point energy takes the form of a Helmholtz free energy.  $S_C$  is computed according to  $S_C = k_B \ln \Omega_C$ , where  $\Omega_C$  counts the number of arrangements of vacant and occupied surface adsorption sites for a given surface configuration, and  $S_C$  is normalized by the slab area. This term is zero for surfaces where all equivalent surface sites are occupied and for bulk systems.

Surface excess free energies<sup>1</sup> as a function of temperature ( $\hat{\gamma}$ ) are then simply the excess free energy present in a system containing a surface, relative to the energy of all species in their (bulk) reference state. In the present calculations, double-sided semi-infinite slabs are used to represent surface facets. The surface energy per unit area ( $\hat{\gamma}_\alpha$ ) of a particular surface configuration ( $\alpha$ ), containing  $n_i$  atoms of various species  $i$ , each having reference energy  $\mu_i$ , is thus:

$$\hat{G}_{\text{slab}, \alpha} = \sum_i \hat{\mu}_i n_i + 2A_\alpha \hat{\gamma}_\alpha$$

---

<sup>1</sup>Since the definition of free energy has now been explicitly described, the remainder of this dissertation will use the term “surface energy” to mean “surface excess free energy” for the sake of brevity.

The factor of two is included to account for the two sides of the slab, each with an area  $A_\alpha$ . The quantity  $\hat{\mu}_i$  is the chemical potential (Gibbs free energy per atom) of the each species  $i$  in its reference state.

Combining with Eq. 4.1:

$$\begin{aligned}\hat{G}_{slab, \alpha} &= E_{DFT, \alpha} + E_{VZP, \alpha} - T(\hat{S}_{V, \alpha} + S_{C, \alpha}) \\ &= \sum \hat{\mu}_i N_i + 2A_\alpha \hat{\gamma}_\alpha\end{aligned}$$

Or:

$$\hat{\gamma}_\alpha = \frac{E_{DFT, \alpha} + E_{VZP, \alpha} - T(\hat{S}_{V, \alpha} + S_{C, \alpha}) - \sum \hat{\mu}_i N_i}{2A_\alpha} \quad (4.2)$$

Finally, the equilibrium particle shape, or Wulff shape, is that which minimizes the total surface energy at fixed volume, where:

$$\hat{\Gamma} = \sum_{\alpha} \hat{\gamma}_\alpha A_\alpha \quad (4.3)$$

The Wulff construction[123] is the geometrical equivalent of Eq. 4.3, that is, that  $\hat{\Gamma}$  is minimized for the convex hull of all surface configurations,  $\alpha$ , each constructed a distance proportional to  $\hat{\gamma}_\alpha$  from the origin. That is,  $\hat{\Gamma}$  is minimized for the closed shape formed when  $h_\alpha = \lambda \hat{\gamma}_\alpha$  for  $h_\alpha$ , the height from the origin of each surface configuration  $\alpha$ , and  $\lambda$ , a scaling factor. A deeper discussion of the Wulff construction is given in Chapter 5.

#### 4.2.2 Calculation details

In this chapter, the commercial plane wave pseudopotential code, VASP (Vienna *Ab initio* Simulation Package) [124], was used for all DFT calculations. Pseudopotentials based on the Perdew-Burke-Ernzerhof (PBE) formalism of the generalized gradient approximation (GGA) [125] with projector augmented wave method (PAW) [126] were used for all atoms. The W ( $5p^6 6s^2 5d^4$ ), Ba ( $5s^6 5p^6 6s^2$ ), and O ( $2s^2 2p^4$ ) electrons were included in the respective valences. Brillouin zone sampling was done with Monkhorst-Pack  $k$ -point meshes with densities at least 30  $k$ -points/ $\text{\AA}^{-1}$  in each direction for each calculation. Atomic positions were relaxed according to calculated interatomic forces until the total energy was converged to better than  $1 \times 10^{-7}$  eV/atom. The plane wave expansion of the wave function was truncated at 520 eV.

For the bulk systems relevant to this chapter—W,  $\text{WO}_3$ , Ba, and BaO—reference energies were determined by converging  $\hat{\mu}_i$  with respect to system size. Supercells



ranging in size up to  $3 \times 3 \times 3$ ,  $2 \times 2 \times 2$ ,  $3 \times 3 \times 3$ , and  $2 \times 2 \times 2$  bulk unit cells were considered for W,  $\text{WO}_3$ , Ba, and BaO respectively. The facet orientations (001), (110), and (112) were considered based on previous characterization results for scandate cathodes and were represented as periodic semi-infinite W slabs with thicknesses of 13, 9, and 19 atomic layers ( $\sim 20.6$  Å,  $\sim 19.12$  Å, and  $\sim 23.4$  Å of W, respectively). Slabs were separated by a minimum vacuum spacing of 32-40 Å. For each surface, the W slab was left bare or decorated with various configurations of adsorbed O or Ba and O atoms, following Zhou et al. [83]. In addition, the  $[2 \times 2]$  reconstructed and  $[2 \times 2]$  supercell of ideal-terminated W (001) surfaces were both considered [120, 127], as was a newly identified  $[2 \times 2]$  “zig-zag” reconstruction of the  $\text{Ba}_x\text{O}/\text{W}$  (112) surface (see Fig. 4.8 in the next section).

The quantities  $\hat{F}_V$  and  $E_{VZP}$  were calculated using PHONOPY, an open source software package that leverages VASP for DFPT calculations [115]. Phonon properties were calculated in the harmonic approximation and were computed separately for bulk and surface slab systems. The software package Wulffmaker [121], which implements the Wulff construction in a user-friendly interface, was used to draw representations of the Wulff shape for selected sets of calculated  $\hat{\gamma}_\alpha$  values.

## 4.3 Results and Discussion

### 4.3.1 Temperature-dependent bulk reference free energies

To compute the surface energies required to determine the Wulff shape, temperature-dependent bulk reference free energies were required. While single primitive cells are sufficient to resolve zero-temperature, ground-state properties of bulk crystals, free energies accounting for vibrational entropy require supercells large enough to capture the set of activated phonons.

Fig. 4.1 shows computed bulk free energies per atom of W (from Eq. 4.1) for different W structures as a function of temperature. Comparison of the quantities  $\hat{F}_V$  of a primitive W cell (equivalent to  $1 \times 1 \times 1$ ),  $3 \times 3 \times 3$  W super cell, W (001) slab, W (110) slab, and W (112) determined convergence with respect to cell volume. As shown in Fig. 4.1, the primitive W unit cell (represented by the black curve) significantly underestimates the contribution of  $\hat{S}_V$ , leading to a nominally constant  $\hat{\mu}_W$ , even at elevated temperatures. The other structures produced similar  $\hat{F}_V$  curves, confirming that structures larger than a primitive cell are required to adequately describe activated phonons. The largest supercell ( $3 \times 3 \times 3$ ) was selected as the converged  $\hat{\mu}_W$  and its  $\hat{F}_V$  curve was used as the W reference for all computed

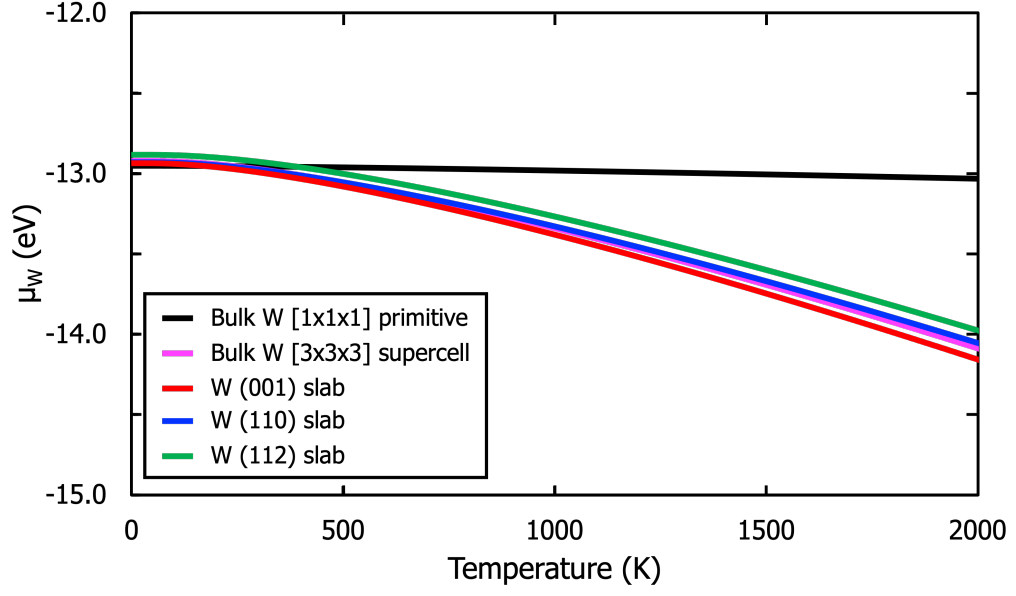


Figure 4.1:  $\hat{\mu}_W$  as a function of temperature for five W structures: two cubic cells and three slabs. Reproduced with permission from Ref. [128].

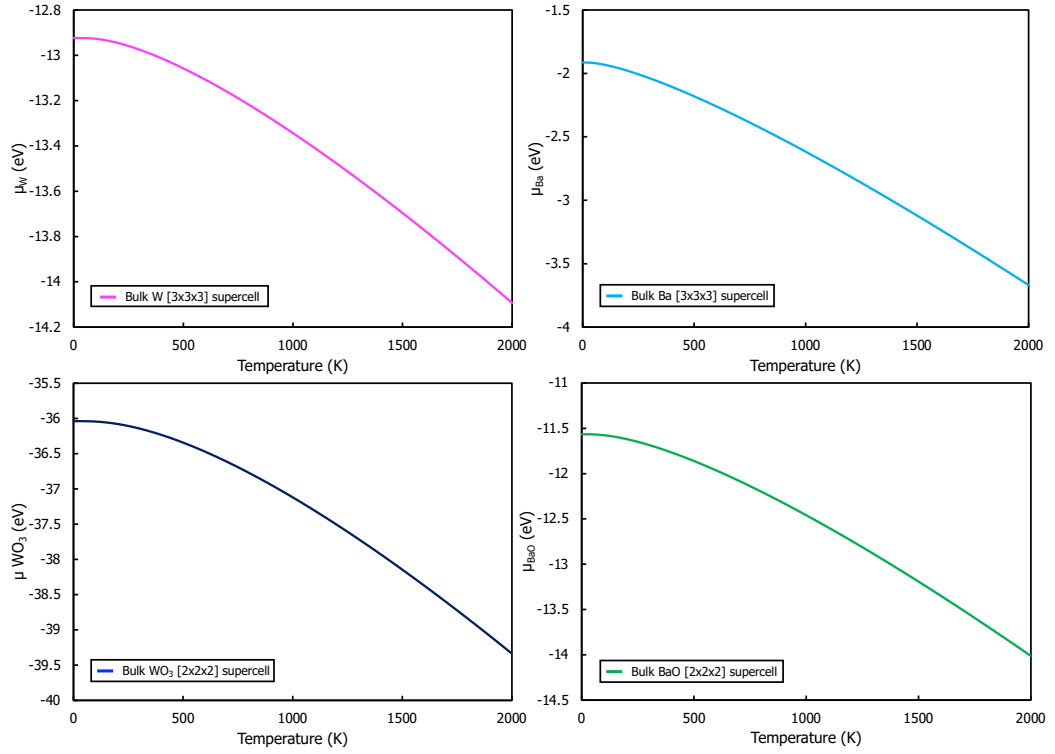


Figure 4.2: Bulk  $\hat{\mu}$  values for (a) W, (b) Ba, (c)  $\text{WO}_3$ , and (d) BaO, each from 0-2000 K. Reproduced with permission from Ref. [128].

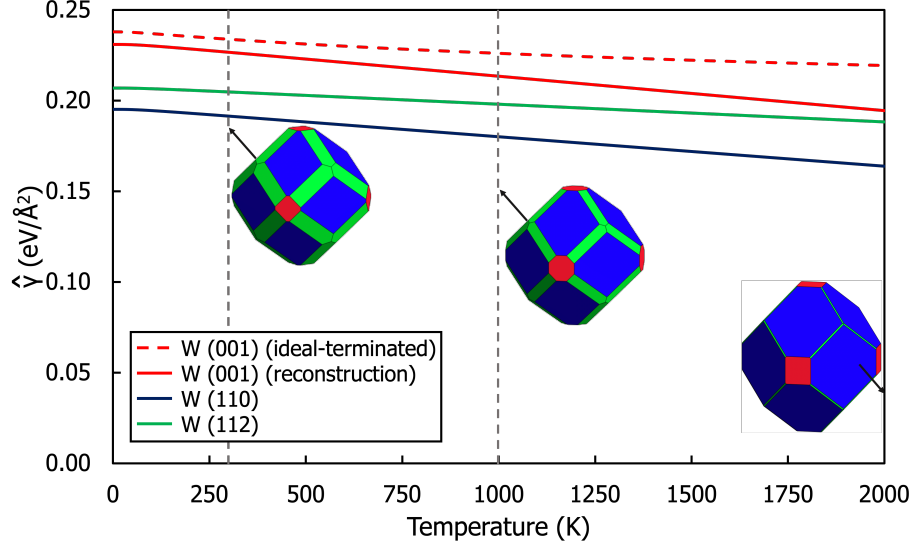


Figure 4.3: Surface energies and correlated equilibrium Wulff shapes of W surfaces at three temperatures: 300 K, 1000 K, 2000 K. Reproduced with permission from Ref. [128].

surface energies. The same approach—computing  $\hat{F}_V$  from supercells of increasing dimensions until convergence—was used to compute  $\hat{\mu}_i$  curves for  $\text{WO}_3$ , Ba, and BaO. Supercells with dimensions  $2 \times 2 \times 2$ ,  $3 \times 3 \times 3$ , and  $2 \times 2 \times 2$  were selected as converged references for these species, respectively, and are reported as a function of temperature in Fig. 4.2.

#### 4.3.2 Temperature-dependent W surface energies

Surface energies as a function of temperature for W (001), (110), and (112) surfaces (that is, W in a pure vacuum) are shown in Fig. 4.3, as well as a selection of resulting Wulff shapes at 300, 1000, and 2000 K. These surface energies do not include a configurational entropy term, since uniform terminations with no vacancies are expected on bare metal surfaces. At all temperatures, the surface energy of W (110) is lower than that of both the W (001) and W (112) surfaces. This result is consistent with previous experiment [129, 130, 131, 132, 133, 134] and calculation [120, 135], which find that W particle shapes are dominated by (110) surfaces. Considering W (001) in isolation, the  $2 \times 2$  reconstructed surface has the lowest free energy at all temperatures. At 0 K, the reconstructed W (001) surface is 6.82 meV lower than the ideal-terminated configuration, similar to the 6.87 meV ( $0.11 \text{ J/m}^2$ ) lower energy reported in Ref. [120]. The ideal and reconstructed W (001) surfaces are shown in Fig. 4.4. The W (112) surface has a lower surface energy than W (001) at all

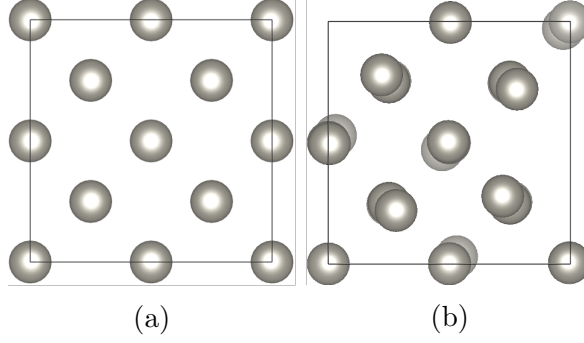


Figure 4.4: The W (001) surface with **(a)** an ideal termination and **(b)** the lower energy reconstruction. Reproduced with permission from Ref. [128].

considered temperatures, and at temperatures below  $\sim 1000$  K the W (112) has low enough surface energy that it would be expected to appear on particles exhibiting the equilibrium shape. At these temperatures achieving the equilibrium shape may be kinetically constrained, though increasing “rounding” of (110)/(110) edges due to the appearance of (112) facets should be expected. At all temperatures corners at the intersection of three (110)-type planes should be expected to be truncated with small (001) facets.

#### 4.3.3 M/MO<sub>x</sub> stability

The equilibrium shape of W particles in a chemical environment containing O, or Ba and O, and specifically the equilibrium W particle shape as a function of both temperature and O<sub>2</sub> partial pressure is considered here. The Ba<sub>x</sub>O/W system is highly relevant for thermionic (“hot”) dispenser cathodes. Extensive studies have shown that Ba cations adsorbed atop O-terminated W surfaces in so-called B-type cathodes dramatically enhance thermionic emission compared to previous generations of thermionic cathodes [80, 83, 136, 128]. In addition, recent studies have shown that B-type cathodes can be further enhanced with the addition of Sc. These scandate cathodes exhibit extremely high emitted current densities, and also a characteristic (001), (110), (112)-terminated shape, highlighting a direct connection between equilibrium shape and device performance during operation [79].

Experiment has shown that while O is present during cathode operation, its availability is not sufficient to oxidize W particles to WO<sub>3</sub>, even after annealing at elevated temperature (1300 K and higher) for hundreds or thousands of hours [79]. Both BaO and metallic Ba are observed to be present inside the sealed environments in which cathodes operate, implying enough O is available to oxidize at least a significant frac-

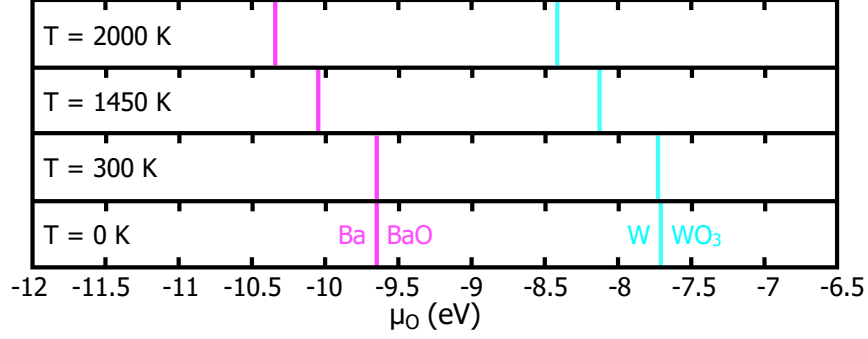


Figure 4.5: The regions of stability for a metal and its respective oxide as a function of temperature for W and Ba. Reproduced with permission from Ref. [128].

tion of available Ba [137]. These observations of the presence of certain bulk phases represent limits on the chemical potential of O in the W particle's environment. For a general oxidation reaction at equilibrium, when a bulk metal  $M$  is in equilibrium with its oxide  $MO_X$ :

$$\begin{aligned}\hat{\mu}_M + X\mu_O &= \hat{\mu}_{MO_X} \\ \text{or } \mu_O &= \frac{\hat{\mu}_{MO_X} - \hat{\mu}_M}{X}\end{aligned}\quad (4.4)$$

When either the metal or the oxide are favored, these become inequalities, with  $\hat{\mu}_M + X\mu_O$  lower when the metal is stable, and  $\hat{\mu}_{MO_X}$  lower when the oxide is favored. For a Ba-, O-, and W-containing system relevant to cathodes, where both metallic W and oxidized Ba (BaO) are present, the expressions  $\hat{\mu}_W + 3\mu_O < \hat{\mu}_{WO_3}$  and  $\hat{\mu}_{Ba} + \mu_O \geq \hat{\mu}_{BaO}$  are true for W and Ba, respectively. Rearranging, this gives limits on the value of  $\mu_O$  implied by experiment:

$$\begin{aligned}\mu_O &< \frac{\hat{\mu}_{WO_3} - \hat{\mu}_W}{3} \\ \text{and } \mu_O &\geq \hat{\mu}_{BaO} - \hat{\mu}_{Ba}\end{aligned}$$

Fig. 4.5 shows these limits on  $\mu_O$ —effectively the equilibrium phase boundaries between W/ $WO_3$  and Ba/ $BaO$ —at 0, 300, 1450, and 2000 K, as derived for computed bulk free energies (chemical potentials) of W,  $WO_3$ , Ba, and  $BaO$  (see Figs. 4.1 and 4.2).

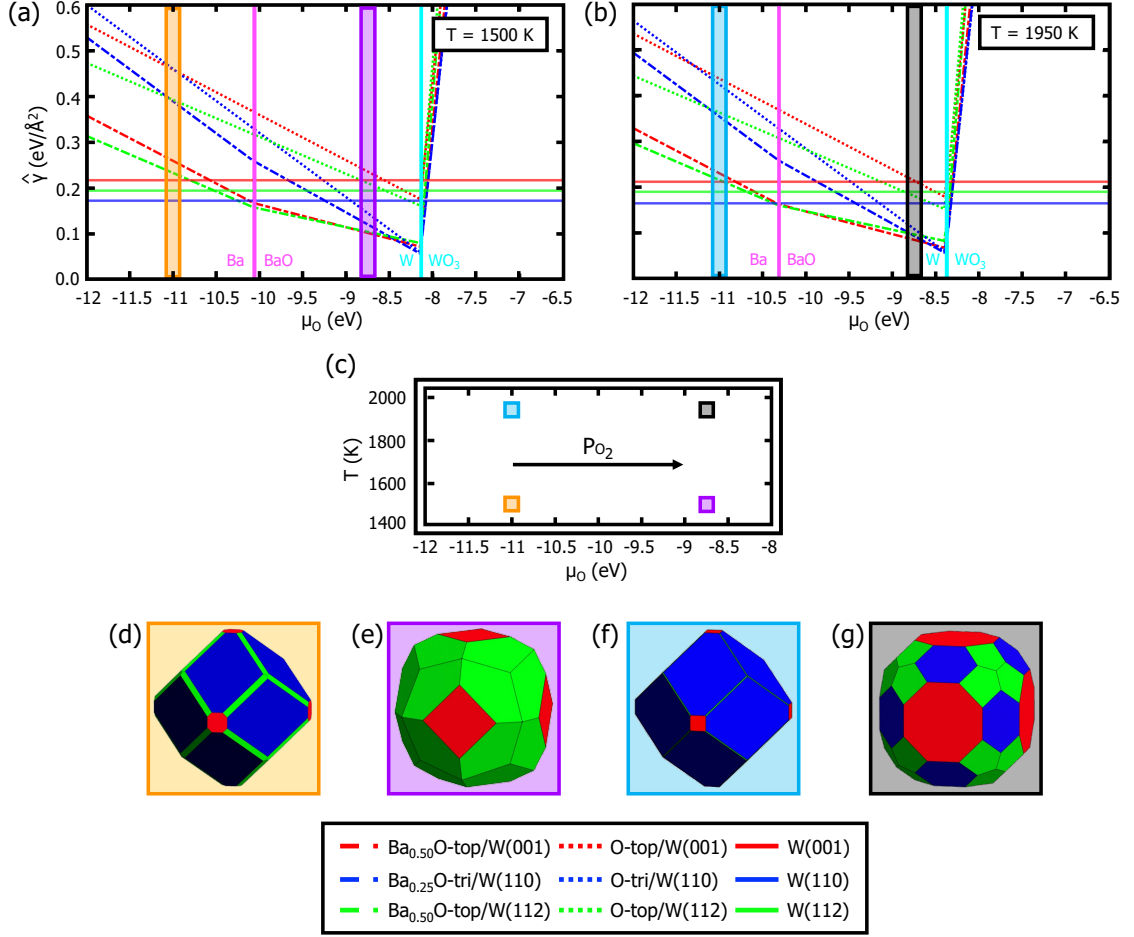


Figure 4.6: Four combinations of  $P_{O_2}$  and  $T$  are highlighted in (c). These pairs are extended to (a) and (b), which show  $\hat{\gamma}$  as a function of  $\mu_O$  at two temperatures: 1500 K and 1950 K. The minimum  $\hat{\gamma}$  surfaces were used to construct four Wulff shapes, each exhibiting varying degrees of (001), (110), and (112) facets, highlighting the critical dependence of  $\hat{\gamma}$  on both  $T$  and  $\mu_O$ . Figs. (d) and (f) are both comprised only of W facets, and appear quite similar except for the slight appearance of (112) in Fig. (d). Fig. (g) prominently exhibits all three facets, and is comprised of the Ba<sub>0.50</sub>O-top/W (001), Ba<sub>0.25</sub>O-tri/W (110), and is the Ba<sub>0.50</sub>O-top/W (112) configurations. Fig. (e) does not exhibit the (110) facet, only including the Ba<sub>0.50</sub>O-top/W (001) and Ba<sub>0.50</sub>O-top/W (112) configurations. At both of these temperatures, W (001) refers to the reconstruction. Reproduced with permission from Ref. [128].

#### 4.3.4 W particles in a Ba/O-containing environment

To assess W particle shapes relevant in cathode environments, the properties of various  $\text{Ba}_x\text{O}/\text{W}$  (hkl),  $\text{O}/\text{W}$  (hkl), and  $\text{W}$  (hkl) surface configurations were computed:  $\text{Ba}_{0.50}\text{O-top}/\text{W}$  (001),  $\text{Ba}_{0.25}\text{O-tri}/\text{W}$  (110),  $\text{Ba}_{0.50}\text{O-top}/\text{W}$  (112) ( $[2 \times 1]$  row and  $[2 \times 2]$  zig-zag),  $\text{O-top}/\text{W}$  (001),  $\text{O-top}/\text{W}$  (110),  $\text{O-top}/\text{W}$  (112),  $\text{W}$  (001) (ideal-terminated and  $2 \times 2$  reconstructed),  $\text{W}$  (110), and  $\text{W}$  (112)<sup>2</sup>. These surfaces were considered because they represent the collection of thermodynamically-stable, lowest surface energy configurations as determined in previous zero-temperature calculations by Zhou et al. [83] for W particles in environments containing Ba and O.

The quantities  $\hat{F}_V$  and  $S_C$  values for each of these surfaces were computed, which, when combined with the temperature-dependent bulk chemical potentials already discussed, determine temperature- and chemical environment-dependent surface energies. In computing  $\hat{F}_V$ , phonon density of states (pDOS) was required for both bulk and slab systems. Plots of pDOS for the nine examined surface configurations are presented in Fig. 4.7. Analysis of the pDOS for surface slabs provides a test of the mechanical stability of the surface configurations considered beyond relaxation of structures according to their interatomic forces, as stable structures are local energy minima, and therefore have no imaginary phonon modes. After first relaxing all surfaces according to their interatomic forces until total energies were converged to within  $1 \times 10^{-7}$  eV, DFPT calculations show no imaginary phonon modes for any of the bare W,  $\text{O}/\text{W}$ , or  $\text{Ba}_x\text{O}/\text{W}$  surfaces except (i) the ideal-terminated W (001) and (ii) the  $\text{Ba}_{0.50}\text{O-top}/\text{W}$  (112) surface. In the case of ideal-terminated W (001),

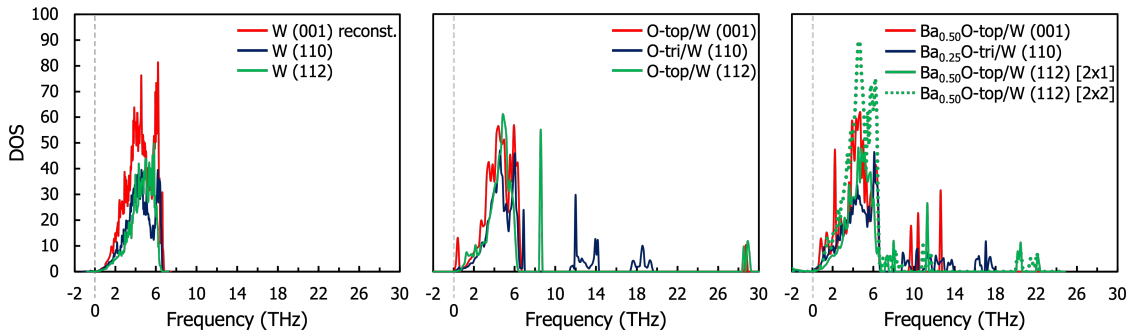


Figure 4.7: Phonon density of states for each of the surfaces examined here. Reproduced with permission from Ref. [128].

<sup>2</sup>Throughout this dissertation, surface configuration designations follow those in Refs. [128] and [83], which indicate metal-oxygen dipoles atop a W facet. For example,  $\text{Ba}_{0.50}\text{O-top}/\text{W}$  (001) indicates a 0.50 monolayer (ML) coverage of Ba cations atop a 1.0 ML of O located directly atop the outermost W atoms of a (001) slab.

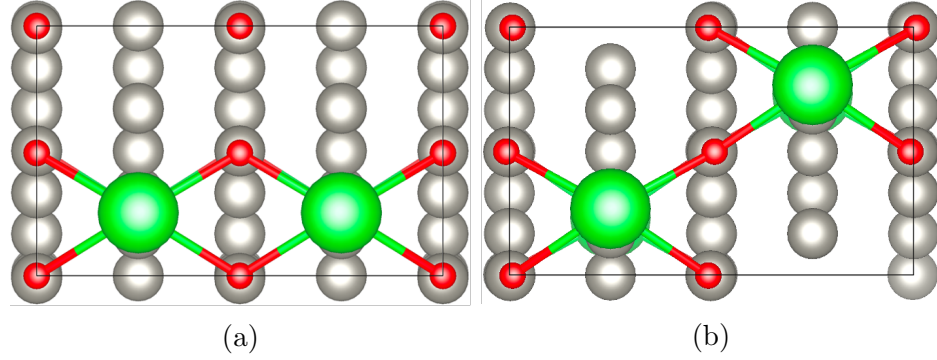


Figure 4.8: The  $\text{Ba}_{0.50}\text{O-top/W (112) } [2 \times 2]$  with Ba atoms in a **(a)** “row” pattern and a **(b)** “zig-zag” pattern. W atoms are gray, O atoms red, and Ba atoms green. Reproduced with permission from Ref. [128].

imaginary modes with frequencies ranging from  $6.0 \times 10^9$  to  $2.3 \times 10^{12}$  Hz simply reflect that the  $[2 \times 2]$  reconstruction, rather than the ideal-terminated surface, is stable, and the (relaxed) reconstructed surface is found to have no imaginary modes. The case of  $\text{Ba}_{0.50}\text{O-top/W (112)}$  is more complicated, with the (relaxed)  $[2 \times 1]$  “row” reconstruction reported by Zhou et al. [83] found to exhibit a single imaginary mode with a frequency of  $8.55 \times 10^8$  Hz. The Ba atoms in this surface are in alternating rows, and the imaginary mode involves an in-plane shift by the surface Ba towards a neighboring (unoccupied) surface site. Further analysis of up to  $[4 \times 2]$   $\text{Ba}_{0.50}\text{O-top/W (112)}$  surfaces shows that a  $[2 \times 2]$  “zig-zag” pattern of Ba atoms yields a reconstruction with slightly lower energy (by  $\sim 1 \text{ eV/\AA}^2$ ), but that also exhibits a low frequency imaginary mode ( $2.32 \times 10^{10}$  Hz). A comparison of the two  $\text{Ba}_{0.50}\text{O-top/W (112)}$  configurations are shown in Fig. 4.8.

Despite DFPT finding this mode to be imaginary (indicating that the surface configuration is not a local minimum), direct, discrete calculation of the energy of the  $\text{Ba}_{0.50}\text{O-top/W (112)}$  “zig-zag” with displacements (of varying magnitude) in the hyperdirection of this mode find the relaxed structure to be the lowest in energy. Because both  $[2 \times 1]$  and  $[2 \times 2]$  “zig-zag” structures are relaxed structures, both imaginary modes are relatively low frequency (implying a slowly varying potential energy surface), and direct calculation of the energy of relaxed “zig-zag” structures displaced according to the imaginary mode confirm a minimum energy configuration, it is hypothesized that the arrangement of Ba atoms on O/W (112) is not unique (at least at any finite temperature). Rather, the calculation is sampling a range of close-lying energy minima (e.g. combinations of “row” and “zig-zag” configurations), suggesting significant disorder in Ba arrangement on this surface and possibly fast Ba surface diffusion. Further examination of the kinetics of this surface are warranted,



but beyond the scope of this dissertation. In computing equilibrium crystal shapes, the low-energy  $[2 \times 2]$  “zig-zag” structure was utilized, though the similar energetics (both zero temperature  $E_{DFT}$  and temperature-dependent  $\hat{F}_V$  are within  $\sim 1\%$  of each other) of the  $[2 \times 2]$  and  $[2 \times 1]$  yield qualitatively indistinguishable equilibrium shapes.

Combining all computed bulk and surface energies, Fig. 4.6 summarizes the effects of varying temperature and  $\mu_O$  by showing equilibrium W crystal shapes [Figs. 4.6a, b, f, and g] at  $T = 1950$  and  $1500$  K and  $\mu_O = -11$  and  $-8.75$  eV. Figs. 4.6c and e show the  $\mu_O$ -dependent surface energies at the two temperatures, and Fig. 4.6d indicates the relative positions of the selected  $(T, \mu_O)$  points in phase space. Surface energies for the nine surface configurations  $[\hat{\gamma}_\alpha(\mu_O)]$  are shown as red, green, and blue curves in Figs. 4.6c and e. Fig. 4.6c shows surface energies at  $1950$  K, and Fig. 4.6e at  $1500$  K. Red curves correspond to (001) surface configurations, blue curves to (110) configurations, and green curves to (112) configurations. At both of these temperatures,  $\text{Ba}_{0.50}\text{O-top/W}$  (112)  $[2 \times 2]$  and  $[2 \times 1]$  exhibit comparable surface energies, and are thus not distinguished in this discussion. W (001) refers to the  $[2 \times 2]$  reconstruction. The M/ $\text{MO}_X$  equilibrium values of  $\mu_O$  are shown as the solid magenta (Ba/BaO) and cyan (W/ $\text{WO}_3$ ) vertical bars. The  $\hat{\gamma}_\alpha(\mu_O)$  curves are discontinuous at these bulk phase boundaries, as would be expected based on Eq. 4.2.

Fig. 4.6d shows a diagram akin to a temperature–pressure phase diagram. Oxygen partial pressure is represented by  $\mu_O$ , the O chemical potential, or, equivalently, the chemical availability of O in the system. Selecting two  $\mu_O$  points in each of the  $1500$  K and  $1950$  K plots of  $\hat{\gamma}_\alpha(\mu_O)$  [blue/orange and gray/purple vertical highlights in Figs. 4.6c and e] is equivalent to selecting four distinct  $(T, \mu_O)$  points on the temperature–pressure diagram, Fig. 4.6c. Figs. 4.6a, b and Figs. 4.6f, g show the equilibrium shapes of W particles at the four different  $(T, \mu_O)$  points. Vibrational entropy is consistently a far more significant component of surface entropy than configurational entropy, though this varies significantly as temperature varies. For example, for the  $\text{Ba}_{0.50}\text{O-top/W}$  (001), at  $100$  K, vibrational entropy is calculated to be  $516\times$  greater than configurational entropy; at  $2000$  K, this ratio increases to  $6542\times$  (vibrational entropy remaining greater). Excluding configurational entropy would have a minor effect on the conclusions drawn from these calculations.

The equilibrium particle shape (Wulff shape) at any particular values of  $T = T^*$  and  $\mu_O = \mu_O^*$  is determined by carrying out the Wulff construction with the set of  $\hat{\gamma}_\alpha(T^*, \mu_O^*)$  values. The Wulff construction yields not only the equilibrium shape, but also information as to the specific surface configurations (orientation,

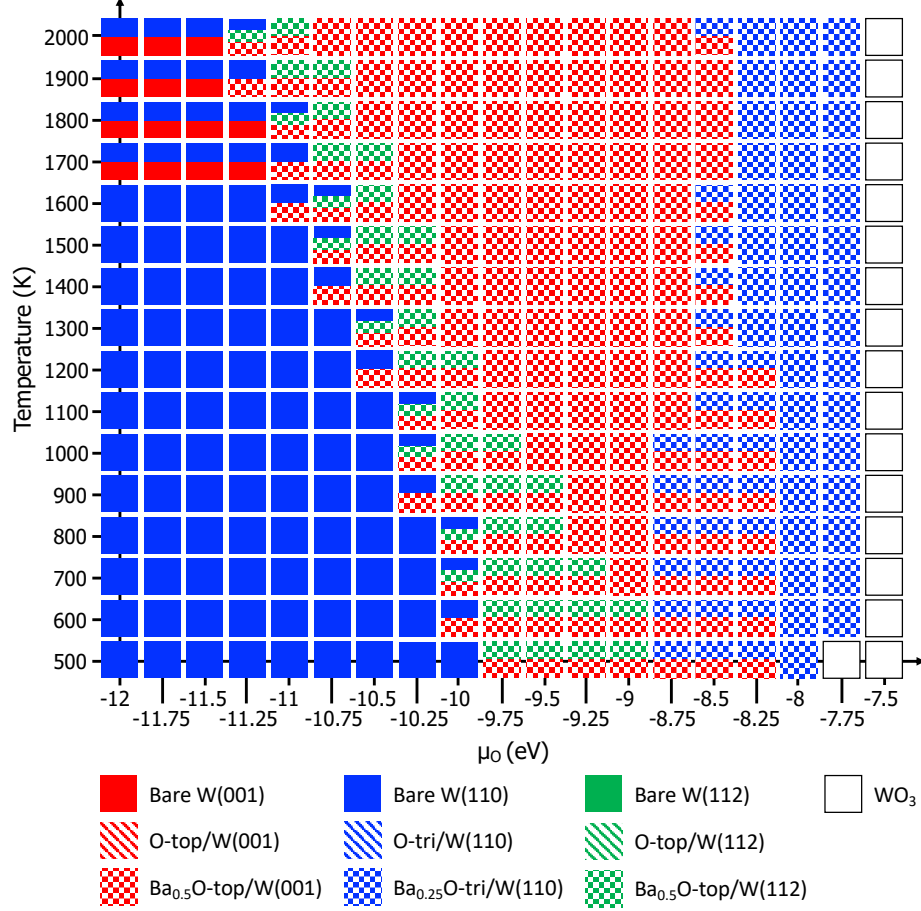


Figure 4.9: Prominent surface facets for W nanoparticles as a function of temperature,  $\mu_O$ , and adsorbed Ba/O species.  $\text{WO}_3$  exists at all temperatures given a  $\mu_O > \sim -8.25$  eV. At low  $\mu_O$  and high  $\mu_O$  (before it fully oxidizes to  $\text{WO}_3$ ) the nanoparticle is predominantly (110) terminated. At low  $\mu_O$ , the surface is bare; at high  $\mu_O$ , the surface is Ba-O-terminated. At moderate  $\mu_O$ , the nanoparticle is dominated by the (112) facet. With the addition of Ba to the O-W system, there is no  $\mu_O$  or temperature wherein a O-terminated configuration is featured on the nanoparticle. Reproduced with permission from Ref. [128].

composition, and surface atom arrangement) that are expressed by W particles at the given conditions. Therefore, the content of Fig. 4.6 can be expanded into a “particle configuration map” indicating both the shape of W particles and the details of the chemistry of the particles’ surfaces at every temperature and  $\mu_O$ .

Fig. 4.9 is a particle configuration map for W particles in a Ba/O-containing environment as a function of  $\mu_O$ . Each box represents a point in  $(T, \mu_O)$  space, with the box’s color and shading indicating the presence of particular surface configurations in the Wulff shape. Red, blue, and green again represent (001), (110), and (112) facets, respectively, and solid, hatched, and checked boxes represent W, O/W, and

Ba<sub>x</sub>O/W (hkl) surface configurations, respectively. The area of a particular color and shading within a box (representing a particular surface configuration) corresponds to the total particle area expressed by the surface configuration at equilibrium. For example, if a box is 60% solid blue and 40% solid red, particles under the correlating conditions would have surface areas comprised of 60% W (110) and 40% W (001). Empty white boxes indicate conditions wherein the W particle will oxidize to form WO<sub>3</sub>.

Examining Fig. 4.9, it can be observed that at low O<sub>2</sub> partial pressure (most negative  $\mu_O$ ), W surfaces (solid color boxes) are preferred, with (110) dominating at all temperatures. This is fully consistent with results for W particles in vacuum, as discussed above, and the fact that strongly negative  $\mu_O$  implies extremely low availability (low partial pressures) of O (or O<sub>2</sub>). As  $\mu_O$  increases—that is, as the partial pressure of O<sub>2</sub> increases—Ba<sub>x</sub>O-terminated facets begin to appear at all temperatures. Once  $\mu_O$  reaches about -10.25 eV, depending on  $T$ , W particles have (i) completely changed shape from principally (110)-terminated to primarily (112)-terminated [with some (001) appearing at elevated temperatures], and (ii) have changed from W to Ba<sub>x</sub>O-terminated. At sufficiently high  $\mu_O$ , as the bulk W/WO<sub>3</sub> phase boundary is approached, both Ba<sub>x</sub>O-terminated (001) and (112) facets disappear, replaced by Ba<sub>x</sub>O-terminated (110) facets.

#### 4.3.5 W particles in an O-containing environment

Intriguingly, O-terminated facets never have sufficiently low surface energy to appear with appreciable area on W particles in environments containing both Ba and O. The present results, though, allow construction of a similar particle configuration map to Fig. 4.9, but for environments where Ba is absent—that is, environments containing only O. This is accomplished by including only bare and O-terminated surfaces in the Wulff construction. Fig. 4.10 is a particle configuration map for W particles in O-only environments as a function of temperature and  $\mu_O$ . Colors and box shadings are the same as in Fig. 4.9.

Comparison of Figs. 4.9 and 4.10 makes immediately clear that the addition of Ba dramatically changes the shape and chemistry of W particle surfaces. In the absence of Ba, W nanoparticles are either O/W (110), or, below a minimum  $\hat{\mu}_O$ , W (110), with a small fraction of W (001) or W (112) present. The addition of Ba suppresses the appearance of W (hkl) surfaces to more O-poor environments, introducing a wide range of  $\mu_O$  values at which Ba<sub>x</sub>O-terminated surfaces dominate. In addition, the availability of Ba dramatically stabilizes (112) facets, which is of critical importance

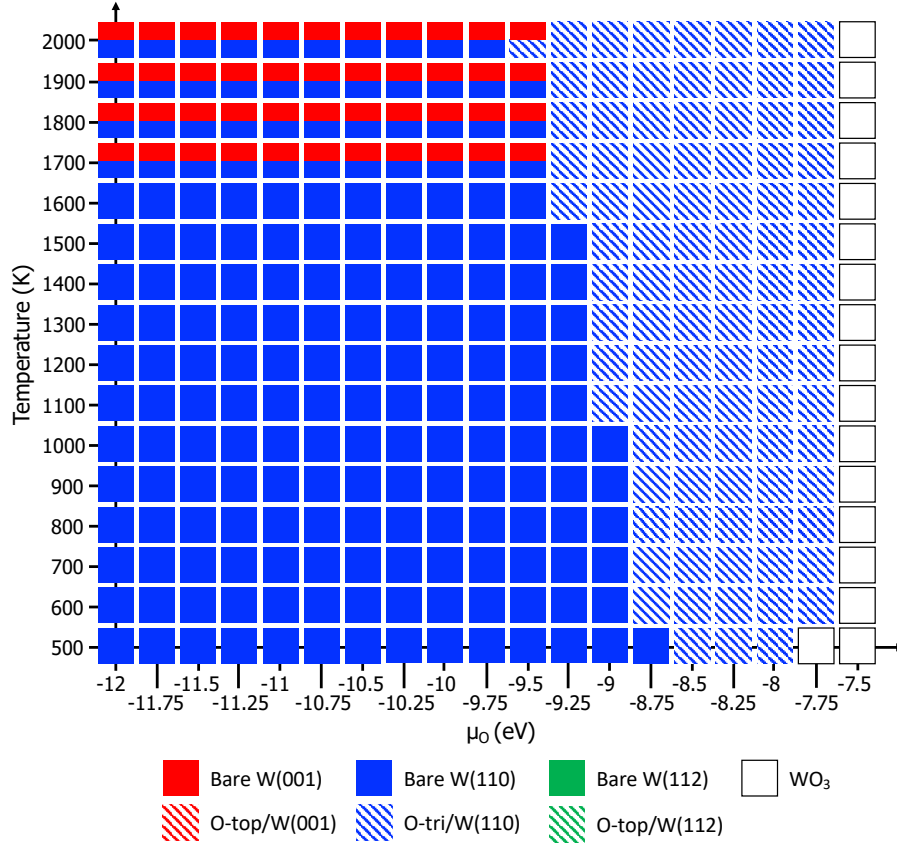


Figure 4.10: Prominent surface facets for W nanoparticles as a function of temperature,  $\mu_O$ , and adsorbed O species.  $\text{WO}_3$  exists at almost all temperatures given a  $\mu_O > -7.75$  eV. While the nanoparticles are terminated with the (110) facet at almost all temperatures and  $\mu_O$ , the facet is O-terminated given a  $\mu_O$  from -9.5 to -8.75 eV, depending on the temperature. Reproduced with permission from Ref. [128].

to thermionic cathodes. It should be noted that while significant amounts of W (112) are stable at low temperatures, as mentioned in the earlier discussion about pure W particles, these shapes likely are kinetically constrained, and likely appear as (110)-terminated particles with (112)-rounded (110)/(110) edges. In aggregate, these results show that both careful control of  $\text{O}_2$  availability and the presence of Ba can produce the essential (112) faceting on W nanocrystals in scandate cathodes.

#### 4.4 Summary

In this chapter, DFT and DFPT calculations were utilized to compute bulk reference free energies and surface excess free energies accounting for vibrational and, where appropriate, configurational entropies of solid particles and particle surfaces. The calculations have been applied to a set of bare and decorated crystal surfaces

relevant to thermionic cathodes, critical components in vacuum electronics. Using these temperature- and chemical potential-dependent surface free energies, particle configuration maps that highlight the shape and surface chemistry of particles at equilibrium over a range of temperatures and environmental conditions (represented by the chemical potential of environmentally available species) have been constructed. Such maps, constructed here for W particles in O- or Ba/O-containing environments, demonstrate the critical role that the availability of Ba plays in controlling both the shape and chemistry of W particle surfaces at application-relevant conditions. In particular, the (112) facets widely observed in thermionic cathodes are shown to only be present when Ba is available, as these facets are not appreciably expressed on W particles in O-only environments. These findings, derived from the specific particle configuration maps computed here, demonstrate the broad power of DFT+DFPT computed particle configuration maps: revealing connections between and insight into particle behavior and properties as a function of experimentally-relevant conditions.

## Chapter 5: Scandate cathode operating conditions from observed Wulff shapes

### 5.1 Motivation

In Chapter 4, a method combining DFT and DFPT to calculate surface excess free energies and predict stable nanoparticle shapes at different chemical conditions and temperatures was presented. This “forward” prediction of particle shape is useful for designing synthesis and processing conditions likely to yield desired particle shapes—assuming such conditions can be directly controlled and made uniform at the nanoscale during particle formation. However, in many situations, even though macroscopic or average conditions can be controlled and the resulting nanoparticle shapes can be observed, the details of local, nanoscale conditions in effect during particle evolution are unclear. In these cases a “reverse” deduction of local conditions (that can then be mapped back to controllable macroscopic conditions) from observed particle shapes would be a powerful approach for revealing the detailed processing-structure-performance relationships governing nanoparticle formation and behavior.

Introduced in the previous chapter, Sc-containing (“scandate”) thermionic cathodes represent an application-focused example of a situation where knowledge of processing-structure-performance relationships controlling, in this case, W nanoparticle formation and evolution is critically needed. Thermionic cathodes are used to generate electron beams and are essential components in a wide range of vacuum electron devices (VEDs) for both military and civilian applications. VEDs relying on thermionic cathodes include satellite and telecommunications communication systems, ion thrusters for small spacecraft, RADAR sensors [138], mm-wave devices for remote sensing and imaging [139], and more [140, 141]. As a potential solution to the ever-increasing demand for longer-lasting, higher current density, and lower power overhead emitters and electron devices, scandate cathodes have received a great deal of attention. Since 1967, researchers have repeatedly demonstrated that scandate cathodes offer up to an order of magnitude increase in emitted current density at fixed or reduced operating temperatures compared to existing state-of-the-art cathodes [142, 143, 144, 145, 146, 147, 148, 149]. Nevertheless, incomplete knowledge of the processing-structure-performance relationships governing scandate cathode fabrication and operation continue to limit their use in most applications. Unpredictable

longevity, low manufacturing yields, and high variability in device performance among cathodes fabricated with the same processes (and even within the same production batch) combine to prevent adoption of scandate cathodes [142, 150, 151, 152, 153].

Similar to previous generations of dispenser cathodes, scandate cathodes consist of loosely sintered W nanoparticles (500-1000 nm in diameter) with Ba-, Ca-, and Al-containing mixed oxide powders impregnating the pores between W crystallites. In scandate cathodes, Sc metal or Sc oxide ( $\text{Sc}_2\text{O}_3$ ) is also incorporated, with different fabrication approaches adding Sc-containing material at different stages of processing and in different forms [77, 78]. The final step in fabricating dispenser cathodes, including scandate cathodes, is an “activation” heat treatment, where the cathode undergoes a high temperature anneal at  $\sim 1180^\circ\text{C}$  ( $\sim 1450$  K) for times on the order of 24 hours, though specific procedures vary by manufacturer [154].

During activation, the microstructure of the constituent W crystallites in scandate cathodes evolve and, by the end of the process, exhibit improved performance relative to cathodes not containing Sc. Critically, this manufacturing process yields cathodes with highly characteristic (i.e. unique and ubiquitous) W particle shapes [79]. This shape [equiaxed crystallites bounded by (001), (110), and (112) facets] is both stable during cathode operation [during which the cathode is held for thousands of hours at temperatures at or above  $850^\circ\text{C}$  (1125 K)] and a hallmark of high-performing cathodes. Therefore, knowledge of the processing conditions leading to this characteristic shape are highly desirable and potentially transformative with respect to repeatable and reliable manufacturing. Unfortunately, Sc cathodes are activated and operated in sealed environments in which the specific chemical conditions are unknown and not directly controllable. In an effort both to uncover the mechanism by which Sc enhances cathode emission and to identify optimal processing conditions for scandate cathode fabrication, significant recent research has focused on understanding the origin of the characteristic shape and the roles that surface composition and annealing temperature play in its stabilization [79, 83]. In this chapter, in an effort to reveal the role of Sc in the processing, structure, and properties of W nanoparticles in scandate cathodes, previous calculations of the  $\text{Ba}_x\text{O}/\text{W}$  (hkl) system were extended to account for the presence of Sc. Computed surface excess free energies (accounting for vibrational entropy) were used to deduce local chemical conditions required to yield the observed characteristic shape. The results discussed here demonstrate the feasibility of reverse engineering the local conditions controlling particle formation and evolution from experimentally observed nanoparticle shapes and provide new insights into the chemical conditions required to fabricate high-performing scandate

cathodes.

## 5.2 Methods

### 5.2.1 Overview

Liu et al. [79] used scanning electron microscopy (SEM) to observe the presence of a characteristic, highly-faceted W nanoparticle shape throughout the microstructure of high-performing scandate cathodes that had been previously activated at temperatures over 1400 K and operated for thousands of hours at temperatures in excess of 1150 K in sealed glass envelopes. The authors concluded that the observed shape was the equilibrium particle shape (or Wulff shape) for W crystallites in the chemical environment present in the sealed envelopes based on the fact that the crystallites had been held at high temperature for extended periods of time and that the shape was characteristic of all W particles observed across the cathodes. In addition, the observed particle shape is markedly different than that expected for W nanoparticles fabricated in environments containing only W and O, where W crystallites are (110)-dominated, as discussed in the previous chapter. Analysis of the angles between facets and the facet shapes determined that only the (001), (110), and (112) facets were present and appeared with relative exposed areas of  $\sim 20\%$ ,  $\sim 10\%$ , and  $\sim 70\%$ , respectively [155]. In seeking to use this observed characteristic W particle shape to deduce the chemical environment present during particle equilibration—that is, during cathode activation—knowledge of the relative exposed surface areas of each facet must be leveraged to determine the relative surface energies of the stable facets.

To this end, one may begin with Gibbs’ 1875 (and P. Curie’s 1885) assertion that a crystal’s equilibrium shape is one which minimizes the excess Gibbs free energy due to the presence of surfaces [156, 157]. Each possible crystal shape  $s$  has a total surface excess Gibbs free energy, which is the sum:

$$\Delta G_s = \sum_j \gamma_j O_j \quad (5.1)$$

for  $j$  surface facets each having  $\gamma_j$  surface Gibbs free energy per unit area and expressed with  $O_j$  area. The equilibrium shape of the crystal will then be that which has a minimum  $\Delta G_s$ , where, for a given crystal volume  $V_c$  is

$$\delta \left( \sum_j \gamma_j O_j \right)_{V_c} = \sum_j \gamma_j \delta(O_j)_{V_c} = 0 \quad (5.2)$$



varying over shapes  $i$  expressing facets  $j$ .

For crystalline solids, surface facets occur as selected atomic planes drawn from the countable set of all planes with integer Miller indexes,  $\{hkl\}$ . The shape of a finite crystalline region will therefore be a closed, convex polyhedron whose faces all correspond to specific  $\{hkl\}$  planes<sup>1</sup>. In this case minimizing  $\Delta G_i$  is a balance between surface excess energy per unit area of facets  $j$  enclosing the crystal and the areas those facets must express in order to close the 3D shape. Specifically Eq. 5.2 implies that facets with larger  $\gamma_j$  will be expressed with lower areas,  $O_j$ .

In 1901, Wulff expressed this energy minimizing balance in explicitly geometric terms. He noted the distance from the center of a symmetric polyhedron to the center of each face ( $d_j$ ) is inversely proportional to the area of the face  $O_j$ . Therefore, he asserted that because the extent to which, at equilibrium, a facet  $j$  is expressed in the equilibrium shape—that is, its area  $O_j$ —must be inversely proportional to  $\gamma_j$  (following Eq. 5.2),  $d_j \propto \gamma_j$ . More formally, for some constant  $\lambda$ , then:

$$d_j = \lambda \gamma_j \quad (5.3)$$

First proved by Laue in 1943, this relationship, known as the Gibbs-Wulff theorem, allows the Wulff shape to be constructed from knowledge of the relative surface energies of all facets likely to appear (that is, facets with relatively low  $\gamma_j$ ). Fig. 5.1 shows the Wulff construction, where radii of length  $d_j$  proportional to  $\gamma_j$  are perpendicular bisectors to facets  $j$ . The equilibrium shape is defined as the volume within the Wulff planes that can be reached from the origin without crossing any other Wulff planes [158]. Fig. 5.1 also highlights that shape (meaning, essentially, relative  $O_j$  values) is determined only by the *relative* surface energies.

In this section, the Wulff construction is inverted, starting with known relative surface areas and deducing relative  $d_j$  values (that is, relative surface energy values) that would yield the observed shape. For the characteristic particle shape observed in scandate cathodes, the analysis may be limited to only (001), (110), and (112) facets, as these are all that are observed, but, in general, any number of observed facets could be included in the procedure. The absolute surface energy values are computed for multiple atomic configurations of each facet as a function of  $T$  and  $\mu_O$  (that is, the O chemical potential, which is a measure of the chemical availability of oxygen, and equivalent to O partial pressure given a known temperature). Then,

---

<sup>1</sup>Moving forward, the family of equivalent planes  $\{hkl\}$  is referred to with a single representative plane (hkl). For example, when considered at the atomic scale, Ba<sub>0.50</sub>O/W (001) is equivalent to Ba<sub>0.50</sub>O/W (00 $\bar{1}$ ); therefore, one may refer simply to (001) without loss of generality.

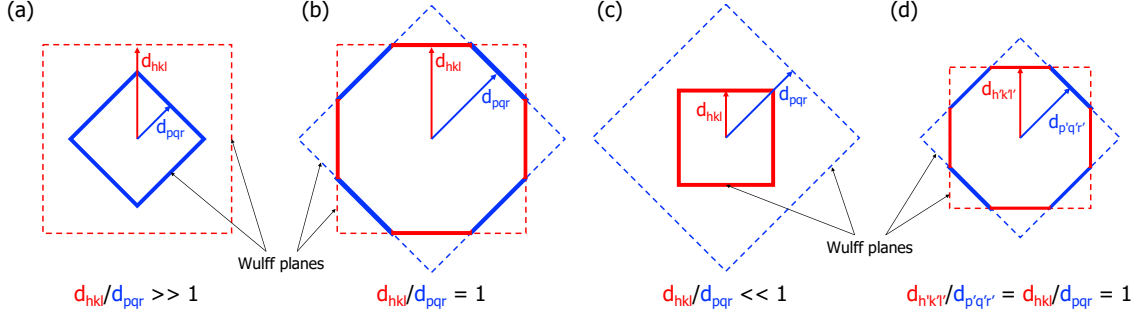


Figure 5.1: Examples of Wulff constructions where (a)  $d_{hkl}/d_{pqr} \gg 1$ , (b)  $d_{hkl}/d_{pqr} = 1$ , (c)  $d_{hkl}/d_{pqr} \ll 1$ , (d)  $d_{h'k'l'}/d_{p'q'r'} = d_{hkl}/d_{pqr} = 1$ . The labels  $hkl$  and  $pqr$  refer to two unique families of planes. Reproduced with permission from Ref. [159].

regions of  $(T, \mu_O)$ -space (that is, processing conditions) that yield the set of relative surface energies required to produce the observed shape are identified.

### 5.2.2 Target surface energy ranges

For any set of known  $(hkl)$  facets enclosing a symmetric convex polygon, the total area of each facet can be computed in terms of the distances of each facet from the center of the polygon. Taking Fig. 5.1b as an example (albeit, rendered in 2D), given some facets  $(hkl)$  and  $(pqr)$ , the angle between the facets is:

$$\cos \theta = \frac{hp + kq + lr}{\sqrt{(h^2 + k^2 + l^2)(p^2 + q^2 + r^2)}} \quad (5.4)$$

This angle is in the plane defined by the vectors  $d_{hkl}$  and  $d_{pqr}$  (which originate at the center of the polygon and terminate at the center of each respective facet), and, combined with the lengths of  $d_{hkl}$  and  $d_{pqr}$ , can be used to compute the distances from the center of each facet to the center of the edge defined by the intersection of  $(hkl)$  and  $(pqr)$ . The orientation (that is, Miller indices of the vector in space) of this edge can be computed as the cross product of the Miller indices of the intersecting planes. Given the orientation of all edges present on the polyhedron and the set of distances from facet centers to facet edges, the areas of each polygon facet can be computed.

This process—arriving at facet geometries (and, specifically, areas) from relative  $d_{hkl}$  values—is a direct implementation of the Wulff construction, and, analytically, the results are functions  $A_{hkl}(d_{hkl})$  that define the Wulff shape. These functions can be inverted (for known, finite sets of expressed facets) to solve for sets of  $d_{hkl}$  values given measured  $A_{hkl}$  values, but this process is mathematically cumbersome.

In specific cases, it is generally more practical and efficient to utilize one of a number of free Wulff shape generator computer or web applications [160, 121] to qualitatively search for a set of  $d_{hkl}$  values that give sets of areas  $A_{hkl}$  that match experiment. This qualitative search process was used here to generate relative  $d_{hkl}$  values that yield the experimentally measured (001), (110), and (112) areas. These  $d_{hkl}$  values have been validated with a direct implementation of the Wulff construction (as discussed above) and confirmation that the identified  $d_{hkl}$  values yield  $A_{hkl}$  values quantitatively consistent with observed particle shapes.

For the present case, from the experimentally observed characteristic W equilibrium shape (Fig. 5.2), Liu et al. [79] determined the fraction of the total area expressed in the form of (001), (110), and (112) facets:  $\sim 20\%$ ,  $\sim 10\%$ ,  $\sim 70\%$ , respectively. Wulff shapes with these relative areas result for  $\{d\}$  values of  $d_{(110)} = 1.00$ ,  $d_{(112)} = 0.945$ , and  $d_{(001)} = 0.927$ , implying relative surface energies (for  $\hat{\gamma}_{(110)}$  chosen as a reference) of  $r_{(001)} = \hat{\gamma}_{(001)}/\hat{\gamma}_{(110)} = 0.927$  and  $r_{(112)} = \hat{\gamma}_{(112)}/\hat{\gamma}_{(110)} = 0.945$ .

It has been previously reported that when GGA-PBE pseudopotentials are used DFT underestimates measured surface energies by up to  $\sim 11\%$  [161]. To account for this potential error,  $(T, \mu_O)$ -space is searched for relative surface energies in ranges  $r_{(001)} \pm \delta_{(001)}$  and  $r_{(112)} \pm \delta_{(112)}$ , where:

$$\begin{aligned}\delta_{(001)} &= 0.5 \left( \frac{1.11\hat{\gamma}_{(001)}}{\hat{\gamma}_{(110)}} - \frac{\hat{\gamma}_{(001)}}{1.11\hat{\gamma}_{(110)}} \right) \\ \delta_{(112)} &= 0.5 \left( \frac{1.11\hat{\gamma}_{(112)}}{\hat{\gamma}_{(110)}} - \frac{\hat{\gamma}_{(112)}}{1.11\hat{\gamma}_{(110)}} \right)\end{aligned}$$

To yield the observed Wulff shape at a particular  $T$  and oxygen availability ( $\mu_O$ ), the set of minimum surface energies (among considered surface configurations) for each facet (that is,  $\hat{\gamma}_{(001)}$ ,  $\hat{\gamma}_{(110)}$ , and  $\hat{\gamma}_{(112)}$ ) must be such that *both* relative surface energies [ $r_{(001)}$  and  $r_{(112)}$ ] fall within target ranges. Collectively the set of target ranges  $[r^*]$  is defined as:

$$[r^*] = \left[ \left[ r_{(001)} - \delta_{(001)}, r_{(001)} + \delta_{(001)} \right] \cup \left[ r_{(112)} - \delta_{(112)}, r_{(112)} + \delta_{(112)} \right] \right] \quad (5.5)$$

### 5.2.3 Computing surface energies

Here, the approach described in the previous chapter is applied to compute temperature- and chemical environment-dependent surface energies—accounting for the vibrational contribution to surface entropy—for a number of  $\text{Ba}_x\text{Sc}_y\text{O}$ -type/W (hkl) surface con-

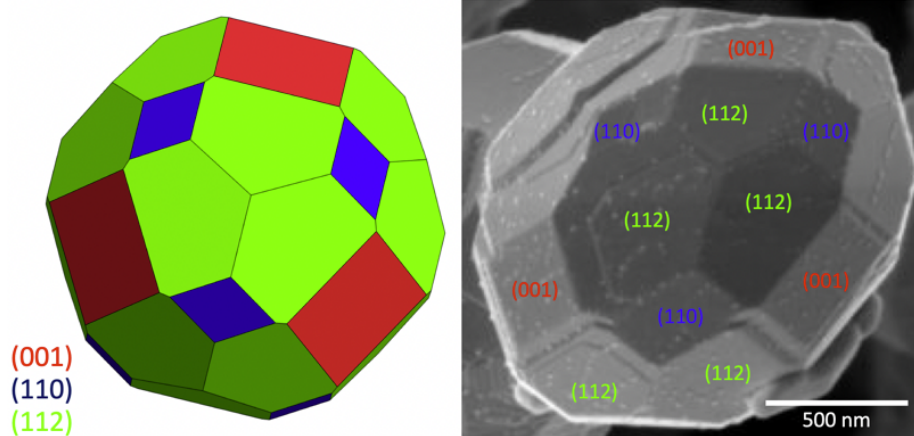


Figure 5.2: (left) Wulff construction of the equilibrium W grain shape present throughout thermionic cathodes (right) SEM images of a high-performance cathode, always exhibiting a characteristic W grain shape. Reproduced with permission from Ref. [159].

figurations<sup>2</sup> potentially relevant to scandate cathodes. While previous efforts predicted W particle shapes when Ba and O are present as a function of  $T$  and  $\mu_O$ , here specific focus is given to Sc-containing cathodes, and, therefore, Sc-containing systems. Although the specific distribution of Sc on W particles in scandate cathodes is not clear, it is widely expected that Sc, like Ba, is present atop O-covered W surfaces. Consequently, a range of such surface configurations have been explored and, for each, the minimum energy atomic positions, surface energy, vibrational densities of states (and surface vibrational energies), and work function have been computed.

Surface energies ( $\hat{\gamma}_\alpha$ ) for Sc-containing surface configurations ( $\alpha$ ) were computed using the thermodynamic approach described in Ref. [128] and provided in Chapter 4 as Eq. 4.2. Because the results described in Chapter 4 showed configurational entropy to be a far less significant contributor to total entropy than vibrational entropy, particularly at elevated temperatures, the present analysis excludes configurational entropy. Of all surface configurations considered, only those that exhibit the minimum surface energy for a given facet  $j$  (at a given  $T$  and  $\mu_O$ ) will be expressed at equilibrium. From the set of minimum surface energies for each facet, relative surface energies were calculated, yielding a map of relative surface energies as a function of  $T$  and  $\mu_O$ . This map is then searched for  $T$  and  $\mu_O$  combinations yielding relative

<sup>2</sup>Here, surface configuration designations follow those in Refs. [83] and [128], where subscripts indicate coverage in MLs of adsorbing species, and “type” indicates the configuration of adsorbed O atoms with respect to W atoms in the substrate facet. For example,  $\text{Ba}_{0.25}\text{Sc}_{0.25}\text{O-top/W (001)}$  indicates an 0.25 monolayer (ML) coverage of both Ba and Sc, and 1.0 ML coverage of O, with “top” indicating that O atoms are located directly atop outermost W atoms on a (001) slab.

surface energies that fall within  $[r^*]$ .

#### 5.2.4 Oxygen thermochemical data

Measurable thermochemical conditions (specifically  $T$  and  $p_{O_2}$ ) can be directly connected to computed energies by referencing chemical potentials to tabulated thermochemical data [112]. In a chemical environment containing  $O_2$  gas, the computed binding energy of  $O_2$  ( $E_{DFT}^{O_2}$ ) is related to  $\mu_O(T, p_{O_2})$  as [162, 163]:

$$\mu_O(T, p) = 0.5\mu_O(T, p^0) + 0.5E_{DFT}^{O_2} + 0.5k_B T \ln(p_{O_2}/p^0) \quad (5.6)$$

Here  $\mu_O(T, p^0)$  (eV) is the tabulated chemical potential of O at standard state pressure ( $p^0 = 750.06$  Torr),  $E_{DFT}^{O_2}$  (eV) is the ground state energy of an  $O_2$  molecule, and  $p_{O_2}$  (Torr) is the  $O_2$  pressure.

#### 5.2.5 Work function

The electron work function of a particular surface configuration ( $\Phi_\alpha$ ) is defined as the difference between the calculated energies of the Fermi and vacuum levels:

$$\Phi_\alpha = E_{vac} - E_{Fermi} \quad (5.7)$$

As described in Ref. [83], this is a robust definition for the work function, since computed total energies of surface slabs are converged with respect to vacuum thickness, implying that there is no electron–electron interaction between periodic slabs through the vacuum region. Therefore, the vacuum energy level was determined as the plane-averaged electrostatic potential energy in the vacuum region far from the slab surfaces, and the Fermi energy is the eigenvalue of the highest-occupied eigenstate.

With knowledge of each surface configuration’s work function, an area-weighted effective work function for a given particle shape can be approximated. Here, an estimate of the effective work function of a surface composed of (001), (110), and (112) facets is made by first computing an area-weighted total thermionic current:  $J_{total} = A_{(001)}J_{(001)} + A_{(110)}J_{(110)} + A_{(112)}J_{(112)}$ . Taking emission from both the overall (multi-faceted) surface and individual facets to have the form of the Richardson-Dushman current ( $J = A_R T^2 \exp(-\Phi/\beta)$  [164, 165, 166]) an effective work function is computed as:

$$\Phi_{eff} = -\beta \ln(A_{001} \exp(-\Phi_{001}/\beta) + A_{110} \exp(-\Phi_{110}/\beta) + A_{112} \exp(-\Phi_{112}/\beta)) \quad (5.8)$$

Here  $\beta = k_B T$  and the Richardson constant ( $A_R$ ) is assumed to be the same for each facet. This approximation does not include potential effects of surface roughness on effective work function, but provides a practical point of comparison for comparing expected emitted thermionic currents.

### 5.2.6 Calculation details

The computational details utilized here encompass all those previously described in §4.2.2. Unique to this series of calculations, all slabs had symmetric terminations except for the  $(\text{BaSc})_{1/3}\text{O-top/W}$  (112) surface configuration, which was not computationally tractable as a symmetric system for all required calculations. The phonon density of states had to be computed as an asymmetric slab with Sc, Ba, and O adatoms at only one termination. Comparing the ground state surface energies of the asymmetric and symmetric  $(\text{BaSc})_{1/3}\text{O/W}$  (112) slabs, it was found that the asymmetric slab overestimates the surface energy of the decorated termination by an acceptably low 1.98 meV. In addition to the software package **Wulffmaker** described previously as a means of visualizing Wulff constructions, the package **Wulffpack** [160] was used in this chapter to calculate the respective area fraction of each surface configuration comprising a particle.

## 5.3 $\text{Ba}_x\text{Sc}_y\text{O/W}$ surface configurations

### 5.3.1 M/ $\text{MO}_x$ stability

In computing  $\hat{\gamma}_\alpha$  values following Eq. 4.2 as a function of oxygen availability, M/ $\text{MO}_x$  phase transformations must be considered to ensure the appropriate reference state is utilized for all atoms in a system. As shown earlier in Eq. 4.4 in Chapter 4, for a general oxidation reaction at equilibrium, when a bulk metal  $M$  is in chemical equilibrium with its oxide  $\text{MO}_X$ , one may write:

$$\begin{aligned}\hat{\mu}_M + X\mu_O &= \hat{\mu}_{\text{MO}_X} \\ \text{or } \mu_O &= \frac{\hat{\mu}_{\text{MO}_X} - \hat{\mu}_M}{X}\end{aligned}$$

In a physical system where either the metal or the oxide are observed to be thermodynamically stable, these reaction equations become inequalities, with  $\hat{\mu}_M + X\mu_O$  lower when the metal is stable, and  $\hat{\mu}_{\text{MO}_X}$  lower when the oxide is favored.

Compositional analysis of post-activation and post-operation high-performing scan-date cathodes has revealed the presence of metallic W, oxidized Ba (BaO), and ox-

idized Sc ( $\text{Sc}_2\text{O}_3$ ) [79]. Based on the conclusion that these phases are stable, for systems relevant to scandate cathodes the following inequalities are true:

$$\begin{aligned}\hat{\mu}_W &< \hat{\mu}_{\text{WO}_3} - 3\mu_O \\ \hat{\mu}_{\text{BaO}} &< \mu_O + \hat{\mu}_{\text{Ba}} \\ \text{and } \hat{\mu}_{\text{Sc}_2\text{O}_3} &< 2\hat{\mu}_{\text{Sc}} + 3\mu_O\end{aligned}$$

Rearranging, this gives limits on the value of  $\mu_O$  implied by experimental observation of stable phases present in scandate cathode systems that can be written as:

$$\begin{aligned}\mu_O &< \frac{\hat{\mu}_{\text{WO}_3} - \hat{\mu}_W}{3} \\ \mu_O &> \hat{\mu}_{\text{BaO}} - \hat{\mu}_{\text{Ba}} \\ \text{and } \mu_O &> \frac{\hat{\mu}_{\text{Sc}_2\text{O}_3} - 2\hat{\mu}_{\text{Sc}}}{3}\end{aligned}$$

These limits—essentially M/MO<sub>X</sub> phase boundaries or transitions—constrain the range of oxygen availabilities present during high temperature cathode processing based on observed species.

Values for  $\hat{\mu}_{\text{WO}_3}$ ,  $\hat{\mu}_W$ ,  $\hat{\mu}_{\text{BaO}}$ ,  $\hat{\mu}_{\text{Ba}}$ ,  $\hat{\mu}_{\text{Sc}_2\text{O}_3}$ ,  $\hat{\mu}_{\text{Sc}}$  have been computed as described above. At all temperatures, the Sc/Sc<sub>2</sub>O<sub>3</sub> equilibrium occurs at the lowest  $\mu_O$ , followed by Ba/BaO, and then W/WO<sub>3</sub>. The specific  $\mu_O$  values for these transitions varies with temperature, and values at 0 K and 2000 K are compared in Table 5.1. In the previous chapter, Fig. 4.5 provided a visual representation of the Ba/BaO and W/WO<sub>3</sub> boundaries.

Table 5.1: Summary M/MO<sub>X</sub> stability transitions (eV) at 0 and 2000 K.

| M/MO <sub>X</sub>                 | 0 K     | 2000 K  | $\Delta$ |
|-----------------------------------|---------|---------|----------|
| W/WO <sub>3</sub>                 | −7.705  | −8.411  | −0.706   |
| Ba/BaO                            | −9.652  | −10.344 | −0.692   |
| Sc/Sc <sub>2</sub> O <sub>3</sub> | −11.056 | −11.576 | −0.520   |

### 5.3.2 Surface energies

Extending previous calculations [83, 167] to account for the inclusion of Sc, the properties of fourteen surface configurations—including W, O/W, Ba<sub>x</sub>O/W, and Ba<sub>x</sub>Sc<sub>y</sub>O/W (001), (110), and (112) configurations as listed in Table 5.2—were computed. These surfaces were studied because they represent a collection of configura-

tions with low surface energies and low work functions. In addition, the position of Sc in these configurations is a surface cation (nominally coplanar with Ba atop the O plane), as is commonly hypothesized to be the case within the scandate cathode community.

Surface energies were computed as a function of  $\mu_O$  for temperatures ranging from 0-2000 K. An example isotherm showing  $\hat{\gamma}(\mu_O)$  at 1450 K is shown in Figs. 5.3a and b. In these figures, phase boundaries demarking M/MO<sub>x</sub> stability are plotted as vertical bars (black for Sc/Sc<sub>2</sub>O<sub>3</sub>, magenta for Ba/BaO, and cyan for W/WO<sub>3</sub>). The region overlaid with a grid of gray dots at higher values of  $\mu_O$  indicates the range of chemical conditions where (bulk) WO<sub>3</sub> is stable (relative to bulk W). Since previous studies (e.g. Liu et al. [79]) do not observe WO<sub>3</sub> crystallites, or WO<sub>3</sub> in or at the surface of W particles, this region of chemical conditions is not consistent with those expected to be present during cathode activation. The temperature 1450 K is highlighted because it is a representative temperature at which scandate cathodes are activated (held at high temperature for times on the order of days), and therefore temperatures at which particle shapes in a scandate cathode are expected to equilibrate.

Fig. 5.3b highlights that at any particular temperature only a subset of considered surface configurations for each facet are minimum energy configurations. These are the only surface configurations expected to be present on equilibrated particles. Considering the full temperature range studied, bare W surfaces are stable at low  $\mu_O$  values, becoming the lowest energy surfaces for all facets as oxygen availability decreases through a point between the Ba/BaO and Sc/Sc<sub>2</sub>O<sub>3</sub> phase boundaries. At high  $\mu_O$  values, generally as oxygen availability increases through the Ba/BaO phase boundary, Ba<sub>x</sub>O/W surfaces are stable for all facets. O/W facets (with no adsorbed cation species) are never the most stable surface configurations regardless of oxygen availability. Sc-containing surface configurations are only stable in very narrow windows of oxygen availability around  $\mu_O = -10.5$  to  $-11.0$  eV and only for (001) and (112) configurations.

At 1450 K, eight configurations are stable for different facets and  $\mu_O$  values: W (001), Ba<sub>0.25</sub>Sc<sub>0.25</sub>O-top/W (001), and Ba<sub>0.50</sub>O-top/W (001); W (110) and Ba<sub>0.25</sub>O-tri/W (110); and W (112), (BaSc)<sub>1/3</sub>O-top/W (112), and Ba<sub>0.50</sub>O-top/W (112). The limited range of chemical conditions over which Sc-containing (001) and (112) facets are stable is highlighted at this temperature. Ba<sub>0.25</sub>Sc<sub>0.25</sub>O-top/W (112) is only stable between  $\mu_O = -12$  and  $-10.9$  eV, with W (112) and Ba<sub>0.50</sub>O-top/W (112) stable at lower and higher oxygen availabilities, respectively. Similarly Ba<sub>0.25</sub>Sc<sub>0.25</sub>O-top/W (001) is only stable between  $\mu_O = -12$  and  $-10.4$  eV, with W (001) and Ba<sub>0.50</sub>O-



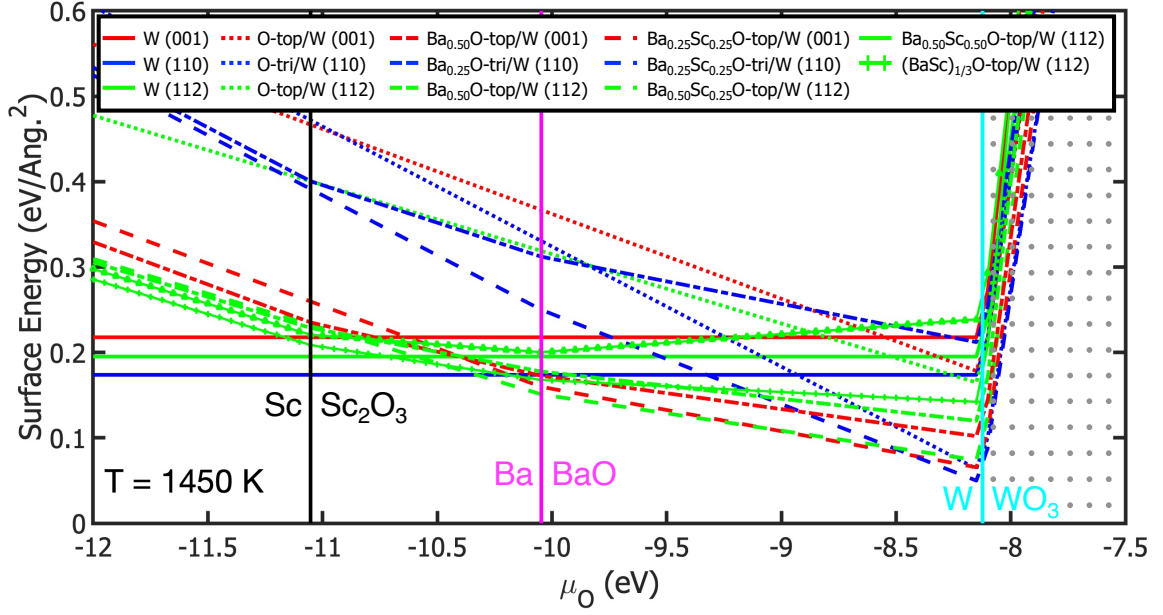
Table 5.2: Surface configurations evaluated in this work.

| Adatom Description                        | Surface Configuration                                  |
|---|--|
| W   | W (001)  |
|   | W (110)  |
|   | W (112)  |
| O/W                                       | O-top/W (001)  |
|   | O-tri/W (110)  |
|   | O-top/W (112)  |
| $\text{Ba}_x\text{O}/\text{W}$            | $\text{Ba}_{0.50}\text{O-top/W (001)}$                 |
|   | $\text{Ba}_{0.25}\text{O-tri/W (110)}$                 |
|   | $\text{Ba}_{0.50}\text{O-top/W (112)}$                 |
| $\text{Ba}_x\text{Sc}_y\text{O}/\text{W}$ | $\text{Ba}_{0.25}\text{Sc}_{0.25}\text{O-top/W (001)}$ |
|   | $\text{Ba}_{0.25}\text{Sc}_{0.25}\text{O-top/W (110)}$ |
|   | $\text{Ba}_{0.25}\text{Sc}_{0.25}\text{O-top/W (112)}$ |
|   | $\text{Ba}_{0.50}\text{Sc}_{0.50}\text{O-top/W (112)}$ |
|   | $(\text{BaSc})_{1/3}\text{O-top/W (112)}$              |

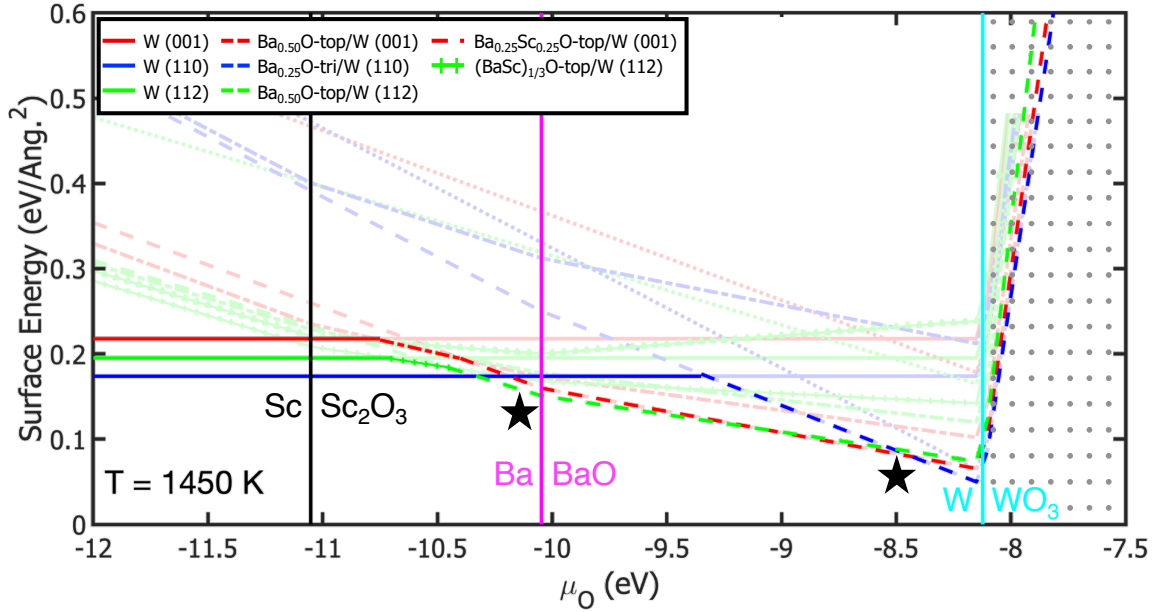
top/W (001) stable at lower and higher oxygen availabilities, respectively. The specific ranges of  $\mu_O$  at which Sc-containing surfaces are stable vary with temperature, shifting to higher oxygen availabilities and narrowing at higher temperatures, and shifting lower and widening at lower temperatures. Considering both that (i) low temperatures hinder kinetic activity and (ii) stability windows for Sc-containing surfaces narrow with increasing temperature, it is likely that stabilizing Sc-containing (001) or (112) surfaces requires careful control of both temperature and oxygen availability.

### 5.3.3 Chemical conditions required to yield observed shapes

Given  $\hat{\gamma}(T, \mu_O)$  values,  $(T, \mu_O)$ -space has been searched for regions where the relative magnitudes of minimum surface energies for the (001), (110) and (112) facets will give rise to the experimentally observed Wulff shape: that is, conditions where relative surface energies fall within  $[r^*]$ , as defined above. Considering first the 1450 K isotherm shown in Fig. 5.3, computed relative surface energies will yield the experimentally observed equilibrium particle shape for  $\mu_O$  between  $-10.24$  and  $-10.02$  eV (a range of  $\Delta_{\mu_O} = 0.22$  eV) *and* between  $-8.76$  and  $-8.45$  eV ( $\Delta_{\mu_O} = 0.31$  eV). These two regions are indicated with stars in Fig. 5.3b and represent conditions under which two different combinations of surface configurations are stable and yield



(a)



(b)

Figure 5.3: (a) An isotherm at 1450 K showing the surface energies of all fourteen surface configurations evaluated. (b) The same data as in (a), but with sections of surface energy curves shown in bold only if/when the surface configuration has the minimum surface for its orientation. Other sections of surface energy curves (where the particular configuration does not have the lowest surface energy for its facet) are lightened to highlight that only a subset of all considered configurations are ever the lowest energy configuration for their facet. The black stars indicate  $\mu_O$  values where relative surface energies that will yield the characteristic Wulff shape occur, and they correspond to similar stars shown in subsequent figures. Reproduced with permission from Ref. [159].

the observed particle shape: (i) at lower  $\mu_O$ : Ba<sub>0.50</sub>O-top/W (001), W (110), and Ba<sub>0.50</sub>O-top/W (112), and (ii) at higher  $\mu_O$ : Ba<sub>0.50</sub>O-top/W (001), Ba<sub>0.25</sub>O-tri/W (110), and Ba<sub>0.50</sub>O-top/W (112). Given that  $kT$  at 1450 K is  $\sim 0.125$  eV, both of these regions are extremely narrow with respect to the range of oxygen availabilities (that is,  $\mu_O$  values) they encompass.

Extending this analysis to temperatures between 0 and 2000 K, chemical conditions where the observed Wulff shape would be expected to form are indicated as gray bands in Fig. 5.4. This diagram links experiment and calculation by mapping oxygen availability in terms of  $\mu_O$  (shown as the background color scale) to equivalent partial pressures as a function of temperature. As in Fig. 5.3, M/MO<sub>x</sub> stability boundaries are indicated with solid black, magenta, and cyan lines for Sc/Sc<sub>2</sub>O<sub>3</sub>, Ba/BaO, and W/WO<sub>3</sub>, respectively, and stars indicate chemical conditions yielding the observed particle shape at 1450 K. The bands of chemical conditions at lower versus higher  $p_{O_2}$  values correspond to the same sets of surfaces described above. In addition, the region indicated with a dotted grid is again the region of stability of (bulk) WO<sub>3</sub>, the presence of which is not consistent with experimental observations.

Fig. 5.4 highlights two important points relating to the availability of oxygen during equilibration of W particle shapes in scandate cathodes: (i) the ranges of stability of the observed shape in terms of  $p_{O_2}$  (and equivalently  $\mu_O$ ) are small (relative to  $kT$ ) at all temperatures, and (ii) forming the observed shape requires conditions characterized by extremely low oxygen partial pressures. Regarding (i), it is widely understood that it is extremely difficult to reliably and repeatably fabricate high performing scandate cathodes and that cathode processing and performance is sensitive to the presence of oxygen. The current results make clear that this is likely a consequence of the fact that optimized cathode particle shapes are stable only in narrow windows of oxygen availability. The extremely low oxygen partial pressures required to yield observed particle shapes characteristic of high-performing scandate cathodes further make clear that chemical gettering is required during fabrication. Specifically, achieving conditions yielding the observed shape in the higher  $p_{O_2}$  band requires gettering below the oxidation threshold of W—e.g. with Ba (a standard practice during fabrication of many types of dispenser cathodes). Achieving conditions required to yield the observed shape in the lower  $p_{O_2}$  band requires sufficient gettering that Ba is either reduced, or at the Ba/BaO stability boundary. In real systems this likely requires gettering with a metal with a greater affinity for oxidation than Ba—e.g. Sc.

As a point of interest, it should be noted that none of the surface configurations found to be stable and exhibiting relative surface energies required to yield the ob-

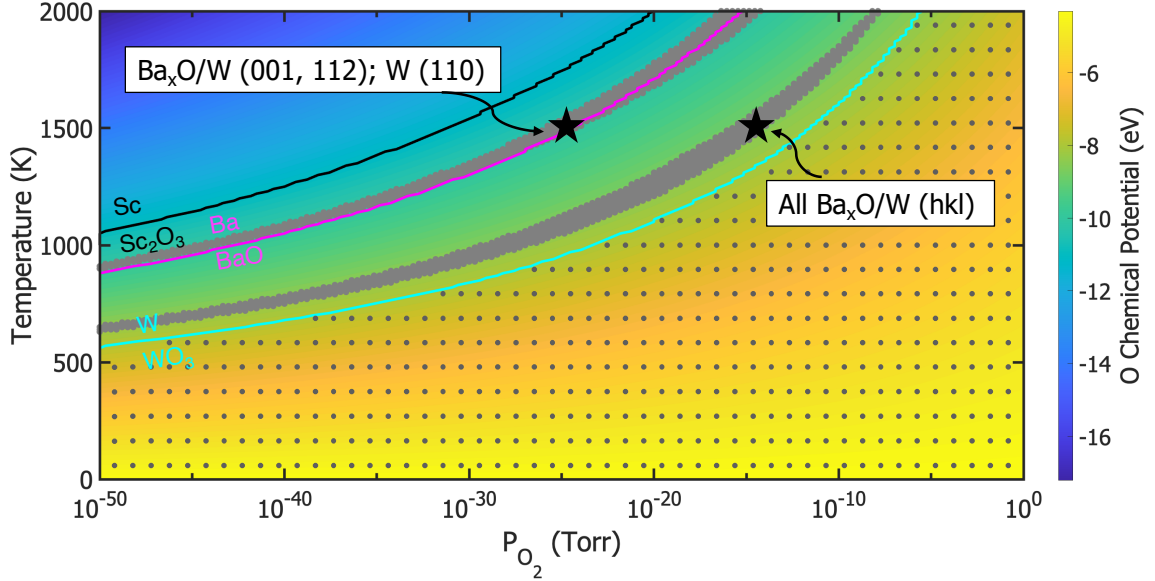


Figure 5.4: Contour plot of  $\mu_O$  as a function of oxygen partial pressure and temperature, overlaid with gray bands indicating conditions wherein the characteristic shape is expected. The stars are equivalent to those in Fig. 5.3b. Reproduced with permission from Ref. [159].

served Wulff shape contain Sc in an adsorbed cation position. This surprising result may indicate that the role of Sc in scandate cathodes is not directly related to modifying surface work functions. Rather, Sc may serve simply as an oxygen sink (or, potentially “cleaner” as has been suggested elsewhere [168]) required to constrain chemical conditions to the specific band necessary to stabilize otherwise favorable (presumably meaning low work function) facets and surface configurations.

#### 5.3.4 Effective work functions

Given sets of specific surface configurations expressed on the equilibrium (Wulff) shape as a function of  $T$  and  $\mu_O$  (or, equivalently  $p_{O_2}$ ), the effective work function of stable, multi-faceted cathode surfaces can be computed. Work functions of all fourteen surface configurations studied here were computed according to Eq. 5.7. Effective work functions of multi-faceted particles exhibiting combinations of these configurations were computed using Eq. 5.8. Fig. 5.5 plots computed effective work functions over the same range of chemical conditions mapped in Fig. 5.4. As above, M/MO<sub>x</sub> phase boundaries are shown with solid lines, the region of (bulk) WO<sub>3</sub> stability is indicated with a grid of dots, and bands of chemical conditions yielding the observed Wulff shape are indicated in gray.

Scandate cathodes have been reported to exhibit effective work functions as low

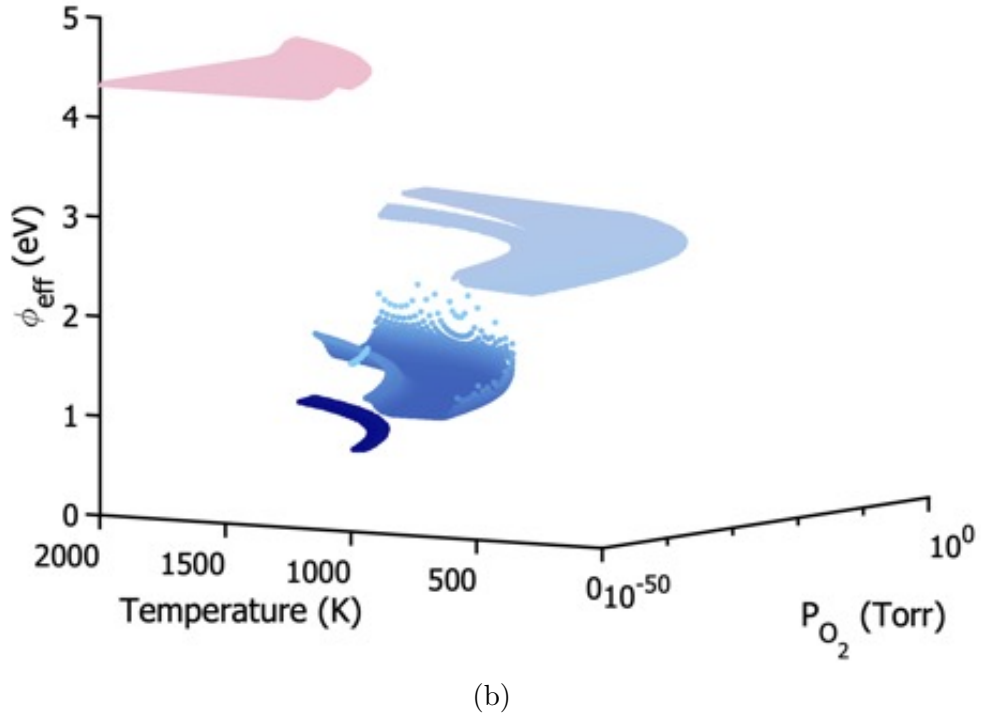
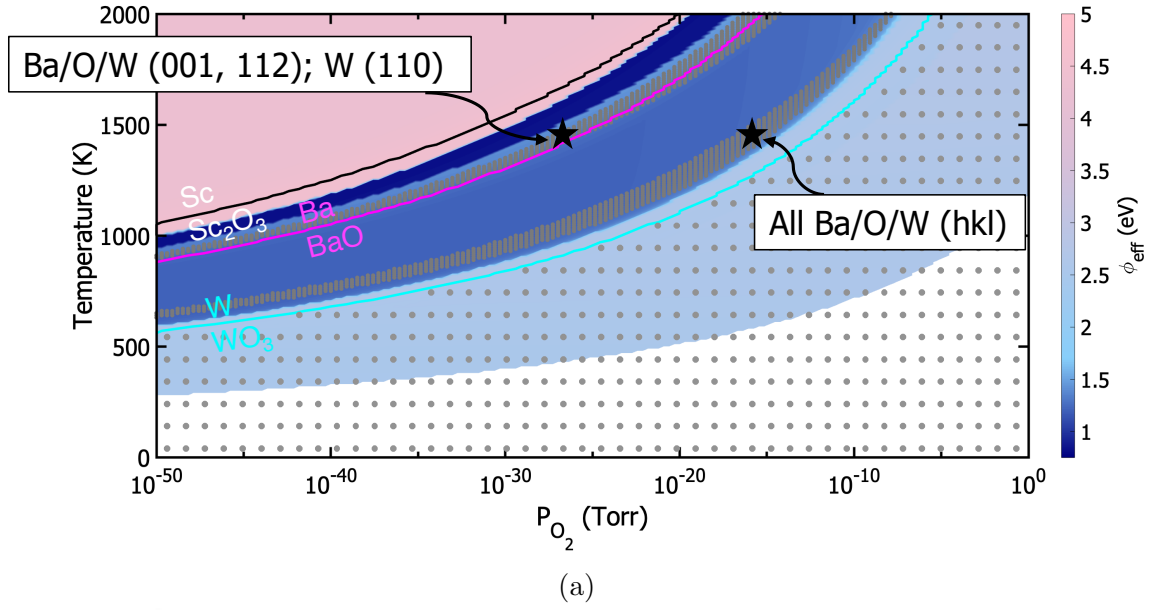


Figure 5.5: **(a)** Contour plot of  $\Phi_{\text{eff}}$  as a function of oxygen partial pressure and temperature, overlaid with gray bands indicating conditions wherein the characteristic shape is expected. **(b)**  $\Phi_{\text{eff}}$  as a function of oxygen partial pressure and temperature plotted as a scatter plot. Reproduced with permission from Ref. [159].

as  $\sim 1$  eV [78, 77]. In general agreement with these observations, stable particles from both regions of  $(T, \mu_O)$ -space that yield the observed particle shape exhibit an effective work function of  $\sim 1.3$  eV [gray bands in Fig. 5.5a]. While particles in these two regions, both of which lie within the medium blue trench in Fig. 5.5b, express two different sets of surface configurations, they both express significant relative surface areas of Ba<sub>0.50</sub>O-top/W (112), which has a work function of 1.23 eV. This surface, due to its high surface area fraction on the Wulff shape [(112) represents  $\sim 70\%$  of the surface area of observed particles] and low work function, dominates the effective work function of all regions of  $(T, \mu_O)$ -space that yield the observed particle shape.

The lowest work function computed among all surfaces studied here was 0.82 eV for the Ba<sub>0.25</sub>Sc<sub>0.25</sub>O-top/W (001) configuration. This result is in agreement with Ref. [83] and is a slightly lower work function than computed for the same surface in Ref. [169]. The emergence of a Sc-containing surface with a work function this low would certainly explain the enhanced emission of thermionic scandate cathodes (compared, for example, to B-type cathodes of similar structure and composition but lacking Sc). However, the Ba<sub>0.25</sub>Sc<sub>0.25</sub>O-top/W (001) surface is only stable [relative to other (001) surface configurations] in a narrow  $\mu_O$  window and under chemical conditions where the relative (001), (110), (112) surface energies do not yield the experimentally observed characteristic shape.

The region of  $(T, \mu_O)$ -space where Ba<sub>0.25</sub>Sc<sub>0.25</sub>O-top/W (001) is stable requires extremely low oxygen partial pressures, even at elevated temperature, and corresponds to the deepest blue (lowest work function) ribbon in Figs. 5.5a and b. These conditions are close to the Sc/Sc<sub>2</sub>O<sub>3</sub> phase boundary—suggesting that the presence of sufficient metallic Sc during cathode activation might getter enough oxygen to achieve the conditions necessary for forming particles expressing this low work function configuration. They are also reasonably close to “low  $\mu_O$ ” conditions that yield the observed characteristic shape, though, when the observed shape is stable, the (001) surfaces are relatively small and are terminated with the Ba<sub>0.50</sub>O-top/W (001) surface, which exhibits  $\Phi = 2.47$  eV.

Fig. 5.5b emphasizes the sudden shifts in effective work function that can occur as  $T$  and  $p_{O_2}$  vary. These dramatic changes are associated with transitions in the particular surface configuration stable on a particular facet. For example, the drop from effective work functions of  $\sim 4.3$  eV (the pink region) to  $\sim 0.85$  eV (deepest blue ribbon) is due entirely to a change in which configuration of the (001) surface is stable: W (001) ( $\Phi = 4.3$  eV) at higher  $T$  and lower  $p_{O_2}$  or Ba<sub>0.25</sub>Sc<sub>0.25</sub>O-top/W (001) ( $\Phi = 0.82$  eV). This stability transition at 1450 K can be seen in Figs. 5.3a and

b around  $\mu_O = -10.7$  eV when the red dash-dot curve ( $\text{Ba}_{0.25}\text{Sc}_{0.25}\text{O-top/W (001)}$ ) falls below the red solid curve ( $\text{W (001)}$ ).

Close examination of the steps in effective work function in Fig. 5.5b shows that some transitions in  $\Phi_{eff}$  are somewhat gradual—for example from the medium blue ( $\Phi_{eff} \sim 1.2$  eV) to light blue ( $\Phi_{eff} \sim 2.5$  eV) regions as  $\mu_O$  increases. These relatively narrow regions of gradual shifts in  $\Phi_{eff}$  reflect ranges of chemical conditions under which the relative surface energies are evolving in such a way that the relative expressed surface areas of different facets are changing. For example, in Fig. 5.5 at 1450 K, the stable configurations from  $p_{O_2} = 10^{-20}$  to  $10^{-10}$  Torr (roughly,  $\mu_O = -9.25$  eV to  $-8.1$  eV in Fig. 5.3)—that is as conditions cross from the medium-to-light blue regions—are  $\text{Ba}_{0.50}\text{O-top/W (001)}$  ( $\Phi_{eff} = 2.47$  eV),  $\text{Ba}_{0.25}\text{O-tri/W (110)}$  ( $\Phi_{eff} = 2.67$  eV), and  $\text{Ba}_{0.50}\text{O-top/W (112)}$  ( $\Phi_{eff} = 1.23$  eV). As the availability of oxygen changes, no facets change configuration. Rather,  $\Phi_{eff}$  changes because the inequivalent slopes of each configuration's  $\hat{\gamma}(\mu_O)$  result in evolving surface energy—and therefore surface area—ratios. This effect, continuously varying relative surface areas, generates relatively smooth (though still dramatic) changes in  $\Phi_{eff}$ .

## 5.4 Additional $\text{Sc}_y$ -containing W surfaces

### 5.4.1 Surface energies, chemical conditions, and work functions

In the previous section, §5.3.4, the role of Sc was speculated based on  $\text{Ba}_x\text{Sc}_y\text{O/W (hkl)}$  configurations, where Sc is a surface cation atop a layer of O atoms. Since that series of calculations did not find any  $\text{Sc}_y$ -containing surfaces present in regions where the surface energies of the stable (001), (110), and (112) configurations yield the characteristic W particle shape, additional efforts were undertaken to study surface configurations where Sc is in other positions. In particular, configurations with Sc directly bonded to W were evaluated. Work by Taylor et al. [170] in the 1960s concluded that the Sc-W system has nearly nonexistent solubility. As such, studies of these types of surface configurations had understandably not been prioritized within the thermionic cathode community.

The first set of surface configurations examined here are of the type  $\text{Ba}_x\text{OSc/W (hkl)}$  and include:  $\text{Ba}_{0.50}\text{O-triSc-top/W (001)}$ ,  $\text{Ba}_{0.25}\text{O-triSc-top/W (110)}$ , and  $\text{Ba}_{0.50}\text{O-triSc-top/W (112)}$ . These configurations were constructed because they are essentially the three  $\text{Ba}_x\text{O/W (hkl)}$  discussed heavily in both this and the previous chapter, albeit with the inclusion of a 1 ML of Sc directly atop the W (hkl) surface. The surface energies of each configuration are shown in Fig. 5.6. Compared to Fig. 5.3,

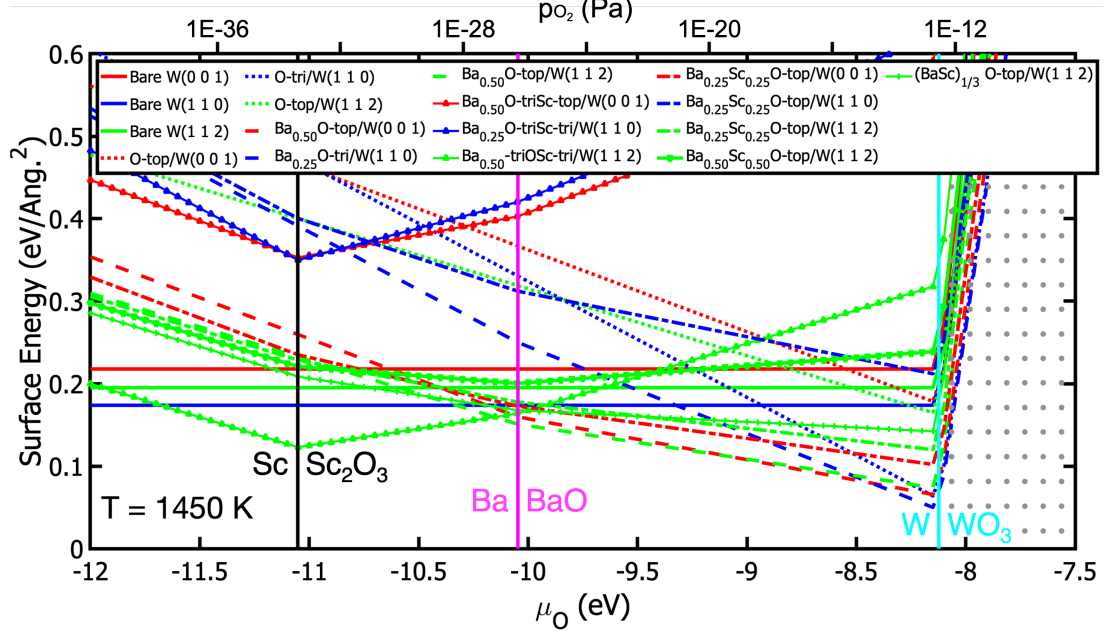
the region above the Ba/BaO transition remains essentially unchanged, particularly with respect to the stable surfaces. However, below the Ba/BaO transition, the Ba<sub>0.50</sub>O-triSc-top/W (112) configuration exhibits the lowest surface energy of the (112) orientation, and, except for a narrow, ultralow  $\mu_O$  window (between  $-10.1$  and  $-10.02$  eV), in all orientations. Interestingly, the low  $\mu_O$  characteristic Wulff shape region (highlighted by black stars in Fig. 5.6) occurs at a  $\mu_O$  where the Ba<sub>0.50</sub>O-triSc-top/W (112) and Ba<sub>0.50</sub>O-top/W (112) surface energies intersect. While the effects of kinetics are not addressed in this dissertation, this junction may possibly be a site of complex Sc kinetic behavior—desorption, diffusion, etc. The stable (001) and (110) surface configurations below the Ba/BaO transition are the same as those in Fig. 5.3.

The low surface energy exhibited by the Ba<sub>0.50</sub>O-triSc-top/W (112) configuration prompted deeper investigation into surface configurations containing Sc-W bonding. This broad campaign includes Sc<sub>y</sub>/W (hkl), O<sub>z</sub>Sc/W (hkl) and Sc<sub>y</sub>O/W (hkl) configurations: Sc-tri/W (001), Sc-top/W (110), Sc-tri/W (112), Sc<sub>0.50</sub>-triO-top/W (001), Sc<sub>0.25</sub>-triO-top/W (110), Sc<sub>0.50</sub>-triO-top/W (112), O<sub>0.50</sub>-triSc-top/W (001), O-topSc-tri/W (001), O<sub>0.25</sub>-triSc-top/W (110), and O<sub>0.50</sub>-triSc-top/W (112). Fig. 5.7 highlights twenty-seven surfaces, adding the Sc<sub>y</sub>-containing surface configurations to all others already discussed.

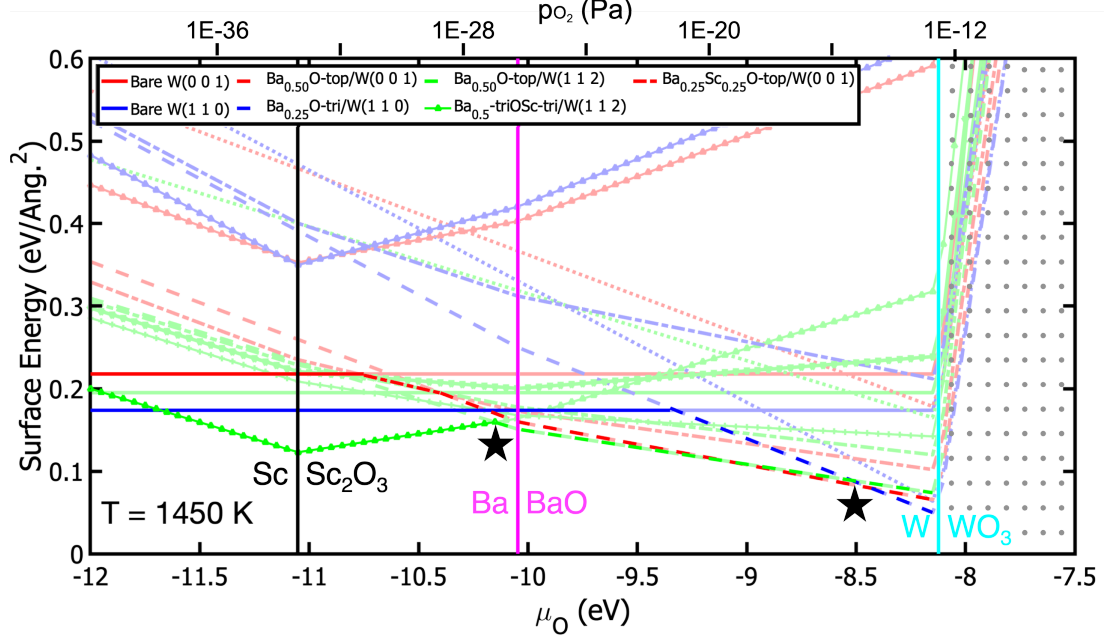
The introduction of these surface configurations significantly changes relative surface energies in the low to medium  $\mu_O$  window. Below the Sc/Sc<sub>2</sub>O<sub>3</sub> transition, the Sc-tri/W (001) configuration exhibits a much lower surface energy than any (110) or (112) configuration. Above the Sc/Sc<sub>2</sub>O<sub>3</sub> transition, the O-topSc-tri/W (001) becomes the lowest energy configuration (among all orientations). Both the Sc-tri/W (001) and O-topSc-tri/W (001) configurations exhibit a lower surface energy than the Ba<sub>0.50</sub>O-triSc-top/W (112) configuration discussed earlier. The low surface energy of the O-topSc-tri/W (001) also appears to remove the characteristic Wulff shape region around  $\mu_O = -10.1$  eV. The surface energy ratios in that window yield a Wulff shape dominated by the (001) facet. This is in contrast to the results discussed in Chapter 4, which at low  $\mu_O$  predict a Wulff shape with a significant amount of (110) faceting if only Ba, O, and W are present. The high  $\mu_O$  region is again dominated by the Ba<sub>x</sub>O/W (hkl) configurations. As such, the high  $\mu_O$  characteristic Wulff shape window is unaffected by the inclusion of the new Sc<sub>y</sub>-containing surface configurations. The contour plots showing the characteristic Wulff shape windows as a function of temperature and oxygen partial pressure of the surfaces plotted in both Figs. 5.6 and 5.7 are shown in Fig. 5.8.

None of the Sc<sub>y</sub>-containing surfaces introduced in this section exhibited a par-



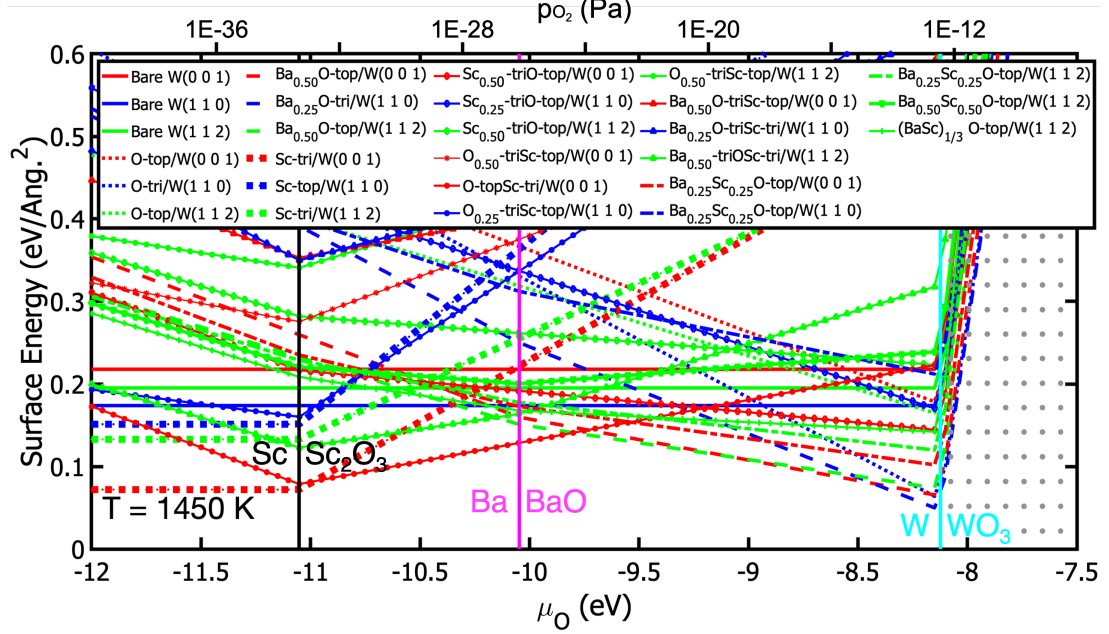


(a)

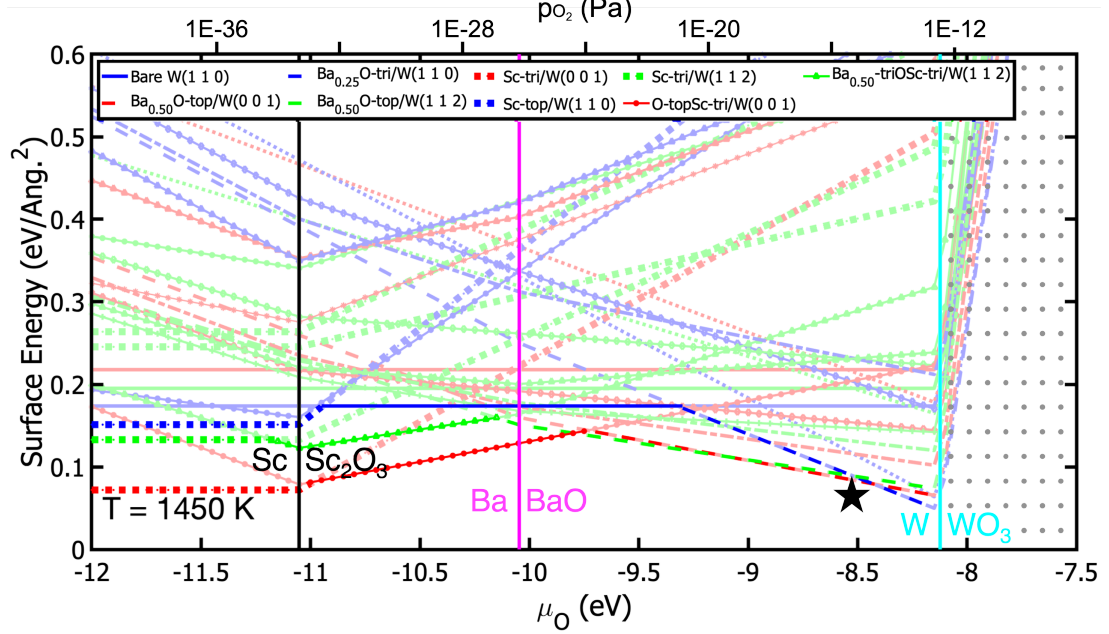


(b)

Figure 5.6: (a) An isotherm at 1450 K showing the surface energies of all seventeen surface configurations evaluated. (b) The same data as in (a), but with sections of surface energy curves shown in bold colors only if/when the surface configuration has the minimum surface for its facet. Other sections of surface energy curves (where the particular configuration does not have the lowest surface energy for its facet) are lightened to highlight that only a subset of all considered configurations are ever the lowest energy configuration for their facet. Black stars indicate  $\mu_O$  yield the characteristic W shape.

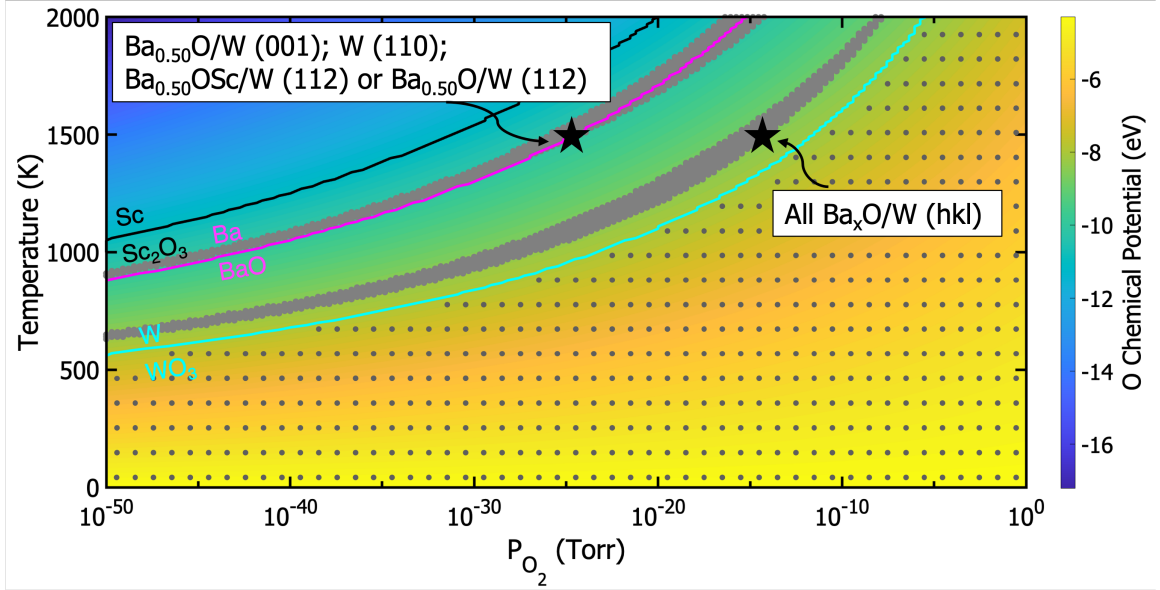


(a)

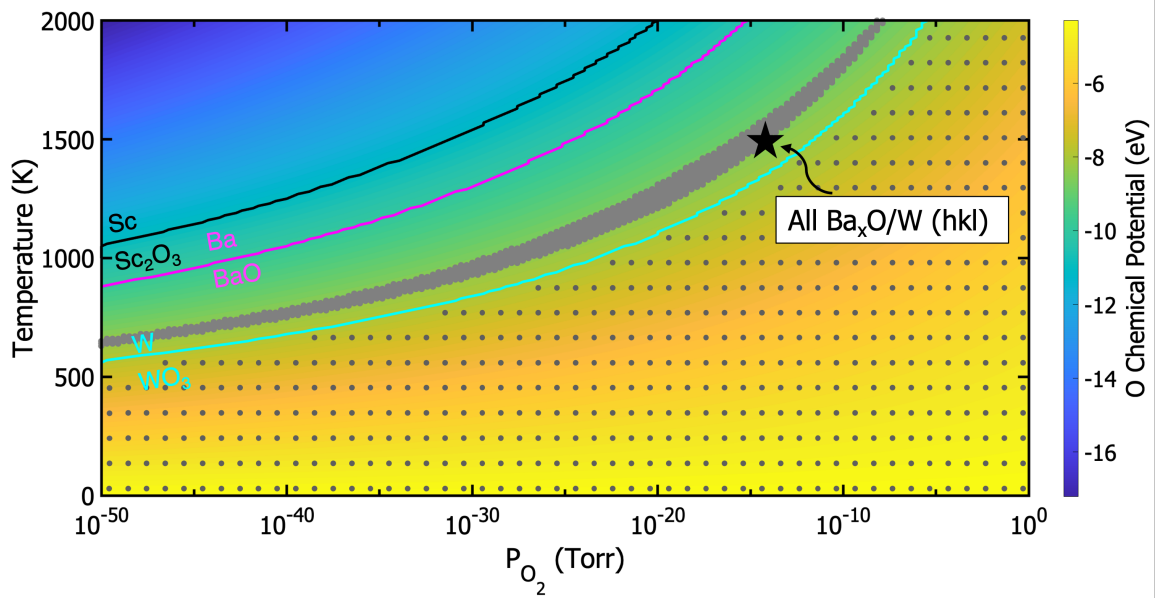


(b)

Figure 5.7: (a) An isotherm at 1450 K showing the surface energies of all twenty-seven surface configurations evaluated. (b) The same data as in (a), but with sections of surface energy curves shown in bold colors only if/when the surface configuration has the minimum surface energy for its facet. Other sections of surface energy curves (where the particular configuration does not have the lowest surface energy for its facet) are lightened to highlight that only a subset of all considered configurations are ever the lowest energy configuration for their facet. Black stars indicate  $\mu_O$  yield the characteristic W shape.



(a)



(b)

Figure 5.8: Contour plots of  $\mu_O$  as a function of oxygen partial pressure and temperature, overlaid with gray bands indicating conditions wherein the characteristic shape is expected. **(a)** The resulting plot of the W, O/W,  $Ba_xO/W$ , and  $Ba_xO_zSc/W$  (hkl) configurations (those plotted in Fig. 5.6). **(b)** The resulting plot of the W, O/W,  $Ba_xO/W$ ,  $Ba_xO_zSc/W$ ,  $Sc_y/W$ ,  $O_zSc/W$ , and  $Sc_yO/W$  (hkl) configurations (those plotted in Fig. 5.7).

ticularly low work function. The  $\text{Sc}_y/\text{W}$  (hkl) surface configurations, which showed exceptionally low surface energies, had work functions ranging from 2.5-4.0 eV. This range encompassed all other surface configurations. As has been a repeated theme in this chapter, it is exceedingly rare that an  $\text{Sc}_y$ -containing surface configuration is both (i) low surface energy and (ii) low work function. This is additional evidence that the role of Sc is likely not directly related to creating low work function surface configurations, but rather to tune environmental conditions.

#### 5.4.2 Sc and imaginary phonon modes

The previous results highlight a common theme: there is evidence that the addition of cations to a surface where Sc is positioned directly atop W increases its excess energy, as shown by the disparities in surface energies displayed by certain groups of configurations in Fig. 5.6. A deeper study of phonon modes and frequencies further supports this statement. Discussed in the previous chapter with respect to the “row” and “zig-zag”  $\text{Ba}_x\text{O}/\text{W}$  (112) surface configurations, the absence of imaginary phonon modes indicates mechanical stability in a crystal. Conversely, their presence indicates instability and major kinetic obstacles to formation. Even a qualitative review of the relationship between particular surface configurations and phonon modes yields tremendous insight into the possible surface composition of W grains during scandate cathode operation. Table 5.3 classifies groups of surface configurations by mechanical and thermodynamic stability. Sets of surface configurations marked with green indicate both thermodynamic and mechanical stability, the former qualifier referring to whether the surface configuration ever exhibits the lowest surface energy of its orientation at any  $(T, \mu_O)$  condition. Orange indicates configurations that are mechanically stable but never thermodynamically stable. Lastly, red indicates configurations that are neither mechanically nor thermodynamically stable at any  $(T, \mu_O)$  condition.

The only set of configurations marked entirely green is  $\text{Sc}_y/\text{W}$  (hkl). As shown in Fig. 5.6, these configurations are all thermodynamically stable at very low  $\mu_O$ . Of all the  $\text{Ba}_x$ -containing surface configurations, only one is both mechanically and thermodynamically stable:  $\text{Ba}_{0.50}\text{O-triSc-top}/\text{W}$  (112). The rest have multiple high frequency imaginary modes. Recall that high and low imaginary modes differ based on the gradient of the potential energy surface—low frequency imaginary modes indicate a gradual, flatter surface while high frequency indicates a steep region. As such, high frequency imaginary modes indicate atoms seeking to build major surface reconstructions (or entirely new configurations) rather than slightly vary atomic position.

Table 5.3: Comparing imaginary modes of  $\text{Sc}_y$ -containing surface configurations.

| Facets | Surface Configurations |                                |                                |   |   |
|--------|------------------------|--------------------------------|--------------------------------|---|---|
|        | $\text{Sc}_y/\text{W}$ | $\text{O}_z\text{Sc}/\text{W}$ | $\text{Sc}_y\text{O}/\text{W}$ | $\text{Ba}_x\text{O}_z\text{Sc}/\text{W}$ | $\text{Ba}_x\text{Sc}_y\text{O}/\text{W}$ |
| (001)  | ●                      | ●                              | ●                              | ●   | ●   |
| (110)  | ●                      | ●                              | ●                              | ●   | ●   |
| (112)  | ●                      | ●                              | ●                              | ●   | ●   |

- mechanically and thermodynamically stable
- mechanically stable
- mechanically unstable

Fig. 5.9 presents the imaginary modes associated with  $\text{Ba}_{0.50}\text{O-triSc-top}/\text{W}$  (001). These modes, represented as hypervectors, correlate to eight unique high imaginary frequencies. The region of greatest “activity,” i.e. the greatest density of imaginary modes, is in the Sc and top layer W region. The direction of these modes is observed to mostly reside in the  $\{001\}$  plane—horizontally along the surface. This suggests that Sc atoms are seeking a lower energy at a position elsewhere in this direction. In other words, they are seeking to surface diffuse. The first layer of W atoms show a similar in-plane set of hypervectors, and it is hypothesized that they would move to “follow” the Sc atoms. This does not necessarily mean that they are seeking to diffuse, rather that bonds with Sc are energetically favorable. These assertions are supported by the earlier observation that only the  $\text{Sc}_y/\text{W}$  surface configurations are thermodynamically and mechanically stable. When Ba and O atoms are not included in a configuration, it is stable. When they are added, Sc atoms become extremely mechanically unstable. These conclusions align well with those drawn by Mroz and Kordesch [168, 171], who, as mentioned in the previous section, have described the role of Sc on the Ba-Sc-O/W (001) surface as an oxygen “cleaner”. However, the idea that W surfaces in scandate cathodes are bare or even  $\text{Sc}_y$ -covered during activation and operation spawns a series of complexities regarding cathode operating mechanism. Mainly, if Ba-O dipoles are the most plausible origin of enhanced electron emission, as is widely accepted in the scandate cathode community [78], then it is not logical that Ba is absent from the W surfaces. If Sc is somehow causing Ba and O to desorb from W surfaces, Ba must somehow be replenished to maintain emission. It is not clear by which mechanism this may occur.

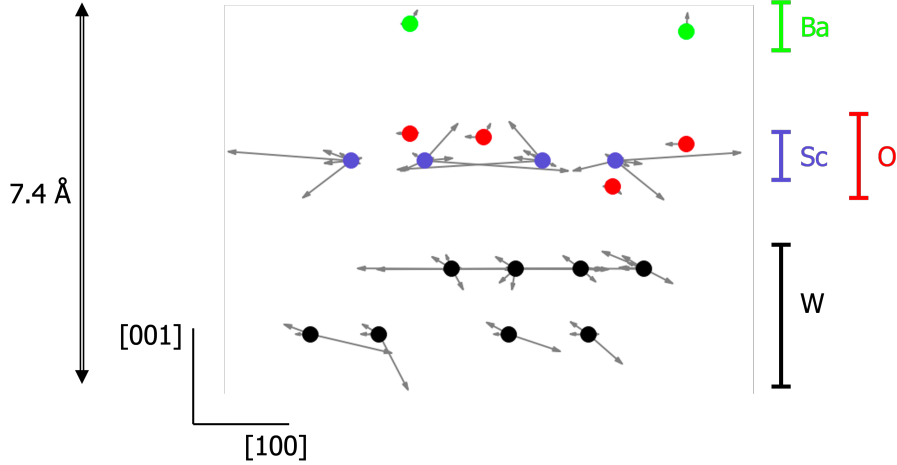


Figure 5.9: Vector representations of imaginary phonon modes exhibited by the  $\text{Ba}_{0.50}\text{O-triSc-top/W}$  (001) configuration.

## 5.5 Summary

While the precise origin of scandate cathodes’ superior performance to similar thermionic cathodes remains obscure [78, 77], observation of a characteristic equilibrium W nanoparticle shape in high-performing scandate cathodes has led to the hypothesis that particle shape and high emission current (at low operating temperatures) are correlated. This has driven interest in “reverse engineering” local chemical conditions in effect during particle equilibration, which occurs during the activation step of thermionic cathode fabrication. Leveraging computed, temperature- and chemical-environment-dependent surface energies, the implementation of an “inverted Wulff construction” revealed the chemical conditions required to produce equilibrium particles with experimentally observed shapes. It was found that the observed characteristic shape will only occur in two narrow regions of  $(T, p_{\text{O}_2})$ -space, implying that extremely careful control of chemical conditions during cathode activation is required yield high-performing cathodes. Such narrow stability windows therefore provides a direct explanation for the long-standing difficulties in reliably fabricating high-performing scandate cathodes [78].

In both regions of  $(T, p_{\text{O}_2})$ -space where the experimentally observed W particle shape is stable, the  $\text{Ba}_{0.50}\text{O-top/W}$  (112) surface configuration, with a work function of 1.23 eV, is present in the largest surface area fraction ( $\sim 70\%$  of total surface area). The large relative area and relatively low work function of this configuration drives a low effective work function of  $\sim 1.3$  eV for particles with the observed shape, a value comparable to those measured for scandate cathodes. There is a window of chemical

conditions where the  $\text{Ba}_{0.25}\text{Sc}_{0.25}\text{O-top/W}$  (001) surface (with a work function of 0.82 eV) is stable, pushing the effective work function of W particles as low as 0.84 eV. Chemical conditions in this window, though, do not yield the observed particle shape, and achieving these conditions requires pushing the overall oxygen availability almost to the  $\text{Sc/Sc}_2\text{O}_3$  oxidation limit and near chemical conditions where only bare W surfaces are stable (with work functions of approximately 4.3 eV). In addition, perhaps intriguingly no Sc-containing surface configurations were found to be stable (relative to Sc-free surface configurations) when the observed characteristic particle shape is stable. In fact, the inclusion of a broad range of Sc-containing surfaces, including the  $\text{Sc}_y\text{W/ (hkl)}$  set, eroded the characteristic shape window predicted around  $\mu_{\text{O}} = -10.1$  eV. The surface energy of the Sc-tri/W (001) configuration is so low that the Wulff shape at this  $\mu_{\text{O}}$  is entirely (001)—starkly different than the (112)-dominated characteristic shape. Combined these findings suggest the possibility that the role of Sc is not to directly modify the surface work function by adsorbing atop O on W crystallites, but rather simply to getter oxygen, driving down oxygen availability to stabilize particular surface configurations, e.g.,  $\text{Ba}_{0.50}\text{O-top/W}$  (112). Both the importance of Sc as a regulator of the chemical environment near cathode surfaces and of the (112) facet itself is consistent with a number of previous studies [79, 83, 168].

Finally, a major theme of this chapter was the potentiality of high-resolution imaging and characterization in conjunction with atomistic calculations to investigate highly-complex, non-uniform, inhomogeneous materials. Detailed knowledge of the characteristic particle shapes (i.e. crystallographic facets and relative area fractions) combined with insight into composition at the surface (elemental identification, surface symmetry, etc.) can, through the methods demonstrated here, be used to determine both the atomic-scale structure and properties of surfaces in a system, as well as the chemical conditions present as the system formed and equilibrated.

## Part II

### Continuum scale



## Chapter 6: Finite Element Method

### 6.1 Overview

“The description of right lines and circles, upon which geometry is founded, belongs to mechanics. Geometry does not teach us to draw these lines, but requires them to be drawn.”

— Sir Isaac Newton, *The Mathematical Principles of Natural Philosophy*, 1729

The Finite Element Method (FEM) is a powerful approach for the numerical solution of boundary- and initial-value problems characterized by partial differential equations (PDEs) [172]. Consequently, the technique has had a monumental impact on virtually all areas of engineering and applied science, including structural analysis, heat transfer, fluid flow, mass transport, and electromagnetic potential. Two fundamental attributes of FEM are the cause of its widespread, enduring success. Firstly, the method is based on the idea of partitioning bounded domains  $\Omega$  in  $\mathbb{R}^n$  into a number  $N$  of small, non-overlapping subdomains, the finite elements, over which functions are approximated by local functions, generally polynomials. Secondly, the boundary- and initial-value problems, to which the method is applied, are formulated in a weak, or integral, form, so that the contributions of each subdomain to the global integrals sum up to produce an integral characterizing the problem over the whole domain. In essence, FEM is a technique involving two steps: (1) the division, or discretization of a domain into subdomains, each represented by a set of element equations and (2) the systematic recombination of all sets of element equations into a global system of equations.

In the first step, approximation of PDEs by local polynomial expressions, i.e. the element equations, can be described as a special case of the Galerkin method [173]. This procedure minimizes the error of approximation by fitting trial functions into the PDE. The residual is the error caused by the trial functions, and the weight functions are polynomial approximation functions that project the residual. The process eliminates all the spatial derivatives from the PDE, thus approximating the PDE locally with a set of algebraic equations for steady state problems and a set of ordinary differential equations for transient problems. In the second step, a global system of equations is generated from the element equations through a transformation of coordinates from the subdomains' local nodes to the domain's global nodes. This

spatial transformation includes appropriate orientation adjustments as applied in relation to the reference coordinate system, a process carried out using coordinate data generated from the subdomains.

## 6.2 Implementation

### 6.2.1 Algebraic approach

The equations governing small elastic deformations of a body  $\Omega$  can be written as:

$$-\nabla \cdot \sigma = f \text{ in } \Omega \quad (6.1)$$

$$\sigma = \lambda \operatorname{tr}(\epsilon)I + 2\mu\epsilon \quad (6.2)$$

$$\epsilon = \frac{1}{2}(\nabla u + (\nabla u)^T) \quad (6.3)$$

where  $\sigma$  is the stress tensor,  $f$  is the body force per unit volume,  $\lambda$  and  $\mu$  are Lamé elasticity parameters for the material in the domain  $\Omega$ ,  $I$  is the identity tensor,  $\operatorname{tr}$  is the trace operator on a tensor,  $\epsilon$  is the symmetric strain-rate tensor, and  $u$  is the displacement vector field.

The Lamé elasticity parameters can be computed from the Young's modulus  $E$  and Poisson's ratio  $\nu$ , according to:

$$\lambda = \frac{E\nu}{(1+\nu)(1-2\nu)} \quad (6.4)$$

$$\mu = \frac{E}{2(1+\nu)} \quad (6.5)$$

Combining Eqs. 6.2 and 6.3, one obtains

$$\sigma = \lambda(\nabla \cdot u)I + \mu(\nabla u + (\nabla u)^T) \quad (6.6)$$

The strain-energy density function  $U$ , following the Saint Venant-Kirchhoff model [174], is:

$$U(\epsilon) = \frac{1}{2}\lambda[\operatorname{tr}(\epsilon)]^2 + \mu \operatorname{tr}(\epsilon^2) \quad (6.7)$$

The variational formulation of Eqs. 6.1, 6.2, and 6.3 consists of forming the inner product of Eq. 6.1 and a vector test function  $v \in \hat{V}$ , where  $\hat{V}$  is a vector-valued test

function space, and integrating over the domain  $\Omega$ :

$$-\int_{\Omega} (\nabla \cdot \sigma) \cdot v \, dx = \int_{\Omega} f \cdot v \, dx \quad (6.8)$$

Since  $\nabla \cdot \sigma$  contains second-order derivatives of the primary unknown  $u$ , the term is integrated by parts.

$$-\int_{\Omega} (\nabla \cdot \sigma) \cdot v \, dx = \int_{\Omega} \sigma : \nabla v \, dx - \int_{\partial\Omega} (\sigma \cdot n) \cdot v \, ds \quad (6.9)$$

where the colon operator is the inner product between tensors (summed pairwise product of all elements) and  $n$  is the outward unit normal at the boundary. The quantity  $\sigma \cdot n$  is known as the traction vector at the boundary and is often prescribed as a boundary condition. One assumes that it is prescribed at a part  $\partial\Omega_T$  of the boundary as  $\sigma \cdot n = T$ . On the remaining part of the boundary, the value of the displacement is given as a Dirichlet condition. Then:

$$\int_{\Omega} \sigma : \nabla v \, dx = \int_{\Omega} f \cdot v \, dx + \int_{\partial\Omega_T} T \cdot v \, ds \quad (6.10)$$

When this expression is inserted into Eq. 6.6 for  $\sigma$ , the variational form of the unknown  $u$  is revealed.

The variational formulation can now be summarized. Find  $u \in V$  such that

$$a(u, v) = L(v) \, \forall v \in \hat{V} \quad (6.11)$$

where

$$a(u, v) = \int_{\Omega} \sigma(u) : \nabla v \, dx \quad (6.12)$$

$$\sigma(u) = \lambda(\nabla \cdot u)I + \mu(\nabla u + (\nabla u)^T) \quad (6.13)$$

$$L(v) = \int_{\Omega} f \cdot v \, dx + \int_{\partial\Omega_T} T \cdot v \, ds \quad (6.14)$$

The inner product of a symmetric tensor  $A$  and an anti-symmetric tensor  $B$  vanishes. If  $\nabla v$  is expressed as a sum of its symmetric and anti-symmetric parts, only the symmetric part will survive in the product  $\sigma : \nabla v$ , as  $\sigma$  is a symmetric tensor. Thus, replacing  $\nabla u$  by the symmetric gradient  $\epsilon(u)$  gives rise to the slightly different variational form

$$a(u, v) = \int_{\Omega} \sigma(u) : \epsilon(v) \, dx \quad (6.15)$$

where  $\epsilon(v)$  is the symmetric part of  $\nabla v$ :

$$\epsilon(v) = \frac{1}{2}(\nabla v + (\nabla v)^T) \quad (6.16)$$

### 6.2.2 Solution

Gaussian elimination, sparse LU decomposition, is generally used to solve linear systems of equations in many FEM softwares. This is a simple, robust method recommended for systems with up to a few thousand unknowns. However, sparse LU decomposition becomes slow and one quickly runs out of memory for larger problems. For large problems, an iterative method is preferred.

Preconditioned Krylov solvers are a popular type of iterative methods that are easily accessible in many FEM programs. For asymmetric boundary conditions, a Krylov solver such as GMRES (generalized minimal residual method) is ideal. GMRES [175] is an iterative method, mathematically equivalent to the generalized conjugate residual method, that uses Krylov subspaces to reduce a high-dimensional problem to a sequence of smaller dimensional problems. If  $A$  is an invertible  $m \times m$  matrix and  $\mathbf{b}$  is a vector of length  $m$ ,  $\mathcal{K}_n(A, \mathbf{b})$  is the order- $n$  Krylov subspace generated by  $A$  and  $\mathbf{b}$ . Rather than inverting  $A$  directly, GMRES uses least squares to determine  $\mathbf{x}_n \in \mathcal{K}_n$  that minimizes the residual  $r_n = \|\mathbf{b} - A\mathbf{x}_n\|^2$ . The algorithm is terminated when the residual is smaller than some predetermined value. In tandem with the GRMES Krylov solver, the work in this dissertation utilizes a SOR (successive over-relaxation) preconditioner. This is a method of solving a linear system of equations  $A\mathbf{x} = \mathbf{b}$  derived by extrapolating the Gauss-Seidel method. If  $A = D - L - U$ , where  $-L, D$  and  $-U$  are the lower triangular, diagonal, and upper triangular parts of  $A$ , then the system of linear equations can be rewritten as:

$$(D + \omega L)\mathbf{x} = \omega\mathbf{b} - [\omega U + (\omega - 1)D]\mathbf{x} \quad (6.17)$$

where  $\omega$  is the relaxation and  $\omega > 1$ .

## Chapter 7: The Kentucky Random Structures Toolkit and a prototypical nanoporous system

### 7.1 Motivation

Nanoporous (NP) materials with microstructural feature sizes at or below 100 nm have a wide range of applications in catalysis [176, 177, 178, 179, 180, 181, 182], actuation [183, 184, 185, 186], sensing [187, 188, 189, 190], electronics [191, 192, 193, 194, 195, 196], medicine [197, 198, 199, 200], optics [201, 202, 203], energy storage [204, 205, 206, 207, 208], and more. While the mechanical properties and deformation behavior of a range of NP materials have been extensively investigated [209, 210, 211, 212, 213, 214, 215, 216, 217, 218, 219, 220, 221, 222, 223, 224], predictive and transferable models for effective bulk elastic constants determined from physically-derived details of NP materials' microstructures are lacking.

The most widely applied model for predicting the elastic and bulk moduli of NP materials from the intrinsic properties of fully dense solids was developed by Gibson and Ashby for a regular geometric structure chosen to represent a low-density, open foam (Fig. 7.1). In the Gibson-Ashby (G-A) model, the stiffness of a NP material relative to the stiffness of a fully dense solid ( $E^*/E_s$ ) is expressed as a power law of the solid fraction ( $\phi$ ) of the NP material [225, 226]:

$$\frac{E^*}{E_s} = C_E \phi^2 \quad (7.1)$$

In this chapter, asterisks indicate effective bulk properties of the NP material, and  $\phi$  is the solid fraction, defined as  $\rho^*/\rho_s$  for  $\rho^*$  and  $\rho_s$  the mass density of the NP structure and the bulk material of which the NP structure consists, respectively. The subscript  $s$  denotes the material properties of a bulk, fully dense solid phase, and  $C_E$  is a constant near unity. Given an arbitrary NP material,  $C_E$  encapsulates all material- and geometry-specific effects, and therefore varies with fabrication and processing details, as well as the composition and crystal structure of the constituent bulk material [225].

The G-A model was developed for a specific, regular—that is, repeating, crystal-like—cellular microstructural geometry (Fig. 7.1), and for a limiting case where the mechanical response of the cellular structure is dominated by bending. This is a limitation, as a hallmark of nearly all NP materials is an inherent randomness of

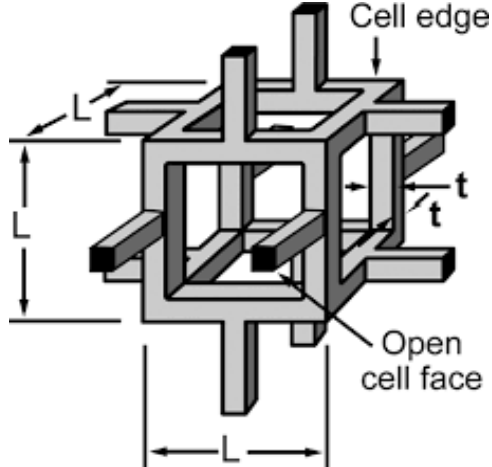


Figure 7.1: The unit cell defining the Gibson-Ashby model for low-density cellular open foams. Reproduced with permission from Ref. [226].

the underlying microstructure (e.g. ligaments and pores in an open-cell structure). Accounting for effects of this randomness is challenging, and only a small number of studies have directly probed the impact of structural disorder on NP materials' mechanical properties. Huber et al. [227] examined the effects of distorting a regular, diamond cubic array of cylindrical ligaments. This approach allowed for the calculation of a quantitative “degree of randomness” that characterized the net distortion of the ligament network from the reference diamond cubic structure. Finite element (FE) calculations of mechanical properties as a function of the “degree of randomness” showed that elastic modulus decreases with increasing distortion. However, this approach considered structures with fixed, constant ligament diameters and connectivity, and introduced disorder by distorting a pre-existing regular array resulting in structures that are not necessarily representative of any particular NP material.

Huber et al. [228] have recently extended their efforts by also considering potential additional effects of network connectivity. By randomly assigning certain ligaments in distorted diamond cubic lattices to have an infinitesimal mechanical stiffness ( $E \rightarrow 0$ )—that is, to be “missing” in a mechanical sense—model structures with effectively variable local and average network connectivities were constructed. Separately, Liu et al. [229, 230] proposed an adjustment of the G-A model seeking to account for dangling or broken ligaments where the net density of a NP material in the calculation of  $\phi$  in Eq. 7.1 was replaced with an “effective reduced density” that discounts dangling or broken ligaments when determining the volume of the NP network. This adjustment was designed to account for the fact that dangling

or broken ligaments cannot bear or distribute applied loads. A similar concept was implemented by Hu et al. [231], who generated “skeletonizations” of NP Au structures by removing any ligaments not part of a closed ring. Soyarslan et al. [232, 233] also considered “skeletonizations,” generating RVEs of spinodal-like stochastic microstructures from a leveled random field. This investigation implemented a radially varying stiffness scaling factor at the ligament-ligament connections to model amassments at the aforementioned junctions. Huber et al. [228], Liu et al. [229, 230], and Hu et al. [231] all found that the presence of dangling or broken ligaments implies that real NP materials will have lower stiffnesses than predicted by the G-A model. These approaches demonstrate that connectivity—and, particularly, network defects or disconnected ligaments—within NP microstructures strongly influences mechanical properties, though none of them permit a general, systematic exploration of the effects of changes in the local or average network topology.

In addition, Pia et al. [234] have explored the contribution that local *bending* deformation makes in determining the linear elastic response of NP materials under simple tension or compression. These efforts have shown that for a repeating, cubic lattice of ligaments whose cross sections vary along their lengths, bending deformation is an important deformation mode that is sensitive to the specific geometry and properties of ligament regions most distant from nodes in the structure. In effect, these results highlight that the presence of voids leads to mixed mode deformation at the microstructural level even in cases of macroscopically simple tensile or compressive loading.

Taken together these recent results demonstrate that accurately modeling the mechanical properties of NP materials requires consideration of the diverse and complex set of microstructural details—including any inherent randomness—characteristic of a particular material. In addition, optimization or design of randomly structured materials requires the ability to comprehensively explore arbitrary changes to local microstructure—and, particularly, the ability to evolve and adjust physically-motivated microstructures—to deduce structure-property relationships dictating observable, effective mechanical properties. To date, no methodology has been reported that allows a general and systematic exploration of how complex (and often random) ligament arrangements or connectivity affects mechanical properties. Nor has a methodology been reported that allows for generation of physically-motivated representative volumes expressing microstructural features specific to particular NP materials.

In this section, the Kentucky Random Structure Toolkit (KRaSTk) [235, 236],

a flexible and extensible software package for generating and computing properties of large numbers of model representative volume elements (mRVEs) for materials with complex structures, is presented. KRaSTk mRVEs are generated from a user-specified geometric seed description of a material’s microstructure that can be derived from experimental observations. Using a seed description representing a prototypical NP material, sets of KRaSTk-generated mRVEs can be used to compute not only effective macroscale mechanical properties, but also probability distributions of these effective properties at the microscale. The potential impact of this approach is demonstrated by systematically examining the relationship between network connectivity in a ligamented NP material and elastic response. Results of finite element calculations on statistically significant sets of mRVEs reveal that network connectivity has a separable and additional effect on both elastic and bulk modulus above and beyond the effects of variations in solid fraction. Finally, it is shown that the effects of variations in network connectivity can be accounted for with an additional power law factor modifying the original G-A model, and that these connectivity effects may explain observed variations in the mechanical properties of NP materials with similar microstructures and solid fractions.

## 7.2 Method overview

NP materials can be described on three length scales: (1) the macroscale, at which the NP material appears and behaves uniformly and generally isotropically, (2) the mesoscale, at which the complex (and often random) structural characteristics that define the NP material are evident and properties are strongly dependent on local geometric features; and (3) the atomic scale, dominated by the intrinsic properties of the solid material(s) composing the NP material itself.

Within this framework the internal structures characteristic of a NP material is classified as the mesoscale, as opposed to “nanoscale”, to highlight that while individual structural features (e.g., a ligament or a pore) may have one or more dimensions on the nanometer scale, it is the significantly larger *ensemble* of these individual features that govern properties of the material as a whole. At the mesoscale, NP materials are generally both complex and diverse, resulting in widely varying local structures and properties. Observed at longer length scales, variations in local properties decrease—that is, the material homogenizes—and observed properties converge to singular effective bulk properties in the macroscopic limit. While there is no precise boundary between the mesoscale and macroscale, the size scale at which homoge-



nization occurs is controlled by the relative sizes and configurations of mesostructural features in each particular NP material, and is characteristic of those materials.

To enable systematic exploration of arbitrary mesostructural complexity over a wide range of length scales (relative to structural feature sizes) a flexible and adaptable structure generation algorithm as been implemented within KRaSTk that generates sets of model representative volume elements (mRVEs) based on a user-specified geometric seed description. The seed description may be either regular (i.e. generating a periodic structure) or random, and will consist of combinations of geometric primitives (e.g. spheres, cylinders, prisms, etc.) and their dimensions as well as rules for their placement within a cuboid computational volume. This approach allows for the generation of mRVEs of arbitrary volume (relative to feature sizes) and representing any mesostructure that can be described as a combination of characteristic geometric shapes or configurations of shapes (i.e. the seed description).

To be representative, mRVEs generated from a particular seed description must be large enough to contain a meaningful sampling of the characteristic structural features that are possible based on the given seed description, while being sufficiently small as to be computationally tractable. In practice, this implies that mRVEs are never in the macroscopic limit, and therefore do not, individually, exhibit the bulk effective properties that would be observed for a macroscopic volume. Instead, aggregate sets of many (unique) mRVEs represent a statistical sampling of the structural motifs that govern the overall effective behavior of a macroscopic sample.

More formally the present approach adopts two related hypotheses: (1) that aggregated properties of many representative mRVEs quantitatively characterize the distribution of scale-equivalent local properties present within a NP material, and (2) that the first moment of the distribution of mRVE properties is the expected value of the bulk effective property for sufficiently large numbers of sampled mRVEs. Specifically, expected bulk effective properties ( $P^*$ ) can be computed as the first moment (arithmetic mean) of individually determined properties ( $P^\alpha$  values determined for an individual mRVE,  $\alpha$ ) from a statistically valid ensemble of representative mRVEs:

$$P^* = \frac{1}{N} \sum_{\alpha=1}^N P^\alpha \quad (7.2)$$

for  $N$ , the total number of mRVEs in the set.

## 7.3 Sampling bulk effective properties with mRVEs

### 7.3.1 Isotropic mRVEs

Many complex-structure materials are isotropic at the macroscale due to their inherently random microstructures. The effective mechanical properties of these random NP materials are therefore fully characterized by two elastic constants:  $E^*$  and  $\nu^*$ , or, equivalently,  $C_{11}^*$  and  $C_{12}^*$ <sup>1</sup>. Having postulated that bulk effective properties may be computed as the average of properties of many mRVEs, computing bulk effective mechanical properties of NP materials reduces to computing (first moments of)  $E^{*,\alpha}$  and  $\nu^{*,\alpha}$  (or, equivalently,  $C_{11}^{*,\alpha}$  and  $C_{12}^{*,\alpha}$ ) determined for many individual mRVEs,  $\alpha$ , generated from the same geometric seed.

In turn,  $E^{*,\alpha}$  and  $\nu^{*,\alpha}$  values can be derived from the computed strain energy densities in mRVEs under known strain states. Here, two applied strain states were considered: uniaxial ( $\epsilon_i = \bar{\epsilon} \neq 0$ ,  $\epsilon_j = \epsilon_k = 0$ ) and hydrostatic ( $\epsilon_i = \epsilon_j = \epsilon_k = \bar{\epsilon} \neq 0$ ) loading. In both cases, all shear strains are zero. In applying these conditions it is convenient to identify the three principle directions for a given mRVE as orthogonal to the faces of the cuboid mRVE. As each mRVE is random and distinct, though, there is no unifying characteristic direction or orientation among different mRVEs, and, for random—and therefore anisotropic—mRVEs, the three uniaxial loading conditions do not result in the same strain energy. Fig. 7.2 illustrates the four unique boundary conditions.

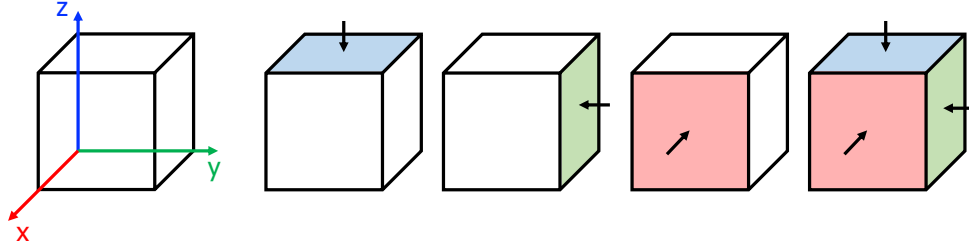


Figure 7.2: Boundary conditions to compute three pairs of elastic constants for each mRVE.

In Voigt notation [237], the strain energy in a given mRVE,  $\alpha$ , is:

$$\hat{U}^\alpha = \frac{1}{2} [C_{ij}^\alpha \bar{\epsilon}_i \bar{\epsilon}_j]$$

<sup>1</sup>As noted above, the superscript asterisk is used to indicate that the property is a bulk effective property of the NP material, in contrast to the bulk intrinsic properties of the solid material from which the NP structure is constructed.

Which, for the hydrostatic ( $\hat{U}^{H,\alpha}$ ) and uniaxial ( $\hat{U}_i^{U,\alpha}$ ) strain states of interest here, gives:

$$\hat{U}^{H,\alpha} = \frac{1}{2} [(C_{11}^\alpha + C_{22}^\alpha + C_{33}^\alpha) \bar{\epsilon}^2 + 2(C_{12}^\alpha + C_{13}^\alpha + C_{23}^\alpha) \bar{\epsilon}^2] \quad (7.3)$$

$$\hat{U}_{i=1,2,3}^{U,\alpha} = \frac{1}{2} [C_{ii}^\alpha \bar{\epsilon}^2] \quad (7.4)$$

In these expressions, quantities with a bar are applied (and therefore known), and hatted values can be computed (here, with FEM).

For randomly structured mRVEs, the set of elastic constants,  $C_{ii}^\alpha$  and  $C_{ij}^\alpha$ , are, strictly, all unique, and Eq. 7.4 is actually three distinct equations. In practice, this means that each mRVE yields three separate  $\hat{U}_i^{U,\alpha}$  values (for  $i$  indicating the particular load axis), and that  $\hat{U}^{H,\alpha}$  reveals only the *sum*  $C_{12}^\alpha + C_{13}^\alpha + C_{23}^\alpha$ , rather than the individual values. Critically, though, individual local samplings of the elastic properties of what is, macroscopically, an isotropic material—where  $C_{ii}^\alpha \equiv C_{11}^{*,\alpha}$  and  $C_{ij}^\alpha \equiv C_{12}^{*,\alpha}$ —were computed. Therefore the three distinct values of  $\hat{U}_i^{U,\alpha}$  can each be combined with  $\hat{U}^{H,\alpha}$  to yield three distinct samplings of the effective bulk properties  $C_{11}^*$  and  $C_{12}^*$ <sup>2</sup> were computed, which take the form:

$$\hat{U}^{H,\alpha} = \frac{1}{2} [3C_{11}^{*,\alpha} \bar{\epsilon}^2 + 6C_{12}^{*,\alpha} \bar{\epsilon}^2] \quad (7.5)$$

$$\hat{U}_i^{U,\alpha} = \frac{1}{2} [C_{11}^{*,\alpha} \bar{\epsilon}^2] \quad (7.6)$$

In this way, a set of  $N$  mRVEs yields  $3N$  pairs of  $C_{11}^{*,\alpha}$  and  $C_{12}^{*,\alpha}$  values, the  $*,\alpha$  superscript indicating that they are samples (extracted from the mRVE  $\alpha$ ) of effective bulk properties ( $*$  superscript).  $C_{11}^{*,\alpha}$  and  $C_{12}^{*,\alpha}$  are related to  $E^{*,\alpha}$  and  $\nu^{*,\alpha}$ :

$$\begin{aligned} (C_{11})_i^{*,\alpha} &= \frac{E_i^{*,\alpha} (1 - \nu_i^{*,\alpha})}{\eta_i^\alpha} \\ (C_{12})_i^{*,\alpha} &= \frac{E_i^{*,\alpha} \nu_i^{*,\alpha}}{\eta_i^\alpha} \\ \text{for } \eta_i^\alpha &\equiv 1 - \nu_i^{*,\alpha} - 2(\nu_i^{*,\alpha})^2 = (1 + \nu_i^{*,\alpha})(1 - 2\nu_i^{*,\alpha}) \end{aligned}$$

---

<sup>2</sup>Note that, setting aside shear, six unique pieces of information can be extracted from each mRVE, namely its six unique elastic constants. Here, the same information homogenized to three pairs of effective elastic constants characterizing the isotropic bulk material represented by each mRVE.

Substituting these expressions for  $(C_{11})_i^{*,\alpha}$  and  $(C_{12})_i^{*,\alpha}$  into Eqs. 7.5 and 7.6 gives:

$$\hat{U}^{H,\alpha} = \frac{E_i^{*,\alpha}}{2\eta_i^{*,\alpha}} \left[ 3(1 - \nu_i^{*,\alpha}) [\bar{\epsilon}]^2 + 6\nu_i^{*,\alpha} [\bar{\epsilon}]^2 \right] \quad (7.7)$$

$$\hat{U}_i^{U,\alpha} = \frac{E_i^{*,\alpha}}{2\eta_i^{*,\alpha}} \left[ (1 - \nu_i^{*,\alpha}) [\bar{\epsilon}]^2 \right] \quad (7.8)$$

$$\text{and } E_i^{*,\alpha} = \frac{2\eta_i^{*,\alpha} \hat{U}_i^{U,\alpha}}{(1 - \nu_i^{*,\alpha}) [\bar{\epsilon}]^2} \quad (7.9)$$

Substituting back into Eq. 7.7 yields:

$$\begin{aligned} \hat{U}^{H,\alpha} &= \frac{\hat{U}_i^{U,\alpha}}{(1 - \nu_i^{*,\alpha}) \bar{\epsilon}^2} \left[ 3(1 - \nu_i^{*,\alpha}) \bar{\epsilon}^2 + 6\nu_i^{*,\alpha} \bar{\epsilon}^2 \right] \\ \text{or } \nu_i^{*,\alpha} &= \frac{3\hat{U}_i^{U,\alpha} - \hat{U}^{H,\alpha}}{-3\hat{U}_i^{U,\alpha} - \hat{U}^{H,\alpha}} \end{aligned} \quad (7.10)$$

With Eq. 7.10,  $E_i^{*,\alpha}$  and  $\eta_i^{*,\alpha}$  may be written solely in terms of uniaxial and hydrostatic strain energies (note that the superscript  $\alpha$  has been omitted from the right-hand side of these expressions for clarity):

$$E_i^{*,\alpha} = \left( 2\eta_i^* \hat{U}_i^U \right) / \left[ \left( 1 - \frac{3\hat{U}_i^U - \hat{U}^H}{-3\hat{U}_i^U - \hat{U}^H} \right) [\bar{\epsilon}]^2 \right] \quad (7.11)$$

$$\eta_i^{*,\alpha} = 1 - \left( \frac{3\hat{U}_i^U - \hat{U}^H}{-3\hat{U}_i^U - \hat{U}^H} \right) - 2 \left( \frac{3\hat{U}_i^U - \hat{U}^H}{-3\hat{U}_i^U - \hat{U}^H} \right)^2 \quad (7.12)$$

The bulk modulus may be calculated directly from the hydrostatic strain energy:

$$K^\alpha = \frac{2\hat{U}^{H,\alpha}}{\epsilon^2} \quad (7.13)$$

where  $\epsilon = \bar{\epsilon}_1 + \bar{\epsilon}_2 + \bar{\epsilon}_3$

It is worth noting that if  $\bar{\epsilon}_1^H \neq \bar{\epsilon}_1^U$ , Eq. 7.10 is simply:

$$\begin{aligned}\hat{U}^H &= \frac{\hat{U}_1^U}{(1 - \nu_1)[\bar{\epsilon}_1^U]^2} \left[ 3(1 - \nu_1)[\bar{\epsilon}_1^H]^2 + 6\nu_1[\bar{\epsilon}_1^H]^2 \right] \\ \hat{U}^H &= \left( \frac{\bar{\epsilon}_1^H}{\bar{\epsilon}_1^U} \right)^2 \left( 3\hat{U}_1^U + \frac{6\nu_1\hat{U}^U}{1 - \nu_1} \right) \\ \nu_1 &= \frac{3\hat{U}_1^U - \delta\hat{U}^H}{-3\hat{U}_1^U - \delta\hat{U}^H} \\ \text{where } \delta &= \left( \frac{\bar{\epsilon}_1^U}{\bar{\epsilon}_1^H} \right)^2\end{aligned}\tag{7.14}$$

And Eq. 7.11 is modified slightly:

$$E^{*,\alpha} = \left( 2\eta^\alpha \hat{U}^U \right) \left/ \left[ \left( 1 - \frac{3\hat{U}^U - \hat{U}^H}{-3\hat{U}^U - \hat{U}^H} \right) [\bar{\epsilon}_1^U]^2 \right] \right.\tag{7.15}$$

utilizing a modified  $\eta$  expression to include  $\delta$ .

### 7.3.2 Orthotropic mRVEs

In many applications, particularly when a material property exhibits a directional dependence as is a main theme of the next chapter, it is necessary to treat the mRVEs as orthotropic, rather than isotropic. An orthotropic mRVE is assumed to exhibit a lower degree of symmetry than an isotropic mRVE, thus requiring a greater number of elastic constants to fully characterize them. For an orthotropic mRVE, the nine non-zero entries in the stiffness matrix, as shown in Eq. 7.16, must be computed.

$$C = \begin{bmatrix} C_{11} & C_{12} & C_{13} & 0 & 0 & 0 \\ C_{12} & C_{22} & C_{23} & 0 & 0 & 0 \\ C_{13} & C_{23} & C_{33} & 0 & 0 & 0 \\ 0 & 0 & 0 & C_{44} & 0 & 0 \\ 0 & 0 & 0 & 0 & C_{55} & 0 \\ 0 & 0 & 0 & 0 & 0 & C_{66} \end{bmatrix}\tag{7.16}$$

Compared to the previous section, where assumptions of isotropy to extract three pairs of  $C_{11}$  and  $C_{12}$  from four calculations for each mRVE were made, here, nine calculations recover nine elastic constants. Fig. 7.3 illustrates the nine unique boundary conditions: three uniaxial, three biaxial, and three simple shear calculations. The Lamé parameters  $E_{11}, E_{22}, E_{33}, \nu_{12}, \nu_{13}, \nu_{32}, G_{23}, G_{13},$  and  $G_{12}$  are then computed

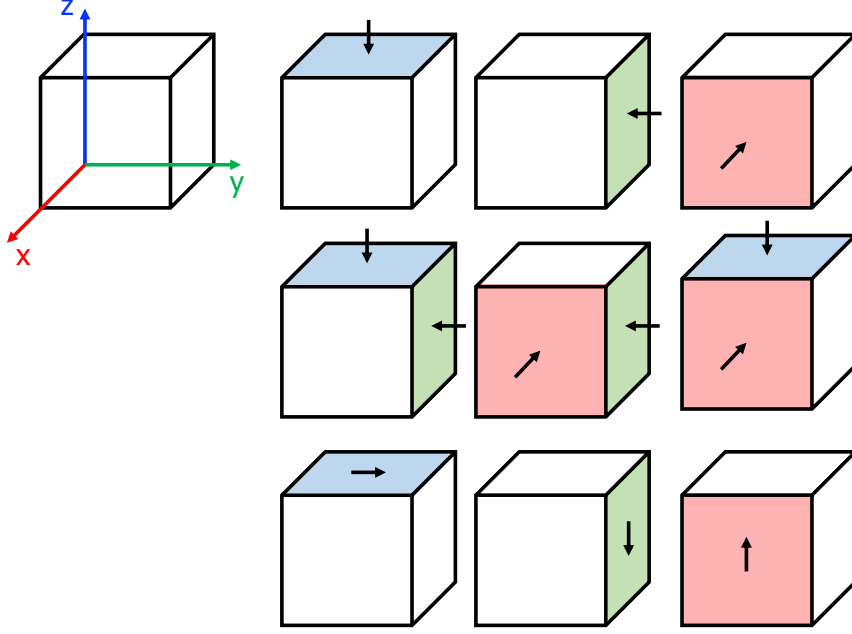


Figure 7.3: Boundary conditions to compute each non-zero elastic constant in the stiffness matrix of an orthotropic material.

according to:

$$\begin{aligned}
 E_{11} &= \frac{C_{11}C_{22}C_{33} + 2C_{23}C_{12}C_{13} - C_{11}C_{23}C_{23} - C_{22}C_{13}C_{13} - C_{33}C_{12}C_{12}}{C_{22}C_{33} - C_{23}C_{23}} \\
 E_{22} &= \frac{C_{11}C_{22}C_{33} + 2C_{23}C_{12}C_{13} - C_{11}C_{23}C_{23} - C_{22}C_{13}C_{13} - C_{33}C_{12}C_{12}}{C_{11}C_{33} - C_{13}C_{13}} \\
 E_{33} &= \frac{C_{11}C_{22}C_{33} + 2C_{23}C_{12}C_{13} - C_{11}C_{23}C_{23} - C_{22}C_{13}C_{13} - C_{33}C_{12}C_{12}}{C_{11}C_{22} - C_{12}C_{12}} \\
 \nu_{12} &= \frac{C_{12}C_{33} - C_{13}C_{23}}{C_{22}C_{33} - C_{23}C_{23}} \\
 \nu_{13} &= \frac{C_{22}C_{13} - C_{12}C_{23}}{C_{22}C_{33} - C_{23}C_{23}} \\
 \nu_{32} &= \frac{C_{11}C_{23} - C_{12}C_{13}}{C_{11}C_{22} - C_{12}C_{12}} \\
 G_{23} &= C_{44} \\
 G_{13} &= C_{55} \\
 G_{12} &= C_{66}
 \end{aligned}$$

## 7.4 Computing mRVE strain energies from FEM

Equation 7.2 postulates that bulk effective mechanical properties can be computed as the average of the properties of many individual mRVEs. Equations 7.10, 7.11, and 7.13 show that the elastic properties of individual mRVEs can be determined from the strain energies in an mRVE under known strain states. In this chapter, finite element (FE) calculations were implemented in the Static Structural Analysis module within **ANSYS Workbench** to compute uniaxial and hydrostatic strain energies for sets of KRaSTk-generated mRVEs.

Uniaxial strain energy calculations were conducted with a compressive displacement boundary condition applied to the ligament faces in one cut surface of an mRVE. Ligament faces in the opposite mRVE surface were set as frictionless supports, while ligament faces in all remaining mRVE surfaces were set to allow motion in only the direction parallel to the applied displacement. Hydrostatic strain energy calculations applied identical compressive displacement boundary conditions to ligament faces in three orthogonal mRVE surfaces, and frictionless supports to the three opposite surfaces. In all cases, displacements of  $\bar{\epsilon} = 0.01$  were used. Solid regions were assigned intrinsic mechanical properties of  $E_s = 165$  GPa,  $K_s = 98.2$  GPa, and  $\nu_s = 0.22$ , representing a relatively stiff isotropic bulk material. Four distinct strain energy calculations were performed for each mRVE, three uniaxial ( $U_1^U$ ,  $U_2^U$ ,  $U_3^U$ ) and one hydrostatic ( $U^H$ ). Adaptive tetrahedron meshes were generated within **ANSYS Workbench** using a resolution set equal to 5 (based on a 0 (coarse) to 7 (fine) scale).

## 7.5 Approach validation

Using the seed description of a prototype network structure defined above, twelve sets of mRVEs were constructed: nine sets of random mRVEs and 3 sets of regular mRVEs. Sets of random mRVEs with network connectivities  $N_C$  of 3, 4, and 6 were studied. Within each  $N_C$  mRVE set, constituent ligaments had different aspect ratios, defined as ligament length divided by average ligament radius. The average ligament radius is simply computed as the average of the radii of the ligament ends. Node radii (and therefore end radii of connecting frustum ligaments) for random mRVEs were selected from three ranges representing “thick” ( $[r_{min}^+, r_{max}^+]$ ), “intermediate” ( $[r_{min}^0, r_{max}^0]$ ), and “thin” ( $[r_{min}^-, r_{max}^-]$ ) ligaments, and these mRVE sets were labelled ‘+’, ‘0’, and ‘−’, respectively. For each set of random mRVEs the ratio of the maximum node radius to the minimum was  $r_{max}/r_{min} = 1.57$ , and  $r_{max}^+$  was chosen to be twice  $r_{max}^-$  with  $r_{max}^0$  intermediate. The number density of nodes in the computational

volume, defined as  $N_{sph}/s^3$ , was the same for all mRVEs, yielding equivalent average ligament lengths. Minimally each node was a distance  $d_{sep}$  from the next nearest node. Individual sets of mRVEs are therefore referred to by their connectivity and relative ligament radii (which is equivalent to ligament aspect ratio given the common ligament lengths), e.g., as ‘6NN<sup>+</sup>’ or ‘4NN<sup>0</sup>’, and so on. Fig. 7.4 shows example mRVEs of 3NN<sup>-</sup>, 3NN<sup>0</sup>, 3NN<sup>+</sup> sets and Table 7.1 includes details of the structural parameters used in generating the mRVEs studied here.

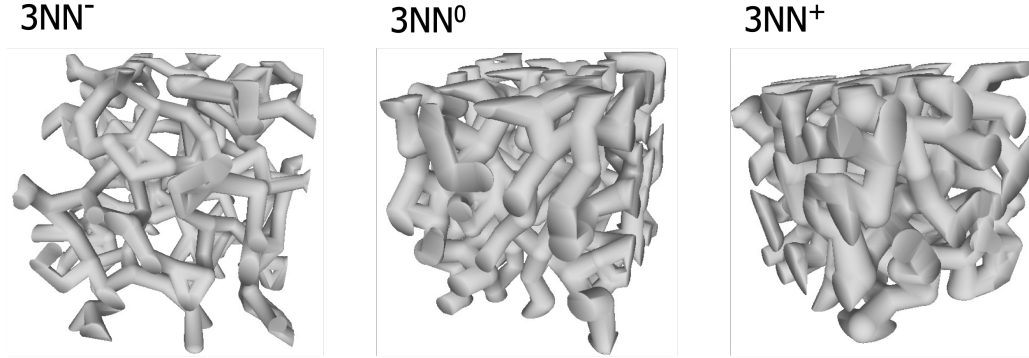


Figure 7.4: Example mRVEs of random structures used in this section. Each are unique due to the varied minimum and maximum sphere radii and network connectivity indicated in Table 7.1. Reproduced with permission from Ref. [236].

Table 7.1: Parameters used to generate all sets of random mRVEs.

| mRVE set         | $N_C$ | $N_C^*$ | $r_{min}$ | $r_{max}$ | $N_{sph}$ | $s$ | $d_{sep}$ |
|------------------|-------|---------|-----------|-----------|-----------|-----|-----------|
| 3NN <sup>+</sup> | 3     | 3.24    | 5.25      | 8.25      | 200       | 100 | 3.5       |
| 3NN <sup>0</sup> | 3     | 3.24    | 4.2       | 6.6       | 200       | 100 | 3.5       |
| 3NN <sup>-</sup> | 3     | 3.25    | 2.625     | 4.125     | 200       | 100 | 3.5       |
| 4NN <sup>+</sup> | 4     | 4.21    | 5.25      | 8.25      | 200       | 100 | 3.5       |
| 4NN <sup>0</sup> | 4     | 4.20    | 4.2       | 6.6       | 200       | 100 | 3.5       |
| 4NN <sup>-</sup> | 4     | 4.21    | 2.625     | 4.125     | 200       | 100 | 3.5       |
| 6NN <sup>+</sup> | 6     | 6.26    | 5.25      | 8.25      | 200       | 100 | 3.5       |
| 6NN <sup>0</sup> | 6     | 6.26    | 4.2       | 6.6       | 200       | 100 | 3.5       |
| 6NN <sup>-</sup> | 6     | 6.29    | 2.625     | 4.125     | 200       | 100 | 3.5       |

The top panel of Fig. 7.5 shows computed  $E_i^\alpha$  values for all random mRVEs. Each point represents results from a single mRVE, and is located at  $(E_x^\alpha, E_y^\alpha - \overline{E_x^\alpha})$ . The bottom panel of Fig. 7.5 shows gamma ( $\Gamma$ -) distributions fit to each set of  $E^\alpha$  values. Gamma distributions were chosen to fit mechanical properties data both because they are positive definite and are a generalization of normal distributions, which



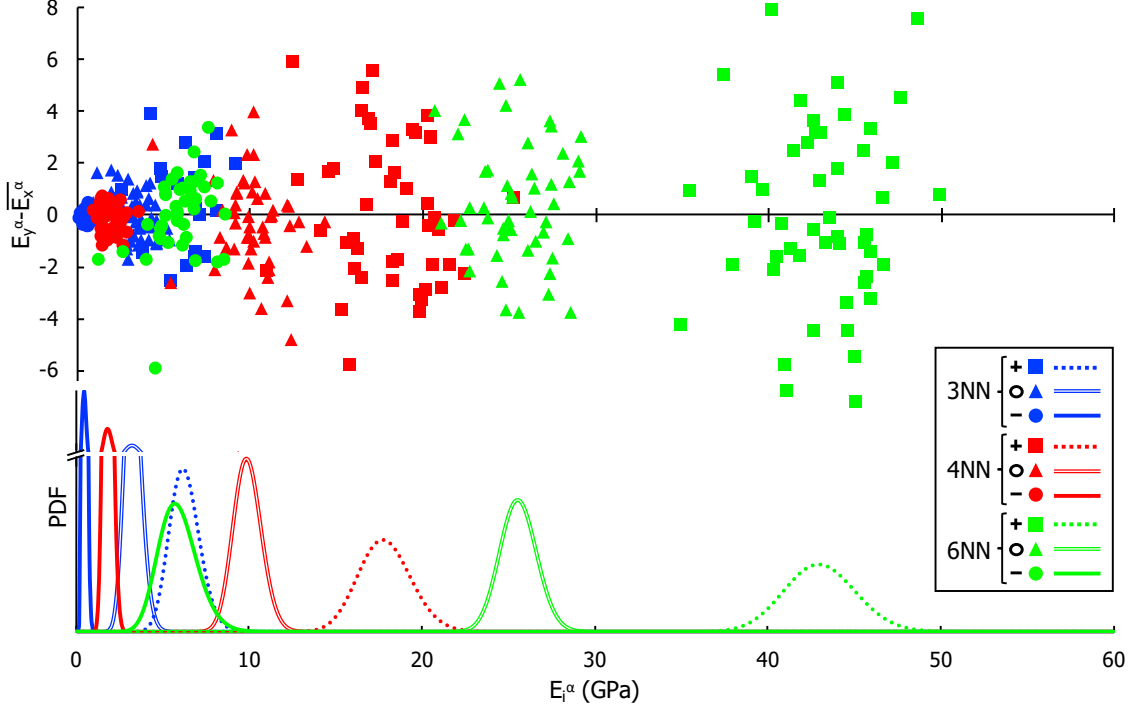


Figure 7.5: (top) Qualitative evidence that there is no correlation between  $E_x^\alpha$  and  $E_y^\alpha$  for individual prototype random network mRVEs,  $\alpha$ . The points located at  $(E_i^\alpha, E_y^\alpha - \overline{E_x^\alpha})$  appear randomly distributed about a central mean ( $\overline{E_x^\alpha}$ ). (bottom)  $E_i^\alpha$  for all mRVEs plotted as  $\Gamma$ -distributions, positioned directly below their respective point clouds. The break on the y-axis indicates that the first three distributions are significantly taller than the rest. Reproduced with permission from Ref. [236].

are expected for mRVEs with larger stiffnesses. A quantitative summary of data in Fig. 7.5 is given in Table 7.2, which lists the effective bulk mechanical properties computed for each mRVE set, including the effective bulk stiffnesses ( $E^*$ ), Poisson ratios ( $\nu^*$ ), and bulk moduli ( $K^*$ )—all computed according to Eq. 7.2. Also reported in Table 7.2 are statistical parameters for the sets of  $E_i^\alpha$  values, including the standard deviation of stiffness values ( $\sigma$ , which is the square root of the variance in  $E^*$ ), the shape and scale parameters for the  $\Gamma$ -distribution fits ( $a$  and  $b$ , respectively), and the correlation in  $E_i^\alpha$  values for each pair of orthogonal directions ( $R_{\{i,j\}}$  for  $i, j = x, y, z$ ; and  $y, z$ ).

Fig. 7.5 (top panel) qualitatively shows that there is no correlation between  $E_x^\alpha$  and  $E_y^\alpha$  values for individual mRVEs—that is, the points  $(E_x^\alpha, E_y^\alpha - \overline{E_x^\alpha})$  show no trend and appear randomly distributed about a mean value. This lack of correlation is quantitatively confirmed for all three direction pairs by computed correlation values below 0.5 for  $(E_x^\alpha, E_y^\alpha)$ ,  $(E_x^\alpha, E_z^\alpha)$ , and  $(E_y^\alpha, E_z^\alpha)$  (see Table 7.2). Therefore, the

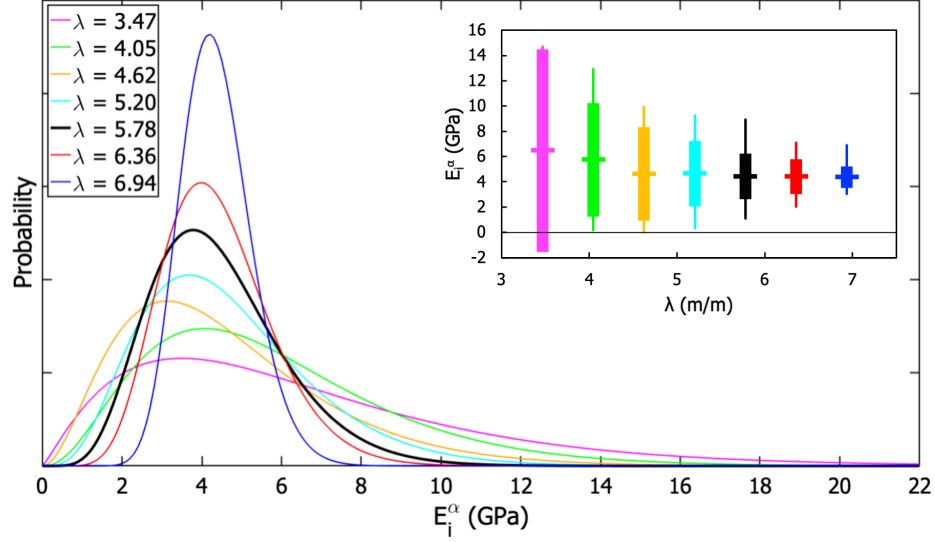
Table 7.2: Effective bulk mechanical properties ( $E^*$ ,  $\nu^*$ , and  $K^*$  in GPa) and their respective statistical distribution parameters for prototype random network mRVE sets. The quantities  $a$ ,  $b$ ,  $\sigma$ , and  $R$  correspond to the gamma shape parameter, gamma scale parameter, standard deviation, and correlation, respectively, for the prototype random network mRVE  $E^*$  results.

| mRVE set         | $E^*$ | $\nu^*$ | $K^*$ | $a$    | $b$  | $\sigma$ | $R_{\{X,Y\}}$ | $R_{\{X,Z\}}$ | $R_{\{Y,Z\}}$ |
|------------------|-------|---------|-------|--------|------|----------|---------------|---------------|---------------|
| 3NN <sup>+</sup> | 6.31  | 0.15    | 2.98  | 53.35  | 0.12 | 0.87     | 0.00          | -0.27         | -0.23         |
| 3NN <sup>0</sup> | 3.33  | 0.15    | 1.59  | 45.64  | 0.07 | 0.50     | 0.16          | 0.00          | -0.31         |
| 3NN <sup>-</sup> | 0.50  | 0.15    | 0.25  | 18.49  | 0.03 | 0.12     | -0.38         | 0.04          | -0.08         |
| 4NN <sup>+</sup> | 17.89 | 0.17    | 8.96  | 139.03 | 0.13 | 1.52     | -0.12         | 0.10          | -0.25         |
| 4NN <sup>0</sup> | 9.93  | 0.18    | 5.16  | 150.72 | 0.07 | 0.81     | -0.11         | -0.19         | -0.26         |
| 4NN <sup>-</sup> | 1.87  | 0.19    | 1.02  | 55.09  | 0.03 | 0.25     | -0.22         | 0.03          | -0.44         |
| 6NN <sup>+</sup> | 43.07 | 0.19    | 23.02 | 437.71 | 0.10 | 2.06     | 0.06          | 0.10          | -0.16         |
| 6NN <sup>0</sup> | 25.63 | 0.20    | 14.04 | 583.73 | 0.04 | 1.06     | 0.37          | 0.25          | 0.22          |
| 6NN <sup>-</sup> | 5.94  | 0.23    | 3.80  | 28.62  | 0.21 | 1.11     | -0.04         | -0.24         | -0.26         |

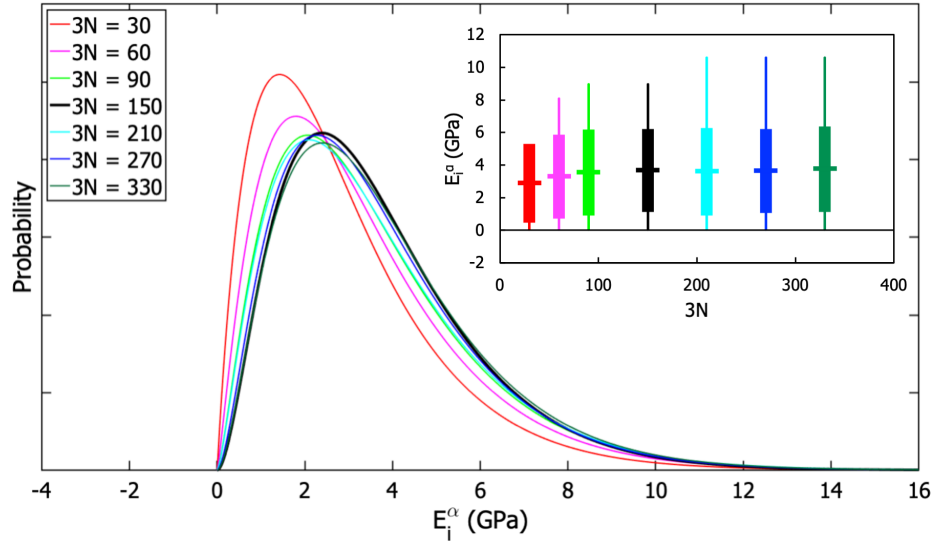
three  $E_i^\alpha$  values computed for each mRVE can be considered three distinct samples of mesoscale mechanical properties. The bottom panel of Fig. 7.5 shows that mean stiffness values and the ranges of stiffnesses within mRVE sets vary with structural parameters.

Fig. 7.6a shows  $\Gamma$ -distributions fit to computed  $E_i^\alpha$  values for sets of 3NN<sup>-</sup> mRVEs constructed in differently sized computational boxes. The size of the computational box is characterized by  $\lambda$ , the ratio of the length of the computational box to the average length of ligaments in the mRVEs. That the number density of nodes in each mRVE is fixed and ligaments connect nearest neighbor nodes implies that the average ligament length is conserved across the mRVEs studied here. Therefore, a larger  $\lambda$  corresponds to an mRVE that samples a larger effective volume of NP structure—and therefore contains more total nodes and ligaments. The inset to Fig. 7.6a shows the mean value of  $E_i^\alpha$  (that is, the effective bulk stiffness,  $E^*$ , indicated with hashes), the standard deviation of  $E_i^\alpha$  values ( $\pm\sigma$ , thick bars), and the absolute range of computed  $E_i^\alpha$  values (thin bars) as a function of  $\lambda$ . Given that there is no correlation between  $E_x^\alpha$ ,  $E_y^\alpha$ , and  $E_z^\alpha$  values, distributions in Fig. 7.6a are fit from the ensemble of all 3NN<sup>-</sup>  $E_i^\alpha$  values (i.e. the collective set of all  $E_x^\alpha$ ,  $E_y^\alpha$ , and  $E_z^\alpha$  values) for a given  $\lambda$ .

For  $\lambda$  below some critical  $\lambda_{min}$ , mRVEs are not large enough relative to the structural feature sizes (i.e. do not contain a large enough volume of the structure) to be representative of the bulk, and computed results will not be converged with respect to mRVE size. For very large  $\lambda$  beyond some  $\lambda_{bulk}$  all mRVEs will be in the macroscopic



(a)



(b)

Figure 7.6: **(a)**  $\Gamma$ -distributions of  $E_i^\alpha$  for the  $3NN^-$  mRVE set as a function of  $\lambda$ , a quantity corresponding to mRVE size with respect to structural feature size. **(b)**  $\Gamma$ -distributions of a set of structures generated according to the  $3NN^-$  parameters as a function of  $E_i^\alpha$ . Since three  $E_i^\alpha$  values are calculated for each mRVE, the quantity  $3N$  corresponds to a number  $N$  of mRVEs. Reproduced with permission from Ref. [236].

limit, and will yield the same singular values for all mechanical properties—though it is expected that such mRVEs would be too large to be computationally tractable. The inset of Fig. 7.6a shows that  $E^*$  converges at  $\lambda_{min} \approx 4.6$ , implying that this is the smallest mRVE size (relative to characteristic structural feature sizes) for which the generated mRVEs are representative of the bulk. For mRVEs with larger  $\lambda$  the

width of the distribution of  $E_i^\alpha$  values (as measured by either  $\sigma$  or the range of  $E_i^\alpha$  values) monotonically decreases, consistent with convergence to a singular bulk value in the macroscopic limit. The value of a  $\lambda_{bulk}$  will depend on the magnitude of variation in properties that can be considered trivial for a specific application, but can reasonably be taken to be much larger than  $\lambda = 7$  as  $\sigma/E^* \approx 0.084$  at this relative computational box size.

Regardless, both the value of  $\lambda_{min}$  and any  $\lambda_{bulk}$  (chosen for a particular maximum allowed variation in properties) are not only important computational parameters (indicating thresholds for computational convergence) but also physically relevant materials parameters specific to particular seed geometries that characterize limiting length scales for the use and application of NP materials. To ensure results converged with respect to mRVE size, computational boxes with  $\lambda = 5.78$  have been used throughout.

Fig. 7.6b shows  $\Gamma$ -distributions fit to computed  $E_i^\alpha$  values for sets of 3NN<sup>-</sup> mRVEs as a function of the number of mRVEs in each set ( $N$ ). For large enough sets of mRVEs from the same geometric seed ( $N > N_{min}$ ), the mean and distributions of computed properties should be insensitive to increasing  $N$ . In such cases, the distributions of properties among mRVEs will arise solely from the intrinsic and representative variability of the structures themselves, not from sampling error with respect to the number of mRVEs. As discussed above, this intrinsic variability will itself depend on the relative size (e.g.  $\lambda$ ) of the mRVEs in the set. Fig. 7.6b shows that  $N_{min} = 30$  mRVEs ( $3N_{min} = 90$   $E_i^\alpha$  values) for the present seed geometry, and to ensure results converged with respect to number of mRVEs, sets of  $N = 50$  mRVEs have been used throughout this section.

It is important to note that the designation of an mRVE as “orthotropic” or “isotropic” must stem from prior knowledge of the modeled material. For example, a material known to be transverse isotropic, like a fibrous mat, must not be evaluated with the four-calculation approach. In a transverse isotropic material, of the three  $E_{xx}$  values, two will be the same and distinct from the other. The isotropic approach would inappropriately average the three elastic constants and misrepresent the material. For an isotropic material, the isotropic approach and the orthotropic approach will yield very similar results. The results of the nine calculation orthotropic approach would simply yield a few redundant values. Fig. 7.7 illustrates this with a set of 35 isotropic, ligament-based mRVEs. An example mRVE is included in the top right of the plot. The group of red points represents the average  $E_{xx}$  of each mRVE using the isotropic approach (four calculations), and the blue points represent the average  $E_{xx}$  of each

mRVE using the orthotropic approach (nine calculations). The average difference between the two approaches is 4%. Since the central focus of the KRaSTk tool is the distribution, or variability of properties exhibited by materials with complex, random structures, this difference in methods is not considered significant.

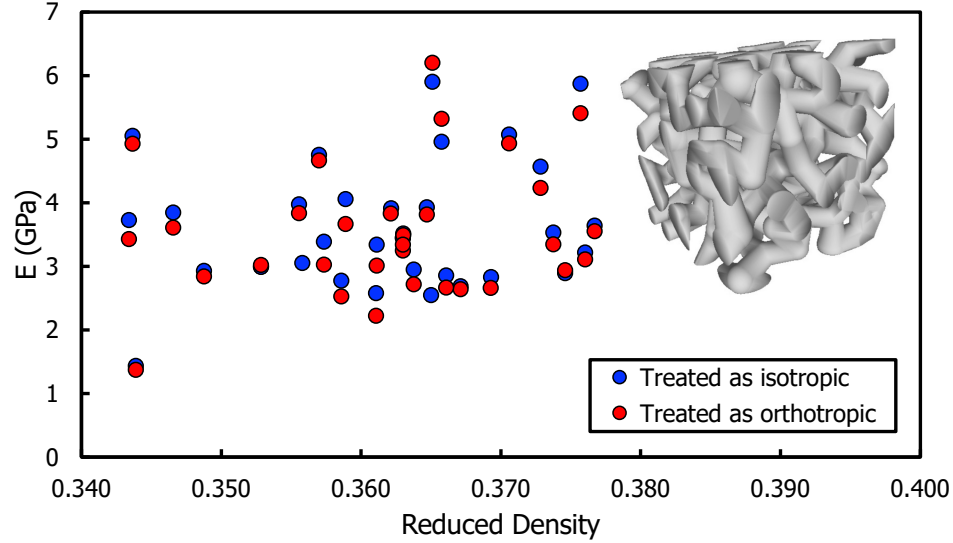
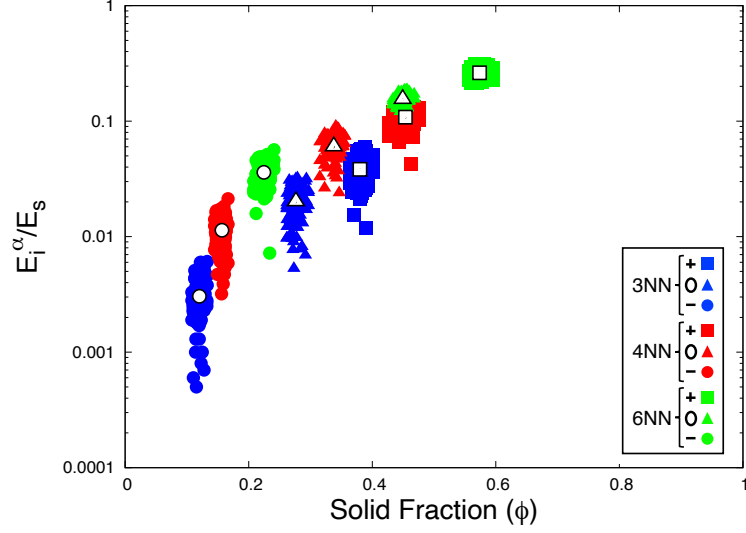


Figure 7.7: Comparison of  $E$  results for a set of mRVEs treated as isotropic and orthotropic.

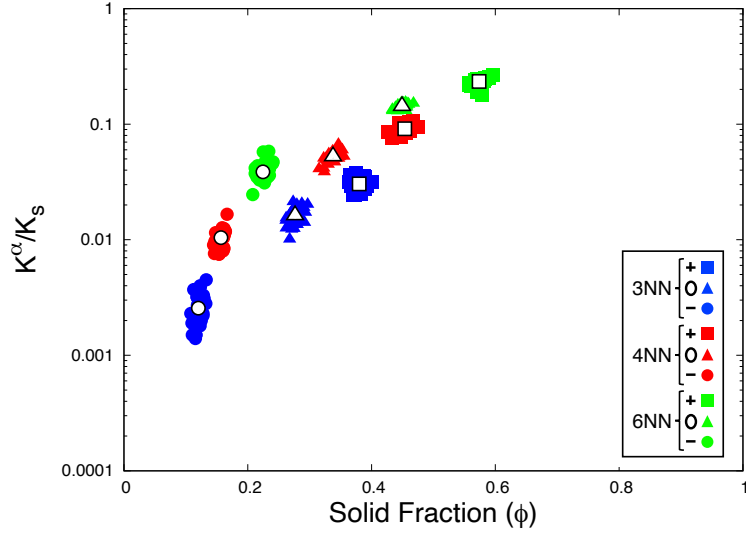
## 7.6 Properties of prototype NP geometry

### 7.6.1 Network connectivity dependence: Extending Gibson-Ashby

Figs. 7.8a and 7.8b plot computed  $E_i^\alpha$  and  $K^\alpha$  values for the nine converged sets of mRVEs ( $\lambda = 5.76$ ,  $N \approx 50$  for each) as a function of the reduced density of each structure ( $\phi^\alpha$ ). Results for 6NN, 4NN, and 3NN mRVE sets are shown with green, red, and blue points, and sets with +, 0, and − ligament thicknesses are shown with squares, triangles, and circles, respectively, for both elastic and bulk modulus.  $E^*$  and  $K^*$  (computed following Eq. 7.2) for each mRVE set are shown with white points, and are reported in Table 7.2. As can be seen, solid fraction alone is not predictive of either  $E^*$  or  $K^*$  when  $N_C$  is allowed to vary. In all cases an increase in  $N_C$  for a given ligament thickness—which, physically, would correspond to an increasingly constrained network structure—results in an increase in both  $E^*$  and  $K^*$  that cannot be explained by the associated increase in solid fraction alone. This is highlighted by, e.g., the 6NN<sup>−</sup> and 3NN<sup>0</sup> mRVE sets, where, despite the fact that the 3NN<sup>0</sup> mRVEs



(a)



(b)

Figure 7.8: **(a)** Effective elastic modulus values and **(b)** effective bulk modulus values for all prototype random network mRVEs. Reproduced with permission from Ref. [236].

exhibit higher solid fractions, the 6NN<sup>−</sup> mRVEs have both higher elastic and bulk moduli.

These results show that increasing connectivity in a porous network structure independently leads to increased stiffness, an effect that would only be captured in the material-specific prefactor  $C_E$  in the G-A model. Notably, for any particular value of  $N_C$ , quantitative fits to calculated  $E_i^\alpha$  values are in excellent agreement with the G-A model with, as expected, different prefactors for 3NN, 4NN, and 6NN

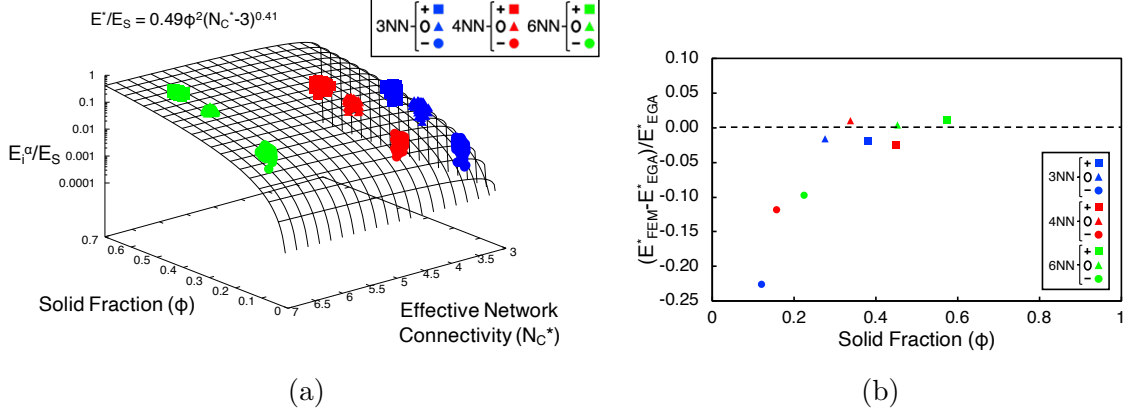


Figure 7.9: **(a)** The surface fit of all prototype random network mRVEs, allowing for future calculation of  $E^*/E_S$  as a function of  $\phi$  and  $N_C^*$ . **(b)** The difference between the  $E^*$  values generated via FEM and via the fit in Fig. 7.9a. Reproduced with permission from Ref. [236].

structures. In addition, Fig. 7.8b shows that bulk moduli values appear to follow a similar trend as elastic moduli, suggesting that they would also be well-modeled by a Gibson-Ashby-like expression. Based on these observations, an empirical extension to the G-A model is proposed that appends a power law factor for the effect of network connectivity and reduces to the original G-A expression (for elastic modulus) when connectivity does not vary. A similar expression for bulk modulus is also proposed, written:

$$\frac{E^*}{E_s} = C_E \phi^2 (N_C^* - 3)^{n_E} \quad (7.17)$$

$$\frac{K^*}{K_s} = C_K \phi^2 (N_C^* - 3)^{n_K} \quad (7.18)$$

The choice of  $(N_C^* - 3)$  for the connectivity term in this “extended Gibson-Ashby” (EGA) model reflects that while structures with  $N_C^*$  values below 3 can yield mechanically non-trivial 3D solids, nodes in such structures with less than three connected ligaments generally represent either the ends of “dangling” ligaments (which do not contribute to mechanical responses) or the junction between two ligaments that can be treated as a single, longer ligament. Therefore the minimum effective network connectivity in a solid is three.

Figs. 7.9a and 7.10a plot computed  $E_i^\alpha$  and  $K^\alpha$  from all nine random mRVE sets as functions of  $\phi^\alpha$  and  $N_C^{*,\alpha}$ , along with least-squares (surface) fits in the form of Eqs. 7.17 and 7.18. Fit parameters are found to be  $C_E = 0.49$ ,  $n_E = 0.41$  for elastic modulus, and  $C_K = 0.41$  and  $n_K = 0.47$  for bulk modulus. Figs. 7.9b and 7.10b show

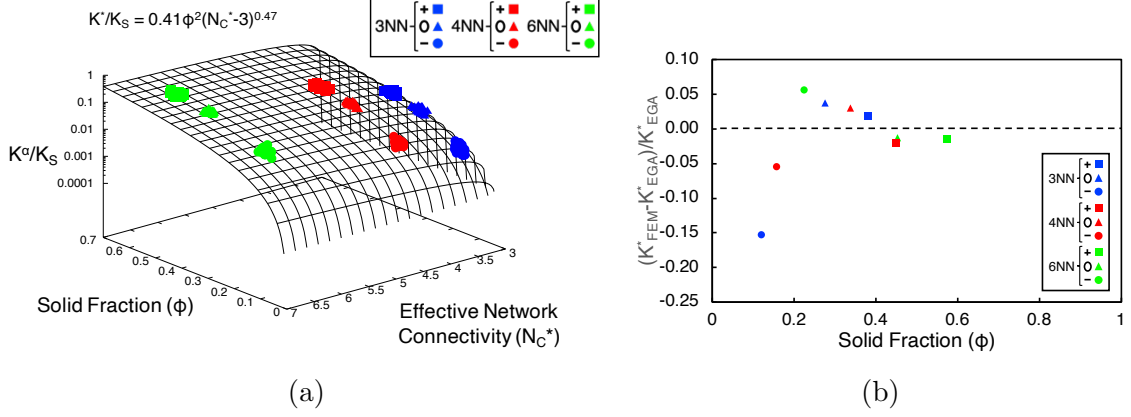


Figure 7.10: **(a)** The surface fit of all prototype random network mRVEs, allowing for future calculation of  $K^*/K_S$  as a function of  $\phi$  and  $N_C^*$ . **(b)** The difference between the  $K^*$  values generated via FEM and via the fit in Fig. 7.10a. Reproduced with permission from Ref. [236].

the normalized variance between FE-computed  $E^*$  and  $K^*$  values and EGA-predicted moduli for the average  $N_C^*$  and  $\phi$  of each mRVE set. Overall, the proposed empirical fit is excellent, with somewhat higher relative variance at solid fractions below  $\sim 0.2$ . It should be noted, however, that the absolute magnitude of  $E^*/E_S$  and  $K^*/K_S$  are quite small at these low solid fractions such that, with respect to the 3NN– set for example, observed variances of up to  $\sim 50\%$  between FEM computed and model-predicted  $E^*$  values represent absolute variances that are only  $\sim 0.1\%$  of the intrinsic fully-dense bulk stiffness.

### 7.6.2 Effect of short- and long-range disorder

Figs. 7.11a and 7.11b show computed  $E^*_{VRH}$  and  $K^*_{VRH}$  values as a function solid fraction for 4NN, 6NN, and 8NN regular structures, analogous to the white points in Figs. 7.8a and 7.8b, which show  $E^*$  results for random mRVEs. The red and green solid curves shown in Figs. 7.11a and 7.11b are the EGA model predictions (Eqs. 7.17 and 7.18) evaluated for  $N_C = 4$  and 6 using coefficients fit from random mRVE data (see above). The black solid curve is the prediction of the original G-A model (Eq. 7.1) (and an equivalent expression for bulk modulus) for prefactors with the value of 1.0. Voigt-Reuss-Hill (VRH)-homogenized  $E^*_{VRH}$  and  $K^*_{VRH}$  values are approximations of the bulk effective properties of a material with identical local structure (here, a regular mRVE) randomly oriented in a contiguous solid. Such structures would have no long-range order (similar to random mRVEs) but would possess short-range or local order (unlike random mRVEs) and might be envisioned as examples of network



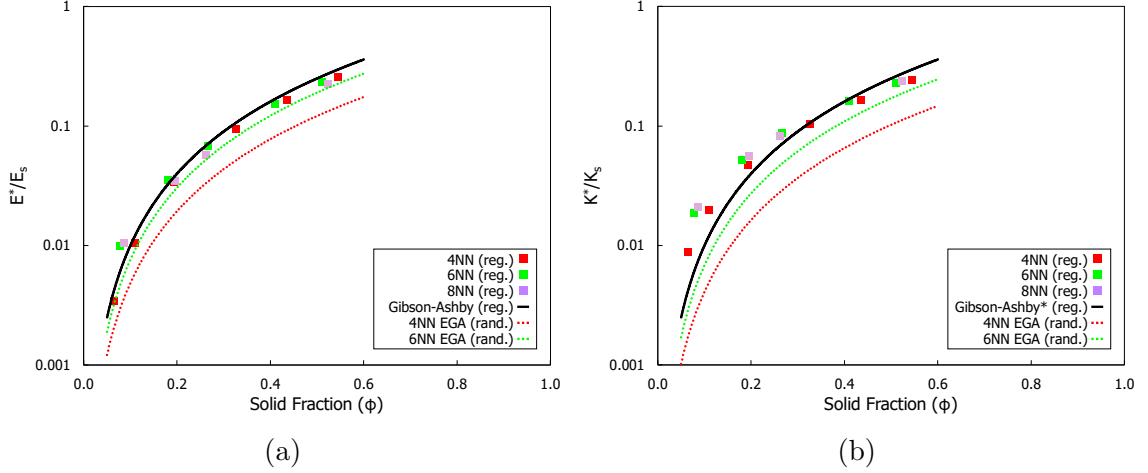


Figure 7.11: **(a)** Voigt-Reuss-Hill elastic modulus approximations for all regular mRVEs. **(b)** Bulk modulus approximations for the regular mRVEs. The 4NN-random and 6NN-random lines were obtained by fitting the relevant data points in Fig. 7.8a. Reproduced with permission from Ref. [236].

glasses.

While the VRH approach only approximates the behavior of an idealized material, Figs. 7.11a and 7.11b suggest that random network structures lacking both long- and short-range order (as represented by the EGA fits to random mRVE data shown in red and green curves) are less stiff than the VRH approximation predicts for network structures lacking only long-range order. This is likely a consequence of the fact that the overall stiffness of a network structure will be strongly influenced by the weakest (e.g. thinnest or least favorably oriented) ligaments in the structure. As regular structures have uniform local structure, no “weakest link” local ligament configurations exist to influence overall properties. Moreover, the effect of weak links in a network structure would be most pronounced in a poorly constrained network—that is, a structure with low connectivity.

It is also of note that  $E_{\text{VRH}}^*$  and  $K_{\text{VRH}}^*$  depend only weakly on network connectivity. This reinforces a “weakest link” analysis in that lower connectivity in (fully) random network structures (e.g. the random mRVEs considered here) would be expected to result in more uneven arrangements of ligaments—and therefore weaker weakest links—than higher connectivity structures. In randomly-oriented *regular* network structures (as represented here by the VRH approximation applied to regular mRVEs), the only (effective) variability in local stiffness would arise from geometric effects (that is, the relative orientation of the load direction) that only weakly depend on connectivity.

### 7.6.3 Transferability of EGA model

While this section has considered a specific seed geometry, many nanoporous materials can be reasonably approximated as collections of nodes connected by ligaments. It is therefore postulated that the form of the EGA model proposed above has wide applicability to a range of NP and general complex-structure materials. It is unclear based on present results alone the degree to which the empirically derived coefficient values extracted here are transferable among different materials with node and ligament structures. The prefactors  $C_E$  and  $C_K$  remain materials-specific parameters that encapsulate details of both (i) the intrinsic material from which the NP structure is formed, and (ii) other details of ligament and network structure. Efforts applying KRaSTk to isolate the magnitude and details of both of these types of effects are underway.

In considering the exponents  $n_E$  and  $n_K$ , which characterize the sensitivity of bulk effective properties to changes in connectivity (with  $n_E$  or  $n_K$  equal to zero indicating no sensitivity) two observations from the present results emerge: that short-range disorder dramatically enhances the effect of connectivity on elastic response (see e.g. Figs. 7.11a and 7.11b), and that bulk modulus (in addition to elastic modulus) varies with connectivity. As noted above, the first point shows that elastic behavior is strongly influenced by differences in local structure (i.e. short-range disorder) that result in weaker regions in a material. The second point, that the elastic response to hydrostatic loading is affected by connectivity, highlights a related finding that in random ligamented structures elastic responses along different directions *of the same volume* are not only inequivalent, but uncorrelated. Both of these observations link the degree of variability in local structure, and therefore local mechanical responses, to the sensitivity of effective bulk properties to network connectivity, and therefore  $n_E$  and  $n_K$  are expected to increase from zero with increasing structural variability (e.g. in ligament thickness, range of effective network connectivities, or increasing inhomogeneity in node distributions in space).

## 7.7 Summary

Using the Kentucky Random Structures Toolkit (KRaSTk), sets of random- and regular-structured model representative volume elements (mRVEs) constructed from a geometric seed description consisting of conical frustum ligaments connecting nearest neighbor spherical nodes have been generated and their mechanical properties computed. Elastic and bulk moduli derived from FE-computed strain energies were

determined for sets of mRVEs with ranges of network connectivities and ligament aspect ratios. Properties of individual randomly-structured mRVEs are taken to be mesoscale samples of the properties of a bulk NP material for mRVEs beyond a minimum size relative to the characteristic size of structural features in the mRVEs. Averages of computed properties over sufficient numbers of mRVEs are therefore measures of expected effective bulk properties. Averages and distributions of computed properties for sets of random mRVEs converged towards a singular bulk value for mRVEs with larger volumes, and were self-similar for sets of  $\sim 30$  or more mRVEs.

Computed elastic properties of random mRVEs illustrate that there is a separable and independent effect of network connectivity on elastic and bulk moduli. Increasingly constrained network structures are stiffer than less constrained structures with the same reduced density. This effect can be captured in an extension to the Gibson-Ashby model of open-foam mechanical properties with the addition of a connectivity-dependent factor, and this extended G-A (EGA) model is found to apply to both elastic and bulk modulus:

$$\begin{aligned}\frac{E^*}{E_s} &= 0.49\phi^2(N_C^* - 3)^{0.41} \\ \frac{K^*}{K_s} &= 0.41\phi^2(N_C^* - 3)^{0.47}\end{aligned}$$

The value of the exponents in the connectivity term are expected to be universal in that they do not depend on the specific bulk material from which the NP structure is formed, but will vary based on the degree of feature-scale disorder present in the NP material—falling to zero (no effect of connectivity) for materials constructed of identical feature-scale structural units. The prefactor values remain material specific and further work is ongoing to reveal additional specific factors that significantly influence these parameters.

Overall, the present results demonstrate a robust method for generating and computing properties of large sets of mRVEs based on a physically motivated geometric seed description of complex or randomly-structured materials. The present approach can be applied to any material that can be described as combinations of geometric primitives, and can be adapted to probe any properties of materials for which FE-based continuum methods are available. While the capabilities of KRaSTk have been demonstrated here for a porous 3D network structure, other potentially impactful applications include, to name a few, the exploration of structure–property relationships in additive materials (e.g. powder sintering-based 3D printed materials),

membrane materials, or nanocrystalline/polycrystalline alloys—all of which exhibit complex and/or random feature-scale structures. In the next chapter, KRaSTk is applied to yet another material and application: metallic foams for micrometeoroid and orbital debris shielding.

## Chapter 8: Stochastic mesoscale mechanical modeling of Duocel

### 8.1 Motivation

Micrometeoroid and orbital debris (MMOD) pose a significant danger to both robotic and crewed spacecraft operating beyond Earth's atmosphere [238, 239, 240, 241, 242, 243]. Despite minuscule size (typically on the order of  $\mu\text{m}$  to  $\text{mm}$ ), particles orbiting Earth at 10-12 km/s have tremendous impact velocities and can cause catastrophic damage [238], as shown in Fig. 8.1. The International Space Station alone has been subjected to hundreds of strikes, including damage to solar arrays, handrails, radiators, and windows. Fortunately, no major failures have resulted from these impacts, such as breach of pressure integrity of the crew modules. However, some of these damages have resulted in noticeable effects to ISS systems and operations, such as power degradation due to damage to solar arrays, cut-gloves from craters on EVA handrails, and an unplanned EVA to stabilize tears in a solar array from a snagged guidewire caused by damage from MMOD.

Albeit with substantial cost and risk, the damage caused by larger objects is generally mitigated by avoidance maneuvers. Currently, about 21,000 objects at least 10 cm in diameter or larger are being tracked by the US Space Surveillance Network (including about 800 objects representing functional satellites) [246]. Only the largest pieces of debris in orbit can be tracked, mainly by using optical sensors. The minimum size of objects that are regularly tracked are 30 cm and 10 cm in geosynchronous orbit and low Earth orbits, respectively. Among the tracked pieces of debris, there are about 200 satellites abandoned in geosynchronous orbits occupying or drifting through

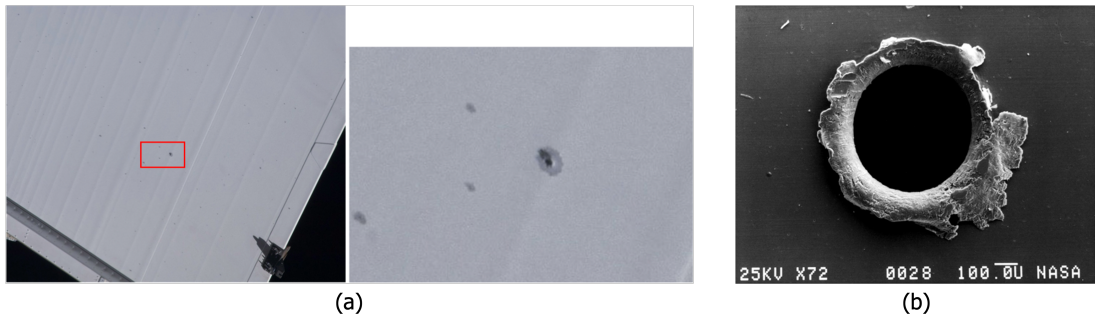


Figure 8.1: Examples of MMOD impacts: **(a)** Surface of an ISS radiator panel [244] and **(b)** MMOD impact on satellite component retrieved during the STS-41C Solar Max repair mission [245].

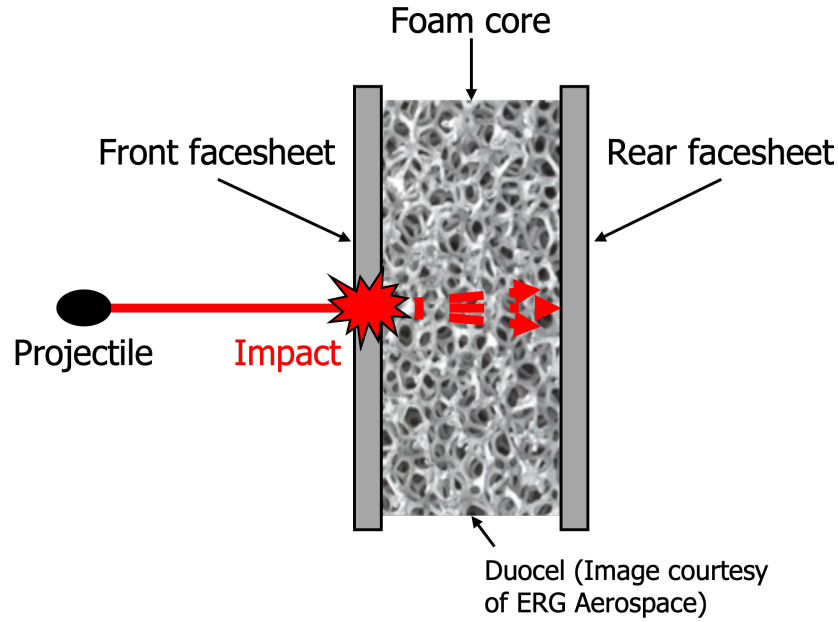


Figure 8.2: A diagram of a projectile striking an open cell metallic foam sandwich panel.

valuable orbital positions and posing a collision hazard for functional spacecraft. However, protection from smaller debris is prohibitively difficult to address in this way, and therefore remains a challenging and increasingly important problem.

Open cell metallic foam sandwich panel structures have proven effective at mitigating damage from MMOD strikes [240, 241, 242]. Commercially available metallic foams sandwiched between solid metallic facesheets are widely used for MMOD shielding on a range of spacecraft. The foam core layer is composed of open, node-ligament networks of randomly oriented polycrystalline metallic ligaments. Ligament lengths and pore sizes vary over some distribution characteristic of the specific material, but typically have lengths on the order of microns. Impacting particles penetrate the outer sacrificial facesheet of the sandwich structure and suffer repeated impacts with ligaments in the foam—deflecting, fragmenting, and vaporizing in the process. Any residual impactor fragments arriving at the back facesheet have sufficiently reduced kinetic energy that they can be stopped by a thinner (and therefore less massive) solid sheet than would be required absent the energy dissipating foam layer. Fig. 8.2 illustrates this operating mechanism.

Operating under powerful imperatives to minimize weight and volume while robustly assuring mission success (within externally determined parameters), component and spacecraft designers require accurate knowledge of Al foam properties and

responses to MMOD strikes. This is complicated by the potentially small sizes of impacting MMODs and the intrinsically random nature of foam-based shielding materials, which exhibit different materials responses depending on the length-scale of the particle/foam interactions. For impacts affecting volumes at size scales similar to that of individual ligaments and/or pores—the “feature” length scale, on the order of microns for many metallic foams—foam properties and responses to MMOD strikes are not characteristic of the bulk foam material, but rather of individual structural features (e.g., pores, ligaments, ligament junctions, etc.) within the structure. At length scales much greater than those of individual pores and ligaments—that is, on the macroscale—uniform, singular bulk properties characteristic of the foam material can be observed and represent the homogenized, or “effective”, response of all structural features (ligaments and pores). Between these length scales—on the mesoscale—material responses become characteristic of the foam material, but are not singular or uniform, instead varying within characteristic distributions depending on the detailed arrangement of features in the affected volume. Recall that in §7.2, it was noted that the terms “mesostructure” or “mesoscale” in these continuum scale chapters do not necessarily refer to features on a particular length scale, but rather the length scale at which an ensemble of features, rather than individual features, determine behavior.

In order to make appropriate design decisions—particularly ones that minimize mass and volume—spacecraft designers require quantitative knowledge of (i) expected bulk materials properties, (ii) distributions of local properties characteristic of the material at the mesoscale, and (iii) the physical lengths which bound the feature-scale, mesoscale, and macroscale. In particular, it is critical to know the length scale above which behavior representative of the bulk material will be observed—that is, the transition length from the feature-scale to mesoscale ( $\lambda_{f \rightarrow m}$ )—as this sets a hard minimum feature size for spacecraft components fabricated from the material. This need for quantitative knowledge of materials properties and responses has led to high demand for accurate, physics-based computational models allowing rapid materials selection (among, e.g., foams with different ligament and pore sizes) and computational prototyping of component performance. To meet these needs, models for the material responses of complex and/or randomly structured materials must necessarily account for the intrinsic inhomogeneity of the bulk material and allow efficient sampling of the materials structure at a range of length scales. The following sections investigate the material response of both defect-free and defected metal foam structures.

## 8.2 Defect-free structures

This section on defect-free structures largely focuses on size effects. KRaSTk was used to compute the properties of many mRVEs at various sizes relative to the key structural features of the seed description, which allowed for determination of bulk effective properties, distributions of mesoscale properties, and the size at which the material’s behavior will transition from feature-scale to mesoscale. The computed properties were then validated by a comparison to independently obtained experimental results for a commercially available Al foam, Duocel, manufactured by ERG Aerospace [247].

### 8.2.1 mRVE generation

The Kentucky Random Structures Toolkit (KRaSTk) was used to generate sets of 200 model representative volume elements (mRVEs) to characterize Duocel foams. For each set, the structural (generation) parameters are shown in Table 8.1. Each set is named according to its class and  $\lambda$ . In this section, classes were distinguished based on reduced density (low, medium, and high). As described in Chapter 7, the quantity  $\lambda$  is defined as the ratio of mRVE side length,  $s$  to characteristic length,  $\ell$ , which is the average length of every ligament in the set. An example set name is L/5.1, which indicates that the set is composed of low density mRVEs with a  $\lambda$  of 5.1. Within each class, an increasing  $\lambda$  is equivalent to a larger sample volume. For example, mRVEs in the L/5.1 are a third of the size as mRVEs in the L/7.3 set (in terms of total volume, not reduced density or solid fraction). A few quantities presented in Table 8.1 are not necessarily independent. For example, the aspect ratio ( $AR$ ) is simply the ratio of characteristic length to node diameter:  $AR = \ell/2r$ . Because each set within a class has the same nodal density (spheres/volume), the characteristic length and aspect ratio remains constant. In contrast to the structures highlighted in the previous chapter, the radii of all nodes in every set regardless of class is identical. The change in reduced density between each class stems entirely from the number of nodes, rather than the size. A set of mRVEs representing each set is shown in Fig. 8.3. Each mRVE is a single example of the 200 built for each set. It is crucial to note that equivalent  $\lambda$ s do not correspond to the same  $s$  values when comparing across classes.



Table 8.1: Structural parameters for each class of mRVEs examined in this section.

| mRVE set | $N_C$ | $r$ | $N_{sph}$ | $s$ | $d_{sep}$ | $\ell$ | $AR$ | $\lambda$ |
|----------|-------|-----|-----------|-----|-----------|--------|------|-----------|
| L/5.1    | 3     | 3.0 | 66        | 100 | 3.0       | 19.4   | 3.23 | 5.1       |
| L/7.4    | 3     | 3.0 | 132       | 144 | 3.0       | 19.4   | 3.23 | 7.4       |
| L/8.8    | 3     | 3.0 | 198       | 171 | 3.0       | 19.4   | 3.23 | 8.8       |
| L/9.4    | 3     | 3.0 | 330       | 182 | 3.0       | 19.4   | 3.23 | 9.4       |
| L/10.3   | 3     | 3.0 | 528       | 200 | 3.0       | 19.4   | 3.23 | 10.3      |
| L/11.1   | 3     | 3.0 | 660       | 215 | 3.0       | 19.4   | 3.23 | 11.1      |
| M/6.8    | 3     | 3.0 | 165       | 100 | 3.0       | 14.8   | 2.47 | 6.8       |
| M/9.7    | 3     | 3.0 | 495       | 144 | 3.0       | 14.8   | 2.47 | 9.7       |
| M/11.6   | 3     | 3.0 | 825       | 171 | 3.0       | 14.8   | 2.47 | 11.6      |
| M/12.3   | 3     | 3.0 | 990       | 182 | 3.0       | 14.8   | 2.47 | 12.3      |
| H/7.7    | 3     | 3.0 | 275       | 100 | 3.0       | 13.0   | 2.16 | 7.7       |
| H/11.1   | 3     | 3.0 | 825       | 144 | 3.0       | 13.0   | 2.16 | 11.1      |
| H/12.3   | 3     | 3.0 | 1100      | 159 | 3.0       | 13.0   | 2.16 | 12.3      |
| H/13.2   | 3     | 3.0 | 1375      | 171 | 3.0       | 13.0   | 2.16 | 13.2      |

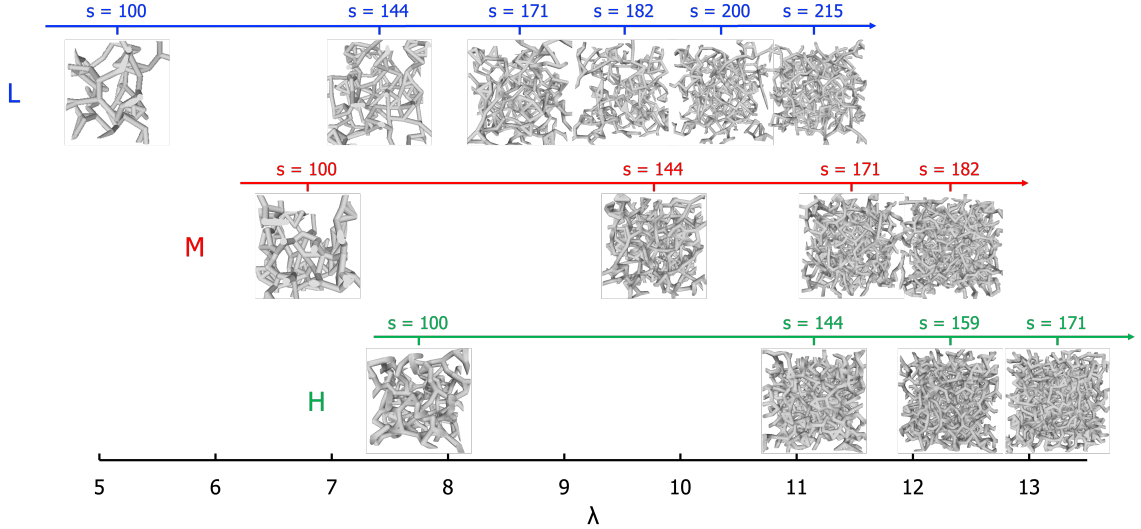


Figure 8.3: A “map” of each set of structures utilized in this section of defect-free mRVEs. Each image is a single example of the hundreds of mRVEs in each set.

### 8.2.2 Computational details

The elastic constants of each mRVE was computed via the method described in §7.3.2 for orthotropic mRVEs. Although these structures were hypothesized to be isotropic and, therefore, the method in §7.3.1 would be appropriate, the calculations in the next section focus precisely on defect-induced directional properties of these same sets of mRVEs. As such, the decision was made to use the same method (orthotropic) and

allow for easier comparison.

Due its ubiquity, there are innumerable software packages available to solve PDEs using FEM. In essence, they are extremely similar, with only the front ends varying significantly to cater to the needs of the user base. The elastic constants presented in this chapter were computed with **FEniCSx**. **FEniCSx** is a collection of free and open-source software components working together to enable the automated solution of differential equations. The components provide scientific computing tools for working with computational meshes, finite-element variational formulations of ordinary and partial differential equations, and numerical linear algebra [248]. Although the calculations in Chapter 7 were conducted with **ANSYS Workbench**, it was discovered that **FEniCSx** was inherently more powerful and flexible, and subsequent studies, including those in this chapter, utilized it as the FEM solver. A Krylov solver incorporating the generalized minimal residual method and a successive over-relaxation pre-conditioner. The absolute tolerance was set to  $1 \times 10^{-7}$  and the relative tolerance to  $1 \times 10^{-5}$ . Geometries were meshed utilizing **mshr**, the mesh generation component of **FEniCSx**. **Mshr** builds simplicial **DOLFIN** meshes in 3D, utilizing **CGAL** and **Tetgen** as mesh generation backends. For each structure, a tetrahedral mesh with a resolution of 150.0 was generated. The resolution quantity is defined as the inverse of the cell size  $h$ , the longest edge in any mesh element. Solid fractions were computed as the assembled mesh volume. For each calculation, displacements were assigned such that 0.5% strains were applied. The material within each ligament was isotropic, with  $E = 69$  GPa,  $\nu = 0.33$ , similar to commonly reported values for polycrystalline Al metal. The  $\Gamma$ -distributions, along with each distribution’s respective shape ( $a$ ) and scale ( $b$ ) parameter, were computed in **MATLAB** using its **GammaDistribution** object in the Statistics and Machine Learning Toolbox. Expectation values (means) for  $\Gamma$ -distributions of  $E$  values were computed as  $\mu_E = a * b$ , and standard deviations of  $E$  values within mRVE sets as  $\sigma_E = (a * b^2)^{1/2}$ . It is imperative to note here that, while mechanical properties are the focus of this chapter, the symbol  $\sigma$  is exclusively used to denote standard deviation—**never** stress. The range  $[\pm\sigma_E]$  was deemed the “standard variability” of the material. As discussed previously, for mRVEs at very large  $\lambda$  values, the standard variability (that is, the intrinsic variability in the observed properties of the material) will fall to zero, representing the transition to the macroscale, the length scale at which the material exhibits singular bulk properties.

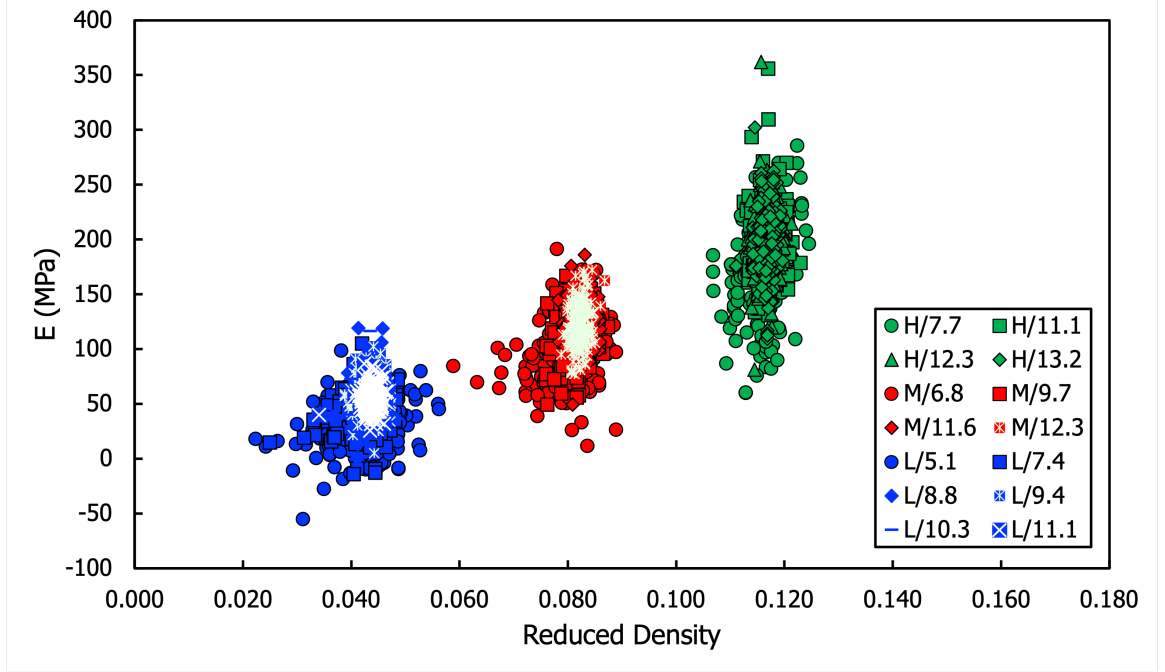


Figure 8.4:  $E$  results for each mRVE set for each class.

### 8.2.3 Feature-scale to mesoscale transition

The three elastic moduli— $E_1$ ,  $E_2$ , and  $E_3$ —computed for each mRVE in each set is shown in Fig. 8.4. Generally, each set of points obscures several others, and it is not possible to differentiate individual sets, let alone observe trends and draw conclusions. Still, one observable feature of this plot is the presence of negative  $E$  results for the L/5.1 set. Since a negative stiffness is nonphysical, one can assert that for a low density foam with a  $\lambda$  of 5.1, too little of the characteristic structural features are present to be mechanically stable.

To visualize the  $E$  results in a way that is far more useful and descriptive, they were replotted as  $\Gamma$ -distributions. Compared to other distributions,  $\Gamma$  was selected because these probability distribution functions (PDFs) are positive-definite and converge to normal distributions. The plots of  $\Gamma$ -distributions in this dissertation never include a y-axis because the focus is on comparing distributions of multiple sets spanning multiple classes. The total area of any PDF, and subsequently each  $\Gamma$ -distribution, is always equal to 1.

Fig. 8.5 shows only the high density mRVEs (sets H/7.7, H/11.1, H/12.3, and H/13.2) in the form of  $\Gamma$ -distributions, with the point clouds of computed values shown in the inset. From this juxtaposition of identical data sets, Fig. 8.5 highlights both how  $\Gamma$ -distributions show the convergence of property distributions with

Table 8.2: The  $\Gamma$ -distribution parameters,  $a$  and  $b$ , and corresponding statistical quantities,  $\mu_E$  and  $\sigma_E$ , for each **L**, **M**, and **H** mRVE set.

| Set    | $\Gamma$ Parameters |       | Statistics |            |
|--------|---------------------|-------|------------|------------|
|        | $a$                 | $b$   | $\mu_E$    | $\sigma_E$ |
| L/5.1  | 2.41                | 13.87 | 33.36      | 21.51      |
| L/7.4  | 6.66                | 6.81  | 45.35      | 17.57      |
| L/8.8  | 8.35                | 6.48  | 54.04      | 18.71      |
| L/9.4  | 13.31               | 4.24  | 56.41      | 15.47      |
| L/10.3 | 26.03               | 2.09  | 54.40      | 10.66      |
| L/11.1 | 25.15               | 2.17  | 54.68      | 10.90      |
| M/6.8  | 10.65               | 9.04  | 96.32      | 29.51      |
| M/9.7  | 22.39               | 5.08  | 113.83     | 24.06      |
| M/11.6 | 41.00               | 3.01  | 123.37     | 19.27      |
| M/12.3 | 38.18               | 3.21  | 122.42     | 19.81      |
| H/7.7  | 16.16               | 10.68 | 172.58     | 42.94      |
| H/11.1 | 49.40               | 3.96  | 195.82     | 27.86      |
| H/12.3 | 50.59               | 3.88  | 196.29     | 27.60      |
| H/13.2 | 48.75               | 4.01  | 195.49     | 28.00      |

increasing  $\lambda$  and how inadequately scatter plots convey the same result. Beginning with H/11.1, both  $\mu_E$  and  $[\pm\sigma_E]$  were identical as the size ( $s$ , and therefore  $\lambda$ ) of the mRVEs increases. Table 8.4 highlights the change, with both  $\mu_E$  and  $[\pm\sigma_E]$  differing for  $\lambda = 7.7$ , but converged for all other cases. This convergence indicates the transition from the feature-scale to the mesoscale and sets a range on the value of  $\lambda_{f \rightarrow m}$  for high density structures:  $7.7 < \lambda_{f \rightarrow m} \leq 11.1$ . At much higher  $\lambda$  values (much larger computational boxes compared to ligament lengths)  $[\pm\sigma_E]$  will approach zero, while  $\mu_E$  will remain fixed, representing the transition from mesoscale to bulk behavior.

The same procedure was followed to determine  $\lambda_{f \rightarrow m}$  for the low and medium density mRVE sets. For medium density structures,  $\mu_E$  and  $[\pm\sigma_E]$  converge as  $\lambda$  approaches 11.6, indicating that  $9.7 < \lambda_{f \rightarrow m} \leq 11.6$  in this case. The results for the low density mRVE sets differ in that there is a differentiation between the convergence of the expectation value,  $\mu_E$  and standard variability ( $[\pm\sigma_E]$ ) as  $\lambda$  increases. Beginning with L/9.4 and persisting through L/10.3 and L/11.1,  $\mu_E$  is around 55 MPa (see

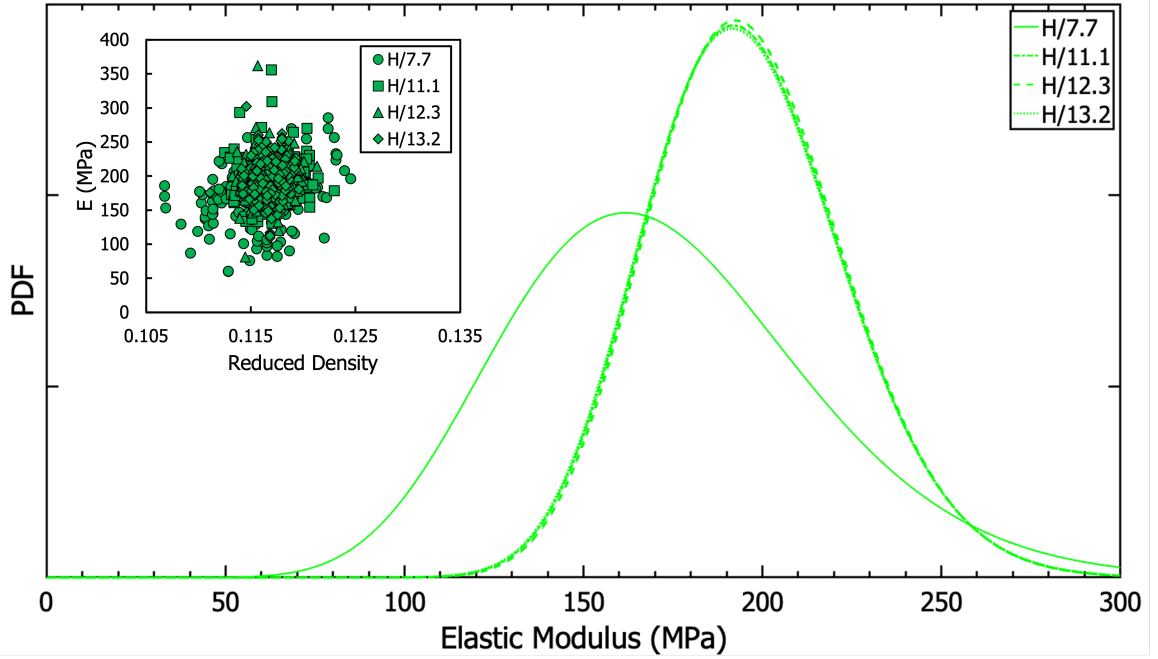


Figure 8.5:  $E$  results for the high density sets, plotted as both scatter and  $\Gamma$ -distributions. The  $\Gamma$  parameters and statistical quantities are found in Table 8.4.

Table 8.4). However, it is not until  $L/10.3$  that a consistent  $[\pm\sigma_E]$  emerges. Further calculations on additional mRVE sets within the M and H classes are required to determine if this phenomenon appears at all densities. It remains that the L results are excellent evidence that variability and averages are two entirely different variables that must both be considered. These results highlights that accurately resolving the variability intrinsic to a material with complex structure (at a particular  $\lambda$ ) requires larger (relative to the feature sizes) volumes than resolving the expectation value of the property.

Based on the results presented in Fig. 8.6 and Table 8.4, the  $\lambda$ s at which all classes (densities) of mRVEs converge can be found. Fig. 8.7 indicates the  $\lambda$  values for all sets and aggregates the ranges established for  $\lambda_{f \rightarrow m}$ . It is immediately clear that computed ranges for  $\lambda_{f \rightarrow m}$  overlap—in the range  $9.7 \leq \lambda_{f \rightarrow m} \leq 10.3$ . This makes physical sense, in that the volume of a complex material *relative to structural feature sizes* required for the material to exhibit characteristic properties should be consistent for similar geometric seed descriptions. Moreover, this result offers further support to the key hypotheses underlying the KRaSTk approach more generally—namely that aggregated properties of many mRVEs characterize the expected behavior of real materials, including both the mean (or expected) materials properties and the intrinsic variability of those properties as a function of size. Extending this logic,

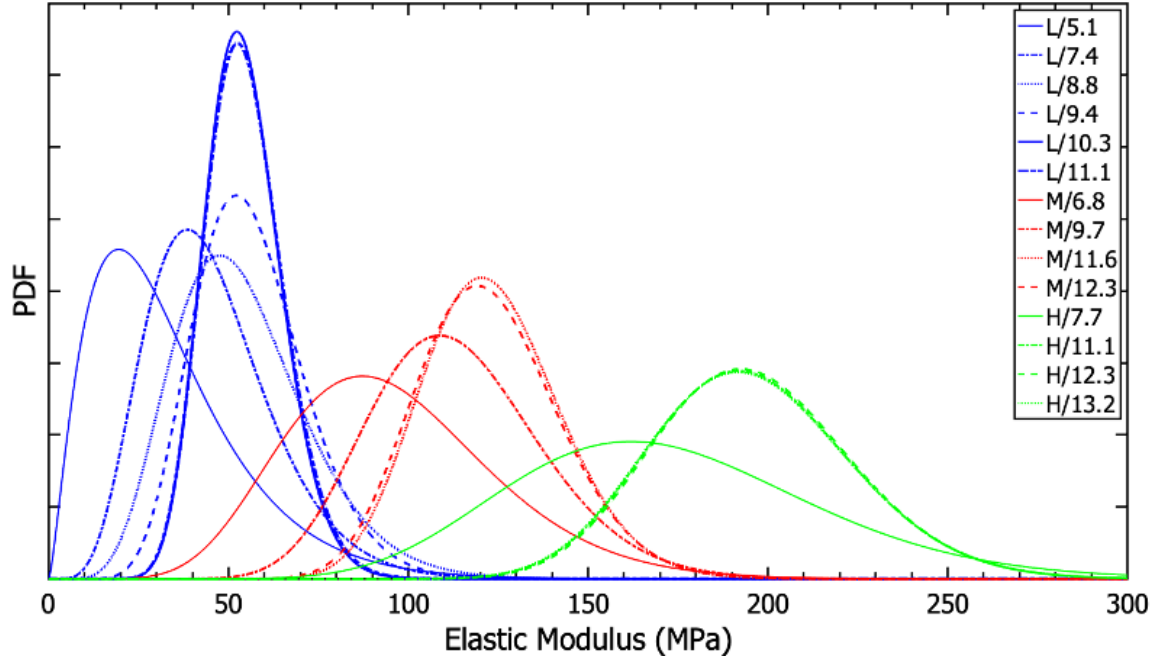


Figure 8.6:  $E$  results for each mRVE set, plotted as  $\Gamma$ -distributions. The  $\Gamma$  parameters and statistical quantities are found in Table 8.4.

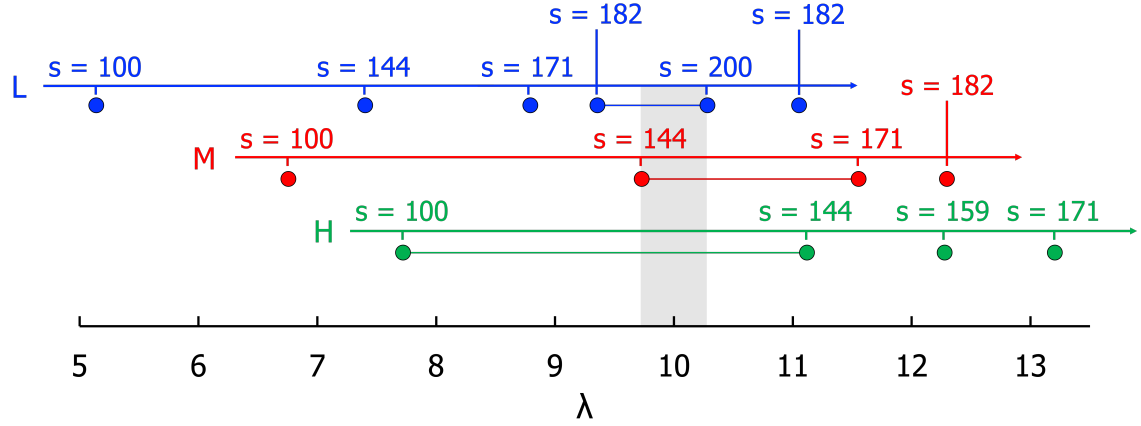


Figure 8.7: The quantity  $\lambda$  is plotted for each mRVE set. Within each class of mRVEs, the range of  $\lambda$  where  $\mu_E$  and  $\sigma_E$  converge below 2% is highlighted with a colored line segment. The black shaded region indicates the range of  $\lambda$ s where the converged windows of each class overlap.

$\lambda_{f \rightarrow m}$  values computed for mRVEs with  $N_C = 3$ , as shown here, should be a ceiling for  $\lambda_{f \rightarrow m}$  in structures with larger  $N_C$ —which necessarily have more geometric features (e.g. ligaments) per unit volume.

While further calculations on mRVE sets with additional  $\lambda$  values would be required to refine the precise value of  $\lambda_{f \rightarrow m}$  for this metallic foam seed geometry, the present results show that  $9.7 \leq \lambda_{f \rightarrow m} \leq 10.3$ . Given that  $\lambda = s/\ell$ , the mRVE side lengths for the feature-to-mesoscale transition occur at:

$$\text{L} : 188.2 \leq s_{f \rightarrow m} \leq 199.8 \quad (8.1)$$

$$\text{M} : 143.6 \leq s_{f \rightarrow m} \leq 152.4 \quad (8.2)$$

$$\text{H} : 126.1 \leq s_{f \rightarrow m} \leq 133.9 \quad (8.3)$$

These values are in arbitrary units such that all ligaments have diameters of 6 units. As can be observed, it is expected that as the density of the material increases the physical volume required to enter the mesoscale decreases, consistent with the qualitative analysis that denser materials have more structural elements per volume, and therefore homogenize at lower volumes.

#### 8.2.4 Stochastic model predictions of Duocel properties

Computed  $\mu_E$  and  $\sigma_E$  values are intended to be directly analogous to measured properties of metallic foams with structures well modeled by the geometric seed employed here—an assertion that can be directly tested by comparing computed properties to those measured for physical foam samples. Here, a commercially available Al metallic foam, Duocel [247], is considered.

Fig. 8.8 plots properties (for both  $N_C = 3$  and  $N_C = 4$  mRVEs) computed in this work along with properties of Duocel samples as measured experimentally by the foam manufacturer, ERG Aerospace [247], according to ISO 13314:2011. Computed properties reported in Fig. 8.8 are for mRVE sets with  $\lambda$  values at or just above the  $\lambda_{f \rightarrow m}$  range discussed above—that is, applicable to equivalent physical samples with sizes on the order of 20-30 $\times$  typical ligament diameters. Analytic predictions of both the Gibson-Ashby model[225, 226] the Extended Gibson-Ashby expression derived in Ref. [236] are also shown.

In Fig. 8.8 red markers indicate  $\mu_E$  values and whiskers indicate the standard variability ( $[\pm\sigma_E]$ ). The inset shows only results obtained from the series of calculations presented in this chapter (red points) and analytic model curves for open-cell foams

based on the Extended Gibson-Ashby equation presented in Ref. [236]:

$$\frac{E^*}{E_s} = 0.49\phi^2(N_C^* - 3)^{0.41} \quad (8.4)$$

The EGA model was developed to extend the longstanding Gibson-Ashby model for the mechanical properties of porous materials by accounting for the connectivity of node-ligament network structures. Careful consideration of Fig. 8.8 reveals that computed elastic properties for mRVEs with  $N_C = 4$  match experimental results both in terms of elastic modulus values [247], but also in terms of the apparent variability of elastic properties among samples. For samples having a reduced density ( $\phi$ ) of  $\approx 0.10$ , the scatter or variation in measured properties as reported by ERG is about  $\pm 39$  MPa. At a similar  $\phi$ , the KRaSTk-computed standard variability is  $\pm 45$  MPa. Similar agreement is observed throughout the considered range of reduced density values. Independent evaluation of ligament connectivity in Duocel foam by ERG (based on micro-CT volumetric imaging) confirms that Duocel does, in fact, have  $N_C = 4$ . Physical sample sizes used for testing are approximately  $50 \text{ mm} \times 50 \text{ mm} \times 65 \text{ mm}$ .

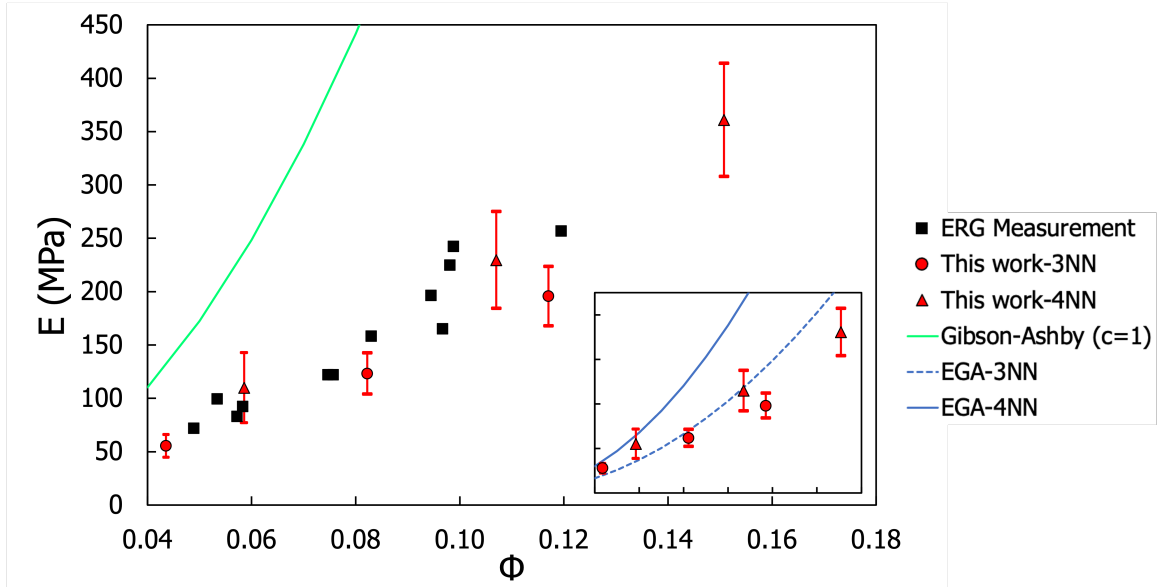


Figure 8.8: Comparison of in-house ERG measurements and KRaSTk-generated results.



### 8.2.5 MMOD interaction scale

Encouraged by these accurate predictions, conversions from dimensionless quantities ( $\lambda_t, s$ ) to physical lengths were computed. Utilizing measurements in the literature [249], the characteristic length of a ligament in a Duocel sample was set equal to the average ligament length in KRaSTk mRVEs. Assuming that the length of a medium density ligament is 1.50 mm (this is an average of the values Ref. [249] lists for  $\sim 8\%$  reduced density 10 and 20 PPI—pores per linear inch—foams) and the length of the medium density mRVE ligament is 14.85, the following conversion was made. With 1.50 mm set equal to 14.85 in KRaSTk’s unitless dimensions, 1 in KRaSTk is approximately 101  $\mu\text{m}$ . Considering that the feature-to-mesoscale transition occurs at a common *relative* size scale ( $\lambda_{f \rightarrow m}$ ) ( $\sim 10$ ) for each reduced density, the minimum sample volume must be about  $10\times$  the characteristic ligament length. Based on the mm $\rightarrow$ KRaSTk conversion, this correlates to about a 15 mm side length for the medium reduced density mRVEs and a wider approximate range of mRVE side lengths of about 12–20 mm, depending on reduced density and PPI.

It is interesting to note that while the feature-to-mesoscale transition occurs at a common *relative* size scale ( $\lambda_{f \rightarrow m}$ ), due to the nature of the node-ligament structure, this transition occurs at varying physical size scales depending on the density of the foam. This has important implications for the use of these materials as components in MMOD shielding. Revisiting Fig. 8.1, the diameter of a representative MMOD strike is approximately 500  $\mu\text{m}$ . On average this is  $30\times$  *shorter* than the feature-scale to mesoscale transition for any reduced density foam. Therefore, bulk (or even mesoscale) materials properties of Duocel will have limited applicability for determining the response of Duocel foam to MMOD strikes—instead, the individual properties of ligaments and/or pores will dominate the materials response.

### 8.3 Defected structures

This section expands beyond defect-free structures and explores the mechanical effects of defects—cylindrical cavities representing the post-collision, residual damage of an MMOD impact. KRaSTk was utilized to assess the disparity in stiffness in the in-plane and through-the-thickness directions of the model representative volume elements as a function of cavity volume. With these results, statistical-based conclusions regarding the effect of MMOD impact-inspired cavities on Duocel were drawn.

### 8.3.1 mRVE generation

KRaSTk was used to generate sets of 50 model representative volume elements (mRVEs) to characterize Duocel foams with penetrating cavities of varying volumes, as shown in (Fig. 8.9). As with the previous section, classes of mRVEs were distinguished based on their reduced density before cavities were introduced: low (L), medium (M), and high (H). The average reduced densities of these classes (again, before cavities are introduced) was  $\sim 6\%$ ,  $\sim 11\%$ , and  $\sim 15\%$ , respectively. Beginning with sets of defect-free mRVEs (0% cavity volume), additional sets were built by increasing cavity volume from 5% to 10% to 20%. The cavities were included by removing a cylindrical volume from the center of the mRVE, parallel to the TTT direction, as shown in Fig. 8.10. Based on the results from the previous section, the  $\lambda$  of each class of mRVEs was  $\lambda_{f \rightarrow m}$ , or the  $\lambda$  at which the feature scale to mesoscale transition occurred. In upcoming sections, these sets are named according to their corresponding reduced density and cavity volume. For example, the low density set with a 20% cavity volume is referred to as L-20.

### 8.3.2 Computational details

The elastic constants of each mRVE was computed via the method described in §7.3.2 for orthotropic mRVEs. While the defect-free mRVEs are isotropic, the introduction of cavities requires a more complete knowledge of elastic constants. The elastic constants were computed with FEniCSx. The computational details in this section are identical to those presented in §8.2.2.

### 8.3.3 Directional disparities due to cavities

The mean elastic moduli of each mRVE set—including the first IP, second IP, and TTT directions—are shown in Fig. 8.11. The inclusion of cylindrical voids of increasing volume correlates with a decrease in elastic modulus. While this simple statement is admittedly intuitive, a deeper analysis revealed more intriguing results. In the high and medium density sets, increasing the cavity volume resulted in increasing the disparity between the moduli of the IP and TTT orientations. The introduction of a cylindrical cavity with an axis parallel to the TTT direction (as shown in Fig. 8.10) initiated weakening in the IP direction. When the cavity volume was 0%—i.e. nonexistent and the structure defect-free—the mRVEs at all reduced densities were isotropic and IP and TTT orientations indistinguishable. As the cavity volume increased to 20%, the mean stiffness in the combined IP directions compared to the TTT direc-

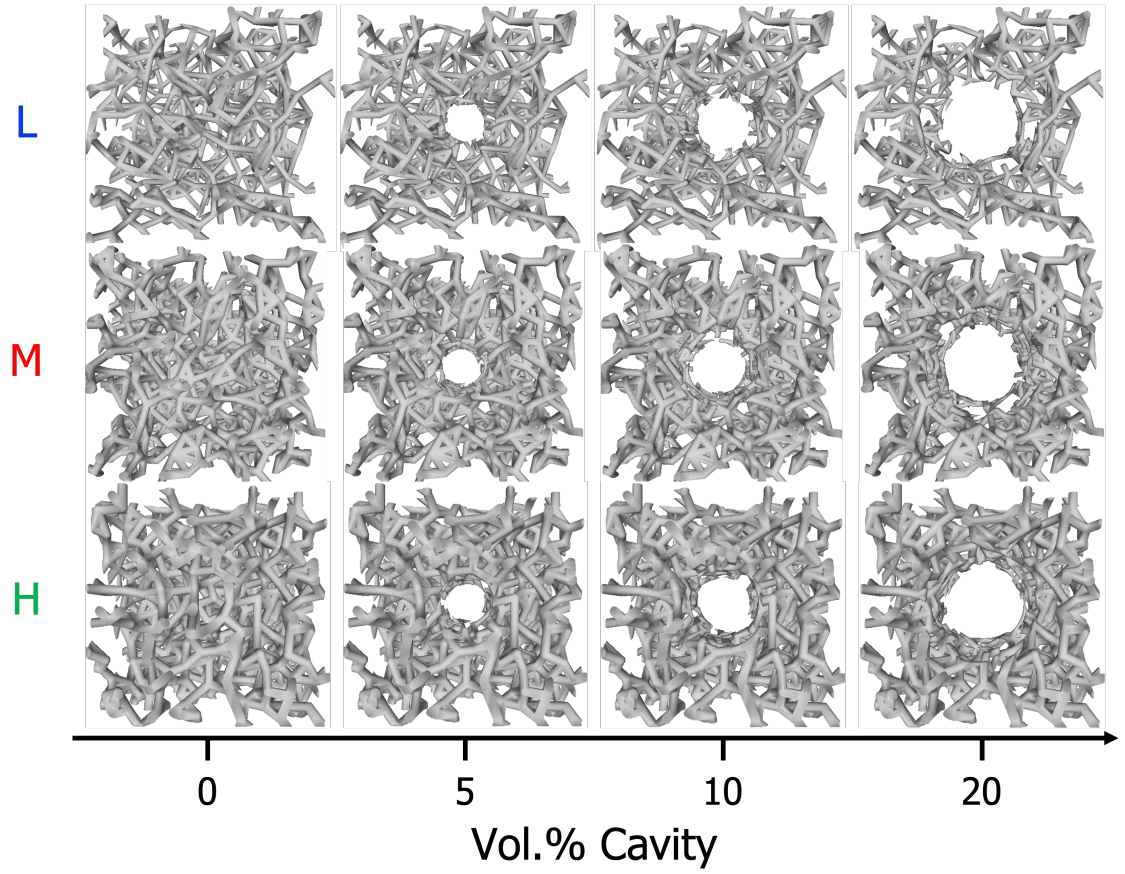


Figure 8.9: Example structures of each of the twelve mRVE sets utilized in this series of calculations.

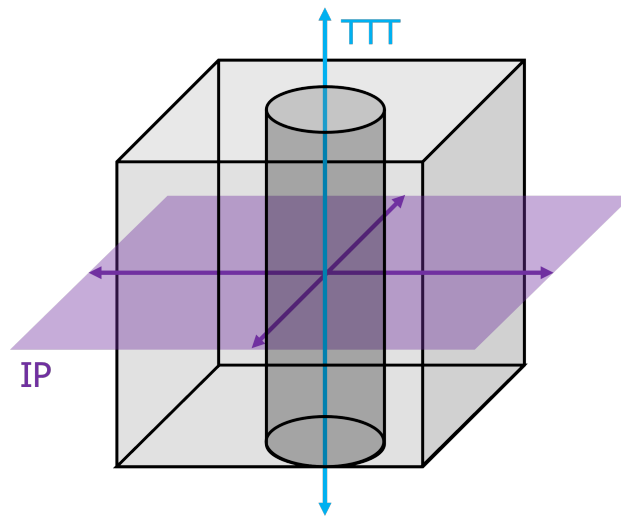


Figure 8.10: A diagram indicating the directions referenced in this section with respect to mRVEs.

tion was  $\sim 2\%$  for the low density sets,  $\sim 17\%$  for the medium density sets, and  $\sim 19\%$  for the high density sets. With respect to the low density sets, it was hypothesized that the initial reduced density of the structures were so low that the inclusion of additional voids did not have a significant impact. For example, the inclusion of a cylindrical cavity that was 20% of the volume of the defect-free (no cavity) low density mRVEs only decreases the reduced density from 5.9% to 4.6% ( $\Delta = 1.3\%$ ). This same comparison in the high density mRVEs saw a decrease of the reduced density from 15.1% to 12.0% ( $\Delta = 3.1\%$ ). The change in reduced density for the high density mRVEs was more than twice that for the low density mRVEs, explaining the difficulty in distinguishing the IP and TTT points in low density mRVE results.

Table 8.3: Reduced average IP and TTT stiffnesses, comparing 0% and 20% volume cavity mRVE sets.

| In-plane (IP)            | Through-the-thickness (TTT) |
|--------------------------|-----------------------------|
| $E_{L-20} = 0.83E_{L-0}$ | $E_{L-20} = 0.80E_{L-0}$    |
| $E_{M-20} = 0.70E_{M-0}$ | $E_{M-20} = 0.86E_{M-0}$    |
| $E_{H-20} = 0.64E_{H-0}$ | $E_{H-20} = 0.82E_{H-0}$    |

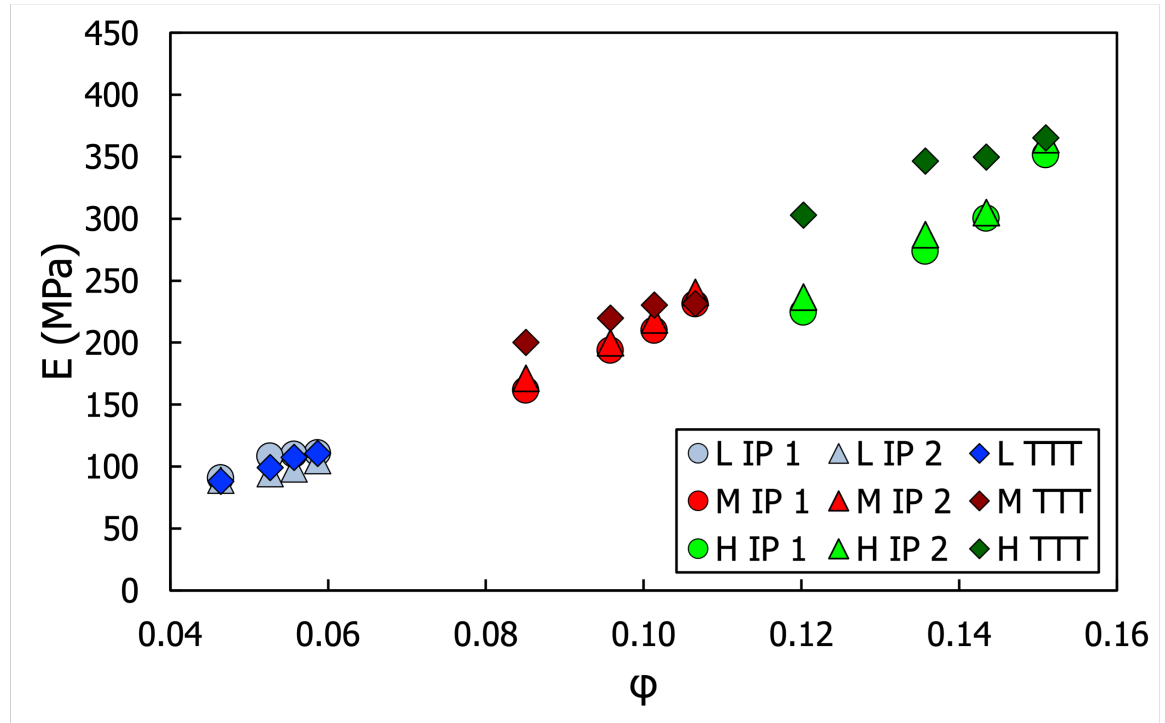


Figure 8.11: A scatter plot showing the mean elastic modulus values of all mRVE sets, including both IP and TTT directions.

The magnitude of reduced average IP and TTT stiffnesses was related to the size of the cavity, as shown in Table 8.3. Again, it is hypothesized that the low density mRVEs did not contain enough material to be severely affected by the inclusion of additional cavities. Comparing the medium and high density results, the IP stiffness appeared to be more highly affected by the inclusion of 20% volume cavities than the TTT stiffness. It is hypothesized that this disparity in directional dependence originated from the resulting distribution of load once the cavity was introduced. When the cylindrical cavity was oriented in the TTT direction, it severed many more load-bearing ligament paths in the transverse (IP) direction than in the TTT direction.

Although discussion of the mean values in this section allowed for the drawing of a few broad conclusions with regard to the behavior of mRVEs containing large cylindrical cavities, KRaSTk allowed for deeper insight gained by a statistical approach. Fig. 8.12 plots the computed elastic modulus values for each mRVE set as  $\Gamma$ -distributions, rather than means. The conclusions drawn in the previous section were supported by these results as well: peaks shifted to the left as the cavity volume increases and peaks for IP and TTT orientations separated as cavity volume increases. As a note, in further discussion, the IP distribution was a combination of values from both the IP directions, hypothesized to be acceptable given the minor deviations exhibited by the expectation values in Fig. 8.11. Even in this presentation, the results were overwhelming and difficult to deconstruct. It was possible to discern by the peak shifts that stiffness decreases with increasing cavity volume, though this information was already evident in Fig. 8.11, and is, admittedly, uninspired.

#### 8.3.4 Stochastic model predictions of cavity effects in Duocel

However, a particularly unique set of results can be distilled from the overlap of distributions, rather than the  $\mu_E$  and  $\sigma_E$  of individual distributions. The overlap coefficient, a similarity measure that measures the overlap between two finite sets  $(X, Y)$  was defined as the size of the intersection divided by the smaller of the size of the two sets:

$$\text{overlap}(X, Y) = \frac{|X \cap Y|}{\min(|X|, |Y|)} \quad (8.5)$$

As the area of each distribution (PDF) generated by KRaSTk is always 1, the quantity the denominator  $\min(|X|, |Y|)$  will always equal 1. In this section, the overlap will be represented by a percentage of the area of an individual distribution. Eq. 8.5 can

Table 8.4: The  $\Gamma$ -distribution parameters,  $a$  and  $b$ , and corresponding statistical quantities,  $\mu_E$  and  $\sigma_E$  of the defected mRVE sets in both the IP and TTT directions.

| Set      | $\Gamma$ Parameters |       | Statistics |            |
|----------|---------------------|-------|------------|------------|
|          | $a$                 | $b$   | $\mu_E$    | $\sigma_E$ |
| L-0 IP   | 8.52                | 12.66 | 107.87     | 36.95      |
| L-0 TTT  | 7.55                | 14.64 | 110.56     | 40.23      |
| L-5 IP   | 7.94                | 13.10 | 103.94     | 36.90      |
| L-5 TTT  | 8.55                | 12.54 | 107.23     | 36.66      |
| L-10 IP  | 5.22                | 19.38 | 101.25     | 44.30      |
| L-10 TTT | 9.51                | 10.42 | 99.12      | 32.14      |
| L-20 IP  | 7.68                | 11.33 | 87.06      | 31.41      |
| L-20 TTT | 8.60                | 10.31 | 88.65      | 30.22      |
| M-0 IP   | 17.85               | 13.22 | 235.88     | 55.84      |
| M-0 TTT  | 14.76               | 15.68 | 231.43     | 60.24      |
| M-5 IP   | 17.95               | 12.14 | 217.95     | 51.44      |
| M-5 TTT  | 16.73               | 13.90 | 232.48     | 56.84      |
| M-10 IP  | 23.07               | 8.68  | 200.27     | 41.70      |
| M-10 TTT | 18.68               | 11.84 | 221.21     | 51.18      |
| M-20 IP  | 14.87               | 11.18 | 166.32     | 43.13      |
| M-20 TTT | 14.85               | 13.47 | 200.00     | 51.91      |
| H-0 IP   | 32.23               | 11.09 | 357.53     | 62.97      |
| H-0 TTT  | 26.36               | 13.85 | 365.15     | 71.1       |
| H-5 IP   | 20.85               | 14.42 | 300.63     | 65.85      |
| H-5 TTT  | 25.64               | 13.62 | 349.23     | 69.0       |
| H-10 IP  | 22.601              | 12.12 | 273.97     | 57.63      |
| H-10 TTT | 48.25               | 7.00  | 337.85     | 48.64      |
| H-20 IP  | 14.89               | 15.46 | 230.23     | 59.66      |
| H-20 TTT | 26.26               | 11.41 | 299.64     | 58.47      |

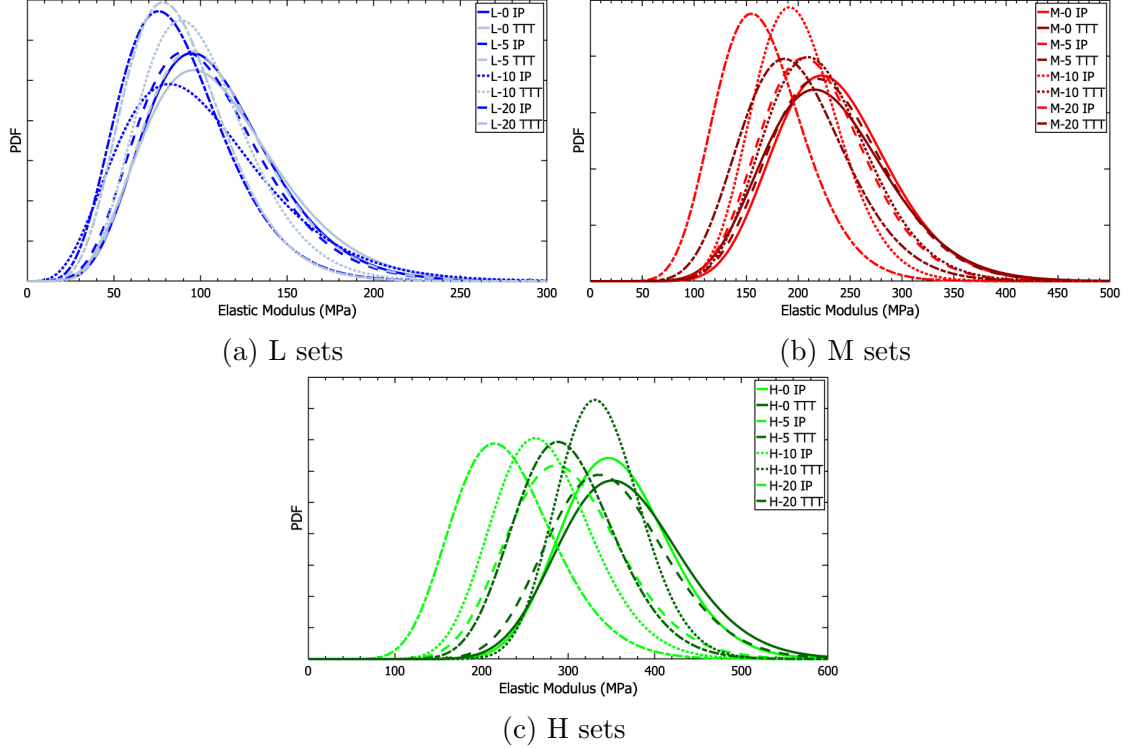


Figure 8.12: Elastic modulus distributions, in both IP and TTT orientations, for all mRVE sets.

be rewritten in terms of distribution area ( $A$ ):

$$A_{\text{overlap}(X,Y)} = \frac{A_{|X \cap Y|}}{A_{\min(|X|,|Y|)}} = \frac{A_{|X \cap Y|}}{1} \quad (8.6)$$

Therefore, the ratio of overlap to total unique area beneath the two distributions, here referred to as the similarity index ( $\eta$ ), is:

$$\eta = \frac{A_{\text{overlap}(X,Y)}}{(A_X + A_Y) - A_{\text{overlap}(X,Y)}} = \frac{A_{\text{overlap}(X,Y)}}{2 - A_{\text{overlap}(X,Y)}} \quad (8.7)$$

For each class of mRVEs, Fig. 8.13 shows the 0% and 20% cavity volume  $\Gamma$ -distributions of both orientations, with the overlapping area shaded. Table 8.5 includes area overlaps in addition to similarity indices. In the IP direction,  $A_{\text{overlap}}$  was shown to steadily decrease as reduced density increased. In the TTT direction, the low and medium density area overlaps were comparable, but decreased significantly for the high density results. Even examining the smallest area overlap distributions (H-IP), there was an overlap of 0.293, correlating to a similarity index of 0.172 and subsequently a 17.2% probability that the elastic modulus of the 20% cavity mRVEs

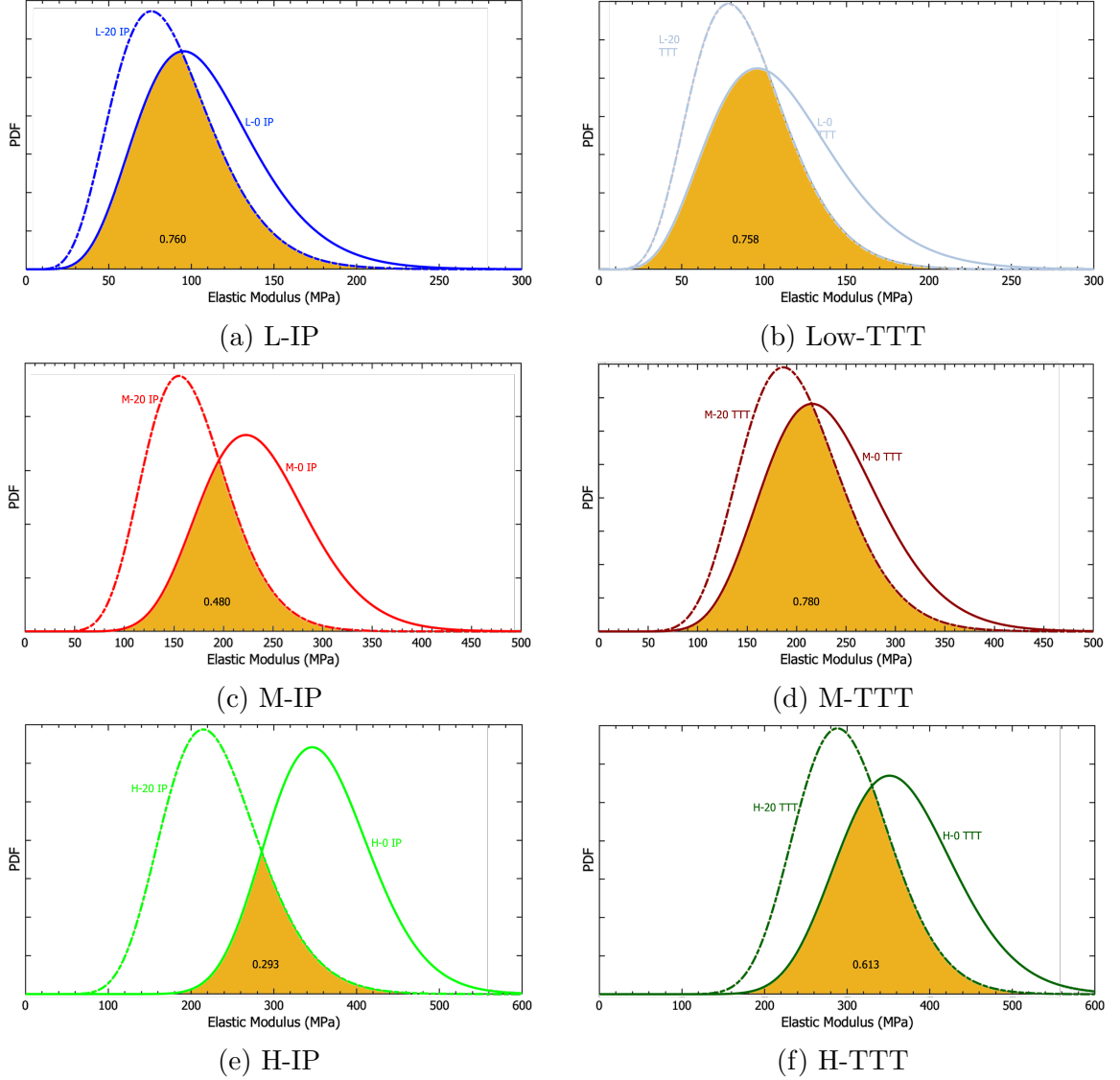


Figure 8.13: Plots showing the overlap between distributions of 0% and 20% cavity volume elastic modulus values, both in the IP and TTT orientations.

was indistinguishable from that of the 0% cavity mRVEs. The high density class of mRVE sets also had the lowest TTT distribution area overlap (0.613) and similarity index (0.442). Fig. 8.14 illustrates the physical implications of these results.

In practice, these results show that there were a relatively high number of instances in which a set of defect-free structures exhibited the same elastic modulus as a set of structures that include a massive cylindrical cavity. In other words, this is evidence that the effects of intrinsically, random and complex microstructure (e.g. standard variability, deviation of distributions) present in each set of mRVEs dominated the effect of cavities (e.g. changes in the expectation values). As uncertainty



Table 8.5: Similarity measures of the 0% and 20% cavity volume  $\Gamma$ -distributions of each reduced density class and both orientations.

| Distributions $(X, Y)$ | Orientation | $A_{\text{overlap}(X,Y)}$ | $\eta$ |
|------------------------|-------------|---------------------------|--------|
| (L-0, L-20)            | IP          | 0.760                     | 0.613  |
| (M-0, M-20)            | IP          | 0.480                     | 0.316  |
| (H-0, H-20)            | IP          | 0.293                     | 0.172  |
| (L-0, L-20)            | TTT         | 0.758                     | 0.610  |
| (M-0, M-20)            | TTT         | 0.780                     | 0.639  |
| (H-0, H-20)            | TTT         | 0.613                     | 0.442  |

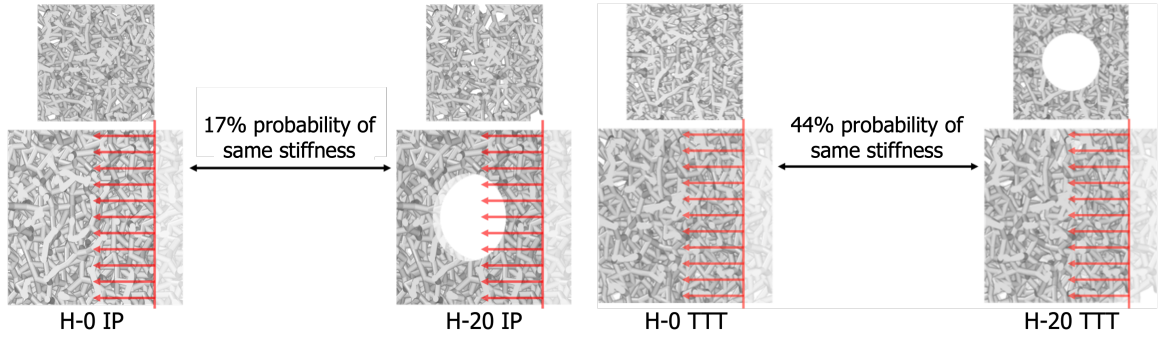


Figure 8.14: A representation of the physical implications of the overlapping  $\Gamma$ -distributions in Figs. 8.13e and 8.13f.

quantification is a major consideration for any NASA mission, a deeper understanding of the range of properties exhibited by a critical component material is essential for assessing the fidelity of shielding materials.

#### 8.4 Summary

This chapter focused on the practical application of KRaSTk to Duocel, a material with a highly-complex, random porous microstructure that is critical to MMOD shielding. The node-ligament network structure of Duocel make it an ideal material for this application, as the repeated impacts of the projectile on ligaments would cause melting and vaporization before penetrating the spacecraft. However, its complex microstructure produces wide variability in properties. In this chapter, the transition from feature-scale to mesoscale dominated behavior with respect to elastic properties was computed. Examining three classes of mRVEs with low, medium, and high reduced densities, the feature-scale to mesoscale transition occurred at the same  $\lambda_t$  for

all classes. The quantity  $\lambda_t$  was in the range  $9.7 - 10.3$  for all classes, indicating that the mRVE length must be  $10\times$  the characteristic length before individual features no longer represent the material. This shared  $\lambda_t$  corresponds to physical mRVE side lengths of 12-20 mm, depending on reduced density. KRaSTk predictions of Duocel were found to be accurate compared to measurements taken by ERG Aerospace, its manufacturer. In particular, mRVEs where  $N_C = 4$  aligned incredibly well, with not only expectation values agreeing but standard variabilities as well.

The final section in this chapter explored the effect of cylindrical, MMOD-inspired cavities in Duocel. As cavity volumes increased, the directional dependence of mechanical properties was determined. For the medium and high reduced density classes of mRVEs, the introduction of cavities, regardless of their volumes, decreased stiffness in both the TTT and IP directions. However, the magnitude of this decrease was far greater for the high density mRVE sets than the medium density. The introduction of cavities to the low density mRVE sets also decreased stiffness in all directions; there was no notable difference in the magnitude of this decrease in the IP or TTT directions. It is hypothesized that this is due to the low initial reduced density in the defect-free (0% volume cavity). Cavities simply did not change the individual low density mRVEs significantly. By analyzing the area overlaps of distributions between defect-free and high cavity volume mRVE sets, it was determined that mechanical properties of Duocel are dominated by inherent structural variability over defects. Even with cavities around 20% in volume, there remained a relatively high probability within each reduced density class that defect-free and defected structures would exhibit the same stiffness in practice. As uncertainty quantification is a major consideration for any NASA mission, this type of analysis will allow for improved assessment parameters for MMOD shielding materials.

## Chapter 9: Conclusions

### 9.1 Concluding remarks

The work presented here addresses outstanding questions in two unrelated applications of complex materials. In Part I, the first chapter introduced a method by which surface excess free energies incorporating vibrational entropy could be used to predict Wulff shape in a particular chemical environment at finite temperature. The following chapter essentially inverted this method to determine the chemical conditions required to form the characteristic microstructure of high-performing scandate cathodes. In Part II, the first chapter introduced KRaSTk, an algorithm by which the distribution of properties for materials with highly-variable, even random, microstructures could be computed. The following chapter focused on applying this method to Duocel, a metallic foam used in MMOD shielding. The variability in mechanical properties was evaluated with respect to length scale, revealing the transition from local, feature-dominated behavior to mesoscale behavior. The effect of defects, in particular cylindrical cavities, on directional properties was also presented. Atomistic techniques—density functional theory and density functional perturbation theory—were central to the scandate cathode sections. Continuum scale approaches—finite element analysis—combined with statistical methods were utilized in the inhomogeneous microstructure sections. The broad scope of computational materials science approaches with respect to complex materials central to a range of [unrelated] scientific applications—surfaces, nanoparticles, NP metals, metallic foams—was demonstrated.

### 9.2 Key findings

The results from the scandate cathode sections in this dissertation can be summarized as follows:

- The addition of Ba to O/W-containing environments dramatically alters the chemistry and shape of W particle surfaces at scandate cathode relevant conditions. In particular, the (112) facets widely observed in thermionic cathodes are shown to only be present when Ba is available, as these facets are not appreciably expressed on W particles in O-only environments.

- Implementing the invert Wulff construction reveals the chemical conditions required to produce equilibrium particles with experimentally observed shapes. The observed characteristic shape will only occur in two narrow regions of  $(T, p_{O_2})$ -space, implying that extremely careful control of chemical conditions during cathode activation is required to reliably and repeatably yield high-performing cathodes.
- In both regions of  $(T, p_{O_2})$ -space where the experimentally observed W particle shape is stable, the  $Ba_{0.50}O$ -top/W (112) surface configuration, with a work function of 1.23 eV, is present in the largest surface area fraction ( $\sim 70\%$  of total surface area). The large relative area and relatively low work function of this configuration drives a low effective work function of  $\sim 1.3$  eV for particles with the observed shape, a value comparable to those measured for scandate cathodes.
- There is a window of chemical conditions where the  $Ba_{0.25}Sc_{0.25}O$ -top/W (001) surface (with a work function of 0.82 eV) is stable, pushing the effective work function of W particles as low as 0.84 eV. Chemical conditions in this window, though, do not yield the observed particle shape.
- No Sc-containing surface configuration is stable (relative to Sc-free surface configurations) when the observed characteristic particle shape is stable. Combined these findings suggest the possibility that the role of Sc is not to directly modify the surface work function by adsorbing atop O on W crystallites, but rather simply to getter oxygen.
- Despite the bulk phase diagram showing no miscibility between Sc and W,  $Sc_y/W$  (hkl) surface configurations exhibit much lower surface energies than any other set; however, they do not have a particularly low work function.
- There is evidence that the addition of cations to a surface where Sc is positioned directly atop W increases its excess energy and initiates mechanical instability, particularly in the region between the Sc monolayer and the first W layer.

The KRaSTk sections of the prototypical nanoporous material and Duocel foam have yielded the following results:

- There is a separable and independent effect of network connectivity on elastic and bulk moduli. Increasingly constrained network structures are stiffer than less constrained structures with the same reduced density. This effect can be

captured in an extension to the Gibson-Ashby model of open-foam mechanical properties with the addition of a connectivity-dependent factor, and this extended G-A (EGA) model is found to apply to both elastic and bulk modulus:

$$\frac{E^*}{E_s} = 0.49\phi^2(N_C^* - 3)^{0.41}$$

$$\frac{K^*}{K_s} = 0.41\phi^2(N_C^* - 3)^{0.47}$$

- The transition between local, feature-driven behavior and mesoscale behavior in Duocel occurs at the same  $\lambda$  (a ratio of sample to characteristic length); however, the conversion of this parameter to physical lengths depends on porosity. As a result, the transition for a low porosity material is at a far higher length scale than a high porosity material.
- KRaSTk predictions align well with measurements made by Duocel's manufacturer, with respect to both the expectation value, or first moment, and the standard variability.
- The introduction of a cylindrical cavity parallel to the through-the-thickness direction transforms a nominally isotropic Duocel into an anisotropic (transverse isotropic) material, weaker in-plane than through-the-thickness.
- Comparing the elastic moduli probability distribution functions of structures with and without a cavity, a significant probability remains that the two structures would be practically indistinguishable.

## Bibliography

- [1] G. L. L. de Buffon, “Essai d’arithmétique morale,” *Euvres philosophiques*, 1777.
- [2] R. Eckhardt, “Stan Ulum, John Von Neumann, and the Monte Carlo Method,” *Los Alamos Science*, p. 11, 1987.
- [3] N. Metropolis, “The Beginning of the Monte Carlo Method,” *Los Alamos Science*, vol. 15, pp. 125–130, 1987.
- [4] T. Haigh, M. Priestley, and C. Rope, “Los Alamos Bets on ENIAC: Nuclear Monte Carlo Simulations, 1947-1948,” *IEEE Annals of the History of Computing*, vol. 36, pp. 42–63, July 2014.
- [5] E. Segrè, *From X-rays to Quarks: Modern Physicists and Their Discoveries*. Courier Corporation, May 2012.
- [6] M. Born and E. Wolf, *Principles of Optics: Electromagnetic Theory of Propagation, Interference and Diffraction of Light*. Cambridge: Cambridge University Press, seventh ed., 1999.
- [7] O. Carnal and J. Mlynek, “Young’s double-slit experiment with atoms: A simple atom interferometer,” *Physical Review Letters*, vol. 66, pp. 2689–2692, May 1991.
- [8] J. C. Maxwell, “Illustrations of the Dynamical Theory of Gases,” *The London, Edinburgh, and Dublin Philosophical Magazine and Journal of Science*, vol. 19, no. 124, pp. 19–32, 1860.
- [9] L. Boltzmann, “Weitere Studien über das Wärmegleichgewicht unter Gas-molekülen,” in *Kinetische Theorie II: Irreversible Prozesse Einführung und Originaltexte* (S. G. Brush, ed.), WTB Wissenschaftliche Taschenbücher, pp. 115–225, Wiesbaden: Vieweg+Teubner Verlag, 1970.
- [10] P. F. Dahl, *Flash of the Cathode Rays: A History of J J Thomson’s Electron*. Boca Raton: CRC Press, Apr. 2014.
- [11] J. Mehra and H. Rechenberg, *The Quantum Theory of Planck, Einstein, Bohr and Sommerfeld: Its Foundation and the Rise of Its Difficulties 1900–1925*.

The Historical Development of Quantum Theory, New York, NY: Springer New York, NY, first ed., 1982.

- [12] H. Kragh, “Max Planck: The reluctant revolutionary,” *physicsworld*, 2000.
- [13] A. Einstein, “über einen die Erzeugung und Verwandlung des Lichtes betreffenden heuristischen Gesichtspunkt,” *Annalen der Physik*, vol. 17, no. 6, pp. 132–148, 1905.
- [14] J. Stachel, “Bohr and the Photon,” in *Quantum Reality, Relativistic Causality, and Closing the Epistemic Circle: Essays in Honour of Abner Shimony* (W. C. Myrvold and J. Christian, eds.), The Western Ontario Series in Philosophy of Science, pp. 69–83, Dordrecht: Springer Netherlands, 2009.
- [15] L. de Broglie, “Recherches sur la théorie des Quanta,” *Annales de Physique*, vol. 10, no. 3, pp. 22–128, 1925.
- [16] D. A. Edwards, “The mathematical foundations of quantum mechanics,” *Synthese*, vol. 42, pp. 1–70, Sept. 1979.
- [17] J. Bernstein, “Max Born and the quantum theory,” *American Journal of Physics*, vol. 73, pp. 999–1008, Nov. 2005.
- [18] L. H. Thomas, “The calculation of atomic fields,” *Mathematical Proceedings of the Cambridge Philosophical Society*, vol. 23, pp. 542–548, Jan. 1927.
- [19] E. Fermi, “Un metodo statistico per la determinazione di alcune priorietà dell’atome,” *Rend. Accad. Naz. Lincei*, vol. 6, no. 32, 1927.
- [20] E. Schrödinger, “An Undulatory Theory of the Mechanics of Atoms and Molecules,” *Physical Review*, vol. 28, pp. 1049–1070, Dec. 1926.
- [21] D. R. Hartree, “The Wave Mechanics of an Atom with a Non-Coulomb Central Field. Part II. Some Results and Discussion,” *Mathematical Proceedings of the Cambridge Philosophical Society*, vol. 24, pp. 111–132, Jan. 1928.
- [22] D. R. Hartree, “The Wave Mechanics of an Atom with a Non-Coulomb Central Field. Part I. Theory and Methods,” *Mathematical Proceedings of the Cambridge Philosophical Society*, vol. 24, pp. 89–110, Jan. 1928.
- [23] V. Fock, “Näherungsmethode zur Lösung des quantenmechanischen Mehrkörperproblems,” *Zeitschrift für Physik*, vol. 61, pp. 126–148, Jan. 1930.

- [24] P. Hohenberg and W. Kohn, “Inhomogeneous Electron Gas,” *Physical Review*, vol. 136, pp. B864–B871, Nov. 1964.
- [25] W. Kohn and L. J. Sham, “Self-Consistent Equations Including Exchange and Correlation Effects,” *Physical Review*, vol. 140, pp. A1133–A1138, Nov. 1965.
- [26] S. Baroni, P. Giannozzi, and A. Testa, “Green’s-function approach to linear response in solids,” *Physical Review Letters*, vol. 58, pp. 1861–1864, May 1987.
- [27] X. Gonze, “Perturbation expansion of variational principles at arbitrary order,” *Physical Review A*, vol. 52, pp. 1086–1095, Aug. 1995.
- [28] R. W. Clough, “The Finite Element Method in Plane Stress Analysis,” *Proceedings of 2nd ASCE Conference on Electronic Computation*, 1960.
- [29] R. Courant, “Variational methods for the solution of problems of equilibrium and vibrations,” *Bulletin of the American mathematical Society*, vol. 49, no. 1, 1943.
- [30] A. Hrennikoff, “Solution of Problems of Elasticity by the Framework Method,” *Journal of Applied Mechanics*, vol. 8, pp. A169–A175, Mar. 1941.
- [31] H. Falkenheimer, “Systematic calculation of the elastic characteristics of hyperstatic systems,” *Le Recherche Aeronautique*, pp. 17–23, 1951.
- [32] B. Langefors, “Analysis of Elastic Structures by Matrix Transformation with Special Regard to Semimonocoque Structures — Journal of the Aeronautical Sciences,” *Journal of the Aeronautical Sciences*, 1952.
- [33] J. H. Argyris and S. Kelsey, *Energy Theorems and Structural Analysis*, vol. 60. London: Butterworths, 1960.
- [34] M. Born and J. R. Oppenheimer, “On the Quantum Theory of Molecules,” *Annalen der Physik*, vol. 389, no. 20, pp. 457–484, 1927.
- [35] P. R. C. Kent, *Techniques and Applications of Quantum Monte Carlo*. PhD thesis, University of Cambridge, Cambridge, 1999.
- [36] A. D. Becke, “Density-functional exchange-energy approximation with correct asymptotic behavior,” *Physical Review A*, vol. 38, pp. 3098–3100, Sept. 1988.



- [37] J. P. Perdew, J. A. Chevary, S. H. Vosko, K. A. Jackson, M. R. Pederson, D. J. Singh, and C. Fiolhais, “Atoms, molecules, solids, and surfaces: Applications of the generalized gradient approximation for exchange and correlation,” *Physical Review B*, vol. 46, pp. 6671–6687, Sept. 1992.
- [38] D. C. Langreth and M. J. Mehl, “Beyond the local-density approximation in calculations of ground-state electronic properties,” *Physical Review B*, vol. 28, pp. 1809–1834, Aug. 1983.
- [39] F. Nogueira, A. Castro, and M. A. L. Marques, “A Tutorial on Density Functional Theory,” in *A Primer in Density Functional Theory* (C. Fiolhais, F. Nogueira, and M. A. L. Marques, eds.), Lecture Notes in Physics, pp. 218–256, Berlin, Heidelberg: Springer, 2003.
- [40] N. W. Ashcroft and N. D. Mermin, *Solid State Physics*. Philadelphia, PA: Saunders College Publishing, 1976.
- [41] H. J. Monkhorst and J. D. Pack, “Special points for Brillouin-zone integrations,” *Physical Review B*, vol. 13, pp. 5188–5192, June 1976.
- [42] J. C. Phillips, “Energy-Band Interpolation Scheme Based on a Pseudopotential,” *Physical Review*, vol. 112, pp. 685–695, Nov. 1958.
- [43] J. C. Phillips and L. Kleinman, “New Method for Calculating Wave Functions in Crystals and Molecules,” *Physical Review*, vol. 116, pp. 287–294, Oct. 1959.
- [44] M. L. Cohen and V. Heine, “The Fitting of Pseudopotentials to Experimental Data and Their Subsequent Application,” in *Solid State Physics* (H. Ehrenreich, F. Seitz, and D. Turnbull, eds.), vol. 24, pp. 37–248, Academic Press, Jan. 1970.
- [45] E. Polak, *Computational Methods in Optimization: A Unified Approach*. Academic Press, May 1971.
- [46] M. Verstraete and Z. Zanolli, “Density Functional Perturbation Theory.” 2014.
- [47] X. Gonze, “Density functional perturbation theory.” 2019.
- [48] H. Hellmann, “Einführung in die quantumchemie leipzig,” *Franz Deutsche*, 1937.
- [49] R. P. Feynman, “Forces in Molecules,” *Physical Review*, vol. 56, pp. 340–343, Aug. 1939.

- [50] R. M. Sternheimer, “Electronic Polarizabilities of Ions from the Hartree-Fock Wave Functions,” *Physical Review*, vol. 96, pp. 951–968, Nov. 1954.
- [51] S. Wang, W. Lu, O. Tovmachenko, U. S. Rai, H. Yu, and P. C. Ray, “Challenge in Understanding Size and Shape Dependent Toxicity of Gold Nanomaterials in Human Skin Keratinocytes,” *Chemical physics letters*, vol. 463, pp. 145–149, Sept. 2008.
- [52] R. A. Yokel, M. T. Tseng, M. Dan, J. M. Unrine, U. M. Graham, P. Wu, and E. A. Grulke, “Biodistribution and biopersistence of ceria engineered nanomaterials: Size dependence,” *Nanomedicine: Nanotechnology, Biology, and Medicine*, vol. 9, pp. 398–407, Apr. 2013.
- [53] E. Blanco, A. Hsiao, A. P. Mann, M. G. Landry, F. Meric-Bernstam, and M. Ferrari, “Nanomedicine in cancer therapy: Innovative trends and prospects,” *Cancer Science*, vol. 102, pp. 1247–1252, July 2011.
- [54] M. Estanqueiro, M. H. Amaral, J. Conceição, and J. M. Sousa Lobo, “Nanotechnological carriers for cancer chemotherapy: The state of the art,” *Colloids and Surfaces. B, Biointerfaces*, vol. 126, pp. 631–648, Feb. 2015.
- [55] E. Pérez-Herrero and A. Fernández-Medarde, “Advanced targeted therapies in cancer: Drug nanocarriers, the future of chemotherapy,” *European Journal of Pharmaceutics and Biopharmaceutics: Official Journal of Arbeitsgemeinschaft Fur Pharmazeutische Verfahrenstechnik e.V.*, vol. 93, pp. 52–79, June 2015.
- [56] Y. Zhu and L. Liao, “Applications of Nanoparticles for Anticancer Drug Delivery: A Review,” *Journal of Nanoscience and Nanotechnology*, vol. 15, pp. 4753–4773, July 2015.
- [57] S. Sultana, M. R. Khan, M. Kumar, S. Kumar, and M. Ali, “Nanoparticles-mediated drug delivery approaches for cancer targeting: A review,” *Journal of Drug Targeting*, vol. 21, pp. 107–125, Feb. 2013.
- [58] R. A. Yokel, J. M. Unrine, P. Wu, B. Wang, and E. A. Grulke, “Nanoceria biodistribution and retention in the rat after its intravenous administration are not greatly influenced by dosing schedule, dose, or particle shape,” *Environmental Science: Nano*, vol. 1, no. 6, pp. 549–560, 2014.

- [59] B. Wang, P. Wu, R. A. Yokel, and E. A. Grulke, "Influence of surface charge on lysozyme adsorption to ceria nanoparticles," *Applied Surface Science*, vol. 258, pp. 5332–5341, May 2012.
- [60] G. D. Barmparis, Z. Lodziana, N. Lopez, and I. N. Remediakis, "Nanoparticle shapes by using Wulff constructions and first-principles calculations," *Beilstein Journal of Nanotechnology*, vol. 6, pp. 361–368, Feb. 2015.
- [61] J. E. Mondloch, E. Bayram, and R. G. Finke, "A review of the kinetics and mechanisms of formation of supported-nanoparticle heterogeneous catalysts," *Journal of Molecular Catalysis A: Chemical*, vol. 355, pp. 1–38, Mar. 2012.
- [62] J. B. Sambur and P. Chen, "Approaches to Single-Nanoparticle Catalysis," *Annual Review of Physical Chemistry*, vol. 65, no. 1, pp. 395–422, 2014.
- [63] F. Raimondi, G. G. Scherer, R. Kötz, and A. Wokaun, "Nanoparticles in Energy Technology: Examples from Electrochemistry and Catalysis," *Angewandte Chemie International Edition*, vol. 44, no. 15, pp. 2190–2209, 2005.
- [64] J. D. Aiken and R. G. Finke, "A review of modern transition-metal nanoclusters: Their synthesis, characterization, and applications in catalysis," *Journal of Molecular Catalysis A: Chemical*, vol. 145, pp. 1–44, Sept. 1999.
- [65] E. L. Lim, C. C. Yap, M. A. Mat Teridi, C. H. Teh, A. R. bin Mohd Yusoff, and M. H. Hj Jumali, "A review of recent plasmonic nanoparticles incorporated P3HT: PCBM organic thin film solar cells," *Organic Electronics*, vol. 36, pp. 12–28, Sept. 2016.
- [66] S. Magdassi, M. Grouchko, and A. Kamysny, "Copper Nanoparticles for Printed Electronics: Routes Towards Achieving Oxidation Stability," *Materials*, vol. 3, pp. 4626–4638, Sept. 2010.
- [67] Y. Lee, J.-r. Choi, K. J. Lee, N. E. Stott, and D. Kim, "Large-scale synthesis of copper nanoparticles by chemically controlled reduction for applications of inkjet-printed electronics," *Nanotechnology*, vol. 19, p. 415604, Sept. 2008.
- [68] S. Mallakpour and M. Madani, "A review of current coupling agents for modification of metal oxide nanoparticles," *Progress in Organic Coatings*, vol. 86, pp. 194–207, Sept. 2015.

- [69] J. W. Boley, E. L. White, and R. K. Kramer, “Mechanically Sintered Gallium–Indium Nanoparticles,” *Advanced Materials*, vol. 27, no. 14, pp. 2355–2360, 2015.
- [70] A. Shavel and L. M. Liz-Marzán, “Shape control of iron oxide nanoparticles,” *Physical Chemistry Chemical Physics*, vol. 11, pp. 3762–3766, May 2009.
- [71] M. H. Magnusson, K. Deppert, J.-O. Malm, J.-O. Bovin, and L. Samuelson, “Gold Nanoparticles: Production, Reshaping, and Thermal Charging,” *Journal of Nanoparticle Research*, vol. 1, pp. 243–251, June 1999.
- [72] L. D. Marks and L. Peng, “Nanoparticle shape, thermodynamics and kinetics,” *Journal of Physics: Condensed Matter*, vol. 28, p. 053001, Feb. 2016.
- [73] M. Naito, T. Yokoyama, K. Hosokawa, and K. Nogi, *Nanoparticle Technology Handbook*. Elsevier, Mar. 2018.
- [74] W. J. Kennedy, S. Izor, B. D. Anderson, G. Frank, V. Varshney, and G. J. Ehlert, “Thermal Reshaping Dynamics of Gold Nanorods: Influence of Size, Shape, and Local Environment,” *ACS Applied Materials & Interfaces*, vol. 10, pp. 43865–43873, Dec. 2018.
- [75] N. Combe, P. Jensen, and A. Pimpinelli, “Changing Shapes in the Nanoworld,” *Physical Review Letters*, vol. 85, pp. 110–113, July 2000.
- [76] W. Gao, Y. Hou, Z. D. Hood, X. Wang, K. More, R. Wu, Y. Xia, X. Pan, and M. Chi, “Direct in Situ Observation and Analysis of the Formation of Palladium Nanocrystals with High-Index Facets,” *Nano Letters*, vol. 18, pp. 7004–7013, Nov. 2018.
- [77] M. N. Seif, Q. Zhou, X. Liu, T. J. Balk, and M. J. Beck, “Sc-Containing (Scandate) Thermionic Cathodes: Mechanisms for Sc Enhancement of Emission,” *IEEE Transactions on Electron Devices*, vol. 69, pp. 3523–3534, July 2022.
- [78] M. N. Seif, Q. Zhou, X. Liu, T. J. Balk, and M. J. Beck, “Sc-Containing (Scandate) Thermionic Cathodes: Fabrication, Microstructure, and Emission Performance,” *IEEE Transactions on Electron Devices*, vol. 69, pp. 3513–3522, July 2022.
- [79] X. Liu, Q. Zhou, T. L. Maxwell, B. Vancil, M. J. Beck, and T. J. Balk, “Scandate Cathode Surface Characterization: Emission Testing, Elemental Analysis

- and Morphological Evaluation,” *Materials Characterization*, vol. 148, pp. 188–200, 2019.
- [80] S. Yamamoto, “Fundamental physics of vacuum electron sources,” *Reports on Progress in Physics*, vol. 69, pp. 181–232, Jan. 2006.
  - [81] G. Gaertner, P. Geittner, and D. Raasch, “Low temperature and cold emission of scandate cathodes,” *Applied Surface Science*, vol. 201, pp. 61–68, Nov. 2002.
  - [82] G. Gaertner and D. Barratt, “Life-limiting mechanisms in Ba-oxide, Ba-dispenser and Ba-Scandate cathodes,” *Applied Surface Science*, vol. 251, pp. 73–79, Sept. 2005.
  - [83] Q. Zhou, X. Liu, T. Maxwell, B. Vancil, T. J. Balk, and M. J. Beck, “BaxScyOz on W (001), (110), and (112) in scandate cathodes: Connecting to experiment via  $\mu_o$  and equilibrium crystal shape,” *Applied Surface Science*, vol. 458, pp. 827–838, Nov. 2018.
  - [84] A. E. Kandjani, M. F. Tabriz, and B. Pourabbas, “Sonochemical synthesis of ZnO nanoparticles: The effect of temperature and sonication power,” *Materials Research Bulletin*, vol. 43, pp. 645–654, Mar. 2008.
  - [85] M. B. Kasture, P. Patel, A. A. Prabhune, C. V. Ramana, A. A. Kulkarni, and B. L. V. Prasad, “Synthesis of silver nanoparticles by sophorolipids: Effect of temperature and sophorolipid structure on the size of particles,” *Journal of Chemical Sciences*, vol. 120, pp. 515–520, Nov. 2008.
  - [86] M. Mazaheri, A. M. Zahedi, and S. K. Sadrnezhad, “Two-Step Sintering of Nanocrystalline ZnO Compacts: Effect of Temperature on Densification and Grain Growth,” *Journal of the American Ceramic Society*, vol. 91, no. 1, pp. 56–63, 2008.
  - [87] B. Dikici, M. Gavali, and F. Bedir, “Synthesis of in situ TiC nanoparticles in liquid aluminum: The effect of sintering temperature,” *Journal of Composite Materials*, vol. 45, pp. 895–900, Apr. 2011.
  - [88] S. E. Shirsath, R. H. Kadam, A. S. Gaikwad, A. Ghasemi, and A. Morisako, “Effect of sintering temperature and the particle size on the structural and magnetic properties of nanocrystalline  $\text{Li}_{0.5}\text{Fe}_{2.5}\text{O}_4$ ,” *Journal of Magnetism and Magnetic Materials*, vol. 323, pp. 3104–3108, Dec. 2011.

- [89] M. Ardestani, H. R. Rezaie, H. Arabi, and H. Razavizadeh, "The effect of sintering temperature on densification of nanoscale dispersed W-20-40%wt Cu composite powders," *International Journal of Refractory Metals and Hard Materials*, vol. 27, pp. 862-867, Sept. 2009.
- [90] L. Zhang, R. He, and H.-C. Gu, "Synthesis and kinetic shape and size evolution of magnetite nanoparticles," *Materials Research Bulletin*, vol. 41, pp. 260-267, Feb. 2006.
- [91] H. Yoshida, K. Matsuura, Y. Kuwauchi, H. Kohno, S. Shimada, M. Haruta, and S. Takeda, "Temperature-Dependent Change in Shape of Platinum Nanoparticles Supported on CeO<sub>2</sub> during Catalytic Reactions," *Applied Physics Express*, vol. 4, p. 065001, May 2011.
- [92] B. Zhu, J. Meng, and Y. Gao, "Equilibrium Shape of Metal Nanoparticles under Reactive Gas Conditions," *The Journal of Physical Chemistry C*, vol. 121, pp. 5629-5634, Mar. 2017.
- [93] F. Tao, S. Dag, L.-W. Wang, Z. Liu, D. R. Butcher, M. Salmeron, and G. A. Somorjai, "Restructuring of hex-Pt(100) under CO Gas Environments: Formation of 2-D Nanoclusters," *Nano Letters*, vol. 9, pp. 2167-2171, May 2009.
- [94] Y. Jiang, H. Li, Z. Wu, W. Ye, H. Zhang, Y. Wang, C. Sun, and Z. Zhang, "In Situ Observation of Hydrogen-Induced Surface Faceting for Palladium-Copper Nanocrystals at Atmospheric Pressure," *Angewandte Chemie International Edition*, vol. 55, no. 40, pp. 12427-12430, 2016.
- [95] G. D. Barmparis and I. N. Remediakis, "Dependence on CO adsorption of the shapes of multifaceted gold nanoparticles: A density functional theory," *Physical Review B*, vol. 86, p. 085457, Aug. 2012.
- [96] B. Zhu, Z. Xu, C. Wang, and Y. Gao, "Shape Evolution of Metal Nanoparticles in Water Vapor Environment," *Nano Letters*, vol. 16, pp. 2628-2632, Apr. 2016.
- [97] X. Tian, T. Wang, L. Fan, Y. Wang, H. Lu, and Y. Mu, "A DFT based method for calculating the surface energies of asymmetric MoP facets," *Applied Surface Science*, vol. 427, pp. 357-362, Jan. 2018.
- [98] Y.-J.-Z. Xu, J.-X. Shang, and F.-H. Wang, "First-principles study of electronic properties and stability of Nb<sub>5</sub>SiB<sub>2</sub> (001) surface," *Chinese Physics B*, vol. 20, p. 037101, Mar. 2011.

- [99] H. Graoui, S. Giorgio, and C. Henry, “Shape variations of Pd particles under oxygen adsorption,” *Surface Science*, vol. 417, pp. 350–360, Nov. 1998.
- [100] H. Wang and C. Xie, “The effects of oxygen partial pressure on the microstructures and photocatalytic property of ZnO nanoparticles,” *Physica E: Low-dimensional Systems and Nanostructures*, vol. 40, pp. 2724–2729, June 2008.
- [101] M. Zysler and D. Zitoun, “Octahedral to Cuboctahedral Shape Transition in 6 nm Pt<sub>3</sub>Ni Nanocrystals for Oxygen Reduction Reaction Electrocatalysis,” *Particle & Particle Systems Characterization*, vol. 37, no. 4, p. 2000002, 2020.
- [102] S. Sun, J. Zhu, S. Gu, X. Li, W. Lei, Y. Jiang, D. Yi, and G. Chen, “First principles investigation of the surface stability and equilibrium morphology of MoO<sub>3</sub>,” *Applied Surface Science*, vol. 467–468, pp. 753–759, Feb. 2019.
- [103] L. Zhu, K. L. Yao, and Z. L. Liu, “First-principles study of the polar (111) surface of Fe<sub>3</sub>O<sub>4</sub>,” *Physical Review B*, vol. 74, July 2006.
- [104] S. M. Souvi, M. Badawi, J.-F. Paul, S. Cristol, and L. Cantrel, “A DFT study of the hematite surface state in the presence of H<sub>2</sub>, H<sub>2</sub>O and O<sub>2</sub>,” *Surface Science*, vol. 610, pp. 7–15, Apr. 2013.
- [105] J. Noh, O. I. Osman, S. G. Aziz, P. Winget, and J.-L. Brédas, “Magnetite Fe<sub>3</sub>O<sub>4</sub> (111) Surfaces: Impact of Defects on Structure, Stability, and Electronic Properties,” *Chemistry of Materials*, vol. 27, pp. 5856–5867, Sept. 2015.
- [106] N. C. Wilson and S. P. Russo, “Ilmenite (0001) surface investigated using hybrid density functional theory,” *Physical Review B*, vol. 84, Aug. 2011.
- [107] A. Barbier, A. Stierle, F. Finocchi, and J. Jupille, “Stability and stoichiometry of (polar) oxide surfaces for varying oxygen chemical potential,” *Journal of Physics: Condensed Matter*, vol. 20, p. 184014, May 2008.
- [108] N. Wilson, *Investigation of Hybrid Density Functional Theory in the Calculation of the Structure and Properties of Transition Metal Oxides*. P.D., RMIT, Melbourne, AUS, 2009.
- [109] Y. Meng, X.-W. Liu, M. Bai, W.-P. Guo, D.-B. Cao, Y. Yang, Y.-W. Li, and X.-D. Wen, “Prediction on morphologies and phase equilibrium diagram of iron oxides nanoparticles,” *Applied Surface Science*, vol. 480, pp. 478–486, June 2019.

- [110] C. A. Ponce, M. A. Caravaca, and R. A. Casali, “Ab Initio Studies of Structure, Electronic Properties, and Relative Stability of SnO<sub>2</sub> Nanoparticles as a Function of Stoichiometry, Temperature, and Oxygen Partial Pressure,” *The Journal of Physical Chemistry C*, vol. 119, pp. 15604–15617, July 2015.
- [111] F. Mittendorfer, N. Seriani, O. Dubay, and G. Kresse, “Morphology of mesoscopic Rh and Pd nanoparticles under oxidizing conditions,” *Physical Review B*, vol. 76, Dec. 2007.
- [112] M. W. Chase, J. L. Curnutt, A. T. Hu, H. Prophet, A. N. Syverud, and L. C. Walker, “JANAF Thermochemical Tables, 1974 Supplement,” *Journal of Physical and Chemical Reference Data*, p. 171, 1974.
- [113] E. Mohammadpour, M. Altarawneh, Z.-T. Jiang, N. Mondinos, and B. Z. Dlugogorski, “Electronic properties and stability phase diagrams for cubic BN surfaces,” *Molecular Simulation*, vol. 43, pp. 267–275, Mar. 2017.
- [114] Y. Zhang and S. Sanvito, “First-principles investigation of the thermodynamic stability of MB<sub>2</sub> materials surfaces (M = Ti/Zr/Hf),” *Journal of the American Ceramic Society*, vol. 101, no. 9, pp. 4118–4127, 2018.
- [115] A. Togo and I. Tanaka, “First principles phonon calculations in materials science,” *Scripta Materialia*, vol. 108, pp. 1–5, Nov. 2015.
- [116] S. Schönecker, X. Li, B. Johansson, S. K. Kwon, and L. Vitos, “Thermal surface free energy and stress of iron,” *Scientific Reports*, vol. 5, p. 14860, Oct. 2015.
- [117] S. Baroni, P. Giannozzi, and E. Isaev, “Density-Functional Perturbation Theory for Quasi-Harmonic Calculations,” *Reviews in Mineralogy and Geochemistry*, vol. 71, pp. 39–57, Jan. 2010.
- [118] M. Geng and H. Jónsson, “Density functional theory calculations and thermodynamic analysis of bridgmanite surface structure,” *Physical Chemistry Chemical Physics*, vol. 21, no. 3, pp. 1009–1013, 2019.
- [119] P. Kempisty and Y. Kangawa, “Evolution of the free energy of the GaN(0001) surface based on first-principles phonon calculations,” *Physical Review B*, vol. 100, Aug. 2019.
- [120] D. Scheiber, O. Renk, M. Popov, and L. Romaner, “Temperature dependence of surface and grain boundary energies from first principles,” *Physical Review B*, vol. 101, p. 174103, May 2020.



- [121] R. V. Zucker, D. Chatain, U. Dahmen, S. Hagège, and W. C. Carter, “New software tools for the calculation and display of isolated and attached interfacial-energy minimizing particle shapes,” *Journal of Materials Science*, vol. 47, pp. 8290–8302, Dec. 2012.
- [122] B. Fultz, “Vibrational thermodynamics of materials,” *Progress in Materials Science*, vol. 55, pp. 247–352, May 2010.
- [123] G. Wulff, “XXY. Zur Frage der Geschwindigkeit des Wachstums und der Auflösung der Krystallflächen,” *Zeitschrift für Kristallographie*, vol. 34, no. 1-6, p. 82, 1901.
- [124] G. Kresse and J. Furthmüller, “Efficient iterative schemes for *ab initio* total-energy calculations using a plane-wave basis set,” *Physical Review B*, vol. 54, pp. 11169–11186, Oct. 1996.
- [125] J. P. Perdew, K. Burke, and M. Ernzerhof, “Generalized Gradient Approximation Made Simple,” *Physical Review Letters*, vol. 77, pp. 3865–3868, Oct. 1996.
- [126] P. E. Blöchl, “Projector augmented-wave method,” *Physical Review B*, vol. 50, pp. 17953–17979, Dec. 1994.
- [127] D. Singh, S.-H. Wei, and H. Krakauer, “Instability of the ideal tungsten (001) surface,” *Physical Review Letters*, vol. 57, pp. 3292–3295, Dec. 1986.
- [128] M. N. Seif and M. J. Beck, “Surface excess free energies and equilibrium Wulff shapes in variable chemical environments at finite temperatures,” *Applied Surface Science*, vol. 540, p. 148383, Feb. 2021.
- [129] R. Kumar and H. E. Grenga, “Surface energy anisotropy of tungsten,” *Surface Science*, vol. 59, pp. 612–618, Oct. 1976.
- [130] A. Szczepkowicz and A. Ciszewski, “Faceting of curved tungsten surface induced by palladium,” *Surface Science*, vol. 515, pp. 441–452, Sept. 2002.
- [131] T. Acsente, R. Negrea, L. Nistor, E. Matei, C. Grisolia, R. Birjega, and G. Dinescu, “Tungsten nanoparticles with controlled shape and crystallinity obtained by magnetron sputtering and gas aggregation,” *Materials Letters*, vol. 200, pp. 121–124, Aug. 2017.

- [132] C. Arnas, A. Chami, L. Couédel, T. Acsente, M. Cabié, and T. Neisius, “Thermal balance of tungsten monocrystalline nanoparticles in high pressure magnetron discharges,” *Physics of Plasmas*, vol. 26, p. 053706, May 2019.
- [133] M. H. Magnusson, K. Deppert, and J.-O. Malm, “Single-crystalline Tungsten Nanoparticles Produced by Thermal Decomposition of Tungsten Hexacarbonyl,” *Journal of Materials Research*, vol. 15, pp. 1564–1569, July 2000.
- [134] J. C. Tracy and J. M. Blakely, “A study of facetting of tungsten single crystal surfaces,” *Surface Science*, vol. 13, pp. 313–336, Feb. 1969.
- [135] A. Jain, S. Ong, G. Hautier, W. Chen, W. Richards, S. Dacek, S. Cholia, D. Gunter, D. Skinner, G. Cedar, and K. Persson, “The Materials Project: A materials genome approach to accelerating materials innovation,” *APL Materials*, vol. 1, no. 1, 2013.
- [136] A. I. Figner, “Metal-porous body having pores filled with barium scandate (Patent No. 3358178),” Dec. 1967.
- [137] M. N. Seif, T. J. Balk, and M. J. Beck, “Desorption from Hot Scandate Cathodes: Effects on Vacuum Device Interior Surfaces after Long-Term Operation,” *Materials*, vol. 13, p. 5149, Jan. 2020.
- [138] J. D. Wilson, E. G. Wintucky, K. R. Vaden, D. A. Force, I. L. Krainsky, R. N. Simons, N. R. Robbins, W. L. Menninger, D. R. Dibb, and D. E. Lewis, “Advances in Space Traveling-Wave Tubes for NASA Missions,” *Proceedings of the IEEE*, vol. 95, pp. 1958–1967, Oct. 2007.
- [139] Z. Pi and F. Khan, “An introduction to millimeter-wave mobile broadband systems,” *IEEE Communications Magazine*, vol. 49, pp. 101–107, June 2011.
- [140] D. Jiang, S. Hong, C. Zhou, D. Wang, and X. Liu, “Preparation of impregnated barium scandate cathode and its application,” in *IVESC 2004. The 5th International Vacuum Electron Sources Conference Proceedings (IEEE Cat. No.04EX839)*, pp. 206–207, Sept. 2004.
- [141] M. C. Green, “Cathode technology overview - current status amp; future directions,” in *2008 IEEE International Vacuum Electronics Conference*, pp. 3–4, Apr. 2008.

- [142] B. Vancil, I. Brodie, J. Lorr, and V. Schmidt, "Scandate Dispenser Cathodes With Sharp Transition and Their Application in Microwave Tubes," *IEEE Transactions on Electron Devices*, vol. 61, pp. 1754–1759, June 2014.
- [143] J. Wang, W. Liu, L. Li, Y. Wang, Y. Wang, and M. Zhou, "A Study of Scandia-Doped Pressed Cathodes," *IEEE Transactions on Electron Devices*, vol. 56, pp. 799–804, May 2009.
- [144] G. Lesny and R. Forman, "Surface studies on scandate cathodes and synthesized scandates," *IEEE Transactions on Electron Devices*, vol. 37, pp. 2595–2604, Dec. 1990.
- [145] R. Raju and C. Maloney, "Characterization of an impregnated scandate cathode using a semiconductor model," *IEEE Transactions on Electron Devices*, vol. 41, pp. 2460–2467, Dec. 1994.
- [146] J. Zhao, Na Li, Ji Li, L. R. Barnett, M. Banducci, D. Gamzina, Z. A. Munir, and N. C. Luhmann, "High Current Density and Long-Life Nanocomposite Scandate Dispenser Cathode Fabrication," *IEEE Transactions on Electron Devices*, vol. 58, pp. 1221–1228, Apr. 2011.
- [147] H. Yuan, X. Gu, K. Pan, Y. Wang, W. Liu, K. Zhang, J. Wang, M. Zhou, and J. Li, "Characteristics of scandate-impregnated cathodes with sub-micron scandia-doped matrices," *Applied Surface Science*, vol. 251, pp. 106–113, Sept. 2005.
- [148] J. Hasker, J. Van Esdonk, and J. Crombeen, "Properties and manufacture of top-layer scandate cathodes," *Applied Surface Science*, vol. 26, pp. 173–195, Aug. 1986.
- [149] S. Sasaki, I. Amano, T. Yaguchi, N. Matsuzaki, E. Yamada, S. Taguchi, and M. Shibata, "Scandate cathode coated with Mo and Sc films," *Applied Surface Science*, vol. 111, pp. 18–23, Feb. 1997.
- [150] C. Crombeen and J. Hasker, "Some experiments on the role of oxygen and surface reactions for tungsten and scandate thermionic emitters," *IEEE Transactions on Electron Devices*, vol. 37, pp. 2585–2588, Dec. 1990.
- [151] W. Liu, K. Zhang, Y. Wang, K. Pan, X. Gu, J. Wang, J. Li, and M. Zhou, "Operating model for scandate cathode with scandia doped tungsten bodies,"

- in *IVESC 2004. The 5th International Vacuum Electron Sources Conference Proceedings*, pp. 62–64, Sept. 2004.
- [152] J. W. Gibson, G. A. Haas, and R. E. Thomas, “Investigation of scandate cathodes: Emission, fabrication, and activation processes,” *IEEE Transactions on Electron Devices*, vol. 36, pp. 209–214, Jan. 1989.
  - [153] S. Sasaki, T. Yaguchi, N. Mori, S. Taguchi, and M. Shibata, “Nonuniform emission distribution on a scandate impregnated cathode,” *Applied Surface Science*, vol. 146, pp. 17–21, May 1999.
  - [154] B. Vancil, W. L. Ohlinger, M. C. Green, C. Osborne, V. Schmidt, and A. Vancil, “New Findings on Powder Synthesis for Scandate Cathode Matrices,” *IEEE Transactions on Electron Devices*, vol. 65, pp. 2077–2082, June 2018.
  - [155] X. Liu, B. K. Vancil, M. J. Beck, and T. J. Balk, “Near-Surface Material Phases and Microstructure of Scandate Cathodes,” *Materials*, vol. 12, p. 636, Feb. 2019.
  - [156] J. W. Gibbs, *The Scientific Papers of J. Willard Gibbs*. Longmans, Green and Company, 1906.
  - [157] P. Curie, “Sur la formation des cristaux et sur les constantes capillaires de leurs différentes faces,” *Bulletin de Minéralogie*, vol. 8, no. 6, pp. 145–150, 1885.
  - [158] J. W. Martin, R. D. Doherty, and B. Cantor, *Stability of Microstructure in Metallic Systems*. Cambridge University Press, Mar. 1997.
  - [159] M. N. Seif, T. J. Balk, and M. J. Beck, “Deducing surface chemistry and annealing conditions from observed nanoparticle shapes: A study of scandate cathodes,” *Applied Surface Science*, vol. 605, p. 154541, Dec. 2022.
  - [160] J. M. Rahm and P. Erhart, “WulffPack: A Python package for Wulff constructions,” *Journal of Open Source Software*, vol. 5, p. 1944, Jan. 2020.
  - [161] S. De Waele, K. Lejaeghere, M. Sluydts, and S. Cottenier, “Error estimates for density-functional theory predictions of surface energy and work function,” *Physical Review B*, vol. 94, p. 235418, Dec. 2016.
  - [162] K. Reuter and M. Scheffler, “Composition, structure, and stability of  $\mathrm{RuO}_2(110)$  as a function of oxygen pressure,” *Physical Review B*, vol. 65, p. 035406, Dec. 2001.

- [163] X. Huang, B. Wang, E. A. Grulke, and M. J. Beck, "Toward tuning the surface functionalization of small ceria nanoparticles," *The Journal of Chemical Physics*, vol. 140, p. 074703, Feb. 2014.
- [164] O. W. Richardson, *The Emission of Electricity from Hot Bodies*. Longmans, Green and Company, 1921.
- [165] O. Richardson, "Thermionic phenomena and the laws which govern them (Nobel lecture)," 1929.
- [166] S. Dushman, "Thermionic Emission," *Reviews of Modern Physics*, vol. 2, pp. 381–476, Oct. 1930.
- [167] V. Vlahos, J. H. Booske, and D. Morgan, "Ab initio investigation of barium-scandium-oxygen coatings on tungsten for electron emitting cathodes," *Physical Review B*, vol. 81, p. 054207, Feb. 2010.
- [168] M. Mroz, M. E. Kordesch, and J. T. Sadowski, "Scandium function in "scan-date" thermionic cathodes: A microspot synchrotron radiation x-ray photoelectron spectroscopy study of co-adsorbed Ba-Sc-O on W(100)," *Journal of Vacuum Science & Technology A*, vol. 37, p. 030602, Apr. 2019.
- [169] V. Vlahos, Y.-L. Lee, J. H. Booske, D. Morgan, L. Turek, M. Kirshner, R. Kowalczyk, and C. Wilsen, "Ab initio investigation of the surface properties of dispenser B-type and scandate thermionic emission cathodes," *Applied Physics Letters*, vol. 94, p. 184102, May 2009.
- [170] A. Taylor, W. M. Hickam, and N. J. Doyle, "Solid solubility limits of Y and Sc in the elements W, Ta, Mo, Nb, and Cr," *Journal of the Less Common Metals*, vol. 9, pp. 214–232, Sept. 1965.
- [171] M. V. Mroz, T. Savina, M. E. Kordesch, J. T. Sadowski, and S. A. Tenney, "Solid-solid dewetting of scandium thin films on the W(100) surface observed using emission microscopy," *Journal of Vacuum Science & Technology B*, vol. 37, p. 012903, Jan. 2019.
- [172] J. T. Oden, "Finite element method," *Scholarpedia*, vol. 5, p. 9836, 2010.
- [173] J. N. Reddy, *Introduction to the Finite Element Method*. New York, NY: McGraw-Hill Education, 4th edition ed., 2019.

- [174] A. J. Gil, “Structural analysis of prestressed Saint Venant–Kirchhoff hyperelastic membranes subjected to moderate strains,” *Computers & Structures*, vol. 84, pp. 1012–1028, June 2006.
- [175] Y. Saad and M. H. Schultz, “GMRES: A Generalized Minimal Residual Algorithm for Solving Nonsymmetric Linear Systems,” *SIAM Journal on Scientific and Statistical Computing*, vol. 7, pp. 856–869, July 1986.
- [176] P. I. Ravikovitch, G. L. Haller, and A. V. Neimark, “Density functional theory model for calculating pore size distributions: Pore structure of nanoporous catalysts,” *Advances in Colloid and Interface Science*, vol. 76–77, pp. 203–226, July 1998.
- [177] J. Snyder, T. Fujita, M. W. Chen, and J. Erlebacher, “Oxygen reduction in nanoporous metal–ionic liquid composite electrocatalysts,” *Nature Materials*, vol. 9, pp. 904–907, Nov. 2010.
- [178] L. C. Nagle and J. F. Rohan, “Nanoporous Gold Catalyst for Direct Ammonia Borane Fuel Cells,” *Journal of The Electrochemical Society*, vol. 158, pp. B772–B778, July 2011.
- [179] R. Zeis, T. Lei, K. Sieradzki, J. Snyder, and J. Erlebacher, “Catalytic reduction of oxygen and hydrogen peroxide by nanoporous gold,” *Journal of Catalysis*, vol. 253, pp. 132–138, Jan. 2008.
- [180] R. Zeis, A. Mathur, G. Fritz, J. Lee, and J. Erlebacher, “Platinum-plated nanoporous gold: An efficient, low Pt loading electrocatalyst for PEM fuel cells,” *Journal of Power Sources*, vol. 165, pp. 65–72, Feb. 2007.
- [181] A. Wittstock, J. Biener, and M. Bäumer, “Nanoporous gold: A new material for catalytic and sensor applications,” *Physical Chemistry Chemical Physics*, vol. 12, no. 40, p. 12919, 2010.
- [182] A. Thomas, “Graphitic carbon nitride materials: Variation of structure and morphology and their use as metal-free catalysts,” *Journal of Materials Chemistry*, vol. 18, no. 41, pp. 4893–4908, 2008.
- [183] H.-J. Jin and J. Weissmüller, “Bulk Nanoporous Metal for Actuation,” *Advanced Engineering Materials*, vol. 12, pp. 714–723, Aug. 2010.

- [184] M. Hakamada, S. Matsumura, and M. Mabuchi, “Electrochemical actuation of nanoporous Ni in NaOH solution,” *Materials Letters*, vol. 70, pp. 132–134, Mar. 2012.
- [185] J. Biener, A. Wittstock, L. A. Zepeda-Ruiz, M. M. Biener, V. Zielasek, D. Kramer, R. N. Viswanath, J. Weissmüller, M. Bäumer, and A. V. Hamza, “Surface-chemistry-driven actuation in nanoporous gold,” *Nature Materials*, vol. 8, pp. 47–51, Jan. 2009.
- [186] E. Detsi, M. S. Sellès, P. R. Onck, and J. T. M. De Hosson, “Nanoporous silver as electrochemical actuator,” *Scripta Materialia*, vol. 69, pp. 195–198, July 2013.
- [187] Z. Liu and P. C. Searson, “Single Nanoporous Gold Nanowire Sensors,” *The Journal of Physical Chemistry B*, vol. 110, pp. 4318–4322, Mar. 2006.
- [188] P. Daggumati, Z. Matharu, and E. Seker, “Effect of Nanoporous Gold Thin Film Morphology on Electrochemical DNA Sensing,” *Analytical Chemistry*, vol. 87, pp. 8149–8156, Aug. 2015.
- [189] F. Ruffino and M. G. Grimaldi, “Nanoporous Gold-Based Sensing,” *Coatings*, vol. 10, p. 899, Sept. 2020.
- [190] H. Zhu, Y. Xu, A. Liu, N. Kong, F. Shan, W. Yang, C. J. Barrow, and J. Liu, “Graphene nanodots-encaged porous gold electrode fabricated via ion beam sputtering deposition for electrochemical analysis of heavy metal ions,” *Sensors and Actuators B: Chemical*, vol. 206, pp. 592–600, Jan. 2015.
- [191] X. Lang, H. Yuan, Y. Iwasa, and M. Chen, “Three-dimensional nanoporous gold for electrochemical supercapacitors,” *Scripta Materialia*, vol. 64, pp. 923–926, May 2011.
- [192] Xingyou Lang, A. Hirata, T. Fujita, and Mingwei Chen, “Nanoporous metal/oxide hybrid electrodes for electrochemical supercapacitors,” *Nature Nanotechnology*, vol. 6, pp. 232–236, Apr. 2011.
- [193] D. Ji, T. Li, and H. Fuchs, “Patterning and applications of nanoporous structures in organic electronics,” *Nano Today*, vol. 31, p. 100843, Apr. 2020.
- [194] B. Paul, E. M. Björk, A. Kumar, J. Lu, and P. Eklund, “Nanoporous Ca<sub>3</sub>Co<sub>4</sub>O<sub>9</sub> Thin Films for Transferable Thermoelectrics,” *ACS Applied Energy Materials*, vol. 1, pp. 2261–2268, May 2018.

- [195] A. A. Ensafi, S. E. Moosavifard, B. Rezaei, and S. K. Kaverlavani, “Engineering onion-like nanoporous  $\text{CuCo}_2\text{O}_4$  hollow spheres derived from bimetal–organic frameworks for high-performance asymmetric supercapacitors,” *Journal of Materials Chemistry A*, vol. 6, pp. 10497–10506, June 2018.
- [196] A. D. Kurilov, V. V. Belyaev, K. D. Nesseimon, E. D. Besprozvannyi, A. O. Osin, O. A. Tokareva, and A. Y. Skvortsov, “Thermal conductivity performance of nanoporous plate for high-power LED lighting and power electronics,” *Journal of Physics: Conference Series*, vol. 1309, p. 012016, Aug. 2019.
- [197] S. P. Adiga, C. Jin, L. A. Curtiss, N. A. Monteiro-Riviere, and R. J. Narayan, “Nanoporous membranes for medical and biological applications,” *Wiley interdisciplinary reviews. Nanomedicine and nanobiotechnology*, vol. 1, no. 5, pp. 568–581, 2009.
- [198] C. E. Ashley, E. C. Carnes, G. K. Phillips, D. Padilla, P. N. Durfee, P. A. Brown, T. N. Hanna, J. Liu, B. Phillips, M. B. Carter, N. J. Carroll, X. Jiang, D. R. Dunphy, C. L. Willman, D. N. Petsev, D. G. Evans, A. N. Parikh, B. Chackerman, W. Wharton, D. S. Peabody, and C. J. Brinker, “The targeted delivery of multicomponent cargos to cancer cells by nanoporous particle-supported lipid bilayers,” *Nature Materials*, vol. 10, pp. 389–397, May 2011.
- [199] E. Gultepe, D. Nagesha, S. Sridhar, and M. Amiji, “Nanoporous inorganic membranes or coatings for sustained drug delivery in implantable devices,” *Advanced Drug Delivery Reviews*, vol. 62, pp. 305–315, Mar. 2010.
- [200] G. Jeon, S. Y. Yang, and J. K. Kim, “Functional nanoporous membranes for drug delivery,” *Journal of Materials Chemistry*, vol. 22, pp. 14814–14834, July 2012.
- [201] M. Bosman, G. R. Anstis, V. J. Keast, J. D. Clarke, and M. B. Cortie, “Light Splitting in Nanoporous Gold and Silver,” *ACS Nano*, vol. 6, pp. 319–326, Jan. 2012.
- [202] T. V. Teperik, V. V. Popov, F. J. García de Abajo, T. A. Kelf, Y. Sugawara, J. J. Baumberg, M. Abdelsalem, and P. N. Bartlett, “Mie plasmon enhanced diffraction of light from nanoporous metal surfaces,” *Optics Express*, vol. 14, no. 25, p. 11964, 2006.



- [203] T. V. Teperik, V. V. Popov, and F. J. García de Abajo, “Void plasmons and total absorption of light in nanoporous metallic films,” *Physical Review B*, vol. 71, p. 085408, Feb. 2005.
- [204] S. R. Gowda, A. Leela Mohana Reddy, X. Zhan, H. R. Jafry, and P. M. Ajayan, “3D Nanoporous Nanowire Current Collectors for Thin Film Microbatteries,” *Nano Letters*, vol. 12, pp. 1198–1202, Mar. 2012.
- [205] C. Hou, X.-Y. Lang, G.-F. Han, Y.-Q. Li, L. Zhao, Z. Wen, Y.-F. Zhu, M. Zhao, J.-C. Li, J.-S. Lian, and Q. Jiang, “Integrated Solid/Nanoporous Copper/Oxide Hybrid Bulk Electrodes for High-performance Lithium-Ion Batteries,” *Scientific Reports*, vol. 3, Dec. 2013.
- [206] S. Kondrat, C. R. Pérez, V. Presser, Y. Gogotsi, and A. A. Kornyshev, “Effect of pore size and its dispersity on the energy storage in nanoporous supercapacitors,” *Energy & Environmental Science*, vol. 5, pp. 6474–6479, Mar. 2012.
- [207] X.-L. Wu, L.-Y. Jiang, F.-F. Cao, Y.-G. Guo, and L.-J. Wan, “LiFePO<sub>4</sub> Nanoparticles Embedded in a Nanoporous Carbon Matrix: Superior Cathode Material for Electrochemical Energy-Storage Devices,” *Advanced Materials*, vol. 21, pp. 2710–2714, July 2009.
- [208] M. P. Klein, B. W. Jacobs, M. D. Ong, S. J. Fares, D. B. Robinson, V. Stavila, G. J. Wagner, and I. Arslan, “Three-Dimensional Pore Evolution of Nanoporous Metal Particles for Energy Storage,” *Journal of the American Chemical Society*, vol. 133, pp. 9144–9147, June 2011.
- [209] N. J. Briot, *Nanomechanical and Scaling Behavior of Nanoporous Gold*. PhD thesis, University of Kentucky, Lexington, KY, 2015.
- [210] Y. Sun, J. Ye, A. M. Minor, and T. J. Balk, “In situ indentation of nanoporous gold thin films in the transmission electron microscope,” *Microscopy Research and Technique*, vol. 72, pp. 232–241, Mar. 2009.
- [211] T. J. Balk, C. Eberl, Y. Sun, K. J. Hemker, and D. S. Gianola, “Tensile and Compressive Microspecimen Testing of Bulk Nanoporous Gold,” *JOM; New York*, vol. 61, pp. 26–31, Dec. 2009.
- [212] J. Biener, A. M. Hodge, A. V. Hamza, L. M. Hsiung, and J. H. Satcher, “Nanoporous Au: A high yield strength material,” *Journal of Applied Physics*, vol. 97, p. 024301, Dec. 2004.

- [213] N. Abdolrahim, D. F. Bahr, B. Revard, C. Reilly, J. Ye, T. J. Balk, and H. M. Zbib, “The mechanical response of core-shell structures for nanoporous metallic materials,” *Philosophical Magazine*, vol. 93, pp. 736–748, Mar. 2013.
- [214] C. A. Volkert, E. T. Lilleodden, D. Kramer, and J. Weissmüller, “Approaching the theoretical strength in nanoporous Au,” *Applied Physics Letters*, vol. 89, p. 061920, Aug. 2006.
- [215] C. A. Volkert and E. T. Lilleodden, “Size effects in the deformation of sub-micron Au columns,” *Philosophical Magazine*, vol. 86, pp. 5567–5579, Nov. 2006.
- [216] J. Biener, A. M. Hodge, J. R. Hayes, C. A. Volkert, L. A. Zepeda-Ruiz, A. V. Hamza, and F. F. Abraham, “Size Effects on the Mechanical Behavior of Nanoporous Au,” *Nano Letters*, vol. 6, pp. 2379–2382, Oct. 2006.
- [217] N. Mameka, K. Wang, J. Markmann, E. T. Lilleodden, and J. Weissmüller, “Nanoporous Gold—Testing Macro-scale Samples to Probe Small-scale Mechanical Behavior,” *Materials Research Letters*, vol. 4, pp. 27–36, Jan. 2016.
- [218] D. Lee, X. Wei, X. Chen, M. Zhao, S. C. Jun, J. Hone, E. G. Herbert, W. C. Oliver, and J. W. Kysar, “Microfabrication and mechanical properties of nanoporous gold at the nanoscale,” *Scripta Materialia*, vol. 56, pp. 437–440, Mar. 2007.
- [219] M. Hakamada and M. Mabuchi, “Mechanical strength of nanoporous gold fabricated by dealloying,” *Scripta Materialia*, vol. 56, pp. 1003–1006, June 2007.
- [220] X.-Y. Sun, G.-K. Xu, X. Li, X.-Q. Feng, and H. Gao, “Mechanical properties and scaling laws of nanoporous gold,” *Journal of Applied Physics*, vol. 113, p. 023505, Jan. 2013.
- [221] C. J. Ruestes, D. Schwen, E. N. Millán, E. Aparicio, and E. M. Bringa, “Mechanical properties of Au foams under nanoindentation,” *Computational Materials Science*, vol. 147, pp. 154–167, May 2018.
- [222] B. Roschning and N. Huber, “Scaling laws of nanoporous gold under uniaxial compression: Effects of structural disorder on the solid fraction, elastic Poisson’s ratio, Young’s modulus and yield strength,” *Journal of the Mechanics and Physics of Solids*, vol. 92, pp. 55–71, July 2016.

- [223] N. J. Briot, T. Kennerknecht, C. Eberl, and T. J. Balk, “Mechanical properties of bulk single crystalline nanoporous gold investigated by millimetre-scale tension and compression testing,” *Philosophical Magazine*, vol. 94, pp. 847–866, Mar. 2014.
- [224] N. J. Briot and T. J. Balk, “Developing scaling relations for the yield strength of nanoporous gold,” *Philosophical Magazine*, vol. 95, pp. 2955–2973, Sept. 2015.
- [225] L. J. Gibson and M. F. Ashby, *Cellular Solids: Structure and Properties*. Cambridge Solid State Science Series, Cambridge: Cambridge University Press, second ed., 1997.
- [226] M. F. Ashby, A. G. Evans, N. A. Fleck, L. J. Gibson, J. W. Hutchinson, and H. N. G. Wadley, *Metal Foams: A Design Guide*. Woburn, MA: Butterworth-Heinemann, 2000.
- [227] N. Huber, R. Viswanath, N. Mameka, J. Markmann, and J. Weißmüller, “Scaling laws of nanoporous metals under uniaxial compression,” *Acta Materialia*, vol. 67, pp. 252–265, Apr. 2014.
- [228] N. Huber, “Connections Between Topology and Macroscopic Mechanical Properties of Three-Dimensional Open-Pore Materials,” *Frontiers in Materials*, vol. 5, 2018.
- [229] L.-Z. Liu, X.-L. Ye, and H.-J. Jin, “Interpreting anomalous low-strength and low-stiffness of nanoporous gold: Quantification of network connectivity,” *Acta Materialia*, vol. 118, pp. 77–87, Oct. 2016.
- [230] L.-Z. Liu and H.-J. Jin, “Scaling equation for the elastic modulus of nanoporous gold with “fixed” network connectivity,” *Applied Physics Letters*, vol. 110, p. 211902, May 2017.
- [231] K. Hu, M. Ziehmer, K. Wang, and E. T. Lilleodden, “Nanoporous gold: 3D structural analyses of representative volumes and their implications on scaling relations of mechanical behaviour,” *Philosophical Magazine*, vol. 96, pp. 3322–3335, Dec. 2016.
- [232] C. Soyarslan, S. Bargmann, M. Pradas, and J. Weissmüller, “3D stochastic bicontinuous microstructures: Generation, topology and elasticity,” *Acta Materialia*, vol. 149, pp. 326–340, May 2018.

- [233] C. Soyarslan, H. Argeso, and S. Bargmann, “Skeletonization-based beam finite element models for stochastic bicontinuous materials: Application to simulations of nanoporous gold,” *Journal of Materials Research*, pp. 1–12, July 2018.
- [234] G. Pia and F. Delogu, “Nanoporous Au: Statistical analysis of morphological features and evaluation of their influence on the elastic deformation behavior by phenomenological modeling,” *Acta Materialia*, vol. 85, pp. 250–260, Feb. 2015.
- [235] M. J. Beck, “Computational Materials Science at the University of Kentucky.” [beckdt.engr.uky.edu](http://beckdt.engr.uky.edu).
- [236] M. N. Seif, D. J. Richardson, K. M. Moody, M. Martin, M. Turner, S. W. Mays, T. John Balk, and M. J. Beck, “Stochastic approach for determining properties of randomly structured materials: Effects of network connectivity,” *Acta Materialia*, p. 117382, Oct. 2021.
- [237] J. F. Nye, *Physical Properties of Crystals: Their Representation by Tensors and Matrices*. New York, NY: Oxford University Press, 1985.
- [238] D. E. L. Christiansen, “Handbook for Designing MMOD Protection,” p. 152, 2009.
- [239] A. Klavzar, M. Chiroli, A. Jung, and B. Reck, “Protective Performance of Hybrid Metal Foams as MMOD Shields,” *Procedia Engineering*, vol. 103, pp. 294–301, 2015.
- [240] E. Buenrostro and D. Whisler, “Impact response of a low-cost randomly oriented fiber foam core sandwich panel,” *Journal of Composite Materials*, vol. 52, pp. 3429–3444, Oct. 2018.
- [241] S. O. Ryan, “Hypervelocity Impact Performance of Open Cell Foam Core Sandwich Panel Structures,” in *Hypervelocity Impact Symposium*, (Freiburg, Germany), Jan. 2010.
- [242] X. Zhang, R. Wang, and Q. Li, “Modeling of Hypervelocity Impact of Sandwiched Open Cell Aluminum Foam,” *Procedia Engineering*, vol. 204, pp. 262–269, 2017.
- [243] M. Kader, M. Islam, P. Hazell, J. Escobedo, M. Saadatfar, A. Brown, and G. Appleby-Thomas, “Modelling and characterization of cell collapse in aluminium foams during dynamic loading,” *International Journal of Impact Engineering*, vol. 96, pp. 78–88, Oct. 2016.

- [244] J. L. Hyde, E. L. Christiansen, and D. M. Lear, “Observations of MMOD Impact Damage to the ISS,” p. 10, 2019.
- [245] NASA, “Independent Review of Orion Micrometeoroid and Orbital Debris Risk Assessment.” [http://www.nasa.gov/offices/nesc/home/Feature\\_Orbital\\_Debris\\_Risk.html](http://www.nasa.gov/offices/nesc/home/Feature_Orbital_Debris_Risk.html), June 2013.
- [246] T. Sgobba, P. D. Wilde, I. Rongier, and F. A. Allahdadi, “Chapter 1 - Introduction to Space Operations Safety,” in *Safety Design for Space Operations* (F. A. Allahdadi, I. Rongier, and P. D. Wilde, eds.), pp. 1–25, Oxford: Butterworth-Heinemann, Jan. 2013.
- [247] ERGAerospace, “Private Communication,” 2021.
- [248] M. Alnæs, J. Blechta, J. Hake, A. Johansson, B. Kehlet, A. Logg, C. Richardson, J. Ring, M. E. Rognes, and G. N. Wells, “The FEniCS Project Version 1.5,” *Archive of Numerical Software*, vol. 3, Dec. 2015.
- [249] W.-Y. Jang, A. M. Kraynik, and S. Kyriakides, “On the microstructure of open-cell foams and its effect on elastic properties,” *International Journal of Solids and Structures*, vol. 45, pp. 1845–1875, Apr. 2008.

## Vita

Mujan N. Seif was born in Dearborn, MI in 1994. She attended the University of Kentucky where she earned a Bachelor of Science in Materials Engineering, graduating in May of 2017. After a year of post-baccalaureate research at the University of Michigan, she began a Ph.D. program in Materials Engineering at the University of Kentucky in 2018, under the supervision of Professor Matthew J. Beck. During her graduate studies, she received the Outstanding Collegiate Member Award from the Society of Women Engineers in 2019, a Space Technology Graduate Research Fellowship from NASA in 2020, and the MSE Outstanding Graduate Student Award from the Department of Chemical and Materials Engineering in 2021 and 2022.

Mujan N. Seif defended her doctoral dissertation in September 2022 and received her Doctor of Philosophy in December of the same year. In the fall of 2022, she joined the Solid Mechanics and Materials Engineering Group at the University of Oxford as a Postdoctoral Researcher.

## Publications

1. **M.N. Seif**, T.J. Balk, M.J. Beck. Deducing surface chemistry and annealing conditions from observed nanoparticle shapes: a study of scandate cathodes. *Applied Surface Science*, (2022): 154541.
2. **M.N. Seif**, Q. Zhou, X. Liu, T.J. Balk, M.J. Beck. “Sc-containing (Scandate) Thermionic Cathodes: Mechanisms for Sc Enhancement of Emission,” *IEEE Transactions on Electron Devices*, 69(7), 2022.
3. **M.N. Seif**, Q. Zhou, X. Liu, T.J. Balk, M.J. Beck. “Sc-containing (Scandate) Thermionic Cathodes: Fabrication, Microstructure, and Emission Performance,” *IEEE Transactions on Electron Devices*, 69(7), 2022.
4. **M.N. Seif**, D.J. Richardson, K.M. Moody, M. Martin, M. Turner, S.W. Mays, T.J. Balk, M.J. Beck. Stochastic approach for determining properties of randomly structured materials: Effects of network connectivity. *Acta Materialia* (2021): 117382.
5. **M.N. Seif**, M.J. Beck. Surface energies and equilibrium Wulff shapes in variable chemical environments at finite temperatures. *Applied Surface Science*, 540(2), 2021.

6. **M.N. Seif**, T.J. Balk, M.J. Beck. Desorption from Hot Scandate Cathodes: Effects on Vacuum Device Interior Surfaces after Long-Term Operation. *Materials*, 13(22), 2020.
7. **M.N. Seif**, M.J. Beck. Shape Memory Polymers: A Joint Chemical and Materials Engineering Hands-On Experience. *Chemical Engineering Education*, 52(1), 2018.